Development of Native Ion Mobility-Mass Spectrometry Approaches for the Structural Characterization of Antibody-Based Therapeutics

by

Rosendo C. Villafuerte-Vega

A dissertation submitted in partial fulfillment
of the requirements for the degree of
Doctor of Philosophy
(Chemistry)
in the University of Michigan
2024

Doctoral Committee:

Professor Brandon T. Ruotolo, Chair
Professor Ryan C. Bailey
Professor Kristina L. Håkansson
Professor Peter M. Tessier

Rosendo C. Villafuerte-Vega

rcvilla@umich.edu

ORCID iD: 0000-0002-3969-7381

© Rosendo C. Villafuerte-Vega 2024

Dedication

To my lifelong friends, Perla, Marilyn, and Nick, for your unconditional love and support. To my Mom, for teaching me to be kind and resilient. To Em, for being a constant light in my life.

Acknowledgements

Pursuing a Ph.D. has been one of the most challenging, rewarding feats that I have undertaken. I am entirely grateful for the individuals who supported me throughout my academic journey. First and foremost, I would like to express my deepest gratitude to my research advisor, Professor Brandon Ruotolo, for his unwavering mentorship, encouragement, and compassion throughout my journey. Brandon, thank you for not only being such a great research advisor, but also for being patient with me as I navigated through many life challenges. Not many individuals would be capable of doing what you do for your students, and it has been an absolute honor and pleasure to learn from such a brilliant mind. I could not have wished for a more outstanding advisor.

Thank you to my committee members: Professor Ryan Bailey, for being so welcoming and enthusiastic during my MCORE visit and providing constructive feedback; Professor Kristina Håkansson, for being my first mentor in mass spectrometry and challenging me to think critically; and Professor Peter Tessier, for sharing his expertise in antibody engineering and addressing my questions regarding antibody structure and function.

I would also like to my collaborators at Bristol Myers Squibb: Dr. Guodong Chen, Dr. Li Tao, Dr. Thomas Slaney, and Dr. Naresh Chennamsetty. Thank you for the opportunity to work on some exciting biologics, for the engaging, productive conversations we had during project update meetings, and for funding a great portion of my research. I would also like to acknowledge the Rackham Graduate School for providing me with a Rackham Merit Fellowship

that funded four semesters of my work. Thank you to my collaborators at the University of Southampton: Professor Mark Cragg, for kickstarting such an exciting collaboration with our lab; Dr. Hayden Fisher, for answering all of my questions despite the time zone difference; and Izzy Elliot, for being a rockstar and helping me make sense of the mass spectrometry data. Thank you to my colleagues at AbbVie, Hetal Sarvaiya, Dr. Yihan Li, Dr. Paramasivam Natarajan, and Dr. Vikram Shenoy, for introducing me to the world of big pharma. Yihan and Hetal – thank you for your support and mentorship during my internship and helping me navigate career opportunities. My internship at AbbVie truly helped me solidify my career goals, and I am excited for what lies ahead.

Thank you to my labmates – both old and new. Dr. Sarah Fantin, for being such a great friend during my first year and helping me survive the pandemic via game nights on Zoom (or was it BlueJeans?). Dr. Daniel Vallejo, for his mentorship during my first year and for being patient with me during my rotations. Dr. Varun Gadkari, for being available to answer any questions that I had regarding instrumentation. Dr. Kristine Parson, for you incredibly fun spirit and helping me navigate a lot of life hurdles and my imposter syndrome. Dr. Yilin Han, for being such a ray of sunshine in the office. Dr. Carolina Rojas-Ramirez, for being one of my biggest cheerleaders even before I joined the group. Dr. Brock Juliano, for making me laugh through our fake rivalry. And Dr. Chae Kyung Jeon, for being my fellow Korean food connoisseur and answering all of my software-related questions.

Henry and Addison, thank you for your incredible contributions to my research and for making me laugh on a daily basis. Nicole, thank you for giving me the opportunity to mentor you. It has been an absolute pleasure to watch you grow and overcome so many challenges. ¡Estoy muy orgulloso de ti! Joseph, thank you for being such a great roommate and friend; you

and Ashley truly made my time in Michigan memorable. Michael, thank you for your willingness to listen to my academic musings, as well as for feeding into my newly discovered old-fashioned obsession. Kiani, my fellow British gal, thank you for being such a great friend, roommate, and mentor. Thank you for your patience, kindness, and compassion. You have been there for me through some tough times, and I appreciate you for every single thing you have done for me. Kate, Caela, Alyssa, Amanda, Ten, Tiam, and Vanessa – I am very excited to see what you all will accomplish, and I hope that your experiences are as rewarding as mine. Marcella, my fellow Latina, I am extremely grateful for our friendship that has developed in the past few months; thank you for letting me spoil Drag Race for you. Iliana, I hope it goes to show that you and I have been through so much during our time in Michigan, but these life events really brought us close and have created a very strong friendship. You are such an incredibly intelligent, kind, and resilient individual, and navigating our Ph.D.s together has truly been a blessing. Despite the fact that you divorced me for a whole year (the disrespect), we have conquered so many goals together and have overcome some of the most challenging events that life has thrown at us. I am incredibly proud of us.

Thank you to all of my friends outside of my research group who have made my time in Michigan enjoyable. Emory, thank you giving me Covid at ASMS, even when you still deny it, and for cheering me on during my job search. Laura, thank you for the laughs and constant confidence boosts – I really needed them. Ashley, thank you for being willing to listen and offer me some great life advice (as well as your dog, Rosie, for all the cuddles). Chris, thank you for the game nights and for always reaching out to check in. Gloria, thank you for being such a great friend while I was in the Bay Area during my internship, and for being one of my first friends when I arrived in Michigan. Nhat and Lizzy, thank you for your friendship and for welcoming

me with open arms whenever I visit you both. Truly, the list of friends I owe thanks to is limitless; I appreciate and love all of you.

To my partner, Tanner – thank you for your unwavering support and understanding as I was going through the dissertation writing process. Your patience and encouragement helped me cross the finish line, even when I constantly reminded you that I wanted to give up. I am deeply grateful for your presence and love during this significant chapter of my life, as well as for feeding me some of your deliciously acclaimed creations from your sparkly clean kitchen. You inspire me to be the best version of myself. I love you dearly, and I am excited for our adventures on the East Coast.

Finally, thank you to my family. To my little sisters, Perla and Marilyn, and my little brother, Nick, thank you for being some of my biggest fans while growing up. All of you inspire me to do my best not only as a big brother but also as a human being. Ma, quiero expresarte mi más profundo agradecimiento por todo lo que has hecho por mí. Gracias por estar pendiente de mí durante mi tiempo fuera de la casa, aunque a veces no contesto el teléfono. Gracias por recordarme que la vida es hermosa y por enseñarme el poder de la resiliencia. ¡Los quiero muchísimo!

Table of Contents

Dedication ii

Acknowledgements iii

List of Tables x

List of Figures xi

List of Appendices xxi

Abstract xxii

Chapter 1: Introduction 1

1.1 Antibody-Based Therapeutics: Impact and Challenges 1

1.2 Structures of Antibody Therapeutics and Related Products 2

1.3 Analytical Platforms for Higher Order Structure (HOS) Characterization 7

1.3.1 Separation Methods 7

1.3.2 Spectroscopy and Other Biophysical Approaches 9

1.3.3 Structural Mass Spectrometry (MS) 11

1.4 Native Ion Mobility-Mass Spectrometry (IM-MS) 14

1.4.1 Ion Generation and Preservation of 'Native-Like' Structures 15

1.4.2 High-Mass Ion Selection and Detection 17

1.4.3 IM Separation: Fundamental Principles 20

1.4.4 Collision-Induced Unfolding (CIU) for HOS and Stability Assessment 23

1.5 Dissertation Overview 26

1.6 References 29

Chapter 2: Ion Mobility-Mass Spectrometry and Collision-Induced Unfolding of Designed Bispecific Antibody Therapeutics....42

2.1 Original Publication....42

2.2 Author Contributions....42

2.3 Abstract....42

2.4 Introduction....43

2.5 Experimental Section....47

2.6 Results and Discussion....50

2.7 Conclusions....60

2.8 References....61

Chapter 3: Ion Mobility-Mass Spectrometry and Collision-Induced Unfolding Unveil Structure-Function Relationships of Human IgG2 Cysteine to Serine Exchange Variants....66

3.1 Original Publication....66

3.2 Author Contributions....66

3.3 Abstract....67

3.4 Introduction....67

3.5 Experimental Section....70

3.6 Results and Discussion....74

3.7 Conclusions....90

3.8 References....92

Chapter 4: Ion Mobility-Mass Spectrometry and Collision-Induced Unfolding Rapidly Characterize the Structural Polydispersity and Stability of an Fc-Fusion Protein....96

4.1 Original Publication....96

4.2 Author Contributions....96

4.3 Abstract....96

4.4 Introduction....98

4.5 Experimental Section 101

4.6 Results and Discussion 107

4.7 Conclusions 119

4.8 References 120

Chapter 5: A Novel *In Vitro* Serum Stability Assay for Antibody Therapeutics Incorporating Internal Standards 126

5.1 Original Publication 126

5.2 Author Contributions 126

5.3 Abstract 126

5.4 Introduction 127

5.5 Experimental Section 130

5.6 Results and Discussion 134

5.7 Conclusions 141

5.8 References 143

Chapter 6: Conclusions and Future Directions 146

6.1 Conclusions 146

6.2 Future Directions 149

6.2.1 Expanding CIU beyond Knob-into-Hole Bispecific Antibodies 149

6.2.2 Isotype Switching and Its Implications on IgG Gas-Phase Structure and Stability 151

6.2.3 Exploring the Effects of Linker Type, Length, and Composition on the HOS of Fc-Fusion Proteins 153

6.2.4 Development of Automated Native MS Approaches to Measure *In Vitro* Serum Stability of Antibody Therapeutics 154

6.3 References 155

Appendices 158

List of Tables

Appendix Table A-1: Average masses assigned to native MS peaks in equilibrium with G10 across all concentrations of G10 probed. 165

Appendix Table A-2: Average masses assigned to native MS peaks in equilibrium with G14 across all concentrations of G14 probed. 169

Appendix Table D-1: Optimized cIM sequence settings for native cIM and CIU experiments. 197

Appendix Table D-2: Comparisons of averaged experimental and literature $^{TW}\Omega_{N2}$ values of protein standards. 198

Appendix Table D-3: Deconvoluted masses of Fc-IL-10 before and after treatment with EndoS2 or PNGase F. 199

Appendix Table D-4: Deconvoluted masses of Fc and IL-10 subunits generated via GlySERIAS^{TM} digestion 200

Appendix Table E-1: International Nonproprietary Names (INNs) of antibodies assessed in this work..... 207

Appendix Table E-2: *In vitro* serum results for NISTmAb in mouse serum. 208

Appendix Table E-3: *In vitro* serum results for NISTmAb in rat serum. 208

Appendix Table E-4: *In vitro* serum results for NISTmAb in cynomolgus monkey serum. 208

Appendix Table E-5: *In vitro* serum results for NISTmAb Fc fragment in mouse serum. 209

Appendix Table E-6: *In vitro* serum results for NISTmAb Fc fragment in rat serum..... 209

Appendix Table E-7: *In vitro* serum results for NISTmAb Fc fragment in cynomolgus monkey serum. 209

List of Figures

Figure 1-1: Structures of IgG and its subclasses**.** (A) The conventional Y-shaped structure of IgG is made up of two Hcs and two Lcs held together by disulfide bridges (yellow). An IgG consists of three different regions: the Fc and two Fabs linked together by a flexible hinge region. Each Hc contains three constant domains (C_H1, C_H2, C_H3, blue) and one variable domain (V_H, light blue), whereas each Lc contains one constant domain (C_L, red) and one variable domain (V_L, salmon). *N*-linked glycans of different compositions are present in the C_H2 domain of the Fc region. (B) Atomic model structure of NISTmAb (IgG1κ) generated in Ref.[22] (C) Structures of the IgG subclasses. Structural variations in the hinge region of each subclass are shown. Figure is partially adapted from Ref.[21] 3

Figure 1-2: Schematic of the Waters Synapt G2 quadrupole-ion mobility-time-of-flight mass spectrometer (Q-IM-ToF-MS). The instrument is composed of four main components: a nESI source for ion generation; a modified, high-mass (up to 32,000 m/z) quadrupole for ion selection; a tri-wave region for ion mobility separation; and a ToF mass analyzer for ion mass detection and analysis. A closer look at the Tri-Wave region (inset) shows four major regions: a trap (blue) and transfer ion guide (pink) pressurized with argon gas; an ion mobility separator (IMS, orange) pressurized with nitrogen gas; and a helium cell operating as a buffer region between the low-pressure ion trap and the high-pressure IMS, minimizing ion activation. Typical gas flow values (mL/min) are shown..... 14

Figure 1-3: Overview of the nESI process. (A) Schematic of droplet formation and fission during ESI in positive ion mode. (B) Representation of the charged residue model (CRM) pathway for flexible IgG-based antibodies as proposed by Ref.[140] Droplets containing partially flexible IgG molecules gradually undergo desolvation and fission events that force them into more compact topologies. The charges (red) of the evaporating droplets are then transferred to the surfaces of individual IgG molecules that have collapsed around their hinge regions..... 16

Figure 1-4: Schematic highlighting the basic principles of an IM-MS experiment. Ions generated via nESI travel through a drift cell pressurized with a neutral gas and held under the influence of a weak electric field (top, middle). Larger, more elongated ions (red) will collide more frequently with background gas molecules, thus taking them longer to traverse the drift cell compared to smaller, more compact ions (blue). Following IM separation, ions are injected into an orthogonal ToF mass analyzer for *m/z* analysis (bottom, middle). Both dimensions of the data can then be plotted as a heat map (right), where ions of the same *m/z* can be conformationally distinguished..... 21

Figure 1-5: Overview of the typical CIU workflow for a Waters Synapt G2 TWIM platform. (A) Protein ions across different charge states are subjected to collisions with background neutral gas molecules in the trap ion guide. (B) As protein ions are collisionally activated in a

stepwise manner, they begin to unfold, leading to an increase in their $^{TW}\Omega$ values. (C) IM-MS data is then processed with CIUSuite 2 (v.2.3), [165] permitting a variety of different data processing modules: the smoothing of data and generation of a CIU fingerprint; the detection of feature $^{TW}\Omega$ values for compact and unfolded conformations; the fitting of a logistic function between adjacent features to determine CIU_{50} values; the RMSD analysis of CIU data to quantitate global differences between proteins; and the comparison of gas-phase stabilities between proteins using CIU_{50} values. 23

Figure 1-6: The current CIU landscape for antibody-based therapeutics. CIU has been applied to various antibody therapeutic modalities such as conventional IgGs (subclasses),[168,169] multi- and bispecific antibodies,[170,171] ADCs,[172,173] and Fc-fusion proteins (discussed in Chapter 4). CQAs such as glycosylation[174] and aggregation[175] have also been probed with CIU, especially in the context of assessing the structures of innovator biologics and their biosimilars.[176,177] CIU has also been extended to the study of large mAb-antigen (Ag) complexes[178] and domain-exchanged mAbs.[179] 25

Figure 2-1: CIU experiments of native, unmodified knob (blue) and hole (orange) homodimers and KiH bsAb heterodimer (green). (A) Averaged CIU fingerprints (n = 3) for the 24^+ charge state (left) with corresponding replicate RMSD baselines (right). All fingerprints show three main features indicated by the dashed white boxes. Normalized $^{TW}CCS_{N2}$ distributions at (B) 5 V, (C) 65 V, (D) 110 V. At lower activation potentials, all antibodies adopt similar $^{TW}CCS_{N2}$ distributions, which significantly diverge at higher acceleration potentials. (E) Pairwise RMSD analysis reveals global HOS differences among antibodies compared to replicate RMSD baselines (dashed lines). (F) CIU_{50} analysis illustrates how the model KiH bsAb adopts a stability between those of knob and hole homodimers. 52

Figure 2-2: CIU data recorded for knob and hole halfmers. (A) Averaged CIU fingerprints (n = 3) for 16^+ charge states. (B) Pairwise RMSD analyses reveal significant differences between halfmer HOSs. (C) CIU_{50} analysis shows significant differences (**** $p < 0.0001$) in protein stabilities. 54

Figure 2-3: CIU data recorded for Fab and Fc fragments. (A) Averaged CIU fingerprints (n = 3) for 13^+ charge states. (B) Pairwise RMSD analysis reveals significant differences between knob and hole Fab fragments. (C) CIU_{50} analysis indicates significant differences (** $p < 0.01$, **** $p < 0.0001$) in fragment stabilities. 55

Figure 2-4: CIU of deglycosylated knob and hole homodimers and KiH bsAb heterodimer 24^+ ions (n = 3). (A) RMSD analysis comparing control and deglycosylated antibodies reveals significant differences in HOS. (B) CIU_{50}-1 and (C) CIU_{50}-2 analysis reveals significant destabilization of antibodies after deglycosylation (** $p < 0.01$, *** $p < 0.001$). (D) Plot of differences in CIU_{50} values between control and deglycosylated antibodies. 58

Figure 3-1: Native IM-MS measurements of ChiLob7/4 variants. (A) Representative IM-MS spectra of C232S + C233S and C232S κC214S variants reveal native-like charge state distributions. Masses ± mass error of the charge states sampled for mass deconvolution are shown. (B) $^{TW}\Omega_{N2}$ values as a function of charge state. $^{TW}\Omega_{N2}$ errors shown were obtained by propagating uncertainties associated with n = 3 technical replicates, calibrated $^{TW}\Omega_{N2}$ values of

*h*IgGs, and experimental $^{TW}\Omega_{N2}$ values of the calibrants used (see Methods). (C) Gaussian peak fittings for the $^{TW}\Omega_{N2}$ distributions of charge state 23^+. Vertical error bars represent the s.d. in intensities technical replicates, while horizontal error bars represent the uncertainties in calibrated $^{TW}\Omega_{N2}$ values. (D) Top: structures of ChiLob7/4 variants highlighting an increase in agonistic activity from red to blue. *h*IgG1 and *h*IgG2 WT are nonagonistic and agonistic, respectively. Bottom: peak width analysis of charge states 22^+ and 23^+. Peak width data are plotted as mean ± s.d. of peak fittings of technical replicates. 75

Figure 3-2: CIU analysis scrutinizes the effects of hinge disulfide variation on *h*IgG structure and stability. (A) Left: Averaged CIU fingerprints (n = 3) for the 24^+ charge state of ChiLob7/4 variants. Right: $^{TW}\Omega_{N2}$ distributions of each variant at 5 (dashed lines, open circles) and 175 V (solid lines, closed circles) during CIU. Vertical and horizontal error bars represent s.d. of technical replicates and calibrated $^{TW}\Omega_{N2}$ uncertainties, respectively. (B) Pairwise RMSD comparisons of C232S κC214S with other variants. (C) Similarity scores comparing the $^{TW}\Omega_{N2}$ distributions of either C232S + C233S (open circles) or C232S κC214S (closed circles) to those of other variants. (D) Left: representative plots showing sigmodal fitting of the first CIU transition. Right: CIU_{50} values for the first CIU transition shown as mean ± s.d. (E) $^{TW}\Omega_{N2}$ values of the first CIU feature shown as mean ± propagated $^{TW}\Omega_{N2}$ error. Data in (A) and (C) are shown as mean ± s.d. of nine comparisons between technical replicates of each variant. 80

Figure 3-3: CIU detects comparable changes in the structures and stabilities of F(ab')$_2$ fragments. (A) Left: Averaged CIU fingerprints (n = 3) for the 21^+ charge state of ChiLob7/4 F(ab')$_2$ fragments. Right: $^{TW}\Omega_{N2}$ distributions of each variant at 4 (dashed lines, open circles) and 120 V (solid lines, closed circles) during CIU. Vertical and horizontal error bars represent s.d. of technical replicates and $^{TW}\Omega_{N2}$ uncertainties, respectively. (B) CIU_{50} values for the CIU transition between features two and three. Data are shown as mean ± s.d. (C) $^{TW}\Omega_{N2}$ values of features one (left) and two (right) shown as mean ± propagated $^{TW}\Omega_{N2}$ error. (D) Pairwise RMSD comparisons of C232S κC214S with other variants. (E) Similarity scores comparing the $^{TW}\Omega_{N2}$ distributions of either C232S + C233S (open circles) or C232S κC214S (closed circles) to those of other variants. Data in (D) and (E) are shown as mean ± s.d. of nine comparisons between technical replicates of each variant. 84

Figure 3-4: CIU rapidly classifies C/S variants of the anti-4-1BB (CD137) mAb, SAP1.3. (A) Left: averaged CIU fingerprints (n = 3) for the 24^+ charge state of each variant. Right: $^{TW}\Omega_{N2}$ distributions of each variant at 5 (dashed lines, open circles) and 175 V (solid lines, closed circles). Vertical and horizontal error bars represent s.d. of technical replicates and $^{TW}\Omega_{N2}$ uncertainties, respectively. (B) CIU_{50} values for the first CIU transition shown as mean ± s.d. (C) $^{TW}\Omega_{N2}$ values of the first CIU feature shown as mean ± propagated $^{TW}\Omega_{N2}$ error. (D) CIU classification workflow: (i) assignment of CIU training data sets to classes, (ii) selection of voltage steps better suited in distinguishing classes; nine voltages were selected (red), (iii) cross-validation analysis tests the accuracy of the classification model, (iv) linear discriminate analysis enables sorting of training data sets into two classes, (v) replicates not used as training data are correctly assigned to their respective classes. Probabilities are shown as mean ± s.d. of classification results for technical replicates..... 86

Figure 3-5: CIU probes the structures and stabilities of novel C/S *h*IgG2 variants. (A) Schemes for the full-length variants with insets highlighting the disulfides present in their hinge regions. (B) Averaged CIU fingerprints (n = 3) for the 24^+ charge state of ChiLob7/4 (top) and SAP1.3 (bottom). Vertical and horizontal error bars represent s.d. of technical replicates and $^{TW}\Omega_{N2}$ uncertainties, respectively. (C) Similarity scores acquired from comparisons to C232S + C233S (open circles) and C232S κC214S (closed circles) variants for ChiLob7/4 (top) and SAP1.3 (bottom). Scores are shown as mean ± s.d. of nine comparisons between technical replicates of each variant. (D) Summary of $^{TW}\Omega_{N2}$ (solid colors) and CIU_{50} values (color stripes) for ChiLob7/4 (top) and SAP1.3 (bottom) variants (n = 3). $^{TW}\Omega_{N2}$ values are shown as mean ± propagated $^{TW}\Omega_{N2}$ error. CIU_{50} values are shown as mean ± s.d. 89

Figure 4-1: Native IM-MS measurements of Fc-IL-10 and a series of protein standards on a Waters Synapt G2 HDMS IM-MS platform. (A) Representative IM-MS spectrum of Fc-IL-10 reveals a narrow charge state distribution ranging from 16^+ to 22^+. (B). $^{TW}\Omega_{N2}$ values for native Fc-IL-10 and protein standards as a function of charge state. Corresponding RSDs (< 0.3%) are shown for technical replicates (n = 3). (C) Rp (Ω/ΔΩ) of Fc-IL-10 and protein standards. IM Rp values extracted from the three most prominent charge states observed for each protein in triplicate (n = 9). 108

Figure 4-2: CIU experiments of Fc-IL-10 before and after treatment with EndoS2 or PNGase F. (A) CIU fingerprints for charge state 17^+. Features are detected by CIUSuite 2 (v2.3) (left) and subsequently utilized for CIU_{50} stability quantitation (right). Feature three (F3*) in native Fc-IL-10 is labeled but omitted during the fitting of CIU_{50} data. (B) $^{TW}\Omega_{N2}$ distributions of native and deglycosylated Fc-IL-10 at different trap collision voltages. More extended conformations increase in intensity with sequential removal of sugar moieties. (C) CIU_{50} analyses (n = 3) of each transition reveal significant destabilization of Fc-IL-10 after deglycosylation (**p < 0.01, **** < 0.0001). (D) Plots of mean differences in CIU_{50} values. Error bars of these mean differences are given in SEM obtained using a one-way ordinary ANOVA with Tukey correction for multiple comparisons within GraphPad Prism. 110

Figure 4-3: Representative MS spectra of Fc-IL-10 digested with GlySERIAS™ with or without EndoS2. Zoomed-in spectra of non-reduced Fc subunits show different glycoforms and linker variants (A) before and (B) after treatment with EndoS2. Zoomed-in spectra of IL-10 homodimer show comparable linker variants across both sample prep conditions. 112

Figure 4-4: IM-MS and CIU measurements of Fc-IL-10 GlySERIAS digests on a Waters SELECT SERIES cIM-MS platform. (A) Representative cIM-MS spectrum of Fc-IL-10 digested with GlySERIAS™ and EndoS2 at 5 V of trap CE. Zoomed-in spectra show the linker and glycoform polydispersity present in non-reduced Fc and IL-10 homodimer subunits. CIU fingerprints of (B) native Fc, (C) deglycosylated Fc, and (D) IL-10 homodimer subunits. Dashed blue, red, and yellow lines correspond to CIU transitions for native Fc, deglycosylated Fc, and IL-10 homodimer, respectively. 115

Figure 4-5: CIU of different Gly-Ser linker variants of IL-10 homodimer. (A) Representative CIU fingerprints of charge state 11^+ demonstrating the transitional state omitted using the feature skipping function deployed within our version of CIUSuite 2 (v2.3). Subsequent CIU_{50}-1 sigmoidal curve fitting reveals subtle shifts in stability between linker variants. (B) Plot of

CIU_{50}-1 as a function of average linker mass. Averaged CIU_{50}-1 values (n = 3) were fitted with a quadratic function. (C) Plot of RMSD Factor Difference as a function of average linker mass. Averaged factor differences (n = 3) were fitted with a linear function. 95% confidence intervals (dashed lines) are displayed. 117

Figure 5-1: The stabilities of (A) NISTmAb and (B) NISTmAb Fc fragment in PBS buffer and serum of three different species: mouse, rat and cynomolgus monkey. 135

Figure 5-2: The stabilities of (A) Tibulizumab, (B) Tidutamab, (C) Erfonrilimab, (D) INBRX-105, (E) Zanidatamab, (F) CTX-009, (G) Tarlatamab, (H) Glofitamab, and (I) TNB-738 in mouse serum with NISTmAb as internal standard. 136

Figure 5-3: (A) NISTmAb and Amivantamab were not baseline resolved during LC separation. (B) NISTmAb and Amivantamab had overlapped protein envelops in raw MS1 spectra extracted from 6 to 7 min. (C) The deconvoluted mass data of raw MS1 spectra in B (solid black line) was a combination of NISTmAb and Amivantamab. The deconvoluted mass data of NISTmAb standard (dashed red line) and Amivantamab standard (dashed blue line) analyzed individually in LC-MS were provided as a comparison. Mass peak area was integrated between 147,367.5 and 149,367.5 Da (solid pink lines)..... 138

Figure 5-4: The stabilities of (A) Bevacizumab, (B) Dupilumab, (C) Palivizumab, (D) Faricimab, (E) Ixekizumab, (F) Evolocumab, (G) Denosumab, (H) Emicizumab, (I) Amivantamab, (J) Teclistamab, (K) Erfonrilimab, (L) Glofitamab in mouse serum with Fc fragment as internal standard. 139

Figure 5-5: Mouse serum stability of (A) Erfonrilimab and (B) Glofitamab with NISTmAb and Fc fragment as internal standards..... 140

Figure 6-1: Schematic representations of various IgG-like and fragment-based formats for bsAbs. IgG-like formats include KiH, CrossMAb, IgG-scFv, DVD-IgG, Duobody, κλ-body, and formats with common light chains. Fragment-based formats include BiTE, DART, Diabody, TandAbs, and $F(ab')_2$. Heavy chains are shown in blue and yellow. Light chains are shown in light blue and yellow. Abbreviations: KiH, knobs-into-holes; scFv, single-chain variable fragment; DVD-Ig, dual-variable-domain immunoglobulin; BiTE, bispecific T-cell engager; DART, dual-affinity-retargeting; TandAb, tandem diabody. 149

Figure 6-2: CIU (charge state 27^+) of hinge-swapped antibody variants with or without $(GS)_3$ linker insertions. (A) Fingerprints across all variants show four main features that differ across variants, where the appearance of feature three is more prevalent in flexible variants. Feature four is more prevalent in rigid *h*IgG2 variants. (B) Fitting of CIU_{50} values for the first and last CIU transitions (left). *h*IgG2-like variants possessed lower stability values compared to more flexible variants across both transitions (right)..... 151

Figure 6-3: Summary of linker types used in fusion protein construction. Created with BioRender.com. 153

Figure 6-4: *In vitro* serum stability assay workflow. (A) *h*IgG samples are spiked into mouse, rat, or cynomolgus monkey serum and incubated at 37°C for 0, 1, 4, and 7 days. (B) Samples

are then purified using an Agilent AssayMAP Bravo affinity purification system, where biotinylated anti-human IgG is immobilized on streptavidin resin and used to capture and purify *h*IgG samples. This purification step needs to be amended to preserve the folded structures of the antibodies being characterized. (C) Purified samples will then be introduced into an Agilent 6560C IM-Q-ToF system using online sample introduction and desalting via the coupling of an Agilent RapidFire system or an alternative SEC platform. Created with BioRender.com 154

Appendix Figure A-1: Spectra of (A) BIg-*Rb*CBM74-BIg or (B) Sas6T in equilibrium with G10. Charge states for unbound protein are annotated with an orange dashed line. Peaks corresponding to different bound states are observed after each charge state of the unbound protein. 165

Appendix Figure A-2: Native MS of 5 μM protein and ligand. Intensities of each species, combined across multiple charge states, were extracted from the mass spectra and used to calculate the fractional abundance of unbound and bound states at equilibrium. (A) Binding affinities (K_d) calculated from the fractional intensity of each species for G10. N/A, not available. (B,C) Nonlinear least-squares fitting of fractional abundance of unbound and bound states for 0–300 μM G10 with BIg–*Rb*CBM74–BIg (B) and Sas6T (C). Error bars represent standard deviation of three technical replicates. (B), Mean of isotopic distribution of single, double, and triple helices over different concentrations of G10. Error bars represent standard deviation of six scans. (E) K_d calculated from the fractional intensity of each species for G14. (F,G) Nonlinear least-squares fitting of fractional abundance of unbound and bound states for 0–300 μM G14 with BIg–*Rb*CBM74–BIg (F) and Sas6T (G). Error bars represent standard deviation of three technical replicates. (H), Mean of isotopic distribution of single, double, and triple helices over different concentrations of G14. Error bars represent standard deviation of six scans. CL, concentration of the ligand; P, protein; PL, protein–ligand. 166

Appendix Figure A-3: High-resolution MS experiments of G10 alone at (A) 5 μM and (B) 150 μM. A zoomed-in mass spectrum (right) shows the isotopic distributions of oligomeric states at each respective concentration. 168

Appendix Figure A-4: Spectra of (A) BIg-*Rb*CBM74-BIg or (B) Sas6T in equilibrium with G14. Charge states for unbound protein are annotated with an orange dashed line. Peaks corresponding to different bound states are observed after each charge state of the unbound protein. 169

Appendix Figure A-5: High-resolution MS experiments of G14 alone at (A) 5 μM and (B) 150 μM. A zoomed-in mass spectrum (right) shows the isotopic distributions of oligomeric states at each respective concentration. 170

Appendix Figure B-1: (A) Native IM-MS spectra of knob, hole, and KiH bsAb constructs at a collision voltage of 5 V. Intact homodimer and heterodimer are observed, as well as low and high molecular weight species. Here, ‘dimer’ refers to a dimer of homodimer or heterodimer. (B) Theoretical average masses of glycoforms typically observed in antibodies. All native intact masses are non-reduced and include the cyclization of all N-terminal glutamines to pyroglutamate forms. 173

Appendix Figure B-2: SEC-MALS for Knob and Hole samples. (A) SEC-MALS profile of Knob and Hole homodimers and halfmers. (B) Calculated masses of homodimer and halfmer species for both Knob and Hole samples. 174

Appendix Figure B-3: CIU fingerprints of knob (A) and hole (B) homodimers and KiH bsAb heterodimer (C) for charge states 22^+ to 24^+ 175

Appendix Figure B-4: RMSD plots of the 24^+ charge state of knob and hole homodimers and KiH bsAb heterodimer. 176

Appendix Figure B-5: Papain digestion of KiH bsAb. (A) Proposed cleavage site of papain above the hinge region, generating Fab and Fc fragments. (B) IM-MS spectra of KiH bsAb papain digest and (C) comparison of experimental and average theoretical masses. Differences observed between experimental and theoretical masses of $F(ab')_2$ are attributed to non-specific cleavage of the bsAb by papain. The theoretical mass for Fc accounts for two G0F glycosylation sites and cyclization of all N-terminal glutamines to pyroglutamate forms. The experimental mass of the Fc domain accounts all possible glycoforms. 176

Appendix Figure B-6: Native Orbitrap MS of (A) knob and (B) hole homodimers and (C) KiH bsAb heterodimer before and after treatment with PNGase F. Each antibody exhibits different levels of heterogeneity resulting from glycosylation. The increased intensities of homodimer ions compared to halfmer ions is the result of utilizing high *m/z* transfer optics. Neighboring peaks correspond to unresolved adducts, where mass differences range from 18 – 40 Da. (D) Deconvoluted masses of control and deglycosylated knob and hole homodimers and KiH bsAb heterodimer. 177

Appendix Figure B-7: CIU fingerprints of native, deglycosylated knob and hole homodimers and KiH bsAb heterodimer. (A) Averaged CIU fingerprints ($n = 3$) for the 24^+ charge state (left) with corresponding replicate RMSD baselines (right). (B) Pairwise RMSD analysis comparing deglycosylated knob and hole homodimers and KiH bsAb heterodimer. 178

Appendix Figure C-1: IM-MS analysis of ChiLob7/4 variants. (A) Representative IM-MS spectra of variants. Corresponding masses ± mass error of the charge states sampled for mass deconvolution are shown. (B) $^{TW}\Omega_{N2}$ distributions of variants across charge states. Vertical and horizontal error bars represent s.d. of technical replicates ($n = 3$) and $^{TW}\Omega_{N2}$ uncertainties, respectively. 179

Appendix Figure C-2: IM-MS analysis of $F(ab')_2$ fragments of ChiLob7/4 variants generated via IdeS digestion. (A) Representative IM-MS spectra of IdeS digests across variants indicate presence and separation of $F(ab')_2$ and Fc fragments. Corresponding masses ± mass error of the charge states sampled for mass deconvolution are shown. (B) $^{TW}\Omega_{N2}$ distributions of variants across different charge states. Vertical and horizontal error bars represent s.d. of technical replicates ($n = 3$) and $^{TW}\Omega_{N2}$ uncertainties, respectively. **c.** $^{TW}\Omega_{N2}$ values as a function of charge state for the most compact feature in (C) Propagated Ω_{N2} errors are shown. 180

Appendix Figure C-3: Averaged CIU fingerprints for charge states 23^+ to 25^+ of ChiLob7/4 full-length variants. RMSDs values shown as mean ± s.d. from comparisons performed between technical replicates (n = 3)..... 181

Appendix Figure C-4: Light chain is dissociated upon collisional activation during CIU. (A) Representative MS/MS spectra of charge state 24^+ at 100 and 175 V across ChiLob7/4 variants. (B) IM-MS/MS spectra of selected variants at 175 V showing evidence of possible interchain disulfide bonds in the C239S variant (shown as dashed yellow lines in the inset cartoon). 182

Appendix Figure C-5: Averaged CIU fingerprints for charge states 19^+ to 21^+ of ChiLob7/4 $F(ab')_2$ fragments. RMSDs values shown as mean ± s.d. from comparisons performed between technical replicates (n = 3). 183

Appendix Figure C-6: Relative activity and size of (A) ChiLob7/4 and (B) SAP1.3 variants. Activity was assessed using the NFκB GFP Jurkat reporter assay. Relative size represents the maximum intramolecular distance (D_{max}) determined from SAXS experiments. 184

Appendix Figure D-1: Design and corresponding amino acid sequence of Fc-IL-10. Fc-IL-10 is a ~90 kDa Fc-fusion protein that consists of wild-type human IL-10 connected to the C-terminus of a human IgG1 Fc domain via a flexible Gly-Ser linker. An N-glycosylation site is present on the Fc polypeptide chain, which increases the mass of the Fc-fusion protein to ~94 kDa. Adapted from patent WO/2021/158938.[1]..... 185

Appendix Figure D-2: Comparison of experimental measurements versus the measurements reported by Bush et al.[2] and Campuzano et al.[3] These measurements from the literature were performed with a modified Synapt G1 HDMS instrument with an RF-confining drift cell and a commercial Synapt G2 HDMS instrument, respectively. Error bars represent the standard deviation of three comparisons (n = 3) between our experimental data and literature values.... 186

Appendix Figure D-3: Peak widths at half maximum of $^{TW}\Omega_{N2}$ distributions of Fc-IL-10 and protein standards on a Waters Synapt G2 HDMS. Peak widths are calculated from the three most prominent charge states in triplicate (n = 9). Error bars represent the standard deviation of these measurements. 186

Appendix Figure D-4: CIU fingerprints of Fc-IL-10 for charge states 17^+ to 21^+ performed on a Waters Synapt G2 HDMS. Three to six features are qualitatively evident across charge states, highlighting that Fc-IL-10 adopts complex structural ensembles along its gas-phase unfolding pathway. 187

Appendix Figure D-5: CIU fingerprints of NISTmAb for charge states 20^+ to 25^+ performed on a Waters Synapt G2 HDMS. Two to four features are qualitatively observed across charge states..... 187

Appendix Figure D-6: Representative MS spectra of Fc-IL-10 prior to (A) and after the addition of either EndoS2 (B) or PNGase F (C). Zoomed-in spectra of charge state 18^+ reveal the presence different glycoforms..... 188

Appendix Figure D-7: CIU analyses of Fc-IL-10 after treatment with EndoS2 or PNGase F for charge states 17^+ to 20^+. For the sake of clarity, only regions corresponding to the greatest shifts in gas-phase stability are shown in orange. Dashed and solid lines correspond to the CIU transitions of native and deglycosylated Fc-IL-10, respectively. 189

Appendix Figure D-8: Representative HCD MS/MS spectrum of IL-10 homodimer (charge state 13^+). The zoomed-in spectrum reveals the presence of three major Gly-Ser linker variants of IL-10 monomer at 60 CE. 190

Appendix Figure D-9: Representative HCD MS/MS spectra of partially reduced Fc subunits. Both native (A,B) and EndoS2-treated (C,D) digests showed both Fc/2 subunits as well as noncovalent dimeric Fc subunits. Dissociation of noncovalent dimeric Fc (charge state 17^+) was achieved using 100 CE, where zoomed-in spectra reveal the presence of two major Gly-Ser linker variants. 191

Appendix Figure D-10: Representative cIM-MS spectrum of native Fc-IL-10 digested with only GlySERIAS™. Zoomed-in spectra highlight the linker and glycoform polydispersity present in non-reduced Fc and IL-10 homodimer subunits. Spectrum was collected at 5 V of trap CE. 192

Appendix Figure D-11: Cyclic $^{TW}\Omega_{N2}$ distributions of non-reduced native Fc (A), EndoS2-treated Fc (B), and IL-10 homodimer (C) at 4 V of trap CE across different charge states. 193

Appendix Figure D-12: CIU_{50}-1 analysis of non-reduced Fc and IL-10 homodimer subunits. (A) IL-10 homodimer unfolds at significantly lower E_{lab} values (n = 3) than Fc subunits across all detectable charge states. (B) Combined E_{lab} values of all charge states (n = 9) for Fc and IL-10 homodimer subunits. 194

Appendix Figure D-13: Representative CIU fingerprints of different Gly-Ser linker variants of IL-10 homodimer. A qualitative comparison of CIU fingerprints (left) show no immediate differences between linker variants. By performing pairwise RMSD comparisons (right) of these variants, global conformational differences can be detected and quantified. RMSD baseline values are shown for each CIU fingerprint (left). 195

Appendix Figure D-14: Effects of linker length on stability and global conformational differences between linker variants of IL-10 homodimer. Plot of (A) CIU_{50}-1 and (B) RMSD Factor Difference as a function of linker mass. Quadratic and linear functions were fitted to each plot, respectively. Averaged values are shown (n =3) with errors bars shown as standard deviation. 95% confidence intervals of each fit are shown (dashed lines). 196

Appendix Figure E-1: Total ion chromatography (TIC) of Fc fragment. Both NISTmAb and partially digested NISTmAb without one Fab arm were observed with low intensities. 202

Appendix Figure E-2: Stability analysis of (A) Tibulizumab, (B) Tidutamab, (C) Erfonrilimab, (D) INBRX-105, (E) Zanidatamab, (F) CTX-009, (G) Tarlatamab, (H) Glofitamab, and (I) TNB-738 with or without NISTmAb as internal standard..... 203

Appendix Figure E-3: Serum stabilities of (A) Tibulizumab and (B) Erfonrilimab with NISTmAb as internal standard in serum of three different species: mouse, rat and cynomolgus monkey..... 204

Appendix Figure E-4: Stability results of (A) Bevacizumab, (B) Dupilumab, (C) Palivizumab, (D) Faricimab, (E) Ixekizumab, (F) Evolocumab, (G) Denosumab, (H) Emicizumab, (I) Amivantamab, (J) Teclistamab, (K) Erfonrilimab, (L) Glofitamab with or without Fc fragment as internal standard. 205

Appendix Figure E-5: Serum stabilities of (A) Bevacizumab and (B) Dupilumab with Fc fragment as internal standard in serums of three different species: mouse, rat and cynomolgus monkey..... 206

List of Appendices

Appendix A: The *Ruminococcus bromii* amylosome protein Sas6 binds single and double helical α-glucan structures in starch.....159

A.1 Original Publication 159

A.2 Overview 159

A.3 Experimental Section 160

A.4 Results and Discussion..... 165

A.5 References 171

Appendix B: Supporting Information for Chapter 2.....173

Appendix C: Supporting Information for Chapter 3.....179

Appendix D: Supporting Information for Chapter 4.....185

D.1 References 200

Appendix E: Supporting Information for Chapter 5 202

Abstract

Monoclonal antibody (mAb)-based therapeutics have revolutionized the landscape of contemporary medicine. By harnessing the power of the immune system in a controlled manner, these therapeutics have drastically improved patient outcomes in the clinic, delivering more personalized, effective treatment options compared to conventional small molecule drugs. These therapeutics, however, possess complex higher order structure (HOS) features that can be altered by post-translational modifications and degradation. Although high-resolution biophysical tools exist for HOS characterization, they often require long timescales not conducive for the rapid screening of candidate molecules. This limitation necessitates new analytical technologies that can probe HOS with minimal sample preparation and purification. To fill this technology gap, this dissertation presents an ion mobility-mass spectrometry (IM-MS) and collision-induced unfolding (CIU)-based framework for evaluating the structures and stabilities of various emerging mAb-based therapeutic modalities.

In Chapter 2, we combine IM-MS with CIU to probe the gas-phase structures and unfolding pathways of a knob-into-hole (KiH) bispecific antibody (bsAb) and its parent mAbs. By measuring the stabilities of mAb fragments and deglycosylated constructs, we provide a general mechanism for the gas-phase unfolding of the KiH bsAb, where low- and high-energy CIU transitions correspond to the unfolding of Fab and Fc domains, respectively. Specifically, our data indicate that the low-energy Fab unfolding event is driven by the stability of the hole Fab domain, while high-energy transitions are associated with the unfolding of the knob portion

of the Fc. Together, these results provide a unique framework for evaluating the domain-level stabilities of both KiH bsAbs and mAbs using CIU.

Chapter 3 leverages the sensitivity of CIU responses to alterations in hinge disulfide bond configurations to build an assay that accurately predicts mAb flexibility for a series of anti-CD40 human(*h*) IgG2 cysteine to serine (C/S) variants in a manner that correlates with receptor agonism. We find that rigid, agonistic variants, which feature a disulfide crossover within their hinges, experience less gas-phase structural collapse and possess lower gas-phase stabilities than flexible, nonagonistic variants. By using a CIU-based classification approach, we accurately identify *h*IgG2 variants that exhibit optimal immunostimulatory activity, thus demonstrating the ability of CIU to predict mAb structure-function relationships for the first time.

In Chapter 4, we shift our focus to probing the HOS of an Fc-Interleukin-10 (Fc-IL-10) fusion protein engineered using flexible glycine-serine (Gly-Ser) linkers. We demonstrate that Fc-IL-10 is highly dynamic in the gas-phase, generating more structural transitions during CIU and broader IM profiles compared to proteins of similar size. Moreover, we elucidate the gas-phase unfolding pathway of Fc-IL-10 using similar approaches presented in Chapter 2, where we find that low- and high-energy transitions are associated with the unfolding of IL-10 and Fc domains, respectively. Importantly, we observe that an increase in Gly-Ser linker length stabilizes IL-10 dimers, highlighting the potential of CIU to inform the engineering of stable Fc-fusion protein therapeutics.

Lastly, Chapter 5 presents a novel *in vitro* serum stability assay that incorporates stable mAb-based internal standards. Our results indicate that the use of NISTmAb and its Fc fragment as internal standards can improve the accuracy and precision of sample recovery calculations, enabling a more confident stability assessment of mAb therapeutics in serum. Collectively, the

methodologies presented in this dissertation underscore the utility of IM-MS and CIU in probing the domain-level stabilities of mAb-based therapeutics and establishing connections between mAb HOS and function.

Chapter 1: Introduction

1.1 Antibody-Based Therapeutics: Impact and Challenges

Since the approval of the first monoclonal antibody (mAb) therapeutic, muromonab-CD3, in 1986, the antibody therapeutic market has grown substantially.[1, 2] The development of mAbs as therapeutic modalities was made feasible after the introduction of the hybridoma technique by Köhler and Milstein in 1975.[3, 4] Subsequent technological and scientific advances over the past thirty years have further enabled the successful translation of antibody therapeutics and related products to the clinic, leading to effective treatments previously unattainable with conventional small-molecule drugs.[5-7] These advancements have led to the approval of approximately 120 antibody products by the U.S. Food and Drug Administration (FDA), and nearly 140 candidates are currently in late-stage clinical development.[2, 8] Collectively, mAb-based therapeutics have become the predominant treatment modality for a plethora of serious human diseases including cancer, autoimmunity, infectious diseases, and chronic inflammatory diseases.[9-12]

Classical mAb therapeutics function by specifically binding target antigens and inducing cytotoxicity via proapoptotic or neutralizing mechanisms, as well as mediating innate immune responses such as antibody-dependent cellular cytotoxicity (ADCC), antibody-dependent cellular phagocytosis (ADCP), and complement-dependent cytotoxicity (CDC).[13, 14] For proper *in vivo* function and potency, these biologically-derived therapeutics must have a correctly folded three-dimensional (3-D) structure. Incorrectly folded structures and aggregation or oligomerization can lead to undesirable immunogenicity and ultimately compromise biological activity.[15] As a result,

understanding the role of higher order structure (HOS) in the function of mAb therapeutics and related products is critical to ensure their clinical safety and efficacy. The native structures of these biologics can be compromised at any stage during their production and administration, which necessitates the need for reliable, structurally sensitive methodologies that can robustly monitor their conformational integrity during drug discovery and development.

1.2 Structures of Antibody Therapeutics and Related Products

All mAb-related therapeutics are structurally intricate; therefore, their biophysical characterization is quite challenging. Currently, the majority of recombinant therapeutic antibodies generated use the immunoglobulin G (IgG) format.[16] Compared to the other Ig classes (IgA, IgD, IgE, and IgM), IgG is one of the most abundant antibodies in human serum and exhibits the longest half-lives in circulation.[17] Structurally, IgGs are tetrameric glycoproteins consisting of two γ heavy chains (Hc) and two κ or λ light chains (Lc) held together by a combination of disulfide bridges and noncovalent interactions between globular domains, resulting in molecular weights near ~150 kDa (Figure 1-1A). Each Hc is comprised of an N-terminal variable domain (V_H), three constant domains (C_H1, C_H2, and C_H3), and a flexible hinge region between C_H1 and C_H2. Conversely, each light chain consists of a single variable (V_L) and constant domain (C_L). The Lc interacts with the V_H and C_H1 regions of the Hc to form the antigen-binding fragment (Fab), while the C_H2 and C_H3 of the two HCs associate to form the crystallizable fragment (Fc).

Functionally, antigen binding specificity is conferred by hypervariable regions within the variable domains of Fab arms known as complementarity-determining regions (CDRs). The Fc region, on the other hand, mediates a myriad of effector functions that influence multiple facets of innate and adaptive immunity such as ADCC, ADCP, and CDC.[18] These effector functions are

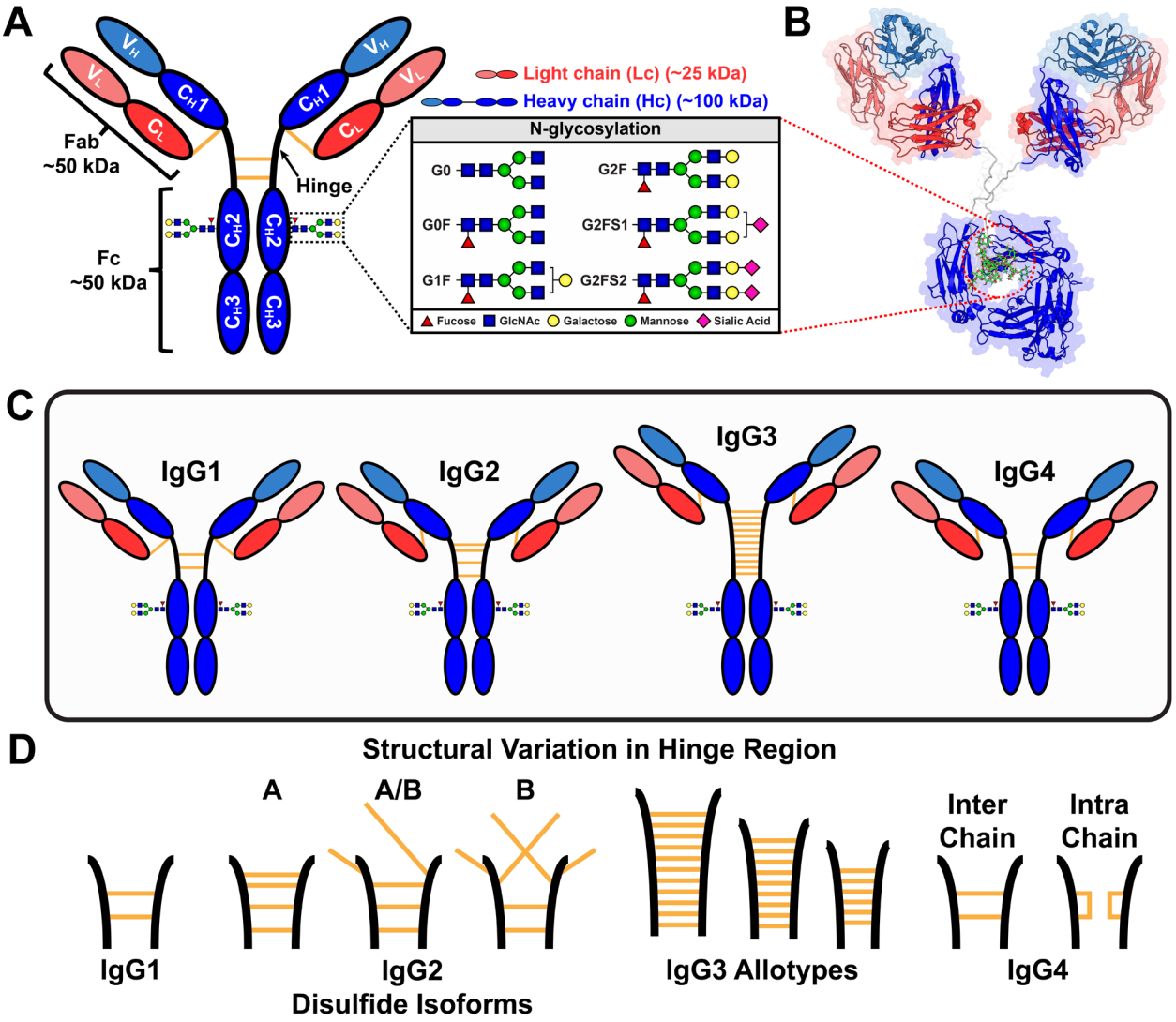

Figure 1-1: Structures of IgG and its subclasses**.** (A) The conventional Y-shaped structure of IgG is made up of two Hcs and two Lcs held together by disulfide bridges (yellow). An IgG consists of three different regions: the Fc and two Fabs linked together by a flexible hinge region. Each Hc contains three constant domains (C_H1, C_H2, C_H3, blue) and one variable domain (V_H, light blue), whereas each Lc contains one constant domain (C_L, red) and one variable domain (V_L, salmon). *N*-linked glycans of different compositions are present in the C_H2 domain of the Fc region. (B) Atomic model structure of NISTmAb (IgG1κ) generated in Ref.[22] (C) Structures of the IgG subclasses. Structural variations in the hinge region of each subclass are shown. Figure is partially adapted from Ref.[21]

further regulated by different levels of glycosylation that occur at a highly conserved asparagine residue (N297) in the C_H2 domain of each Hc.[19-21] This site exhibits complex-type biantennary glycans with different amounts of core fucose (Fuc), bisecting N-acetyl glucosamine (GlcNAc), galactose (Gal), and terminal N-acetylneuraminic acid (Neu5Ac or sialic acid) that fill a large

open pocket between the C_H2 domains[22] (Figure 1-1B). Structurally, the removal of these N-glycans causes a partial closure of the native open conformation of the Fc region, leading to the subsequent loss of biological activities facilitated by Fcγ receptors (FcγRI, FcγRIIa/b/c, and FcγRIIIa/b) and the complement protein, C1q.[20, 23] The molecular composition of these glycans can also affect antibody function. For example, the lack of core fucosylation boosts ADCC activity by increasing interactions with FcγRIIA, while sialylation confers anti-inflammatory properties by inhibiting FcγR binding.[24, 25] Undeniably, N-glycosylation has a multifaceted effect on antibody structure and function, highlighting it as a critical quality attribute (CQA) that needs to be monitored and characterized.

The hinge region of IgGs acts as a flexible linker between Fab arms and the Fc region, and the length, flexibility, and composition of this region exhibit high variability. As such, IgGs can be further divided into subclasses (IgG1, IgG2, IgG3, and IgG4, in order of their decreasing abundance in human serum) that display differences in their hinges and upper C_H2 domains (Figure 1-1C). Notably, the subclasses differ in their interchain disulfide connectivities within their hinge regions, with two interchain disulfide bridges in IgG1 and IgG4, four in IgG2, and eleven in IgG3. Each subclass also possesses an interchain disulfide bridge that connects the carboxy-terminal cysteine each Lc to C220 (in IgG1) or C131 (in IgG2, IgG3, and IgG4) in the C_H1 domain of each Hc.[26]

Regarding hinge length and flexibility, the hinge region of IgG1 is comprised of 15 amino acid residues, making it flexible. In contrast, IgG2 has the shortest hinge of all the subclasses, encompassing only 12 amino acids, and contains a poly-proline helix that is stabilized by up to four interchain disulfide bonds that make it very rigid. IgG2 can distinctively undergo disulfide switching due to natural redox reactions that occur while circulating in the

bloostream, leading to A, A/B, and B structural isoforms that differ in Fab-Fc orientation and flexibility (Figure 1-1D).[27] IgG3, on the other hand, possesses the longest hinge out of all the subclasses, encompassing up to 62 amino acids that vary between IgG3 allotypes.[28, 29] The extended hinge of IgG3 thus permits high rotational freedom and flexibility. Lastly, the IgG4 hinge is comprised of 12 amino acids, making it shorter than the hinge of IgG1, and it possesses an intermediate flexibility between that of IgG1 and IgG2.[30] Compared to IgG1, which contains a rigid cysteine-proline-proline-cysteine (CPPC) motif in its hinge region, the cysteines within the IgG4 hinge core region (cysteine-proline-serine-cysteine-proline, CPSCP) can easily form intrachain disulfide bonds, resulting in a mixture of covalently and non-covalently linked half molecules.[31] Non-covalently linked half-molecules can then reassociate with the half-molecules of other IgG4s *in vivo* through a process known as Fab-arm exchange, generating molecules that are functionally monovalent and bispecific for antigen binding.[32, 33] Due to the aforementioned differences in length and composition, the flexibility of the IgG subclasses can be represented in the order of IgG3 > IgG1 > IgG4 > IgG2, which also closely signifies the relative binding affinities of each for FcγRs and C1q.[26, 30] Since hinge flexibility modulates the relative movement and positioning of Fab and Fc regions, antigen-binding capacities, immune complex formation, and other immunostimulatory activities can also be affected.[30, 34-36]

Most clinically approved recombinant therapeutic antibodies belong to the IgG1, IgG2, and IgG4 subclasses and their variants due to favorable half-lives, and most are IgG1-based.[16] Generally, when designing mAb-based therapeutics, thorough attention must be given to the biological attributes of the targets, the cells that express these targets, and the proposed mechanisms of action (e.g., ADCC, ADCP).[37] Although IgG3 displays the highest affinity for most FcγRs, it possesses the shortest half-life among the IgG subclasses, its purification is costly

due to the absence of binding to protein A, and its polymorphic nature increases its risk for instability and immunogenicity.[28, 37] However, recent efforts have shown that the IgG3 subclass is associated with enhanced protection against a range of intracellular pathogens such as bacteria, parasites, and viruses.[28, 38] For instance, the IgG3 hinge was shown to deliver the most potent intracellular eradication of adenovirus among the four IgG subclasses.[36]

Subsequently, the fruitful clinical application of conventional IgG mAbs has inspired the development of other antibody formats including antibody drug conjugates (ADCs),[39, 40] antibody fusion proteins,[41] bispecific/multispecific antibodies,[42] and antibody fragments.[43] These antibody formats have been successfully accepted as alternative therapeutic agents for a broad range of diseases; however, their expression and manufacturing can be challenging and introduce higher levels of molecular complexity. For example, the production of ADCs leads to a heterogenous pool of molecules varying in drug-to-antibody ratios (DARs) and conjugation sites. This heterogeneity, in turn, can impact the biophysical and biochemical properties of ADCs, which can lead to alterations in structural stability and increase their propensity to aggregate.[44, 45] Additionally, bispecific antibodies (bsAbs) have garnered significant attention due to their dual binding specificity, granting them the ability to target two different antigens simultaneously. The expression and manufacturing of bsAbs require the appropriate pairing of light and heavy chains for the desired specificity; however, this process is often impeded by issues arising from increased structural complexity spanning from biophysical instability to antibody chain mispairing.[46, 47] In the same light, linking proteins (e.g., cytokines) to an IgG Fc domain when engineering Fc-fusion proteins can lead to instability; therefore, care must be taken to ensure the proper folding of each separate protein element during fusion protein design.[48, 49]

1.3 Analytical Platforms for Higher Order Structure (HOS) Characterization

Compared to small molecules, antibody therapeutics, and related products, are engineered using recombinant DNA technology. During any stage of the manufacturing process, these products are susceptible to microheterogeneities associated with a variety of post-translational modifications (PTMs) (e.g., glycosylation, disulfide bond formation) and degradation pathways (e.g., oxidation, deamidation, aggregation).[50, 51] These modifications, in turn, can provoke subtle changes in HOS that can profoundly influence stability, target binding, pharmacokinetics (PK), and pharmacodynamics (PD).[52] As a result, growing concerns regarding the quality, efficacy, and safety of a product throughout its life cycle have steered the development of various analytical strategies that investigate the aforementioned critical quality attributes (CQAs) at different levels, ranging from primary structure (e.g., amino acid sequence, PTMs) to HOS (e.g., protein folding, dynamics).[53-55] In regards to the assessment of protein therapeutic HOS, both separation- and spectroscopy-based platforms are most often used, in addition to other biophysical platforms.

1.3.1 Separation Methods

A variety of separation techniques based on either liquid chromatography (LC) or electrophoresis have been developed to scrutinize protein therapeutics and their heterogeneity. These orthogonal analytical methods aim to separate main protein isoforms from microvariants and impurities, like host cell proteins (HCPs), that are generated during the manufacturing process.[56] Importantly, many separation methods operate using non-denaturing conditions that conserve the folded, native structure of proteins during analysis. As a result, these methods are valuable for elucidating the mechanistic details involved in the formation of protein complexes, as well for tracking the formation of antibody-antigen complexes and monitoring the aggregation rates of protein therapeutic agents.

Among current non-denaturing LC methods, size exclusion (SEC), hydrophobic interaction (HIC), and ion-exchange (IEC) chromatography have been extensively utilized in the development and characterization of biopharmaceuticals.[56, 57] IEC is particularly useful in the separation and assessment of protein charge variants (i.e., acidic and basic variants) resulting from different chemical and enzymatic modifications; it is also useful in the removal of a wide range of impurities such as HCPs, DNA, and endotoxins during early or late stage purification steps.[58-60] SEC, which separates proteins based on their hydrodynamic radius (size), has been extensively utilized for the evaluation of protein fragmentation and aggregation since the mild mobile phase conditions used have minimal impact on non-covalent protein-protein interactions and the conformational state of proteins.[61] When coupled with multi-angle light scattering (MALS), the absolute molar masses, oligomeric states, and hydrodynamic radii of native proteins in solution can be accurately calculated, independent of the protein retention times acquired using SEC alone.[62, 63] Alternatively, HIC can be used to separate proteins based on their surface hydrophobicity. Specifically, HIC has been widely exploited in the analysis of ADCs, particularly in the separation of different DAR species of thiol conjugated (cysteine linked) antibodies.[64] Since ADC cytotoxic payloads must penetrate the lipid membrane to properly function, they need to be lipophilic in nature. As a result, their conjugation increases the hydrophobicity of the resulting ADCs, leading to an increase in protein retention time.[64, 65]

Capillary electrophoresis (CE)-based methods have also garnered extensive use in the analysis of biopharmaceuticals due to their high-resolution separations, high peak capacities, and compact instrumental designs. Generally, experiments across different electrophoretic modes apply a high electric field to separate proteins based on differences in their size, charge, and hydrophobic properties without the need of a stationary phase that is necessary in LC-based

separations.[56] Chief among these modes in capillary zone electrophoresis (CZE), which separates proteins based their mass-to-charge ratios. This CE mode, in particular, has permitted the detection of mAb proteoforms as well as low-abundance truncated species and aggregates when analyzed under non-denaturing conditions.[66, 67] Another CE mode, capillary isoelectric focusing (cIEF), achieves the separation of proteins based on their isoelectric points (pIs).[56] Recently, cIEF has been utilized in a narrow pH range as a sample stacking method in native CZE separations, permitting the detection and characterization of glycol-proteoforms, variants, and aggregates of SigmaMAb and NISTmAb.[68] Importantly, all the aforementioned LC and CE approaches have been hyphenated to mass spectrometry (MS) for the structural characterization of mAb-based therapeutics.[69-72] Further implications of MS as an indispensable tool in the characterization of protein therapeutic HOS will be discussed later in this chapter.

1.3.2 Spectroscopy and Other Biophysical Approaches

Besides separation methods, the existing toolkit for the characterization of mAb-based therapeutics also comprises an assortment of biophysical techniques capable of providing HOS information at various resolutions. Structural biology tools like X-ray crystallography, nuclear magnetic resonance (NMR) spectroscopy, and cryo-electron microscopy (cryo-EM) are critical for the production of atomically-resolved high-quality structures of proteins and protein complexes; however, each technique has both advantages and limitations, particularly in the context of antibody-based therapeutics.

X-ray crystallography provides a detailed structural blueprint of the arrangement of atoms within a protein by analyzing the diffraction patterns generated when X-rays are directed at a crystallized protein sample.[73] As a result, x-ray crystallography is often considered the gold standard for epitope mapping, for it provides an atomically resolved picture of antibody-antigen

interactions.[74] However, producing high-quality crystals of full-length mAbs, especially when bound to their respective antigens, is difficult due to their large size and inherent conformational dynamism and flexibility. Therefore, most of the structures deposited in the Protein Data Bank (PDB) are those of antibody fragments (e.g., Fab, Fc, and $F(ab')_2$), while only four full-length IgG antibody crystal structures are currently publicly available.[75-78]

Crystalline structures obtained from X-ray crystallography are static; therefore, they do not fully represent the dynamic structural features of antibodies and other flexible protein therapeutics in solution. In contrast, NMR spectroscopy can provide atomic-level insights into protein structure and dynamics in solution.[79] In NMR spectroscopy, a protein sample is placed in a strong magnetic field and is exposed to pulses of radio waves of specific frequencies. The behavior of the atomic nuclei within the protein is then analyzed to evaluate their local environments within the protein structure, and such information is used in combination with molecular dynamics (MD) simulations to produce atomic models.[80] However, this method is typically limited to proteins smaller than a full-length IgG (~150 kDa), and large amounts of purified samples are needed.[81]

Although in its infancy, cryo-EM has successfully permitted the visualization of large macromolecular complexes (>100 kDa), including antibody-antigen assemblies, at near-atomic resolution.[82, 83] Cryo-EM involves quickly freezing protein samples in a thin layer of vitreous ice to perverse their native structure. Using an electron microscope, images of the frozen samples can be captured from different angles; these images can then be combined to generate 3-D models of proteins.[84] Compared to X-ray crystallography, cryo-EM permits the generation of countless images of flash-frozen of proteins that cannot easily form high-quality crystals. Despite this complementary advantage, cryo-EM requires large quantities of purified protein and

sophisticated computational methods for data analysis, making it resource-intensive, low-throughput, and unsuitable for early-stage protein therapeutic candidate screening and characterization.[85]

Collectively, the sample requirements, low-throughput, cost, and difficulty of atomic-level techniques have limited their routine use within the biopharmaceutical pipeline. As a result, other classical, more straightforward approaches such as ultraviolet spectroscopy (UV),[86] circular dichroism (CD),[87] Fourier-transform infrared (FT-IR) spectroscopy,[88] analytical ultracentrifugation (AUC),[89] dynamic light scattering (DLS),[90] and differential scanning calorimetry (DSC)[91] have dominated the biophysical characterization of antibody-based therapeutics and related products. Although these techniques are sensitive and free of molecular size limitations, they provide low-resolution structural information that is spatially averaged over the entire protein population, and they assess a very limited number of specific moieties within a protein structure. For example, DSC is often considered the gold standard for the thermodynamic stability analysis of antibody therapeutics in solution.[92] Globally, DSC measures changes in heat capacities as a function of temperature; these changes are indicative of thermal transitions occurring within a protein, such as unfolding. However, DSC suffers from lengthy data acquisition times, requires large amounts of purified sample, and often provides ambiguous information for complex samples.

1.3.3 Structural Mass Spectrometry (MS)

Over the past two decades, MS has become an indispensable analytical tool in pharmaceutical research and development, enabling the rapid assessment of protein therapeutic primary structure, PTMs, and HOS using minimal quantities of protein sample in the presence of microheterogeneities.[53, 55] As previously described, MS can be coupled to both LC- and CE-

based separation methods, further ameliorating its ability to provide intact- and peptide-level information from complex mixtures. Regarding MS-based structural biology, a variety of different approaches can provide complementary information about protein HOS. Surface labeling-based approaches, such as hydrogen deuterium-exchange (HDX) or hydroxyl radical protein footprinting (HRPF), can robustly examine protein-protein and protein-small molecule interactions in solution; thus, these methods have been very effective in performing antibody epitope mapping.[93-95] Despite their advancements, these technologies still predominantly rely on peptide-centric proteomics strategies that may not provide complete sequence coverage of large proteins that exhibit high structural dynamism, and they often generate complex datasets that require sophisticated computational tools for accurate analysis and interpretation.[96, 97]

In contrast, native MS has emerged as a transformative technology in structural biology that can capture and assess the native-like architectures of proteins and their non-covalent complexes.[98] Native MS differs from other forms of MS in that proteins are introduced into the mass analyzer under mild conditions, typically utilizing non-denaturing solvents and volatile salts (e.g., ammonium acetate), to preserve their native-like conformations from solution into the gas-phase. As a result, native MS can provide valuable insights into protein size, composition, stoichiometry, and conformational heterogeneity, as well as its interactions with ligands or other biomolecules.[99] Importantly, these measurements can be performed rapidly with high sensitivity, and they require small quantities of sample and minimal sample preparation.[100]

One of the first demonstrations of native MS for the analysis of antibodies successfully captured an antibody-antigen complex, revealing a 1:2 antibody:antigen stoichiometry.[101] Native MS has also been applied to the accurate quantitation of DAR values for cysteine-conjugated ADCs by permitting the analysis of intact constructs; this type of intact analysis of thiol-drug

ADCs is typically unachievable with conventional denaturing LC-MS approaches.[102-104] As previously mentioned, the coupling of separation methods such as SEC,[105, 106] IEC,[107, 108] HIC,[69, 109] and CE[70] with native MS has also enabled the separation of various microheterogeneities and proteoforms within therapeutic antibodies. Furthermore, commercial ion-trap-based platforms like Orbitrap mass analyzers have been optimized for mass measurements of large macromolecular assemblies.[98] Recent Orbitrap-based mass analyzers, in particular, have incorporated improved ion optics in the front end of the instrument that have greatly improved ion cooling and desolvation of large macromolecular complexes.[110, 111] These modifications have enabled high-resolution native MS measurements that unravel the structural features and heterogeneities of ribosomal particles,[111, 112] viral assemblies,[111, 113] megadalton (mDa) IgM and antibody-antigen complexes,[114, 115] and heavily glycosylated protein therapeutics.[116, 117]

Native MS has also been coupled with ion mobility to reveal additional HOS information regarding protein structure, dynamics, and stability.[118] The adoption of native ion mobility-mass spectrometry (IM-MS) for industrial analytical characterization, however, has been a slow process.[119] Nevertheless, as antibody therapeutic modalities (e.g., bsAbs, ADCs, and Fc-fusion proteins) continue to evolve beyond the conventional IgG scaffold, there is a growing need to study these biomacromolecules under conditions that mimic native-like, physiologically environments. To address this need, this dissertation focuses on the development and validation of native IM-MS-based approaches for the characterization of protein HOS across different antibody-based therapeutic modalities. An overview of native IM-MS, as well as its applicability in studying conformationally dynamic protein therapeutics, will be discussed in the following section.

1.4 Native Ion Mobility-Mass Spectrometry (IM-MS)

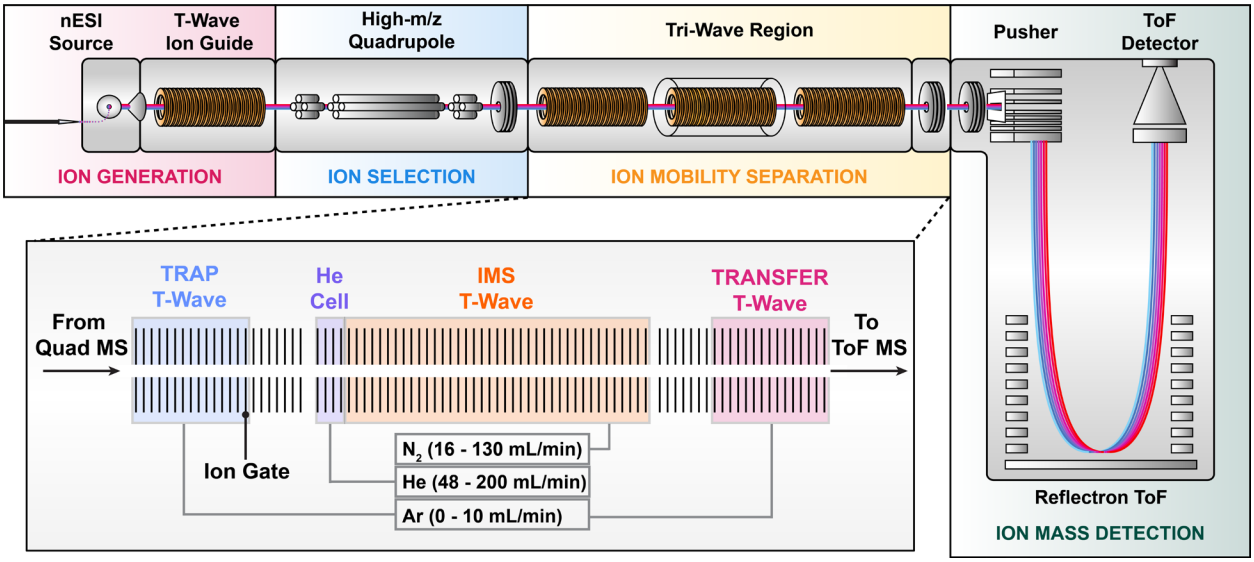

Figure 1-2: Schematic of the Waters Synapt G2 quadrupole-ion mobility-time-of-flight mass spectrometer (Q-IM-ToF-MS). The instrument is composed of four main components: a nESI source for ion generation; a modified, high-mass (up to 32,000 m/z) quadrupole for ion selection; a tri-wave region for ion mobility separation; and a ToF mass analyzer for ion mass detection and analysis. A closer look at the Tri-Wave region (inset) shows four major regions: a trap (blue) and transfer ion guide (pink) pressurized with argon gas; an ion mobility separator (IMS, orange) pressurized with nitrogen gas; and a helium cell operating as a buffer region between the low-pressure ion trap and the high-pressure IMS, minimizing ion activation. Typical gas flow values (mL/min) are shown.

Since the release of the first commercial IM-MS instrument, the Waters Synapt, in 2006, IM-MS has garnered much interest in the biopharmaceutical industry for its ability in analyzing various classes of molecules ranging in size, charge, and chemical composition.[120] When combined with nano-electrospray ionization (nESI) and native solution conditions, IM-MS has shown great promise in revealing HOS information of antibody-based therapeutics and related products by means of their rotationally averaged collision cross sections (Ω).[118] For instance, some of the first IM-MS measurements of therapeutic antibodies successfully captured mAbs in complex with JAM-A, an antigenic protein overexpressed in tumor cells,[121] and resolved the hinge disulfide structural isoforms of human IgG2s.[122] Both of these studies were conducted using travelling-wave ion mobility (TWIM) separations on the first-generation Waters Synapt

IM-MS platform. A second-generation rendition of this instrument, the Synapt G2 HDMS, was released in 2009 and has demonstrated improvements in mobility resolution and Ω accuracy.[123, 124] A schematic of this platform, which consists of a nESI source, a quadrupole mass analyzer, a T-Wave IM separator, and an orthogonal time-of-flight (ToF) mass analyzer, is shown in Figure 1-2. Because the majority of the measurements presented in this dissertation were performed on this system, the rest of this section will focus on TWIM-based separations and ToF-MS measurements. The generation of gas-phase protein ions via nESI will first be discussed.

1.4.1 Ion Generation and Preservation of 'Native-Like' Structures

Since the late 1980s, ESI has enabled the generation of intact gas-phase ions from various large biological macromolecules and their complexes in solution.[125] Considered a "soft" ionization technique, ESI produces multiply charged ($z > 1$) ions with minimal activation. The generation of multiply charged ions, in turn, permits the detection of large biomolecules (e.g., proteins and nucleic acids) on MS platforms with limited mass-to-charge (m/z) ranges.[126] Subsequent discussion of the ESI process will be limited to the commonly used positive ion mode, in which the spraying capillary is held at a positive potential. Mechanistically, ESI begins by applying a high voltage to a conductive capillary containing analyte solution (Figure 1-3A). Subsequently, the solution at the tip of the capillary forms into a Taylor cone that emits a fine spray of charged droplets. These droplets are then gently dried down with the assistance of a nebulizing gas, resulting in a reduction in droplet diameter. As a result, the charge density of the shrinking droplets increases until the Columbic repulsion spatially separating positive charges becomes greater than the surface tension of the droplet, leading to droplet fission. The maximum amount of charge that can be carried by a droplet before inducing these fission events is known

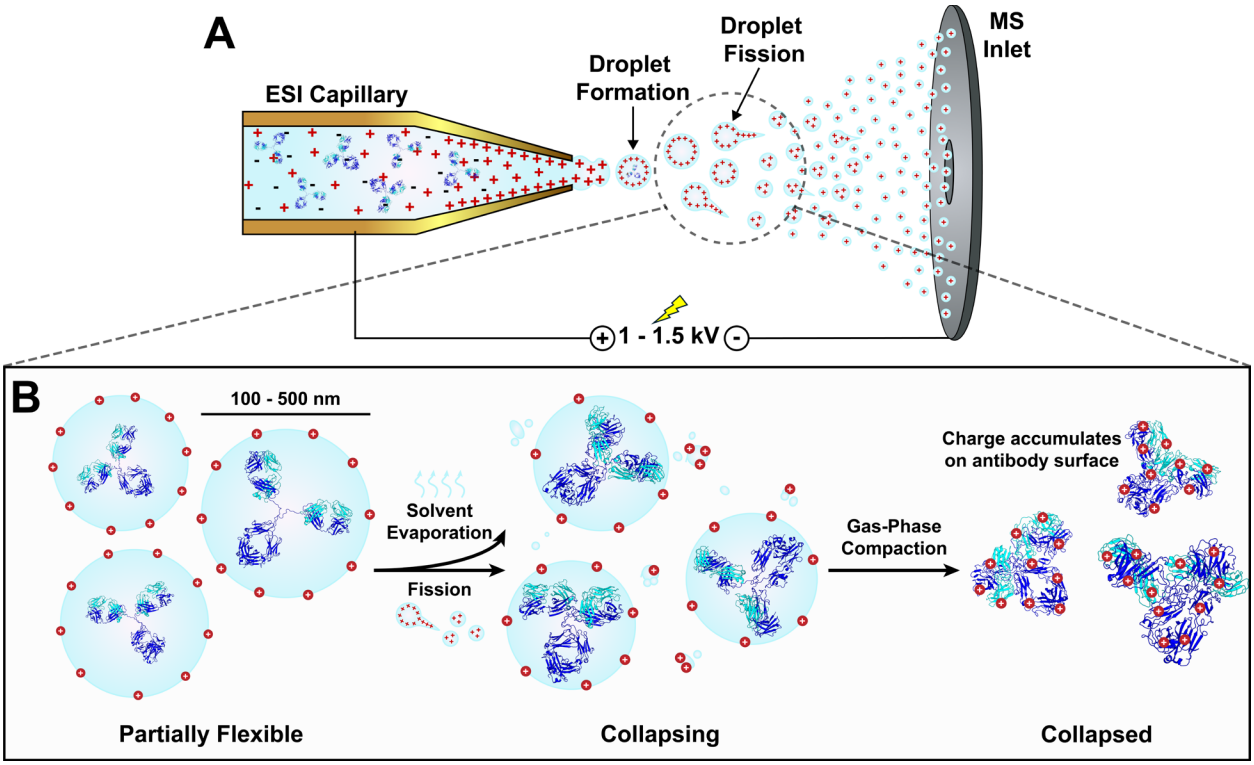

Figure 1-3: Overview of the nESI process. (A) Schematic of droplet formation and fission during ESI in positive ion mode. (B) Representation of the charged residue model (CRM) pathway for flexible IgG-based antibodies as proposed by Ref.[140] Droplets containing partially flexible IgG molecules gradually undergo desolvation and fission events that force them into more compact topologies. The charges (red) of the evaporating droplets are then transferred to the surfaces of individual IgG molecules that have collapsed around their hinge regions.

as the Rayleigh limit.[127] Multiple successive desolvation and fission events can occur, leading to multiply charged gas-phase ions that enter the mass spectrometer.

The generation of charged gas-phase analyte ions during ESI can be explained by three different models: the ion evaporation model (IEM), the charged residue model (CRM), and the chain ejection model (CEM).[128] The IEM applies to the desolvation of small molecules, in which ions migrate to the surface of the charged droplet and then are ejected.[129] The generation of gas-phase ions for larger biomolecules, like proteins, progresses by either the CRM or CEM, depending on the structural state of the molecule in solution. Compact, globular proteins follow the CRM, where droplets containing a single analyte evaporate to dryness. The charge of the droplet is then transferred to the protein, where the net charge is dependent on the available

surface area of the protein and is often close to that of the Rayleigh limit.[130-133] In contrast, unfolded and disordered proteins follow the CEM, where exposed hydrophobic residues cause them to migrate toward the surface of the charged droplet.[134] They are subsequently ejected from the droplet, carrying charge with them. The rest of this section will focus on the CRM as it pertains to the generation of native-like, folded structures of antibodies in the gas phase.

Typically, the modern implementation of ESI for native MS involves flow rates of nL/min and capillary tips with inner diameters of 5 to 10 μm. This variation of ESI, nESI, produces smaller sized droplets (100 to 500 nm in diameter), typically from solutions of volatile salts such as ammonium acetate, that can eliminate the need for additional heating or a nebulizing gas to aid in desolvation, resulting in higher ionization efficiencies and tolerances to non-volatile salts.[135] Thus, nESI is able to preserve the structures and non-covalent interactions of proteins, generating more native-like architectures per the CRM that closely resemble those in solution as evidenced by recent efforts in native MS coupled with soft-landing technology.[136, 137] However, several studies suggest that during native IM-MS experiments, globular proteins can undergo partial structural collapse due to the self-solvation of charged and polar sidechains on the protein surface during nESI.[138, 139] This collapse is especially acute for nonglobular, flexible proteins like IgG-based therapeutic antibodies, which experience as much as 40% structural compaction around their hinge regions with no significant changes in secondary structure content.[140-143] Within this context, Politis *et al.*[140] proposed that charge transfer per the CRM occurs concurrently or after the partial collapse of IgG structures, leading to a distribution of kinetically-trapped, compact conformations in the gas-phase that can be successively analyzed with IM-MS (Figure 1-3B).

1.4.2 High-Mass Ion Selection and Detection

All current TWIM-based platforms are hybrid mass spectrometers, consisting of both quadrupole and orthogonal ToF mass analyzers. Importantly, these platforms exclusively utilize a geometry where IM separation is performed after ion filtering with the quadrupole. Briefly, a quadrupole mass filter functions by applying direct current (DC) and radiofrequency (RF) voltages to two pairs of parallel conductive rods that are spatially perpendicular to one another. The application of DC and RF voltages, in turn, creates static and oscillating electric fields within the quadrupole, respectively. The interplay between these fields will then cause ions with particular *m/z* ratios to undergo stable trajectories through the quadrupole, permitting them to pass through for subsequent IM separation and ToF-MS detection. Here, the quadrupole can serve as a narrow-band mass filter where an individual ion of a specific *m/z* value can be selected via the tuning of both DC and RF voltages. Alternatively, the quadrupole can also serve as a broad-band mass filter when using it in RF-only mode, permitting a range of ions to follow stable trajectories and be transmitted for further analysis.[144] The Synapt G2 used in this work, in particular, possesses a modified quadrupole that operates at a reduced RF frequency, making it capable of selecting ions up to 32,000 *m/z* and transmitting large macromolecular assemblies.[145] Following the quadrupole, ions can also be subjected to collision induced dissociation (CID) or collision-induced unfolding (CIU) in the T-Wave ion trap; details covering these collisional activation strategies, and their applicability of protein therapeutic characterization, will be covered in detail later in this chapter.

While the quadrupole acts to filter and transmit specific ions of interest, the ToF mass analyzer serves as a detector in hybrid mass spectrometers. In fact, ToF mass analyzers have proven to be effective in the analysis of large macromolecular assemblies due to their high mass range, sensitivity, fast data acquisitions, and compatibility with IM.[98] Upon entering the ToF

pusher region, ions are accelerated by an electric potential, causing them to acquire similar kinetic energies. This acceleration is performed orthogonal to the continuous ion beam generated via ESI in order to satisfy the pulsed nature of ToF mass analyzers.[146] When departing this acceleration region, they enter a field-free region where they are separated according to their velocities before reaching a detector, typically either a collision dynode or multichannel plate[147]. In this case, *m/z* ratios are determined by measuring the time it takes for ions to traverse through the field-free region.[148] That is, an ion with a mass *m* and a total charge $q = ze$ accelerated by a potential, V_s, will exhibit kinetic energy (E_k) that is converted from its electric potential energy (E_{el}):

$$E_k = \frac{1}{2}mv^2 = qV_s = zeV_s = E_{el} \qquad \text{(Equation 1-1)}$$

where *z* is the ion charge; *e* is the elementary charge of an electron; and *v* is the velocity of the ion. The velocity of the ion can then be obtained by rearranging Equation 1-1:

$$v = \left(\frac{2zeV_s}{m}\right)^{1/2} \qquad \text{(Equation 1-2)}$$

Because the time *t* needed to traverse the drift region of length *L* is given by

$$t = \frac{L}{v} \qquad \text{(Equation 1-3)}$$

Equation 1-2 can be re-written by substituting *v* with Equation 1-3 to give:

$$t^2 = \frac{m}{z}\left(\frac{L^2}{2eV_s}\right) \qquad \text{(Equation 1-4)}$$

This equation reveals that the *m/z* ratio of a given ion can be calculated from its measured flight time in the drift region of the ToF mass analyzer. Moreover, it further demonstrates that the larger the mass of the ion is, the slower it takes for it to reach the detector.

At times, ions of the same *m/z* ratio can start at different positions within the pusher and acquire different levels of kinetic energies upon entering the flight tube, causing them to possess different velocities. Consequently, there is a decrease in mass resolution, as these ions will have different flight times. Therefore, a reflectron is often added to compensate for this spread in ion arrival times and improve mass resolution. A reflection functions as an electrostatic mirror that reflects ions back towards the detector. More energetic ions will penetrate deeper into the reflection, causing them to travel a longer distance to the detector compared to less energetic ions.[148] As a result, ions of the same *m/z* ratio but different initial kinetic energies will reach the detector at the same time, leading to an improvement in mass resolution. Reflectrons can also increase the ion drift path length, which further improves ion separation and mass resolution.[149] It is important to highlight that these measurements are performed on a microsecond timescale, making ToF mass analyzers compatible with millisecond IM separations.[150]

1.4.3 IM Separation: Fundamental Principles

IM is an ever-evolving technique in gas-phase structural biology that separates ions of proteins based on their charge, shape, and size (Figure 1-4). After ionization, ions are introduced into an ion guide pressured with an inert neutral gas (e.g., nitrogen or helium) held under the influence of a relatively weak electric field.[151, 152] Larger, more elongated ions will experience more collisions with background gas neutrals, causing them to take more time (drift time, t_D) to traverse the IM chamber compared to smaller, more compact ions. Moreover, ions possessing higher charge will experience stronger separation field strengths and drift through the IM separator at a faster rate. Under these conditions, the measured drift time of an ion can be related back to its Ω since ions with larger Ω values will demonstrate a higher propensity to collide with

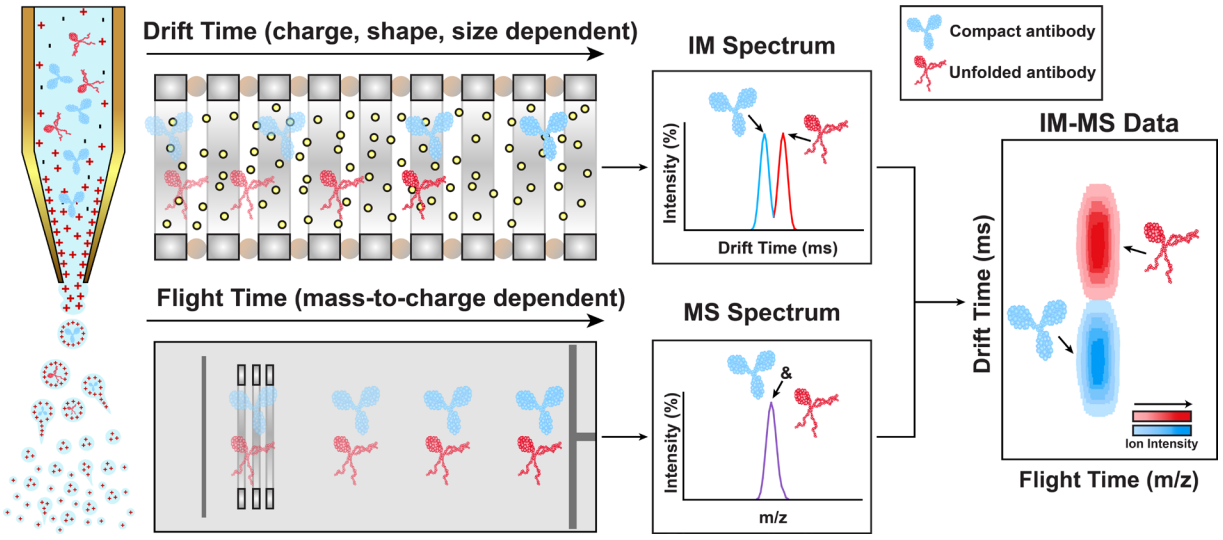

Figure 1-4: Schematic highlighting the basic principles of an IM-MS experiment. Ions generated via nESI travel through a drift cell pressurized with a neutral gas and held under the influence of a weak electric field (top, middle). Larger, more elongated ions (red) will collide more frequently with background gas molecules, thus taking them longer to traverse the drift cell compared to smaller, more compact ions (blue). Following IM separation, ions are injected into an orthogonal ToF mass analyzer for *m/z* analysis (bottom, middle). Both dimensions of the data can then be plotted as a heat map (right), where ions of the same *m/z* can be conformationally distinguished.

the background neutral gas. Following IM separation, these ions are analyzed according to their *m/z* ratios with a ToF mass analyzer.[151, 152]

Over the years, various IM platforms have been developed that incorporate different methods of IM separation. For brevity, further discussion will focus on two frequently used IM platforms in gas-phase structural biology research: drift tube and travelling-wave separators. Understanding both of these approaches is necessary in order to highlight how Ω is related to ion mobility.

Drift tube ion mobility (DTIM) is often depicted as the classical IM model due to its relative ease of operation and ability to directly quantify an ion's mobility from which Ω values can be derived.[120, 151] A unique property of DTIM is the uniform electric field (*E*) that is applied to a series of stacked-rings in the drift cell; this static field propagates ions through the drift region. Here, ion velocity (*v*) is correlated to its mobility (*K*) through the following equation:

$$v = KE \qquad \text{(Equation 1-5)}$$

Ion velocity, in this case, can be calculated using the experimentally derived drift time (t_D) of the ion and the length (L) of the drift tube:

$$K = \frac{L}{t_D E} \qquad \text{(Equation 1-6)}$$

Based on the measured K values, the $^{DT}\Omega$ value of the ion can then be derived using the Mason-Schamp equation:

$$\Omega = \frac{3ze}{16N}\left[\frac{2\pi}{\mu k_b T}\right]^{1/2}\frac{1}{K} \qquad \text{(Equation 1-7)}$$

where e is the charge of an electron, z is the ion charge, N is the buffer gas density; μ is the reduced mass of the ion-neutral gas pair; k_b is the Boltzmann constant; and T is the drift region temperature.[153, 154]

Despite the simplicity of the DTIM platform, most applications of IM in the characterization of proteins have been performed on TWIM platforms due to their earlier commercialization. Similar to DTIM, TWIM devices utilize a set of stacked-ring electrodes that propel ions through the separator; however, the electric potential applied is not uniform throughout the cell. Instead, TWIM uses an oscillating electric field to generate a series of voltage waves that propel ions through the drift cell.[124, 155] To create this field, DC voltages are applied to the ring electrodes, creating a wave that is propagated through the separator as the DC voltages move to adjacent ring electrodes at a specified velocity. Concurrently, RF voltages are superimposed on the propelling DC voltages as a way to radially confine ions and minimize ion diffusion. The height and velocity of this so-called 'travelling-wave' can be adjusted, permitting the optimization of TWIM separations for a variety of different biological systems.[118]

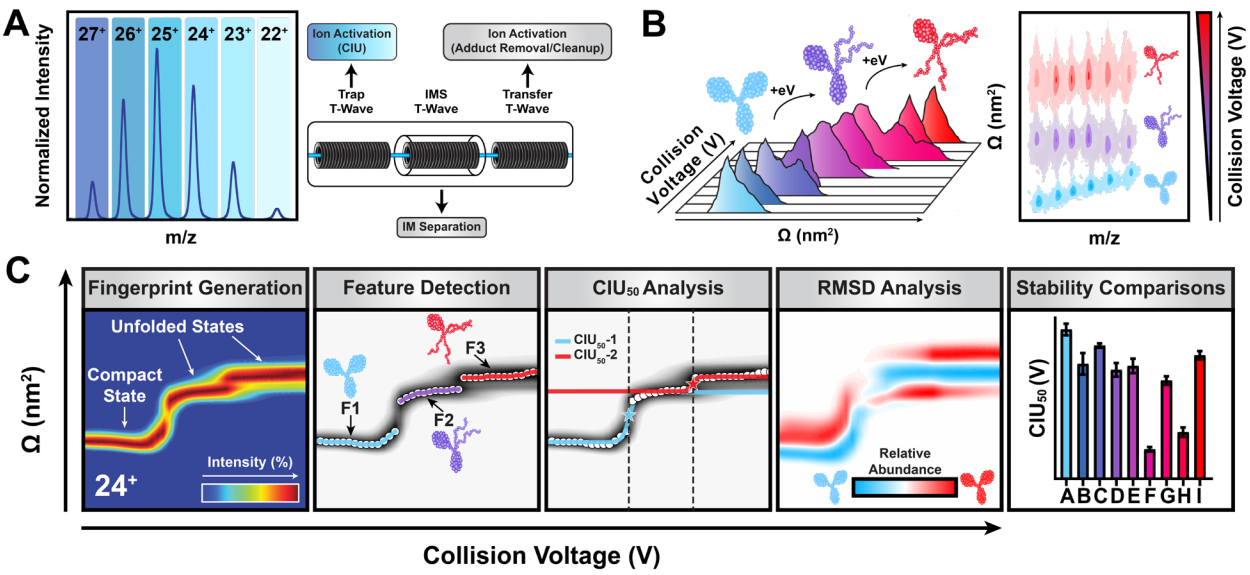

Figure 1-5: Overview of the typical CIU workflow for a Waters Synapt G2 TWIM platform. (A) Protein ions across different charge states are subjected to collisions with background neutral gas molecules in the trap ion guide. (B) As protein ions are collisionally activated in a stepwise manner, they begin to unfold, leading to an increase in their $^{TW}\Omega$ values. (C) IM-MS data is then processed with CIUSuite 2 (v.2.3), [165] permitting a variety of different data processing modules: the smoothing of data and generation of a CIU fingerprint; the detection of feature $^{TW}\Omega$ values for compact and unfolded conformations; the fitting of a logistic function between adjacent features to determine CIU_{50} values; the RMSD analysis of CIU data to quantitate global differences between proteins; and the comparison of gas-phase stabilities between proteins using CIU_{50} values.

However, due to the complex nature of TWIM separations, the mobility of an ion is no longer directly related to $^{TW}\Omega$ per Equation 1-7. Therefore, TWIM devices must be calibrated with ions of known mobilities ($^{TW}\Omega$ values) prior to measuring the $^{TW}\Omega$ values of unknowns.[156] CCS calibrations of TWIM data were first performed using a power-law relationship.[152] Recent efforts in TWIM calibration methodologies, however, have produced $^{TW}\Omega$ values with high accuracy using blend function that encompasses the effects of velocity relaxation and take into account the radial distribution of ions.[157] These calibrations can be successfully performed using a small set of calibrant species, eliminating the need to carefully select calibrants that match the molecular class of the analytes being probed. As such, $^{TW}\Omega$ values throughout this dissertation were calculated using this new calibration approach.

1.4.4 Collision-Induced Unfolding (CIU) for HOS and Stability Assessment

Experimentally determined Ω values serve as valuable metrics for integrative structural biology studies, for they can be combined with other biophysical and computational (e.g., molecular dynamics) methods to help elucidate the structures of proteins and their complexes.[158] However, Ω measurements are limited in information content when viewed alone. Despite recent efforts in improving IM resolution, current IM platforms still face significant challenges in adequately resolving structural differences between large, iso-cross-sectional proteins. This limitation especially applies to large, conformationally dynamic proteins like antibodies, where drift time distributions do not demonstrate any significant improvement in resolution ($t_D/\Delta t_D$) between conformers on high-resolution spectrometers like the latest cyclic IM-MS platform.[159]

To address these limitations in current IM resolution, CIU technologies are continuously being developed to leverage IM-MS in resolving subtle differences in the unfolding and dissociation pathways of iso-cross-sectional proteins.[160, 161] In CIU, isolated gas-phase protein ions are activated through energetic collisions with a background inert neutral gas in a stepwise manner prior to IM separation. These collisions lead to an increase in ion internal energies and prompts them to unfold (Figure 1-5A,B).[160, 162] Typically, large, multi-domain ions undergo several CIU transitions that lead to changes in Ω values corresponding to a number of unfolded intermediates or features that can be sampled by IM. These unfolded intermediates can then be tracked using a two-dimensional (2-D) heatmap, known as a "CIU fingerprint," that plots Ω values (or drift times) as a function of collision (acceleration) voltage (Figure 1-5C). Various methods for generating these fingerprints have been described that also offer different quantitative metrics to interpret subtle changes in protein HOS.[163-167] CIUSuite 2,[165] in particular, offers a comprehensive package of automated statistical fitting and modeling methods that can rapidly quantity feature Ω values, model transitions between adjacent features for gas-phase

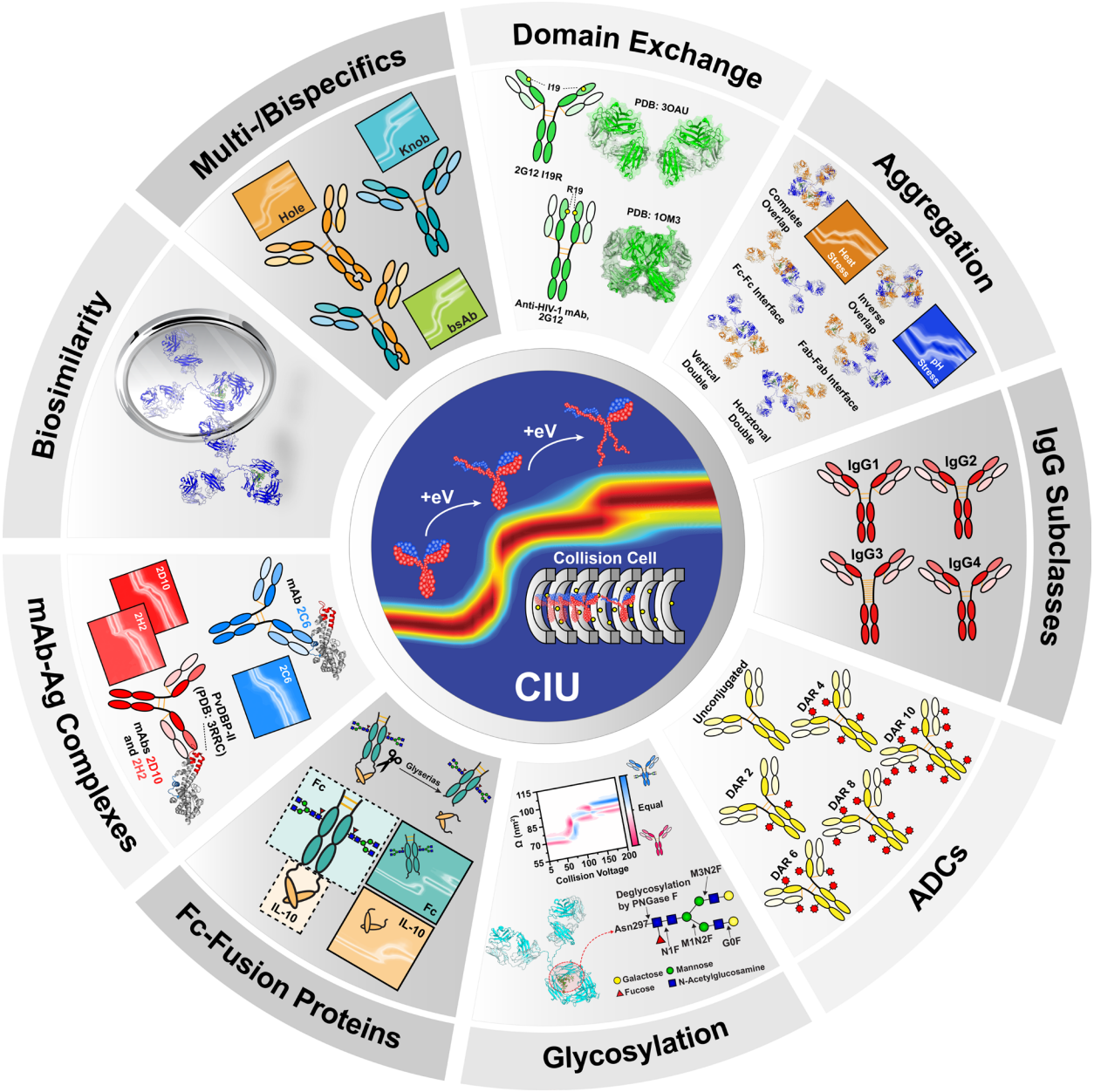

Figure 1-6: The current CIU landscape for antibody-based therapeutics. CIU has been applied to various antibody therapeutic modalities such as conventional IgGs (subclasses),[168,169] multi- and bispecific antibodies,[170,171] ADCs,[172,173] and Fc-fusion proteins (discussed in Chapter 4). CQAs such as glycosylation[174] and aggregation[175] have also been probed with CIU, especially in the context of assessing the structures of innovator biologics and their biosimilars.[176,177] CIU has also been extended to the study of large mAb-antigen (Ag) complexes[178] and domain-exchanged mAbs.[179]

stability assessments, and compare global differences between the unfolding pathways of iso-cross-sectional proteins (Figure 1-5C).

The establishment of data processing and visualization tools like CIUSuite 2 have enabled the rapid stability and structural assessment of a range of antibody-based therapeutics, their CQAs, and their immune complexes as summarized in Figure 1-6.[168-179] Moreover, recent advancements in the automation of CIU when coupled with online separation methods like SEC[180, 181] and IEC[182] have further extended its feasibility as a high-throughput tool for HOS assessment within the biopharmaceutical pipeline. Though these online approaches can be practical in screening the structures and stabilities of large sample libraries, the short elution times of these techniques limit the number of voltage steps that can be performed during CIU, requiring additional sample injections that consequently compromise throughput.

Despite the success in extracting valuable empirical HOS information from CIU experiments, the mechanistic underpinnings of antibody gas-phase unfolding pathways remain largely unknown. Some granularity has been afforded through correlations between gas-phase and solution-phase unfolding pathways of mAb-biotin drug conjugates,[172] but the random conjugation of biotin molecules made it difficult to identify domain-correlated shifts in stability. Moreover, the utility of CIU in determining antibody function and potency has yet to be fully considered. The ability of CIU to determine structure-function relationships of antibody therapeutics can potentially assist in rapidly identifying clinically potent and effective mAb candidates. This dissertation, in part, addresses these gaps in our understanding of the gas-phase behavior of antibody therapeutics and related products, as well as further validates CIU as a valuable HOS analytical method for early drug discovery and development efforts.

1.5 Dissertation Overview

This dissertation largely focuses on the development and establishment of native IM-MS and CIU-based workflows for the characterization of various antibody-based therapeutic

modalities. The scope of the work ranges from scrutinizing the gas-phase unfolding mechanisms of antibodies to rapidly elucidating antibody structure-function relationships. In a more general sense, CIU is presented as a powerful technique in assessing the structures and stabilities of conformationally dynamic protein therapeutics with highly flexible regions.

Chapter 2 describes a native IM-MS and CIU-based workflow for the characterization of engineered bsAbs constructed using knobs-into-holes (KiH) technology. Both the parent mAbs and the KiH bsAb were assessed using these approaches, showcasing that the bsAb retains HOS memory from its parent mAbs. Importantly, a quantitative assessment of CIU data permitted the annotation of antibody CIU pathways for the first time using both intact and middle-level CIU approaches, where each CIU transition could be traced back to specific regions within the KiH bsAb. This work was done in collaboration with Bristol Myers Squibb and has been previously published as: **Villafuerte-Vega, R. C.; Li, H.W.; Slaney, T.R.; Chennamsetty, N.; Chen, G.; Tao, L.; Ruotolo, B.T. Ion Mobility-Mass Spectrometry and Collision-Induced Unfolding of Designed Bispecific Antibody Therapeutics. *Anal. Chem.* 2023, 95, 17, 6962 – 6970, DOI: 10.1021/acs.analchem.3c00344.**

In **Chapter 3**, the ability of CIU to rapidly classify a range of anti-CD40 agonist mAbs is investigated. A series of human IgG2 cysteine to serine (C/S) exchange variants that differed in hinge flexibility were assessed. Results across both full-length and $F(ab')_2$ fragments demonstrated that CIU can detect subtle changes in mAb stability and gas-phase compaction in a manner that strongly correlates with receptor agonism. These trends were consistent across two clinically relevant anti-CD40 mAbs, ChiLob7/4 and SAP1.3. Finally, the implementation of a CIU-based classification algorithm permitted the identification of agonistic mAbs in an automated fashion, highlighting the ability of CIU-based assays to determine structure-function

relationships with high accuracy. This work is currently in preparation for publication and was performed in collaboration with Mark S. Cragg and colleagues at the University of Southampton.

Extending beyond the conventional IgG scaffold, **Chapter 4** describes the development of IM-MS and CIU approaches for the characterization of an Fc-Interleukin-10 (Fc-IL-10) fusion protein engineered using flexible glycine-serine linkers. IM-MS and CIU revealed that Fc-IL-10 was structurally more dynamic in the gas-phase compared to proteins of similar size as well as large, flexible proteins like antibodies, which led to wider mobility distributions and multiple CIU transitions. Moreover, middle-level IM-MS and CIU experiments of isolated Fc and IL-10 (dimer) domains assisted in the annotation of CIU data for the intact Fc-IL-10 fusion protein, and they further provided insights into the effects of linker length on IL-10 dimer stability. This work was fulfilled in collaboration with Bristol Myers Squibb, and has been published as: **Villafuerte-Vega, R. C.; Li, H.W.; Berman, A.E.; Slaney, T.R.; Chennamsetty, N.; Chen, G.; Tao, L.; Ruotolo, B.T. Ion Mobility-Mass Spectrometry and Collision-Induced Unfolding Rapidly Characterize the Structural Polydispersity and Stability of an Fc-Fusion Protein.** ***Anal. Chem.*** **2024, DOI: 10.1021/acs.analchem.4c01408.**

Chapter 5 extends beyond native MS protein stability measurements and encompasses the development of a routine *in vitro* serum stability assay for antibody therapeutics that incorporates internal standards. The *in vitro* stability of 19 antibodies was assessed in the serums of various preclinical species including mouse, rat, and cynomolgus monkey. The incorporation of internal standards in this workflow allowed for a more confident interpretation of antibody therapeutic stability in serum, for it accounted for any random or systemic errors that occurred during sample preparation and instrumental analysis. This work was performed during a summer internship at AbbVie, and a manuscript is currently being prepared for publication.

Finally, **Chapter 6** provides a summary of the main research findings presented in this dissertation, as well as discusses their impact on the broader native MS and IM-MS communities. Importantly, the future of IM-MS and CIU-based technologies in the development of antibody-based therapeutics and related products will also be discussed. Future directions for each project will also be proposed, which aim to further our structural understanding of these protein therapeutic modalities in the gas-phase.

1.6 References

[1] Lu, R.-M.; et al. Development of therapeutic antibodies for the treatment of diseases. *J. Biomed. Sci.* **2020**, *27* (1). DOI: 10.1186/s12929-019-0592-z.

[2] Lyu, X.; et al. The global landscape of approved antibody therapies. *Antib. Ther.* **2022**, *5* (4), 233-257. DOI: 10.1093/abt/tbac021.

[3] Köhler, G.; Milstein, C. Continuous cultures of fused cells secreting antibody of predefined specificity. *Nature* **1975**, *256* (5517), 495-497. DOI: 10.1038/256495a0.

[4] Mitra, S.; Tomar, P. C. Hybridoma technology; advancements, clinical significance, and future aspects. *J. Genet. Eng. Biotechnol.* **2021**, *19* (1), 159. DOI: 10.1186/s43141-021-00264-6.

[5] Keri, D.; Walker, M.; Singh, I.; Nishikawa, K.; Garces, F. Next generation of multispecific antibody engineering. *Antib. Ther.* **2024**, *7* (1), 37-52. DOI: 10.1093/abt/tbad027.

[6] Kang, T. H.; Jung, S. T. Boosting therapeutic potency of antibodies by taming Fc domain functions. *Exp. Mol. Med.* **2019**, *51* (11), 1-9. DOI: 10.1038/s12276-019-0345-9.

[7] Jhajj, H. S.; Lwo, T. S.; Yao, E. L.; Tessier, P. M. Unlocking the potential of agonist antibodies for treating cancer using antibody engineering. *Trends Mol. Med.* **2023**, *29* (1), 48-60. DOI: 10.1016/j.molmed.2022.09.012.

[8] Crescioli, S.; et al. Antibodies to watch in 2024. *mAbs* **2024**, *16* (1). DOI: 10.1080/19420862.2023.2297450.

[9] Carter, P. J.; Rajpal, A. Designing antibodies as therapeutics. *Cell* **2022**, *185* (15), 2789-2805. DOI: 10.1016/j.cell.2022.05.029.

[10] Kumar, M.; Jalota, A.; Sahu, S. K.; Haque, S. Therapeutic antibodies for the prevention and treatment of cancer. *J. Biomed. Sci.* **2024**, *31* (1). DOI: 10.1186/s12929-024-00996-w.

[11] Jin, S.; et al. Emerging new therapeutic antibody derivatives for cancer treatment. *Signal Transduct. Target Ther.* **2022**, *7* (1). DOI: 10.1038/s41392-021-00868-x.

[12] Casadevall, A.; Pirofski, L.-A.; Joyner, M. J. The Principles of Antibody Therapy for Infectious Diseases with Relevance for COVID-19. *mBio* **2021**, *12* (2). DOI: 10.1128/mbio.03372-20.

[13] Van Erp, E. A.; Luytjes, W.; Ferwerda, G.; Van Kasteren, P. B. Fc-Mediated Antibody Effector Functions During Respiratory Syncytial Virus Infection and Disease. *Front. Immunol.* **2019**, *10*. DOI: 10.3389/fimmu.2019.00548.
[14] Van De Donk, N. W. C. J.; Usmani, S. Z. CD38 Antibodies in Multiple Myeloma: Mechanisms of Action and Modes of Resistance. *Front. Immunol.* **2018**, *9*. DOI: 10.3389/fimmu.2018.02134.
[15] Swanson, M. D.; Rios, S.; Mittal, S.; Soder, G.; Jawa, V. Immunogenicity Risk Assessment of Spontaneously Occurring Therapeutic Monoclonal Antibody Aggregates. *Front. Immunol.* **2022**, *13*. DOI: 10.3389/fimmu.2022.915412.
[16] Tang, Y.; et al. Impact of IgG subclass on molecular properties of monoclonal antibodies. *mAbs* **2021**, *13* (1). DOI: 10.1080/19420862.2021.1993768.
[17] Schroeder, H. W.; Cavacini, L. Structure and function of immunoglobulins. *J. Allergy Clin. Immunol.* **2010**, *125* (2), S41-S52. DOI: 10.1016/j.jaci.2009.09.046.
[18] Van Der Horst, H. J.; Nijhof, I. S.; Mutis, T.; Chamuleau, M. E. D. Fc-Engineered Antibodies with Enhanced Fc-Effector Function for the Treatment of B-Cell Malignancies. *Cancers* **2020**, *12* (10), 3041. DOI: 10.3390/cancers12103041.
[19] Cobb, B. A. The history of IgG glycosylation and where we are now. *Glycobiology* **2020**, *30* (4), 202-213. DOI: 10.1093/glycob/cwz065.
[20] Mimura, Y.; Saldova, R.; Mimura-Kimura, Y.; Rudd, P. M.; Jefferis, R. Importance and Monitoring of Therapeutic Immunoglobulin G Glycosylation. Springer International Publishing, 2021; pp 481-517.
[21] De Taeye, S. W.; Rispens, T.; Vidarsson, G. The Ligands for Human IgG and Their Effector Functions. *Antibodies* **2019**, *8* (2), 30. DOI: 10.3390/antib8020030.
[22] Bergonzo, C.; Gallagher, D. T. Atomic Model Structure of the NIST Monoclonal Antibody (NISTmAb) Reference Material. *J. Res. Natl. Inst. Stand. Technol.* **2021**, *126*. DOI: 10.6028/jres.126.012.
[23] Kiyoshi, M.; Tsumoto, K.; Ishii-Watabe, A.; Caaveiro, J. M. M. Glycosylation of IgG-Fc: a molecular perspective. *Int. Immunol.* **2017**, *29* (7), 311-317. DOI: 10.1093/intimm/dxx038.
[24] Kaneko, Y.; Nimmerjahn, F.; Ravetch, J. V. Anti-Inflammatory Activity of Immunoglobulin G Resulting from Fc Sialylation. *Science* **2006**, *313* (5787), 670-673. DOI: 10.1126/science.1129594.
[25] Shields, R. L.; et al. Lack of Fucose on Human IgG1 N-Linked Oligosaccharide Improves Binding to Human FcγRIII and Antibody-dependent Cellular Toxicity. *J. Biol. Chem.* **2002**, *277* (30), 26733-26740. DOI: 10.1074/jbc.m202069200.
[26] Vidarsson, G.; Dekkers, G.; Rispens, T. IgG Subclasses and Allotypes: From Structure to Effector Functions. *Front. Immunol.* **2014**, *5*. DOI: 10.3389/fimmu.2014.00520.
[27] Dillon, T. M.; et al. Structural and Functional Characterization of Disulfide Isoforms of the Human IgG2 Subclass. *J. Biol. Chem.* **2008**, *283* (23), 16206-16215. DOI: 10.1074/jbc.m709988200.
[28] Chu, T. H.; Patz, E. F.; Ackerman, M. E. Coming together at the hinges: Therapeutic prospects of IgG3. *mAbs* **2021**, *13* (1), 1882028. DOI: 10.1080/19420862.2021.1882028.
[29] Michaelsen, T. E.; Frangione, B.; Franklin, E. C. Primary structure of the "hinge" region of human IgG3. Probable quadruplication of a 15-amino acid residue basic unit. *J. Biol. Chem.* **1977**, *252* (3), 883-889. DOI: 10.1016/s0021-9258(19)75181-3.

[30] Roux, K. H.; Strelets, L.; Michaelsen, T. E. Flexibility of human IgG subclasses. *J. Immunol.* **1997**, *159* (7), 3372-3382. DOI: 10.4049/jimmunol.159.7.3372.
[31] Bloom, J. W.; Madanat, M. S.; Marriott, D.; Wong, T.; Chan, S. Y. Intrachain disulfide bond in the core hinge region of human IgG4. *Protein Sci.* **1997**, *6* (2), 407-415. DOI: 10.1002/pro.5560060217.
[32] Labrijn, A. F.; et al. Therapeutic IgG4 antibodies engage in Fab-arm exchange with endogenous human IgG4 in vivo. *Nat. Biotechnol.* **2009**, *27* (8), 767-771. DOI: 10.1038/nbt.1553.
[33] Rispens, T.; Ooijevaar-De Heer, P.; Bende, O.; Aalberse, R. C. Mechanism of Immunoglobulin G4 Fab-arm Exchange. *J. Am. Chem. Soc.* **2011**, *133* (26), 10302-10311. DOI: 10.1021/ja203638y.
[34] Galanti, M.; Fanelli, D.; Piazza, F. Conformation-controlled binding kinetics of antibodies. *Sci. Rep.* **2016**, *6* (1), 18976. DOI: 10.1038/srep18976.
[35] Liu, X.; et al. Human immunoglobulin G hinge regulates agonistic anti-CD40 immunostimulatory and antitumour activities through biophysical flexibility. *Nat. Commun.* **2019**, *10* (1). DOI: 10.1038/s41467-019-12097-6.
[36] Foss, S.; et al. Potent TRIM21 and complement-dependent intracellular antiviral immunity requires the IgG3 hinge. *Sci. Immunol.* **2022**, *7* (70). DOI: 10.1126/sciimmunol.abj1640.
[37] Yu, J.; Song, Y.; Tian, W. How to select IgG subclasses in developing anti-tumor therapeutic antibodies. *Journal of Hematology & Oncology* **2020**, *13* (1). DOI: 10.1186/s13045-020-00876-4.
[38] Damelang, T.; Rogerson, S. J.; Kent, S. J.; Chung, A. W. Role of IgG3 in Infectious Diseases. *Trends Immunol.* **2019**, *40* (3), 197-211. DOI: 10.1016/j.it.2019.01.005.
[39] Birrer, M. J.; Moore, K. N.; Betella, I.; Bates, R. C. Antibody-Drug Conjugate-Based Therapeutics: State of the Science. *J. Natl. Cancer Inst.* **2019**, *111* (6), 538-549. DOI: 10.1093/jnci/djz035.
[40] Tsuchikama, K.; Anami, Y.; Ha, S. Y. Y.; Yamazaki, C. M. Exploring the next generation of antibody–drug conjugates. *Nat. Rev. Clin. Oncol.* **2024**, *21* (3), 203-223. DOI: 10.1038/s41571-023-00850-2.
[41] Silver, A. B.; Leonard, E. K.; Gould, J. R.; Spangler, J. B. Engineered antibody fusion proteins for targeted disease therapy. *Trends Pharmacol. Sci.* **2021**, *42* (12), 1064-1081. DOI: 10.1016/j.tips.2021.09.009.
[42] Klein, C.; Brinkmann, U.; Reichert, J. M.; Kontermann, R. E. The present and future of bispecific antibodies for cancer therapy. *Nat. Rev. Drug. Discov.* **2024**. DOI: 10.1038/s41573-024-00896-6.
[43] Kholodenko, R. V.; Kalinovsky, D. V.; Doronin, I. I.; Ponomarev, E. D.; Kholodenko, I. V. Antibody Fragments as Potential Biopharmaceuticals for Cancer Therapy: Success and Limitations. *Curr. Med. Chem.* **2019**, *26* (3), 396-426. DOI: 10.2174/0929867324666170817152554.
[44] Guo, J.; et al. Characterization and Higher-Order Structure Assessment of an Interchain Cysteine-Based ADC: Impact of Drug Loading and Distribution on the Mechanism of Aggregation. *Bioconjugate Chem.* **2016**, *27* (3), 604-615. DOI: 10.1021/acs.bioconjchem.5b00603.
[45] McKertish, C.; Kayser, V. Advances and Limitations of Antibody Drug Conjugates for Cancer. *Biomedicines* **2021**, *9* (8), 872. DOI: 10.3390/biomedicines9080872.

[46] Madsen, A. V.; Pedersen, L. E.; Kristensen, P.; Goletz, S. Design and engineering of bispecific antibodies: insights and practical considerations. *Front. Bioeng. Biotechnol.* **2024**, *12*. DOI: 10.3389/fbioe.2024.1352014.
[47] Klein, C.; et al. Progress in overcoming the chain association issue in bispecific heterodimeric IgG antibodies. *mAbs* **2012**, *4* (6), 653-663. DOI: 10.4161/mabs.21379.
[48] Chen, X.; Zaro, J. L.; Shen, W.-C. Fusion protein linkers: Property, design and functionality. *Adv. Drug Deliv. Rev.* **2013**, *65* (10), 1357-1369. DOI: 10.1016/j.addr.2012.09.039.
[49] Ghorbani Aghdam, A.; et al. Therapeutic Fc fusion protein misfolding: A three-phasic cultivation experimental design. *PLoS One* **2019**, *14* (1), e0210712. DOI: 10.1371/journal.pone.0210712.
[50] Walsh, G.; Jefferis, R. Post-translational modifications in the context of therapeutic proteins. *Nat. Biotechnol.* **2006**, *24* (10), 1241-1252. DOI: 10.1038/nbt1252.
[51] Nowak, C.; et al. Forced degradation of recombinant monoclonal antibodies: A practical guide. *mAbs* **2017**, *9* (8), 1217-1230. DOI: 10.1080/19420862.2017.1368602.
[52] Sifniotis, V.; Cruz, E.; Eroglu, B.; Kayser, V. Current Advancements in Addressing Key Challenges of Therapeutic Antibody Design, Manufacture, and Formulation. *Antibodies* **2019**, *8* (2), 36. DOI: 10.3390/antib8020036.
[53] Chen, G.; Tao, L.; Li, Z. Recent advancements in mass spectrometry for higher order structure characterization of protein therapeutics. *Drug. Discov. Today* **2022**, *27* (1), 196-206. DOI: 10.1016/j.drudis.2021.09.010.
[54] Alhazmi, H. A.; Albratty, M. Analytical Techniques for the Characterization and Quantification of Monoclonal Antibodies. *Pharmaceuticals* **2023**, *16* (2), 291. DOI: 10.3390/ph16020291.
[55] Beck, A.; Wagner-Rousset, E.; Ayoub, D.; Van Dorsselaer, A.; Sanglier-Cianférani, S. Characterization of Therapeutic Antibodies and Related Products. *Anal. Chem.* **2013**, *85* (2), 715-736. DOI: 10.1021/ac3032355.
[56] Fekete, S.; Guillarme, D.; Sandra, P.; Sandra, K. Chromatographic, Electrophoretic, and Mass Spectrometric Methods for the Analytical Characterization of Protein Biopharmaceuticals. *Anal. Chem.* **2016**, *88* (1), 480-507. DOI: 10.1021/acs.analchem.5b04561.
[57] Farsang, E.; et al. Coupling non-denaturing chromatography to mass spectrometry for the characterization of monoclonal antibodies and related products. *J. Pharm. Biomed. Anal.* **2020**, *185*, 113207. DOI: 10.1016/j.jpba.2020.113207.
[58] Khawli, L. A.; et al. Charge variants in IgG1. *mAbs* **2010**, *2* (6), 613-624. DOI: 10.4161/mabs.2.6.13333.
[59] Fekete, S.; Beck, A.; Veuthey, J.-L.; Guillarme, D. Ion-exchange chromatography for the characterization of biopharmaceuticals. *J. Pharm. Biomed. Anal.* **2015**, *113*, 43-55. DOI: 10.1016/j.jpba.2015.02.037.
[60] Liu, H. F.; Ma, J.; Winter, C.; Bayer, R. Recovery and purification process development for monoclonal antibody production. *mAbs* **2010**, *2* (5), 480-499. DOI: 10.4161/mabs.2.5.12645.
[61] Berkowitz, S. A.; Houde, D. J. Size-Exclusion Chromatograph (SEC) in Biopharmaceutical Process Development. Elsevier, 2015; pp 139-169.

[62] Minton, A. P. Recent applications of light scattering measurement in the biological and biopharmaceutical sciences. *Anal. Biochem.* **2016**, *501*, 4-22. DOI: 10.1016/j.ab.2016.02.007.
[63] Sahin, E.; Roberts, C. J. Size-Exclusion Chromatography with Multi-angle Light Scattering for Elucidating Protein Aggregation Mechanisms. Humana Press, 2012; pp 403-423.
[64] Fekete, S.; Veuthey, J.-L.; Beck, A.; Guillarme, D. Hydrophobic interaction chromatography for the characterization of monoclonal antibodies and related products. *J. Pharm. Biomed. Anal.* **2016**, *130*, 3-18. DOI: 10.1016/j.jpba.2016.04.004.
[65] Fleming, R. ADC Analysis by Hydrophobic Interaction Chromatography. Springer US, 2020; pp 147-161.
[66] Belov, A. M.; et al. Analysis of Proteins, Protein Complexes, and Organellar Proteomes Using Sheathless Capillary Zone Electrophoresis - Native Mass Spectrometry. *J. Am. Soc. Mass Spectrom.* **2017**, *28* (12), 2614-2634. DOI: 10.1007/s13361-017-1781-1.
[67] Belov, A. M.; et al. Complementary middle-down and intact monoclonal antibody proteoform characterization by capillary zone electrophoresis – mass spectrometry. *Electrophoresis* **2018**, *39* (16), 2069-2082. DOI: 10.1002/elps.201800067.
[68] Shen, X.; et al. Investigating native capillary zone electrophoresis-mass spectrometry on a high-end quadrupole-time-of-flight mass spectrometer for the characterization of monoclonal antibodies. *Int. J. Mass Spectrom.* **2021**, *462*, 116541. DOI: 10.1016/j.ijms.2021.116541.
[69] Wei, B.; Han, G.; Tang, J.; Sandoval, W.; Zhang, Y. T. Native Hydrophobic Interaction Chromatography Hyphenated to Mass Spectrometry for Characterization of Monoclonal Antibody Minor Variants. *Anal. Chem.* **2019**, *91* (24), 15360-15364. DOI: 10.1021/acs.analchem.9b04467.
[70] Schwenzer, A. K.; Kruse, L.; Jooß, K.; Neusüß, C. Capillary electrophoresis-mass spectrometry for protein analyses under native conditions: Current progress and perspectives. *Proteomics* **2024**, *24* (3-4). DOI: 10.1002/pmic.202300135.
[71] Haberger, M.; et al. Rapid characterization of biotherapeutic proteins by size-exclusion chromatography coupled to native mass spectrometry. *mAbs* **2016**, *8* (2), 331-339. DOI: 10.1080/19420862.2015.1122150.
[72] Liu, A. P.; Yan, Y.; Wang, S.; Li, N. Coupling Anion Exchange Chromatography with Native Mass Spectrometry for Charge Heterogeneity Characterization of Monoclonal Antibodies. *Anal. Chem.* **2022**, *94* (16), 6355-6362. DOI: 10.1021/acs.analchem.2c00707.
[73] Maveyraud, L.; Mourey, L. Protein X-ray Crystallography and Drug Discovery. *Molecules* **2020**, *25* (5), 1030. DOI: 10.3390/molecules25051030.
[74] Toride King, M.; Brooks, C. L. Epitope Mapping of Antibody-Antigen Interactions with X-Ray Crystallography. Springer New York, 2018; pp 13-27.
[75] Harris, L. J.; Larson, S. B.; Hasel, K. W.; McPherson, A. Refined Structure of an Intact IgG2a Monoclonal Antibody. *Biochemistry* **1997**, *36* (7), 1581-1597. DOI: 10.1021/bi962514+.
[76] Harris, L. J.; Skaletsky, E.; McPherson, A. Crystallographic structure of an intact IgG1 monoclonal antibody. *J. Mol. Biol.* **1998**, *275* (5), 861-872. DOI: 10.1006/jmbi.1997.1508.

[77] Saphire, E. O.; et al. Crystal Structure of a Neutralizing Human IgG Against HIV-1: A Template for Vaccine Design. *Science* **2001**, *293* (5532), 1155-1159. DOI: 10.1126/science.1061692.
[78] Scapin, G.; et al. Structure of full-length human anti-PD1 therapeutic IgG4 antibody pembrolizumab. *Nat. Struct. Mol. Biol.* **2015**, *22* (12), 953-958. DOI: 10.1038/nsmb.3129.
[79] Wüthrich, K. Protein structure determination in solution by NMR spectroscopy. *J. Biol. Chem.* **1990**, *265* (36), 22059-22062. DOI: 10.1016/s0021-9258(18)45665-7.
[80] Cavalli, A.; Salvatella, X.; Dobson, C. M.; Vendruscolo, M. Protein structure determination from NMR chemical shifts. *PNAS* **2007**, *104* (23), 9615-9620. DOI: 10.1073/pnas.0610313104.
[81] Tugarinov, V.; Muhandiram, R.; Ayed, A.; Kay, L. E. Four-Dimensional NMR Spectroscopy of a 723-Residue Protein: Chemical Shift Assignments and Secondary Structure of Malate Synthase G. *J. Am. Chem. Soc.* **2002**, *124* (34), 10025-10035. DOI: 10.1021/ja0205636.
[82] Palte, R. L.; et al. Cryo-EM structures of inhibitory antibodies complexed with arginase 1 provide insight into mechanism of action. *Commun. Biol.* **2021**, *4* (1). DOI: 10.1038/s42003-021-02444-z.
[83] Fernandez-Martinez, D.; Tully, M. D.; Leonard, G.; Mathieu, M.; Kandiah, E. Structural insights into the bi-specific cross-over dual variable antibody architecture by cryo-EM. *Sci. Rep.* **2023**, *13* (1). DOI: 10.1038/s41598-023-35678-4.
[84] Weissenberger, G.; Henderikx, R. J. M.; Peters, P. J. Understanding the invisible hands of sample preparation for cryo-EM. *Nat. Methods* **2021**, *18* (5), 463-471. DOI: 10.1038/s41592-021-01130-6.
[85] Renaud, J.-P.; et al. Cryo-EM in drug discovery: achievements, limitations and prospects. *Nat. Rev. Drug. Discov.* **2018**, *17* (7), 471-492. DOI: 10.1038/nrd.2018.77.
[86] Mach, H.; Middaugh, C. R. Ultraviolet Spectroscopy as a Tool in Therapeutic Protein Development. *J. Pharm. Sci.* **2011**, *100* (4), 1214-1227. DOI: 10.1002/jps.22385.
[87] Joshi, V.; Shivach, T.; Yadav, N.; Rathore, A. S. Circular Dichroism Spectroscopy as a Tool for Monitoring Aggregation in Monoclonal Antibody Therapeutics. *Anal. Chem.* **2014**, *86* (23), 11606-11613. DOI: 10.1021/ac503140j.
[88] Derenne, A.; Derfoufi, K.-M.; Cowper, B.; Delporte, C.; Goormaghtigh, E. FTIR spectroscopy as an analytical tool to compare glycosylation in therapeutic monoclonal antibodies. *Anal. Chim. Acta.* **2020**, *1112*, 62-71. DOI: 10.1016/j.aca.2020.03.038.
[89] Bou-Assaf, G. M.; et al. Best Practices for Aggregate Quantitation of Antibody Therapeutics by Sedimentation Velocity Analytical Ultracentrifugation. *J. Pharm. Sci.* **2022**, *111* (7), 2121-2133. DOI: 10.1016/j.xphs.2021.12.023.
[90] Nobbmann, U.; et al. Dynamic light scattering as a relative tool for assessing the molecular integrity and stability of monoclonal antibodies. *Biotechnol. Genet. Eng. Rev.* **2007**, *24* (1), 117-128. DOI: 10.1080/02648725.2007.10648095.
[91] Johnson, C. M. Differential scanning calorimetry as a tool for protein folding and stability. *Arch. Biochem. Biophys.* **2013**, *531* (1-2), 100-109. DOI: 10.1016/j.abb.2012.09.008.
[92] Chennamsetty, N.; Voynov, V.; Kayser, V.; Helk, B.; Trout, B. L. Design of therapeutic proteins with enhanced stability. *PNAS* **2009**, *106* (29), 11937-11942. DOI: 10.1073/pnas.0904191106.

[93] Masson, G. R.; Jenkins, M. L.; Burke, J. E. An overview of hydrogen deuterium exchange mass spectrometry (HDX-MS) in drug discovery. *Expert Opin. Drug Discov.* **2017**, *12* (10), 981-994. DOI: 10.1080/17460441.2017.1363734.
[94] Jones, L. M.; Sperry, J. B.; Carroll, J. A.; Gross, M. L. Fast Photochemical Oxidation of Proteins for Epitope Mapping. *Anal. Chem.* **2011**, *83* (20), 7657-7661. DOI: 10.1021/ac2007366.
[95] Jethva, P. N.; Gross, M. L. Hydrogen deuterium exchange and other mass spectrometry-based approaches for epitope mapping. *Front. Anal. Sci.* **2023**, *3*. DOI: 10.3389/frans.2023.1118749.
[96] Johnson, D. T.; Di Stefano, L. H.; Jones, L. M. Fast photochemical oxidation of proteins (FPOP): A powerful mass spectrometry–based structural proteomics tool. *J. Biol. Chem.* **2019**, *294* (32), 11969-11979. DOI: 10.1074/jbc.rev119.006218.
[97] Masson, G. R.; et al. Recommendations for performing, interpreting and reporting hydrogen deuterium exchange mass spectrometry (HDX-MS) experiments. *Nat. Methods* **2019**, *16* (7), 595-602. DOI: 10.1038/s41592-019-0459-y.
[98] Tamara, S.; Den Boer, M. A.; Heck, A. J. R. High-Resolution Native Mass Spectrometry. *Chem. Rev.* **2022**, *122* (8), 7269-7326. DOI: 10.1021/acs.chemrev.1c00212.
[99] Karch, K. R.; Snyder, D. T.; Harvey, S. R.; Wysocki, V. H. Native Mass Spectrometry: Recent Progress and Remaining Challenges. *Annu. Rev. Biophys.* **2022**, *51* (1), 157-179. DOI: 10.1146/annurev-biophys-092721-085421.
[100] Rosati, S.; Yang, Y.; Barendregt, A.; Heck, A. J. R. Detailed mass analysis of structural heterogeneity in monoclonal antibodies using native mass spectrometry. *Nat. Protoc.* **2014**, *9* (4), 967-976. DOI: 10.1038/nprot.2014.057.
[101] Tito, M. A.; et al. Probing Molecular Interactions in Intact Antibody: Antigen Complexes, an Electrospray Time-of-Flight Mass Spectrometry Approach. *Biophys. J.* **2001**, *81* (6), 3503-3509. DOI: 10.1016/s0006-3495(01)75981-4.
[102] Valliere-Douglass, J. F.; McFee, W. A.; Salas-Solano, O. Native Intact Mass Determination of Antibodies Conjugated with Monomethyl Auristatin E and F at Interchain Cysteine Residues. *Anal. Chem.* **2012**, *84* (6), 2843-2849. DOI: 10.1021/ac203346c.
[103] Campuzano, I. D. G.; et al. Native-MS Analysis of Monoclonal Antibody Conjugates by Fourier Transform Ion Cyclotron Resonance Mass Spectrometry. *Anal. Chem.* **2018**, *90* (1), 745-751. DOI: 10.1021/acs.analchem.7b03021.
[104] Chen, J.; Yin, S.; Wu, Y.; Ouyang, J. Development of a Native Nanoelectrospray Mass Spectrometry Method for Determination of the Drug-to-Antibody Ratio of Antibody–Drug Conjugates. *Anal. Chem.* **2013**, *85* (3), 1699-1704. DOI: 10.1021/ac302959p.
[105] Schachner, L.; et al. Characterization of Chain Pairing Variants of Bispecific IgG Expressed in a Single Host Cell by High-Resolution Native and Denaturing Mass Spectrometry. *Anal. Chem.* **2016**, *88* (24), 12122-12127. DOI: 10.1021/acs.analchem.6b02866.
[106] Jones, J.; Pack, L.; Hunter, J. H.; Valliere-Douglass, J. F. Native size-exclusion chromatography-mass spectrometry: suitability for antibody–drug conjugate drug-to-antibody ratio quantitation across a range of chemotypes and drug-loading levels. *mAbs* **2020**, *12* (1), 1682895. DOI: 10.1080/19420862.2019.1682895.

[107] Bailey, A. O.; et al. Charge variant native mass spectrometry benefits mass precision and dynamic range of monoclonal antibody intact mass analysis. *mAbs* **2018**, *10* (8), 1214-1225. DOI: 10.1080/19420862.2018.1521131.
[108] Phung, W.; et al. Characterization of bispecific and mispaired IgGs by native charge-variant mass spectrometry. *Int. J. Mass Spectrom.* **2019**, *446*, 116229. DOI: 10.1016/j.ijms.2019.116229.
[109] Yan, Y.; Xing, T.; Wang, S.; Daly, T. J.; Li, N. Online coupling of analytical hydrophobic interaction chromatography with native mass spectrometry for the characterization of monoclonal antibodies and related products. *J. Pharm. Biomed. Anal.* **2020**, *186*, 113313. DOI: 10.1016/j.jpba.2020.113313.
[110] Fort, K. L.; et al. Expanding the structural analysis capabilities on an Orbitrap-based mass spectrometer for large macromolecular complexes. *Analyst* **2018**, *143* (1), 100-105. DOI: 10.1039/c7an01629h.
[111] van De Waterbeemd, M.; et al. High-fidelity mass analysis unveils heterogeneity in intact ribosomal particles. *Nat. Methods* **2017**, *14* (3), 283-286. DOI: 10.1038/nmeth.4147.
[112] Van De Waterbeemd, M.; et al. Dissecting ribosomal particles throughout the kingdoms of life using advanced hybrid mass spectrometry methods. *Nat. Commun.* **2018**, *9* (1). DOI: 10.1038/s41467-018-04853-x.
[113] Van De Waterbeemd, M.; et al. Examining the Heterogeneous Genome Content of Multipartite Viruses BMV and CCMV by Native Mass Spectrometry. *J. Am. Soc. Mass Spectrom.* **2016**, *27* (6), 1000-1009. DOI: 10.1007/s13361-016-1348-6.
[114] Greisch, J.-F.; et al. Extending Native Top-Down Electron Capture Dissociation to MDa Immunoglobulin Complexes Provides Useful Sequence Tags Covering Their Critical Variable Complementarity-Determining Regions. *Anal. Chem.* **2021**, *93* (48), 16068-16075. DOI: 10.1021/acs.analchem.1c03740.
[115] Dyachenko, A.; et al. Tandem Native Mass-Spectrometry on Antibody–Drug Conjugates and Submillion Da Antibody–Antigen Protein Assemblies on an Orbitrap EMR Equipped with a High-Mass Quadrupole Mass Selector. *Anal. Chem.* **2015**, *87* (12), 6095-6102. DOI: 10.1021/acs.analchem.5b00788.
[116] Wohlschlager, T.; et al. Native mass spectrometry combined with enzymatic dissection unravels glycoform heterogeneity of biopharmaceuticals. *Nat. Commun.* **2018**, *9* (1). DOI: 10.1038/s41467-018-04061-7.
[117] Čaval, T.; Tian, W.; Yang, Z.; Clausen, H.; Heck, A. J. R. Direct quality control of glycoengineered erythropoietin variants. *Nat. Commun.* **2018**, *9* (1). DOI: 10.1038/s41467-018-05536-3.
[118] Christofi, E.; Barran, P. Ion Mobility Mass Spectrometry (IM-MS) for Structural Biology: Insights Gained by Measuring Mass, Charge, and Collision Cross Section. *Chem. Rev.* **2023**, *123* (6), 2902-2949. DOI: 10.1021/acs.chemrev.2c00600.
[119] Skeene, K.; Khatri, K.; Soloviev, Z.; Lapthorn, C. Current status and future prospects for ion-mobility mass spectrometry in the biopharmaceutical industry. *Biochim. Biophys. Acta. Proteins Proteom.* **2021**, *1869* (12), 140697. DOI: 10.1016/j.bbapap.2021.140697.
[120] Campuzano, I. D. G. CHAPTER 13. The Role of Ion Mobility for Antibody Characterisation: A Biopharmaceutical Perspective. Royal Society of Chemistry, 2021; pp 336-366.

[121] Atmanene, C.; et al. Extending Mass Spectrometry Contribution to Therapeutic Monoclonal Antibody Lead Optimization: Characterization of Immune Complexes Using Noncovalent ESI-MS. *Anal. Chem.* **2009**, *81* (15), 6364-6373. DOI: 10.1021/ac9007557.
[122] Bagal, D.; Valliere-Doughlass, J. F.; Balland, A.; Schnier, P. D. Resolving Disulfide Structural Isoforms of IgG2 Monoclonal Antibodies by Ion Mobility MassSpectrometry. *Anal. Chem.* **2010**, *82*, 6751-6755. DOI: 10.1021/ac1013139.
[123] Zhong, Y.; Hyung, S.-J.; Ruotolo, B. T. Characterizing the resolution and accuracy of a second-generation traveling-wave ion mobility separator for biomolecular ions. *Analyst* **2011**, *136* (17), 3534. DOI: 10.1039/c0an00987c.
[124] Giles, K.; Williams, J. P.; Campuzano, I. Enhancements in travelling wave ion mobility resolution. *Rapid Commun. Mass Spectrom.* **2011**, *25* (11), 1559-1566. DOI: 10.1002/rcm.5013.
[125] Fenn, J. B.; Mann, M.; Meng, C. K.; Wong, S. F.; Whitehouse, C. M. Electrospray Ionization for Mass Spectrometry of Large Biomolecules. *Science* **1989**, *246* (4926), 64-71. DOI: 10.1126/science.2675315.
[126] Banerjee, S.; Mazumdar, S. Electrospray Ionization Mass Spectrometry: A Technique to Access the Information beyond the Molecular Weight of the Analyte. *Int. J. Anal. Chem.* **2012**, *2012*, 1-40. DOI: 10.1155/2012/282574.
[127] Smith, J. N.; Flagan, R. C.; Beauchamp, J. L. Droplet Evaporation and Discharge Dynamics in Electrospray Ionization. *J. Phys. Chem. A* **2002**, *106* (42), 9957-9967. DOI: 10.1021/jp025723e.
[128] Konermann, L.; Ahadi, E.; Rodriguez, A. D.; Vahidi, S. Unraveling the mechanism of electrospray ionization. *Anal. Chem.* **2013**, *85* (1), 2-9. DOI: 10.1021/ac302789c.
[129] Iribarne, J. V.; Thomson, B. A. On the evaporation of small ions from charged droplets. *J. Chem. Phys.* **1976**, *64* (6), 2287-2294. DOI: 10.1063/1.432536.
[130] Kebarle, P.; Verkerk, U. H. Electrospray: From ions in solution to ions in the gas phase, what we know now. *Mass Spectrom. Rev.* **2009**, *28* (6), 898-917. DOI: 10.1002/mas.20247.
[131] Kaltashov, I. A.; Mohimen, A. Estimates of Protein Surface Areas in Solution by Electrospray Ionization Mass Spectrometry. *Anal. Chem.* **2005**, *77* (16), 5370-5379. DOI: 10.1021/ac050511+.
[132] Fernandez De La Mora, J. Electrospray ionization of large multiply charged species proceeds via Dole's charged residue mechanism. *Anal. Chim. Acta.* **2000**, *406* (1), 93-104. DOI: 10.1016/s0003-2670(99)00601-7.
[133] McAllister, R. G.; Metwally, H.; Sun, Y.; Konermann, L. Release of Native-like Gaseous Proteins from Electrospray Droplets via the Charged Residue Mechanism: Insights from Molecular Dynamics Simulations. *J. Am. Chem. Soc.* **2015**, *137* (39), 12667-12676. DOI: 10.1021/jacs.5b07913.
[134] Ahadi, E.; Konermann, L. Modeling the Behavior of Coarse-Grained Polymer Chains in Charged Water Droplets: Implications for the Mechanism of Electrospray Ionization. *J. Phys. Chem. B* **2012**, *116* (1), 104-112. DOI: 10.1021/jp209344z.
[135] Wilm, M.; Mann, M. Analytical Properties of the Nanoelectrospray Ion Source. *Anal. Chem.* **1996**, *68* (1), 1-8. DOI: 10.1021/ac9509519.
[136] Westphall, M. S.; et al. Three-dimensional structure determination of protein complexes using matrix-landing mass spectrometry. *Nat. Commun.* **2022**, *13* (1). DOI: 10.1038/s41467-022-29964-4.

[137] Esser, T. K.; et al. Cryo-EM of soft-landed β-galactosidase: Gas-phase and native structures are remarkably similar. *Sci. Adv.* **2024**, *10* (7). DOI: 10.1126/sciadv.adl4628.
[138] Breuker, K.; McLafferty, F. W. Stepwise evolution of protein native structure with electrospray into the gas phase, 10^{-12} to 10^{2} s. *PNAS* **2008**, *105* (47), 18145-18152. DOI: 10.1073/pnas.0807005105.
[139] Warnke, S.; von Helden, G.; Pagel, K. Protein structure in the gas phase: the influence of side-chain microsolvation. *J. Am. Chem. Soc.* **2013**, *135* (4), 1177-1180. DOI: 10.1021/ja308528d From NLM Medline.
[140] Hansen, K.; et al. A Mass-Spectrometry-Based Modelling Workflow for Accurate Prediction of IgG Antibody Conformations in the Gas Phase. *Angew. Chem.* **2018**, *130* (52), 17440-17445. DOI: 10.1002/ange.201812018.
[141] Pacholarz, K. J.; et al. Dynamics of Intact Immunoglobulin G Explored by Drift-Tube Ion-Mobility Mass Spectrometry and Molecular Modeling. *Angew. Chem. Int. Ed.* **2014**, *53* (30), 7765-7769. DOI: 10.1002/anie.201402863.
[142] Devine, P. W. A.; et al. Investigating the Structural Compaction of Biomolecules Upon Transition to the Gas-Phase Using ESI-TWIMS-MS. *J. Am. Soc. Mass Spectrom.* **2017**, *28* (9), 1855-1862. DOI: 10.1007/s13361-017-1689-9 From NLM Medline.
[143] Campuzano, I. D. G.; Larriba, C.; Bagal, D.; Schnier, P. D. Ion Mobility and Mass Spectrometry Measurements of the Humanized IgGk NIST Monoclonal Antibody. In *State-of-the-Art and Emerging Technologies for Therapeutic Monoclonal Antibody Characterization Volume 3. Defining the Next Generation of Analytical and Biophysical Techniques*; Schiel, J. E., Davis, D. L., Borisov, O. V., Eds.; ACS Symposium Series; American Chemical Society, 2015; DOI: 10.1021/bk-2015-1202.ch004.
[144] Pringle, S. D.; et al. An investigation of the mobility separation of some peptide and protein ions using a new hybrid quadrupole/travelling wave IMS/oa-ToF instrument. *Int. J. Mass Spectrom.* **2007**, *261* (1), 1-12. DOI: 10.1016/j.ijms.2006.07.021.
[145] Sobott, F.; Hernández, H.; McCammon, M. G.; Tito, M. A.; Robinson, C. V. A Tandem Mass Spectrometer for Improved Transmission and Analysis of Large Macromolecular Assemblies. *Anal. Chem.* **2002**, *74* (6), 1402-1407. DOI: 10.1021/ac0110552.
[146] Guilhaus, M.; Selby, D.; Mlynski, V. Orthogonal acceleration time-of-flight mass spectrometry. *Mass Spectrom. Rev.* **2000**, *19* (2), 65-107. DOI: 10.1002/(sici)1098-2787(2000)19:2<65::aid-mas1>3.0.co;2-e.
[147] Chernushevich, I. V.; Loboda, A. V.; Thomson, B. A. An introduction to quadrupole–time-of-flight mass spectrometry. *J. Mass. Spectrom.* **2001**, *36* (8), 849-865. DOI: 10.1002/jms.207.
[148] De Hoffmann, E. Mass Spectrometry. *Kirk-Othmer Encyclopedia of Chemical Technology* **2005**. DOI: 10.1002/0471238961.1301191913151518.a01.pub2.
[149] Mamyrin, B. A. Time-of-flight mass spectrometry (concepts, achievements, and prospects). *Int. J. Mass Spectrom.* **2001**, *206* (3), 251-266. DOI: 10.1016/s1387-3806(00)00392-4.
[150] Valentine, S. J.; Kulchania, M.; Barnes, C. A. S.; Clemmer, D. E. Multidimensional separations of complex peptide mixtures: a combined high-performance liquid chromatography/ion mobility/time-of-flight mass spectrometry approach. *Int. J. Mass Spectrom.* **2001**, *212* (1-3), 97-109. DOI: 10.1016/s1387-3806(01)00511-5.

[151] Dodds, J. N.; Baker, E. S. Ion Mobility Spectrometry: Fundamental Concepts, Instrumentation, Applications, and the Road Ahead. *J. Am. Soc. Mass Spectrom.* **2019**, *30* (11), 2185-2195. DOI: 10.1007/s13361-019-02288-2.
[152] Ruotolo, B. T.; Benesch, J. L. P.; Sandercock, A. M.; Hyung, S.-J.; Robinson, C. V. Ion mobility–mass spectrometry analysis of large protein complexes. *Nat. Protoc.* **2008**, *3* (7), 1139-1152. DOI: 10.1038/nprot.2008.78.
[153] Mason, E. A.; McDaniel, E. W. Transport Properties of Ions in Gases. **1988**. DOI: 10.1002/3527602852.
[154] Gabelica, V.; et al. Recommendations for reporting ion mobility Mass Spectrometry measurements. *Mass Spectrom. Rev.* **2019**, *38* (3), 291-320. DOI: 10.1002/mas.21585.
[155] Giles, K.; et al. Applications of a travelling wave-based radio-frequency-only stacked ring ion guide. *Rapid Commun. Mass Spectrom.* **2004**, *18* (20), 2401-2414. DOI: 10.1002/rcm.1641.
[156] Bush, M. F.; et al. Collision Cross Sections of Proteins and Their Complexes: A Calibration Framework and Database for Gas-Phase Structural Biology. *Anal. Chem.* **2010**, *82* (22), 9557-9565. DOI: 10.1021/ac1022953.
[157] Richardson, K.; Langridge, D.; Dixit, S. M.; Ruotolo, B. T. An Improved Calibration Approach for Traveling Wave Ion Mobility Spectrometry: Robust, High-Precision Collision Cross Sections. *Anal. Chem.* **2021**, *93* (7), 3542-3550. DOI: 10.1021/acs.analchem.0c04948.
[158] Politis, A.; et al. Integrating Ion Mobility Mass Spectrometry with Molecular Modelling to Determine the Architecture of Multiprotein Complexes. *PLoS One* **2010**, *5* (8), e12080. DOI: 10.1371/journal.pone.0012080.
[159] Deslignière, E.; et al. Benefits and Limitations of High-Resolution Cyclic IM-MS for Conformational Characterization of Native Therapeutic Monoclonal Antibodies. *Anal. Chem.* **2023**, *95* (8), 4162-4171. DOI: 10.1021/acs.analchem.2c05265.
[160] Dixit, S. M.; Polasky, D. A.; Ruotolo, B. T. Collision induced unfolding of isolated proteins in the gas phase: past, present, and future. *Curr. Opin. Chem. Biol.* **2018**, *42*, 93-100. DOI: 10.1016/j.cbpa.2017.11.010.
[161] Castel, J.; Delaux, S.; Hernandez-Alba, O.; Cianferani, S. Recent advances in structural mass spectrometry methods in the context of biosimilarity assessment: from sequence heterogeneities to higher order structures. *J. Pharm. Biomed. Anal.* **2023**, *236*, 115696. DOI: 10.1016/j.jpba.2023.115696.
[162] Shelimov, K. B.; Clemmer, D. E.; Hudgins, R. R.; Jarrold, M. F. Protein Structure in Vacuo: Gas-Phase Conformations of BPTI and Cytochrome c. *J. Am. Chem. Soc.* **1997**, *119*, 2240-2248.
[163] Eschweiler, J. D.; Rabuck-Gibbons, J. N.; Tian, Y.; Ruotolo, B. T. CIUSuite: A Quantitative Analysis Package for Collision Induced Unfolding Measurements of Gas-Phase Protein Ions. *Anal. Chem.* **2015**, *87* (22), 11516-11522. DOI: 10.1021/acs.analchem.5b03292.
[164] Migas, L. G.; France, A. P.; Bellina, B.; Barran, P. E. ORIGAMI: A software suite for activated ion mobility mass spectrometry (aIM-MS) applied to multimeric protein assemblies. *Int. J. Mass Spectrom.* **2018**, *427*, 20-28. DOI: 10.1016/j.ijms.2017.08.014.
[165] Polasky, D. A.; Dixit, S. M.; Fantin, S. M.; Ruotolo, B. T. CIUSuite 2: Next-Generation Software for the Analysis of Gas-Phase Protein Unfolding Data. *Anal. Chem.* **2019**, *91* (4), 3147-3155. DOI: 10.1021/acs.analchem.8b05762.

[166] Sivalingam, G. N.; Cryar, A.; Williams, M. A.; Gooptu, B.; Thalassinos, K. Deconvolution of ion mobility mass spectrometry arrival time distributions using a genetic algorithm approach: Application to α1-antitrypsin peptide binding. *Int. J. Mass Spectrom.* **2018**, *426*, 29-37. DOI: 10.1016/j.ijms.2018.01.008.
[167] Allison, T. M.; et al. Quantifying the stabilizing effects of protein–ligand interactions in the gas phase. *Nat. Commun.* **2015**, *6* (1), 8551. DOI: 10.1038/ncomms9551.
[168] Tian, Y.; Han, L.; Buckner, A. C.; Ruotolo, B. T. Collision Induced Unfolding of Intact Antibodies: Rapid Characterization of Disulfide Bonding Patterns, Glycosylation, and Structures. *Anal. Chem.* **2015**, *87* (22), 11509-11515. DOI: 10.1021/acs.analchem.5b03291.
[169] Botzanowski, T.; et al. Middle Level IM–MS and CIU Experiments for Improved Therapeutic Immunoglobulin Subclass Fingerprinting. *Anal. Chem.* **2020**, *92* (13), 8827-8835. DOI: 10.1021/acs.analchem.0c00293.
[170] Villafuerte-Vega, R. C.; et al. Ion Mobility-Mass Spectrometry and Collision-Induced Unfolding of Designed Bispecific Antibody Therapeutics. *Anal. Chem.* **2023**, *95* (17), 6962-6970. DOI: 10.1021/acs.analchem.3c00344.
[171] Desligniere, E.; et al. Combination of IM-Based Approaches to Unravel the Coexistence of Two Conformers on a Therapeutic Multispecific mAb. *Anal. Chem.* **2022**, *94* (22), 7981-7989. DOI: 10.1021/acs.analchem.2c00928.
[172] Tian, Y.; Lippens, J. L.; Netirojjanakul, C.; Campuzano, I. D. G.; Ruotolo, B. T. Quantitative collision-induced unfolding differentiates model antibody–drug conjugates. *Protein Sci.* **2019**, *28* (3), 598-608. DOI: 10.1002/pro.3560.
[173] Deslignière, E.; et al. State-of-the-Art Native Mass Spectrometry and Ion Mobility Methods to Monitor Homogeneous Site-Specific Antibody-Drug Conjugates Synthesis. *Pharmaceuticals* **2021**, *14* (6), 498. DOI: 10.3390/ph14060498.
[174] Tian, Y.; Ruotolo, B. T. Collision induced unfolding detects subtle differences in intact antibody glycoforms and associated fragments. *Int. J. Mass Spectrom.* **2018**, *425*, 1-9. DOI: 10.1016/j.ijms.2017.12.005.
[175] Vallejo, D. D.; et al. Ion Mobility–Mass Spectrometry Reveals the Structures and Stabilities of Biotherapeutic Antibody Aggregates. *Anal. Chem.* **2022**, *94* (18), 6745-6753. DOI: 10.1021/acs.analchem.2c00160.
[176] Vallejo, D. D.; et al. Collision-Induced Unfolding Reveals Stability Differences in Infliximab Therapeutics under Native and Heat Stress Conditions. *Anal. Chem.* **2021**, *93* (48), 16166-16174. DOI: 10.1021/acs.analchem.1c03946.
[177] Pisupati, K.; et al. A Multidimensional Analytical Comparison of Remicade and the Biosimilar Remsima. *Anal. Chem.* **2017**, *89* (9), 4838-4846. DOI: 10.1021/acs.analchem.6b04436.
[178] Huang, Y.; Salinas, N. D.; Chen, E.; Tolia, N. H.; Gross, M. L. Native Mass Spectrometry, Ion mobility, and Collision-Induced Unfolding Categorize Malaria Antigen/Antibody Binding. *J. Am. Soc. Mass Spectrom.* **2017**, *28* (11), 2515-2518. DOI: 10.1007/s13361-017-1782-0.
[179] Watanabe, Y.; et al. Signature of Antibody Domain Exchange by Native Mass Spectrometry and Collision-Induced Unfolding. *Anal. Chem.* **2018**, *90* (12), 7325-7331. DOI: 10.1021/acs.analchem.8b00573.

[180] Deslignière, E.; et al. Toward Automation of Collision-Induced Unfolding Experiments through Online Size Exclusion Chromatography Coupled to Native Mass Spectrometry. *Anal. Chem.* **2020**, *92* (19), 12900-12908. DOI: 10.1021/acs.analchem.0c01426.
[181] Juliano, B. R.; et al. Development of an Automated, High-Throughput Methodology for Native Mass Spectrometry and Collision-Induced Unfolding. *Anal. Chem.* **2023**, *95* (45), 16717-16724. DOI: 10.1021/acs.analchem.3c03788.
[182] Van Schaick, G.; et al. Online Collision-Induced Unfolding of Therapeutic Monoclonal Antibody Glyco-Variants through Direct Hyphenation of Cation Exchange Chromatography with Native Ion Mobility–Mass Spectrometry. *Anal. Chem.* **2023**, *95* (8), 3932-3939. DOI: 10.1021/acs.analchem.2c03163.

Chapter 2: Ion Mobility-Mass Spectrometry and Collision-Induced Unfolding of Designed Bispecific Antibody Therapeutics

2.1 Original Publication

This chapter is originally published as: Rosendo C. Villafuerte-Vega, Henry W. Li, Thomas R. Slaney, Naresh Chennamsetty, Guodong Chen, Li Tao, and Brandon T. Ruotolo. "Ion Mobility-Mass Spectrometry and Collision-Induced Unfolding of Designed Bispecific Antibody Therapeutics." *Anal. Chem.* 2023, 95, 17, 6962 – 6970, DOI: 10.1021/acs.analchem.3c00344.

2.2 Author Contributions

R.C.V., B.T.R., T.S., G. C., and L.T. designed and conceived the experiments described. R.C.V. collected, analyzed, and plotted Synapt G2 and UHMR data, as well as drafted the manuscript. B.T.R and R.C.V. analyzed all data. H.W.L. assisted in collecting and analyzing Synapt G2 data. T.S., N.C., G.G., and L.T. provided all antibodies used in this work, as well as curated the SEC-MALS results shown in Appendix Figure B-2.

2.3 Abstract

Bispecific antibodies (bsAbs) represent a critically important class of emerging therapeutics capable of targeting two different antigens simultaneously. As such, bsAbs have been developed as effective treatment agents for diseases that remain challenging for conventional monoclonal antibody (mAb) therapeutics to access. Despite these advantages, bsAbs are intricate molecules, requiring both the appropriate engineering and pairing of heavy

and light chains derived from separate parent mAbs. Current analytical tools for tracking the bsAb construction process have demonstrated a limited ability to robustly probe the higher order structure (HOS) of bsAbs. Native ion mobility-mass spectrometry (IM-MS) and collision induced unfolding (CIU) have proven to be useful tools in probing the HOS of mAb therapeutics. In this report, we describe a series of detailed and quantitative IM-MS and CIU datasets that reveal HOS details associated with a knob-into-hole (KiH) bsAb model system and its corresponding parent mAbs. We find that quantitative analysis of CIU data indicates that global KiH bsAb stability occupies an intermediate space between the stabilities recorded for its parent mAbs. Furthermore, our CIU data identifies the hole-containing half of the KiH bsAb construct to be least stable, thus driving much of the overall stability of the KiH bsAb. An analysis of both intact bsAb and middle-level fragments allows us to associate the first and second CIU transitions observed for the intact KiH bsAb to the unfolding Fab and Fc domains, respectively. This result is likely general for CIU data collected for low charge state mAb ions and is supported by data acquired for deglycosylated KiH bsAb and mAb constructs, each of which indicate greater destabilization of the second CIU transition observed in our data. When integrated, our CIU analysis allows us to link changes in the first CIU transition primarily to the Fab region of the hole-containing halfmer, while the second CIU transition is likely strongly connected to the Fc region of the knob-containing halfmer. Taken together, our results provide an unprecedented roadmap for evaluating the domain-level stabilities and HOS of both KiH bsAb and mAb constructs using CIU.

2.4 Introduction

Bispecific antibodies (bsAbs) have become promising therapeutic modalities since they merge the specificities of two different monoclonal antibodies (mAbs). This unique quality of

bsAbs not only permits the targeting of two distinct epitopes or antigens simultaneously, but it also paves the way for innovative functionalities that are unattainable with conventional mAb-based therapeutics. Examples of such treatment strategies include the redirection and activation of immune effector cell cytotoxic activity to specifically eradicate tumor cells,[1-3] the selective inhibition of enzymes across the blood brain barrier responsible for amyloid-β (Aβ) peptide production,[4, 5] and the dual targeting and neutralization of two independent growth factors associated with neovascular eye diseases.[6, 7] These therapeutic capabilities have led to the market approval of two bsAbs by the US Food and Drug Administration, while well over 100 bsAbs are currently in clinical development.[8]

Advancements in antibody engineering and development have cultivated many different commercialized technology platforms within pharmaceutical and biotechnology companies for novel bsAb construction.[9] These technologies have led to the generation of primarily two different architectural classes of bsAbs: 1) fragment-based formats that join various antigen-binding moieties into one entity without a fragment crystallizable (Fc) region and 2) immunoglobulin G (IgG)-like molecules containing two different fragment antigen-binding (Fab) regions connected by an Fc domain. In most cases, the latter 'IgG format' for bsAbs exhibits greater solubility, stability, and plasma half-life when compared to other constructs due to its large size and resistance to catabolism by the neonatal Fc receptor, FcRn.[10] However, the production of bsAbs using this format is challenging since dual specificity is dependent on the co-expression of variable domains from two separate light chains and two separate heavy chains. Therefore, one of the major challenges is the chain association issue, where different chain combinations can theoretically result in 10 different antibodies of which only one matches the target functional bsAb.[9, 11]

Protein engineering approaches, such as the "knobs-into-holes" (KiH) concept, have been developed to address the bsAb chain association problem and enforce the proper heterodimerization of engineered heavy chains. This design strategy involves the mutation of amino acid residues at the interface between C_H3 domains of each heavy chain, where targeted residues are replaced with bulkier amino acids in the "knob" variant and smaller amino acids in the "hole" variant.[12] However, the characterization of bsAb therapeutics extends beyond their proper assembly. Antibody therapeutics are large (~150 kDa), exhibiting significantly more structural complexity and heterogeneity than conventional small molecule drugs. Additionally, changes in higher order structure (HOS) caused by KiH engineering, post-translational modifications, or degradation can result in the inhibition of molecular binding, an increased potential for immunogenicity, and a higher rate of aggregation.[13-16] Therefore, a thorough characterization of KiH bsAb HOS is crucial not only to define bsAb structure-function relationships but also to ensure the stability, efficacy, and safety of the final therapeutic.[17, 18]

A comprehensive range of biophysical techniques have been well-established for the characterization of mAb therapeutic HOS and stability. Tools such as circular dichroism (CD),[19] differential scanning calorimetry (DSC),[20] and size exclusion chromatography (SEC)[21] offer a global perspective on mAb stability and conformation, but they lack the resolution needed to distinguish subtle conformational changes. By contrast, techniques such as nuclear magnetic resonance (NMR) spectroscopy,[22] X-ray crystallography,[23] and cryogenic electron microscopy (cryo-EM)[24] provide atomically resolved structural information, but they typically require extensive sample preparation, large quantities of homogenous sample, lengthy data acquisition times, and complex data interpretation.[25] Currently, no full-length IgG-like bsAb crystal structures are publicly available, and only bsAb fragment structures have been reported.[26, 27]

Recently, native ion mobility-mass spectrometry (IM-MS) has emerged as a useful structural biology tool capable of probing the HOS of mAb therapeutics from a few micrograms of sample in the presence of structural heterogeneity and impurities. IM separates gas-phase protein ions based on their charge and rotationally averaged collision cross sections (CCSs) on the millisecond timescale.[28] When coupled with MS, two ions of the same mass-to-charge (*m/z*) ratio but different CCSs can be readily distinguished. IM-MS measurements have been shown to monitor the dynamics of bsAb formation resulting from Fab-arm exchange (FAE),[29] resolve disulfide structural isoforms of IgG2 mAbs,[30] and assess antibody-drug conjugate (ADC) structural heterogeneity.[31] Moreover, collision-induced unfolding (CIU) has enabled IM-MS to synchronously provide both protein structure and conformational stability information.[32] In CIU experiments, protein ions are collisionally heated prior to IM separation to elicit protein unfolding in the gas-phase. CIU has discriminated differences based on disulfide patterns,[33] glycosylation levels,[34, 35] domain exchanging properties,[36] and drug conjugation.[37, 38] CIU has also probed a bsAb formed via FAE of wt-IgG4s, highlighting that such bsAb can retain structural information from both its parent mAbs.[39] Despite past progress, quantitative CIU has yet to be deployed in the HOS evaluation of engineered KiH bsAb modalities, and the individual contributions of parent mAbs to bsAb HOS remain unclear.

In this report, we describe the first application of quantitative CIU to real-world, engineered bsAbs. Specifically, we extend the capabilities of native IM-MS and CIU to robustly characterize the HOS of a model KiH bsAb and its parent 'knob' and 'hole' homodimer mAbs. We define biophysical connections between these constructs by quantifying the global differences observed between CIU fingerprints and comparing their stabilities. We further convert the bsAb and its parent mAbs into fragments of various types to evaluate their domain-

level stabilities. By comparing the stabilities of isolated domains, we can localize contributions from each parent mAb in our KiH bsAb CIU transitions, where we discover evidence of Fab domains unfolding in lower-energy CIU transitions. After enzymatically removing *N*-linked glycans from the Fc regions of our constructs, we find evidence of destabilization occurring primarily in higher-energy CIU transitions, permitting us to pinpoint the unfolding of the Fc region in our CIU fingerprints. We conclude by discussing the potential impact of native IM-MS and CIU workflows on the HOS characterization of KiH bsAbs.

2.5 Experimental Section

Sample Preparation. KiH bsAb heterodimer (10 mg/mL) and 'knob' and 'hole' homodimer mAbs (2 mg/mL) were produced, purified, and formulated in their respective formulation buffer at Bristol Myers Squibb (New Brunswick, NJ). Here, we define 'homodimer' as intact mAb containing either 'knob' or 'hole' mutations, 'halfmer' as the half-molecule of 'knob' and 'hole' homodimer mAbs, and 'heterodimer' as intact KiH bsAb formed from the dimerization of 'knob' and 'hole' halfmers. All antibodies studied here were of the IgG isotype and IgG2 subclass, where one disulfide bond in the hinge region was mutated out. Glycerol-free PNGase F (500,000 units/mL) was purchased from New England Biolabs (Ipswich, MA). Papain from papaya latex was supplied as a buffered aqueous suspension and acquired from Sigma Aldrich (St. Louis, MO).

All native, unmodified samples were buffer exchanged into 200 mM ammonium acetate (pH 6.8 – 7.0) using Micro Bio-Spin P-6 columns (Bio-Rad, Hercules, CA) and diluted to working concentrations of 1 mg/mL (~6.7 μM) of intact homodimer or heterodimer. Removal of *N*-glycans from antibody constructs was achieved using PNGase F under non-denaturing conditions overnight per the vendor's recommended protocol. A control without PNGase F was

incubated concurrently. For the papain digestion of the KiH bsAb, papain was first activated with 5 mM cysteine for 30 min at 37ºC. Excess cysteine was then removed by buffer exchanging the activated papain into digestion buffer (200 mM ammonium acetate, 5 mM EDTA, pH 6.8 – 7.0) using Micro Bio-Spin P-6 columns. KiH bsAb (1 mg/mL) sample was buffer exchanged into digestion buffer followed by the addition of activated papain to achieve a 1:100 (papain:bsAb) ratio. The digest was then incubated for 2 hr at 37ºC to cleave the KiH bsAb above the hinge region and generate intact Fab and Fc fragments. A control without papain was also incubated to track potential disulfide bond reduction caused by any residual cysteine in the digestion buffer. Little to no disulfide bond reduction was observed. All deglycosylated and papain-digested samples were quenched on ice and immediately buffer exchanged into 200 mM ammonium acetate (pH 6.8 – 7.0) using Bio-Spin P-6 columns.

Native MS Analysis. High resolution native MS experiments were performed on a standard commercial Q Exactive Orbitrap MS with Ultra High Mass Range (UHMR) platform (Thermo Scientific, San Jose, CA). Samples were further diluted to ~2 μM before analysis. Sample (~3 μL) was transferred to a gold-coated borosilicate capillary needle (prepared in house), and ions were generated via direct infusion using a commercial Thermo Fisher Nanospray Flex Ion Source (ES071) with a static nanospray ionization (NSI) probe operated in positive ion mode. Capillary voltages were held at 1.1 – 1.2 kV, and the inlet capillary was heated to 275ºC. Nitrogen was used as the collision gas, and the trapping pressure was set to 3. Low *m/z* detector optimization and high *m/z* transfer optics were used to optimize the transmission of mAb homodimer and KiH bsAb heterodimer ions. In-source trapping was enabled with the desolvation voltage fixed at -50 V for improved ion transmission and efficient

salt adduct removal. Transient times were set at 128 ms (resolution of 25,000 at *m/z* 400). Mass spectra were then processed and deconvoluted using UniDec software.[40]

Native IM-MS and CIU. IM-MS and CIU experiments were performed using a quadrupole-ion mobility-time-of-flight mass spectrometer (Q-IM-ToF-MS) instrument (Synapt G2 HDMS, Waters, Milford, MA). Sample (~3 μL) was transferred to a gold-coated borosilicate capillary needle, and ions were generated by direct infusion utilizing a nano-electrospray ionization (nESI) source set to the positive mode. The nESI capillary was operated at voltages of 1.1 – 1.5 kV. For intact and halfmer species, the sampling cone was operated at 40 V, while for Fab and Fc fragments, it was operated at 20 V to prevent in-source activation. The backing pressure was set to ~7.3 to 7.5 mbar. The helium cell flow rate was operated at 200 mL/min and pressurized to 1.4 x 10-3 mbar. The trap travelling wave ion guide was pressurized to 4.9 x 10-2 mbar of argon gas. The travelling-wave IM separator was operated at a pressure of ~3.4 mbar, and IM separation was achieved with a travelling wave height and velocity of 40 V and 600 m/s, respectively. The ToF-MS was operated over an m/z range of 1000 – 12,000 at a pressure of 2.3 x 10^{-6}. Ions were subjected to collisions in the travelling-wave ion trap prior to IM separation to perform CIU. For intact KiH bsAb, knob, and hole constructs, tandem-MS was utilized to select charge state 24^{+}. For ions corresponding to halfmer, charge state 16^{+} was selected. The collisional voltages were then ramped from 5 V to 200V in 5 V intervals to construct each CIU fingerprint. For Fab and Fc fragment measurements, charge state 13^{+} was selected, and collision voltages were ramped from 5 V to 140 V in 5 V increments since collisional activation above 140 V resulted in fragmentation. Polyalanine ions, bovine serum albumin, and glutamate dehydrogenase were used as CCS calibrants. All data collection was performed in triplicate.

IM and MS data were viewed using DriftScope and Masslynx V4.1 software, respectively (Waters, Milford, MA). Mass spectra were deconvoluted using UniDec software.[40] Drift times were extracted at each collision voltage using TWIMExtract (v1.5).[41] $^{TW}CCS_{N2}$ calculations were performed using IMSCal software.[42] Extracted drift time data were then analyzed using a home-built software package, CIUSuite 2 (v2.2).[43] CIU fingerprints were 2-D smoothed with a Savitzky-Golay function with a smoothing window of 5 and 2 smoothing iterations. The collision voltage axis was interpolated with an axis scaling factor of 2 for intact constructs and 4 for halfmers and Fab and Fc fragments. Standard feature detection was performed using a minimum feature length of 3 steps, an allowed width of 0.75 drift time axis units, and a maximum CV gap length of 0. CIU_{50} values were then assigned using max centroiding mode with a transition region padding of 15 CV and a maximum CV gap length of 0. CIU_{50} represents the collision voltage at which 50% of a more compact state of the antibody transitions to a more unfolded state, and it defines the midpoint between adjacent features. Root-mean-square-deviation analysis (RMSD) analysis was performed using the compare function in CIUSuite 2. All CIU fingerprints shown are the average of three replicates.

2.6 Results and Discussion

Native IM-MS and CIU of knob and hole homodimers and KiH bsAb heterodimer. The native IM-MS spectra of knob, hole, and KiH bsAb samples reveal various ion populations corresponding to intact homodimer and heterodimer, as well as low and high molecular weight species (Appendix Figure B-1A). Knob and hole spectra show high abundances of halfmers, highlighting that KiH mutations (knob: T366W, hole: T366S, L368A, Y407V) impede efficient halfmer dimerization into homodimer. Size-exclusion chromatography with multi-angle light scattering (SEC-MALS) data showed mass fractions of ~56% and ~43% for homodimers and

halfmers, respectively (Appendix Figure B-2). Differences in halfmer abundances in our native IM-MS data are likely the result of ionization efficiency differences between the two ion classes tracked in these experiments. IM-MS data for the KiH bsAb, on the other hand, shows very minimal halfmer populations, revealing the effective association of knob and hole halfmers into heterodimer. All intact antibodies present narrow charge state distributions (21^+ to 26^+), indicating the preservation of native-like structural information in the gas-phase compared to denatured species.[44-46] Moreover, all glycosylation sites are conserved for each antibody, and averaged deconvoluted masses include all glycoforms such as those commonly found in standard mAbs (Appendix Figure B-1B).

To further probe the HOS of knob and hole homodimers and KiH bsAb heterodimer, we performed CIU on a range of charge states (22^+ to 24^+). Previous studies have indicated that ion charge state influences the number of transitions in its CIU fingerprint, where lower charge states produce CIU data that correlates with the number of protein domains.[47, 48] As expected, the lowest charge state, 22^+, requires higher acceleration voltages to unfold, giving rise to fewer CIU intermediates when compared to more highly-charged ions (Appendix Figure B-3). We observe three main CIU features for 23^+ and 24^+ KiH bsAb ions, where the intensity of the most unfolded feature detected at higher collision voltages is most prominent in the latter charge state. For our analyses described below, we chose to focus on 24^+ ions due to their large relative intensities and more prominent third CIU features. Globally, our analysis reveals both similarities and differences across the parent homodimer mAbs and the KiH bsAb studied here (Figure 2-1). Notably, all antibodies undergo a similar number of CIU transitions. Technical replicates

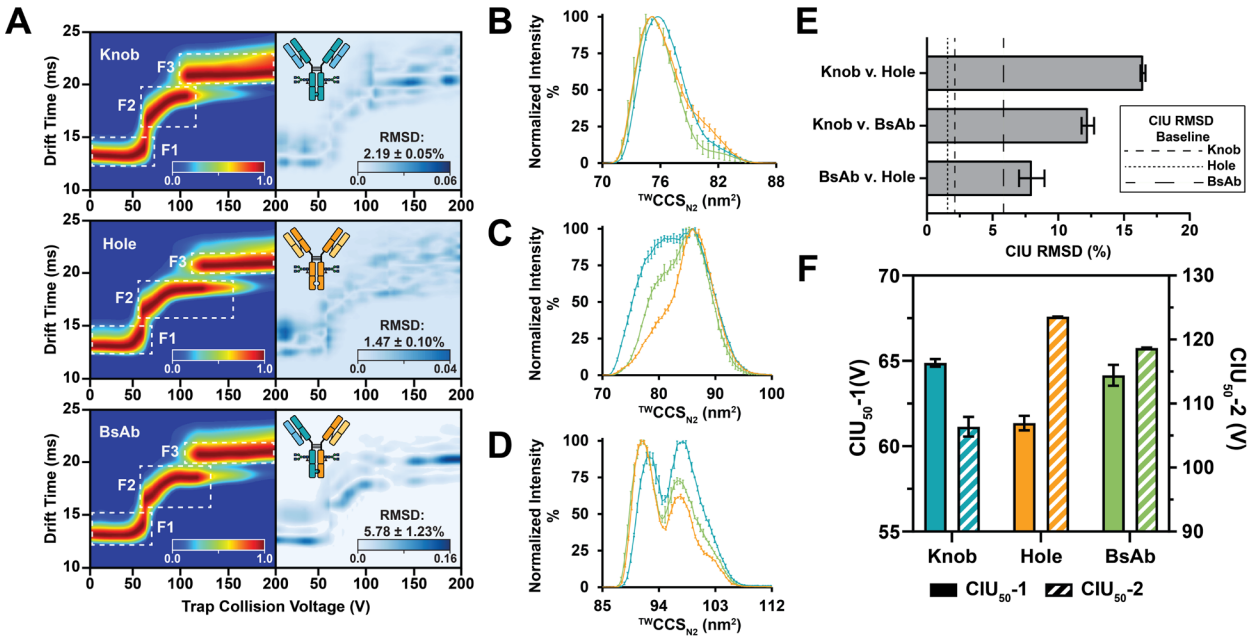

Figure 2-1: CIU experiments of native, unmodified knob (blue) and hole (orange) homodimers and KiH bsAb heterodimer (green). (A) Averaged CIU fingerprints (n = 3) for the 24^+ charge state (left) with corresponding replicate RMSD baselines (right). All fingerprints show three main features indicated by the dashed white boxes. Normalized $^{TW}CCS_{N2}$ distributions at (B) 5 V, (C) 65 V, (D) 110 V. At lower activation potentials, all antibodies adopt similar $^{TW}CCS_{N2}$ distributions, which significantly diverge at higher acceleration potentials. (E) Pairwise RMSD analysis reveals global HOS differences among antibodies compared to replicate RMSD baselines (dashed lines). (F) CIU_{50} analysis illustrates how the model KiH bsAb adopts a stability between those of knob and hole homodimers.

produce baseline RMSDs of < 6%, which indicate consistent, reproducible CIU data for all samples (Figure 2-1A). To better quantify differences among our intact constructs, we first utilized the classification workflow within CIUSuite 2 to select collision voltages that exhibit the greatest differences in arrival time distributions (ATDs) between CIU fingerprints.[43, 49] Conversion of IM drift times to $^{TW}CCS_{N2}$ values reveal broad $^{TW}CCS_{N2}$ ensembles that are essentially indistinguishable by IM-MS alone at 5 V (Figure 2-1B). However, $^{TW}CCS_{N2}$ data captured at collision voltages of 65 V (Figure 2-1C) and 110 V (Figure 2-1D), reveal significantly different distributions of $^{TW}CCS_{N2}$. At these higher collision voltages, we observe that the KiH bsAb occupies an intermediate space of $^{TW}CCS_{N2}$ values between those of knob and hole homodimer mAbs, which agrees with previous CIU findings of a bsAb formed via FAE.[39]

Interestingly, the $^{TW}CCS_{N2}$ distributions recorded for the KiH bsAb at 65 V are similar to those produced by knob homodimer CIU data. At 110 V, however, KiH bsAb CIU data switches to produce $^{TW}CCS_{N2}$ distributions like those of hole homodimer CIU data. These observations provide early evidence suggesting bsAb stability is discreetly connected to both parent homodimer mAbs for the KiH model studied here.

To build upon these observations, we performed pairwise RMSD analyses between CIU data recorded for all antibodies in order to probe global conformational differences (Figure 2-1E). A comparison of knob and hole homodimers yields an RMSD of 16.45 ± 0.19%, indicating significant differences in global homodimer mAb HOS. When CIU data collected for knob and hole homodimers are compared to KiH bsAb data, however, we observe decreased RMSD values. Specifically, a comparison between knob homodimer and the KiH bsAb CIU fingerprints produces an RMSD of 12.25 ± 0.48%, while a comparison between hole homodimer and the KiH bsAb produces an RMSD of 7.98 ± 0.96% (Appendix Figure B-4). These comparisons reveal that the KiH bsAb CIU data, and by extension bsAb global stability, most closely resembles that of the hole homodimer for the model system studied here. Next, we shifted our focus to evaluating differences in CIU_{50}-based stability values between knob, hole, and KiH bsAb. CIU_{50} analyses of knob, hole, and KiH bsAb constructs indicate that KiH bsAb stability can indeed be characterized as intermediate between its parent homodimers if initial protein unfolding is used as the primary method of evaluating protein stability. Specifically, CIU_{50}-1 values, which correspond to the first CIU transition recorded in our fingerprints, indicate that the hole homodimer (61.36 ± 0.42 V) is less stable than both the knob homodimer (64.88 ± 0.23 V) and the KiH bsAb (64.16 ± 0.62 V) (Figure 2-1F). Conversely, CIU_{50}-2 values, which are linked to the second, higher-energy CIU transition detected in our experiments, reveal that

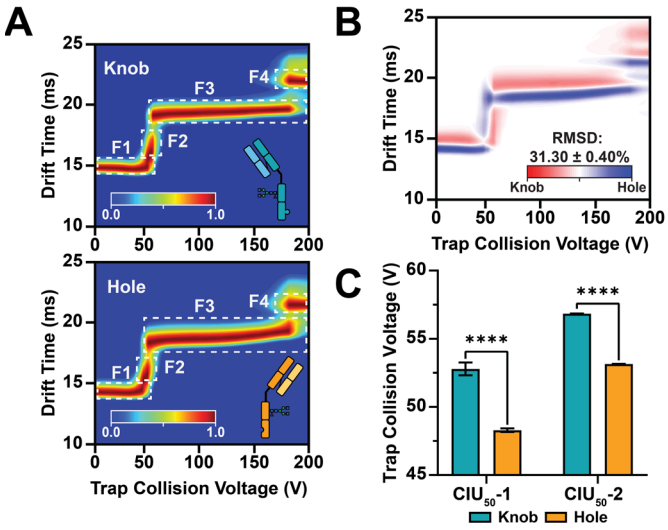

Figure 2-2: CIU data recorded for knob and hole halfmers. (A) Averaged CIU fingerprints ($n = 3$) for 16^+ charge states. (B) Pairwise RMSD analyses reveal significant differences between halfmer HOSs. (C) CIU_{50} analysis shows significant differences (**** $p < 0.0001$) in protein stabilities.

the knob homodimer (106.38 ± 1.52 V) unfolds at collision voltages lower than those of both the hole homodimer (123.57 ± 0.02 V) and the KiH bsAb (118.67 ± 0.07 V). Our data indicates that the KiH bsAb studied here exhibits CIU-based composite stabilities of 51.4% knob and 48.6% hole for CIU_{50}-1 and 46.3% knob and 53.7% hole for CIU_{50}-2. We quantified these stability contributions by summing each CIU_{50} value of knob and hole together for each transition then divided each measured CIU_{50} by this total. Taken together, these results suggest that the CIU_{50}-1 and CIU_{50}-2 values recorded in our fingerprints are likely reporting on the local stabilities of different domains within the KiH bsAb and mAb constructs studied here.

Middle-level CIU reveals knob and hole domain contributions to KiH bsAb HOS.

To better assign regions of the KiH bsAb to specific CIU features, we performed CIU experiments targeting antibody fragment ions generated under native conditions. First, we recorded CIU data for 16^+ knob and hole halfmers (Figure 2-2A) present in our homodimer mAb IM-MS spectra (Appendix Figure B-1A). In these fingerprints, we observe four main CIU features across both constructs, but RMSD analysis reveals significant differences in their native-like structures (31.30 ± 0.40%) when compared to baseline RMSD values recorded for technical replicates (3.02 ± 0.54% and 1.48 ± 0.23% for knob and hole halfmers, respectively) (Figure 2-2B). CIU_{50} analysis further reveals that knob halfmer is significantly more stable than the hole

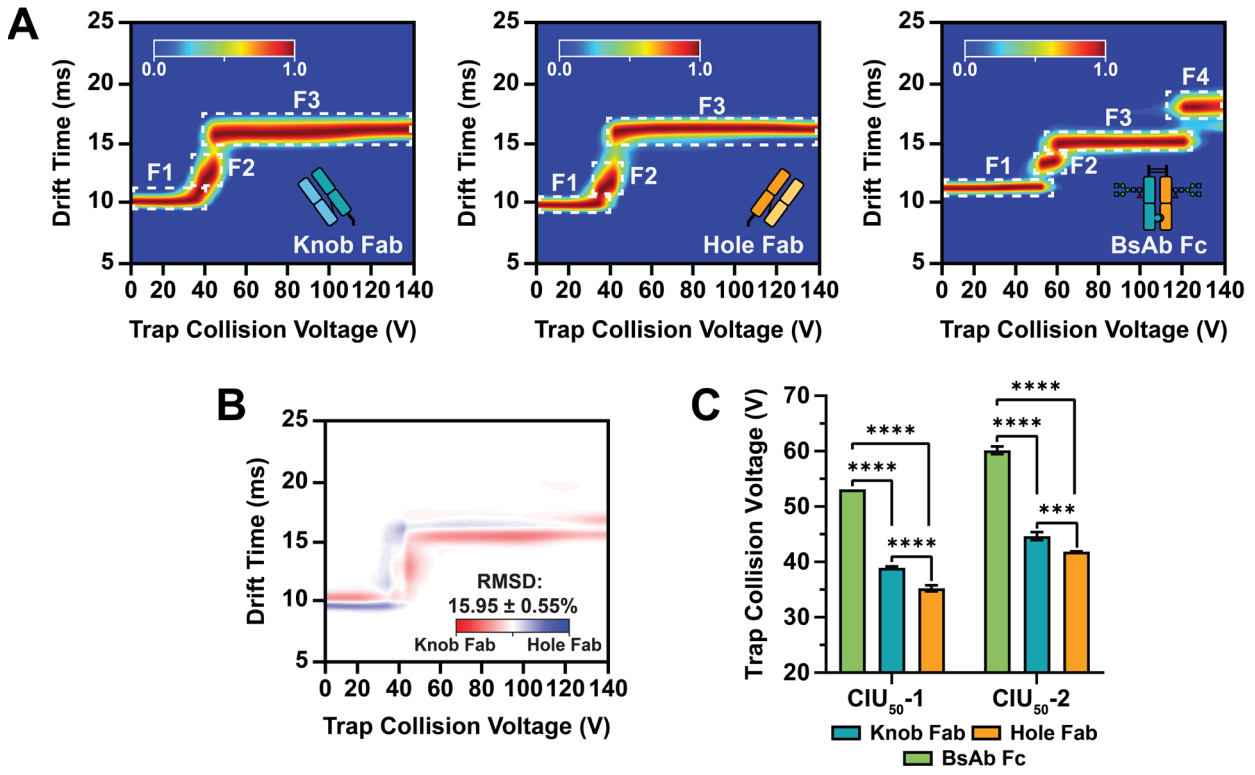

Figure 2-3: CIU data recorded for Fab and Fc fragments. (A) Averaged CIU fingerprints (n = 3) for 13^+ charge states. (B) Pairwise RMSD analysis reveals significant differences between knob and hole Fab fragments. (C) CIU_{50} analysis indicates significant differences (** $p < 0.01$, **** $p < 0.0001$) in fragment stabilities.

halfmer across the first two unfolding transitions observed (Figure 2-2C). These differences in stability correlate strongly with our prior measurements of intact hole and knob homodimer CIU_{50}-1 values. We note that knob and hole halfmers differ in experimental mass by ~2%. Previous studies have demonstrated that protein primary structure can influence CIU patterns.[47] Therefore, it is likely that the differences we observe in knob and hole halfmer stability are connected, in part, to the sequence differences associated with each halfmer. We hypothesize that the Fab regions, which contain hypervariable complementarity-determining regions (CDRs) that determine specific antigen binding, are the main contributors to the differences in CIU detected in our data.

To continue our efforts in assigning CIU features observed in the KiH bsAb to specific domains or regions within its structure, we performed CIU on the Fab and Fc fragments generated via papain digestion. Here, papain cleaves above the hinge region to produce a knob Fab, a hole Fab, and a chimeric Fc held together by hinge disulfides and non-covalent interactions (Appendix Figure B-5). CIU fingerprints for Fab fragments reveal three CIU features for both knob and hole Fabs (Figure 2-3A). The CIU fingerprint of the chimeric Fc domain, on the other hand, shows four CIU features. Although IM-MS and CIU of middle-level fragments of mAbs have been performed previously, most involved $F(ab')_2$ and non-covalent Fc produced via IdeS digestion.[34, 36, 50] Botzanowski and coworkers, in particular, described a compaction phase in non-covalent Fc CIU data at higher collision voltages.[50] Notably, we do not observe a compaction phase in our Fc CIU fingerprint, indicating that the fragments studied here are not directly comparable to those previously reported in the literature. As such, these CIU experiments provide new insights into individual Fab and Fc HOS and stability for KiH bsAbs. Technical replicates recorded for knob Fab, hole Fab, and chimeric Fc fragments yield RMSD baselines of 2.08 ± 0.28%, 1.41 ± 0.21%, and 4.85 ± 0.70%, respectively. Although knob and hole Fabs share qualitatively similar CIU fingerprints, difference analysis reveals an RMSD of 15.59 ± 0.55%, indicating that these fragments differ greatly in terms of their HOS (Figure 2-3B). Like our halfmer data, we note that the Fabs studied here differ in mass by ~2%. Thus, the differences in HOS that we observe are most likely connected to the hypervariable regions of the CDRs of each Fab. Furthermore, a stability assessment of these fragments quantitatively shows that the knob Fab is significantly more stable than the Hole Fab across both CIU_{50}-1 and CIU_{50}-2 values recorded (Figure 2-3C). Interestingly, our data also indicate that the Fc domain is significantly more stable than both knob and hole Fab domains. This difference in stability is

most likely related to the strong non-covalent interactions that exist between the C_H3 domains within each heavy chain, as well as the knob and hole mutations promoting heavy chain dimerization.[51-53]

Removal of *N*-glycans impact knob and hole homodimer and KiH bsAb heterodimer conformation and stability. Previous work has demonstrated that CIU is sensitive to different levels of mAb glycosylation, where the removal of sugars leads to the destabilization of mAb HOS.[33-35] Furthermore, the removal of glycans has been shown to decrease the thermal stability of C_H2 domains within the mAb Fc region.[54] Therefore, to better assign CIU transitions corresponding to the unfolding of the Fc domain of our model KiH bsAb, we removed *N*-linked glycans from the C_H2 domains of knob, hole, and KiH bsAb constructs and probed their resulting stabilities using CIU.

To better track the progress of our deglycosylation reactions, we performed high-resolution native orbitrap MS experiments to resolve individual homodimer mAb and KiH bsAb glycoforms both prior to and after the addition of PNGase F. Our results provide evidence for a wide range of glycoforms for knob, hole, and KiH bsAb constructs. Notably, the KiH bsAb exhibits high glycan heterogeneity, containing at least 12 different glycoforms (Appendix Figure B-6). This observation is most likely attributed to the unique glycan populations present on each separate knob and hole heavy chain in the assembled KiH bsAb, further increasing its complexity. Specifically, we not only observe mass shifts of 162 Da, corresponding to a hexose, but also shifts of 291 Da, corresponding to either a *N*-acetyl neuraminic acid (Neu5Ac) or a sialic acid. In contrast, knob and hole homodimer glycoforms differ primarily by 162 Da, with the knob homodimer native MS containing a single 291 Da shift in the mAb glycoforms detected. Glycan removal results in average mass shifts of 4362.4 ± 336.8, 2121.8 ± 210.6, and 3854.7 ±

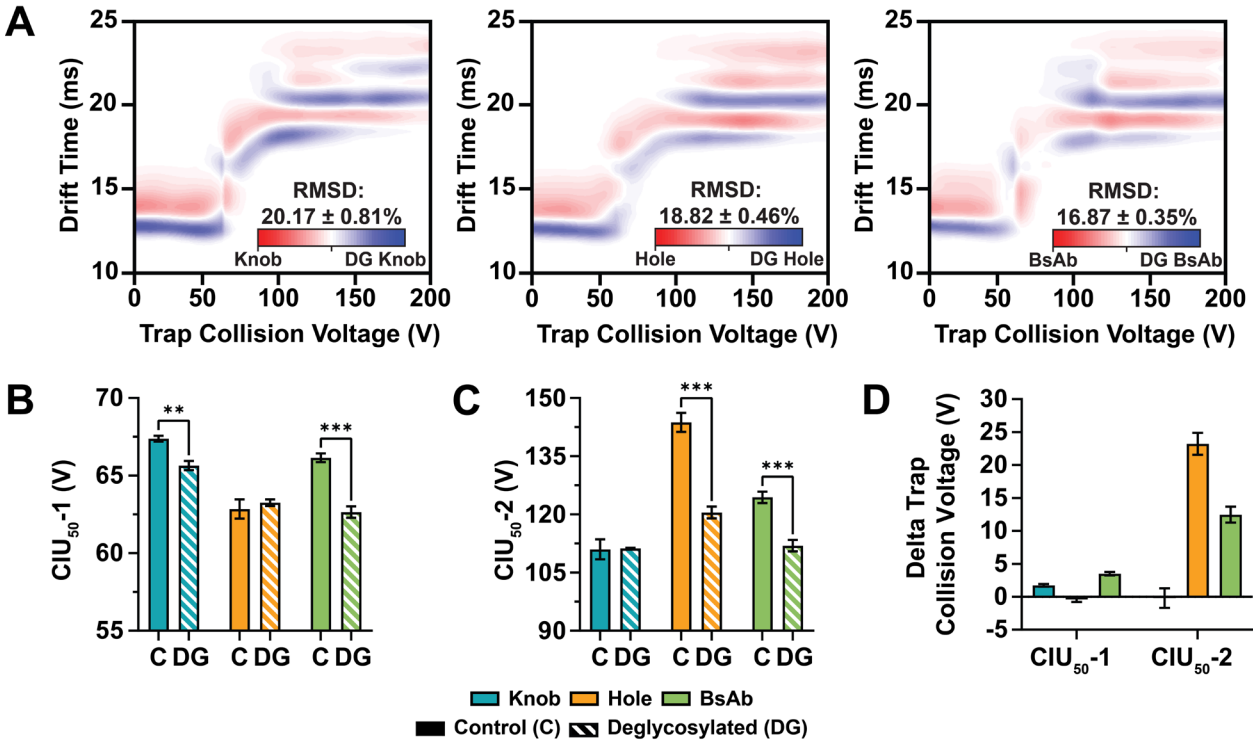

Figure 2-4: CIU of deglycosylated knob and hole homodimers and KiH bsAb heterodimer 24^+ ions (n = 3). (A) RMSD analysis comparing control and deglycosylated antibodies reveals significant differences in HOS. (B) CIU_{50}-1 and (C) CIU_{50}-2 analysis reveals significant destabilization of antibodies after deglycosylation (** $p < 0.01$, *** $p < 0.001$). (D) Plot of differences in CIU_{50} values between control and deglycosylated antibodies.

654.0 Da for knob, hole, and KiH bsAb constructs, respectively, all in line with expectations for PNGase F deglycosylation.[34] The variability observed in the homodimer mAb or KiH bsAb mass lost following PNGase F treatment is a reflection of the unique glycosylation patterns observed for each antibody studied here.

CIU experiments for both control and deglycosylated antibodies reveal the same number of features as those observed in our initial CIU data, alongside clear shifts in protein stability. RMSD analysis reveals significant differences between control and deglycosylated forms (~17 – 20%) compared to baseline RMSDs of < 4% (Figure 2-4A). Pre-CIU IM drift times for our deglycosylated homodimer mAbs and KiH bsAb are universally shorter than those produced by control (glycosylated) antibodies and thus produce CIU intermediates that are similarly shifted.

Interestingly, an RMSD analysis comparing deglycosylated knob, hole, and KiH bsAb constructs reveals that the deglycosylated bsAb most closely resembles the deglycosylated hole homodimer (Appendix Figure B-7), a result that agrees well with our initial CIU experiments on the glycosylated forms of these antibodies discussed above (Figure 2-1).

A quantitative analysis of CIU_{50} data reveals an asymmetric effect on protein stability upon the removal of glycans from each antibody (Figure 2-4B,C). CIU_{50}-1 values point to a significant decrease in gas-phase stability for deglycosylated knob homodimer (65.65 ± 0.28 V) and KiH bsAb (62.65 ± 0.37 V) when compared to controls (73.35 ± 0.36 V and 66.15 ± 0.28 for knob homodimer and KiH bsAb, respectively). Deglycosylated hole homodimer, on the other hand, shows no detectable change in CIU_{50}-1. In comparison, our CIU_{50}-2 results point to a significant decrease in stability for deglycosylated hole homodimer (120.50 ± 1.53 V) and KiH bsAb (111.94 ± 1.46 V) compared to controls (143.73 ± 2.44 V and 124.41 ± 1.49 V for hole homodimer and KiH bsAb, respectively), with no change observed in knob CIU_{50}-2. By plotting the differences in CIU_{50} recorded between our control and deglycosylated antibodies, we can delineate which CIU transition is most affected by deglycosylation (Figure 2-4D). Overall, we observe greater differences in CIU_{50}-2 when compared to CIU_{50}-1, with the latter transition shifting < 5V (maximally ~6%) across all applicable constructs and the former generating shifts of 10 – 25 V (maximally ~17%). We note that the knob homodimer exhibits a destabilized CIU_{50}-2 when compared with both bsAb and hole constructs even before deglycoyslation as discussed above. Previously, the resolved structure of another model knob-knob Fc has shown that knob-knob Fc is destabilized due to a change in the relative orientation of C_H3 domains provoked by the knob point mutation.[55] Therefore, it is possible that the T366W mutation in the

C_H3 domains of knob heavy chains is affecting the non-covalent interactions at the C_H3- C_H3 interface of the knob homodimer, permitting flexibility and leading to lower CIU_{50}-2 values.

2.7 Conclusions

Here, we demonstrate the capabilities of IM-MS in combination with CIU to establish HOS connections between a model KiH bsAb and its parent homodimer mAbs. We found CCS alone to be insufficient to resolve the subtle HOS differences between the antibodies studied here. In contrast, CIU fingerprints permitted us to resolve and differentiate each iso-cross-sectional antibody. Overall, our findings indicate that our model KiH bsAb adopts an intermediate cross-sectional and stability profile between those of its parent knob and hole homodimer mAbs, an observation driven by stability contributions of each parent halfmer to KiH bsAb stability.

Importantly, our analysis of a model KiH bsAb and its parent mAbs has enabled us to assign many details surrounding the CIU of a model KiH bsAb for the first time. By studying mAb and bsAb fragments, alongside deglycosylated constructs, our data strongly point to the first and second CIU transitions of the KiH bsAb and the parent mAbs in this work to be related to Fab and Fc domains unfolding, respectively. In particular, the CIU profiles recorded for Fab fragments in comparison to liberated chimeric Fc domains indicated lesser stabilities for the Fab domains in a manner that reflected their relative stabilities in larger constructs (e.g., halfmers and homodimers). The larger stability of the Fc, in combination with the larger influence of deglycosylation on CIU_{50}-2, supports the notion that higher-energy CIU transitions in the KiH bsAb are related to Fc CIU, while lower energy transitions are connected to Fab CIU. A greater degree of granularity can be assigned to KiH bsAb CIU than the generalities detailed above, which we argue are likely applicable to all mAb CIU collected for ions having sufficiently lower

charge states. For this work's model KiH bsAb, our results indicate that the lower energy, Fab dominated, unfolding event is likely driven by the stability of the hole Fab domain, which all of our CIU data indicates is the least stable element of the KiH bsAb construct, and subsequent higher-energy CIU transitions are related to the unfolding of C_H2 and C_H3 domains within the knob-containing portion of the Fc. However, we acknowledge that these findings offer a simple explanation of the gas-phase unfolding mechanism of a model KiH bsAb. Future work will target the thorough evaluation of bsAb and mAb CIU pathways. Comparisons of KiH bsAbs constructed using different IgG subclasses, for instance, would provide further information regarding KiH bsAb stability.

Our ability to interpret the details of bsAb CIU, coupled with our enhanced understanding of the biophysical underpinnings of a model KiH bsAb's stability, has the potential to provide critical information in support of KiH bsAb discovery and development. Future work in our group aims to further develop IM-MS and CIU workflows to rapidly probe the suitability and HOS details of KiH bsAb construction. For example, we foresee combined native MS, IM-MS and CIU, available in a high-throughput mode, to reveal variations in KiH bsAb conformational dynamics and stability provoked by changes in protein sequence, enabling us to relate HOS changes to overall KiH bsAb fitness for subsequent development efforts.

2.8 References

[1] Segal, D. M.; Weiner, G. J.; Weiner, L. M. Bispecific antibodies in cancer therapy. *Curr. Opin. Immunol.* **1999**, *11* (5), 558-562. DOI: 10.1016/s0952-7915(99)00015-1.

[2] Li, B.; et al. CD89-mediated recruitment of macrophages via a bispecific antibody enhances anti-tumor efficacy. *OncoImmunology* **2018**, *7* (1), e1380142. DOI: 10.1080/2162402x.2017.1380142.

[3] Bacac, M.; et al. A Novel Carcinoembryonic Antigen T-Cell Bispecific Antibody (CEA TCB) for the Treatment of Solid Tumors. *Clin. Cancer Res.* **2016**, *22* (13), 3286-3297. DOI: 10.1158/1078-0432.ccr-15-1696.

[4] Atwal, J. K.; et al. A Therapeutic Antibody Targeting BACE1 Inhibits Amyloid-β Production in Vivo. *Sci. Transl. Med.* **2011**, *3* (84), 84ra43-84ra43. DOI: 10.1126/scitranslmed.3002254.
[5] Yu, Y. J.; et al. Therapeutic bispecific antibodies cross the blood-brain barrier in nonhuman primates. *Sci. Transl. Med.* **2014**, *6* (261), 261ra154-261ra261. DOI: 10.1126/scitranslmed.3009835.
[6] Chakravarthy, U.; et al. Phase I Trial of Anti–Vascular Endothelial Growth Factor/Anti-angiopoietin 2 Bispecific Antibody RG7716 for Neovascular Age-Related Macular Degeneration. *Ophthalmol. Retina* **2017**, *1* (6), 474-485. DOI: 10.1016/j.oret.2017.03.003.
[7] Regula, J. T.; et al. Targeting key angiogenic pathways with a bispecific CrossMAb optimized for neovascular eye diseases. *EMBO Mol. Med.* **2016**, *8* (11), 1265-1288. DOI: 10.15252/emmm.201505889.
[8] Ma, J.; et al. Bispecific Antibodies: From Research to Clinical Application. *Front. Immunol.* **2021**, *12*. DOI: 10.3389/fimmu.2021.626616.
[9] Labrijn, A. F.; Janmaat, M. L.; Reichert, J. M.; Parren, P. W. H. I. Bispecific antibodies: a mechanistic review of the pipeline. *Nat. Rev. Drug. Discov.* **2019**, *18* (8), 585-608. DOI: 10.1038/s41573-019-0028-1.
[10] Kontermann, R. E.; Brinkmann, U. Bispecific antibodies. *Drug Discov. Today* **2015**, *20* (7), 838-847. DOI: 10.1016/j.drudis.2015.02.008.
[11] Klein, C.; et al. Progress in overcoming the chain association issue in bispecific heterodimeric IgG antibodies. *mAbs* **2012**, *4* (6), 653-663. DOI: 10.4161/mabs.21379.
[12] Ridgway, J. B. B.; Presta, L. G.; Carter, P. 'Knobs-into-holes' engineering of antibody C_H3 domains for heavy chain heterodimerization. *Protein Eng. Des. Sel.* **1996**, *9* (7), 617-621. DOI: 10.1093/protein/9.7.617.
[13] Zhou, Q.; Qiu, H. The Mechanistic Impact of N-Glycosylation on Stability, Pharmacokinetics, and Immunogenicity of Therapeutic Proteins. *J. Pharm. Sci.* **2019**, *108* (4), 1366-1377. DOI: 10.1016/j.xphs.2018.11.029.
[14] Dingman, R.; Balu-Iyer, S. V. Immunogenicity of Protein Pharmaceuticals. *J. Pharm. Sci.* **2019**, *108* (5), 1637-1654. DOI: 10.1016/j.xphs.2018.12.014.
[15] Hermeling, S.; Crommelin, D. J. A.; Schellekens, H.; Jiskoot, W. Structure-Immunogenicity Relationships of Therapeutic Proteins. *Pharm. Res.* **2004**, *21* (6), 897-903. DOI: 10.1023/b:pham.0000029275.41323.a6.
[16] Roberts, C. J. Therapeutic protein aggregation: mechanisms, design, and control. *Trends Biotechnol.* **2014**, *32* (7), 372-380. DOI: 10.1016/j.tibtech.2014.05.005.
[17] Gabrielson, J. P.; Weiss, W. F. Technical Decision-Making with Higher Order Structure Data: Starting a New Dialogue. *J. Pharm. Sci.* **2015**, *104* (4), 1240-1245. DOI: 10.1002/jps.24393.
[18] Berkowitz, S. A.; Engen, J. R.; Mazzeo, J. R.; Jones, G. B. Analytical tools for characterizing biopharmaceuticals and the implications for biosimilars. *Nat. Rev. Drug. Discov.* **2012**, *11* (7), 527-540. DOI: 10.1038/nrd3746.
[19] Joshi, V.; Shivach, T.; Yadav, N.; Rathore, A. S. Circular Dichroism Spectroscopy as a Tool for Monitoring Aggregation in Monoclonal Antibody Therapeutics. *Anal. Chem.* **2014**, *86* (23), 11606-11613. DOI: 10.1021/ac503140j.

[20] Moreno, M. R.; et al. Study of stability and biophysical characterization of ranibizumab and aflibercept. *Eur. J. Pharm. Biopharm.* **2016**, *108*, 156-167. DOI: 10.1016/j.ejpb.2016.09.003.
[21] Goyon, A.; et al. Characterization of 30 therapeutic antibodies and related products by size exclusion chromatography: Feasibility assessment for future mass spectrometry hyphenation. *J. Chromatogr. B* **2017**, *1065-1066*, 35-43. DOI: 10.1016/j.jchromb.2017.09.027.
[22] Brinson, R. G.; et al. Enabling adoption of 2D-NMR for the higher order structure assessment of monoclonal antibody therapeutics. *mAbs* **2019**, *11* (1), 94-105. DOI: 10.1080/19420862.2018.1544454.
[23] Zheng, H.; Hou, J.; Zimmerman, M. D.; Wlodawer, A.; Minor, W. The future of crystallography in drug discovery. *Expert Opin. Drug Discov.* **2014**, *9* (2), 125-137. DOI: 10.1517/17460441.2014.872623.
[24] Hao, Y.; Yu, X.; Bai, Y.; McBride, H. J.; Huang, X. Cryo-EM Structure of HER2-trastuzumab-pertuzumab complex. *PLoS One* **2019**, *14* (5), e0216095. DOI: 10.1371/journal.pone.0216095.
[25] Chen, G.; Tao, L.; Li, Z. Recent advancements in mass spectrometry for higher order structure characterization of protein therapeutics. *Drug. Discov. Today* **2022**, *27* (1), 196-206. DOI: 10.1016/j.drudis.2021.09.010.
[26] Strop, P.; et al. Generating Bispecific Human IgG1 and IgG2 Antibodies from Any Antibody Pair. *J. Mol. Biol.* **2012**, *420* (3), 204-219. DOI: 10.1016/j.jmb.2012.04.020.
[27] Lewis, S. M.; et al. Generation of bispecific IgG antibodies by structure-based design of an orthogonal Fab interface. *Nat. Biotechnol.* **2014**, *32* (2), 191-198. DOI: 10.1038/nbt.2797.
[28] Ruotolo, B. T.; Benesch, J. L. P.; Sandercock, A. M.; Hyung, S.-J.; Robinson, C. V. Ion mobility–mass spectrometry analysis of large protein complexes. *Nat. Protoc.* **2008**, *3* (7), 1139-1152. DOI: 10.1038/nprot.2008.78.
[29] Debaene, F.; et al. Time Resolved Native Ion-Mobility Mass Spectrometry to Monitor Dynamics of IgG4 Fab Arm Exchange and "Bispecific" Monoclonal Antibody Formation. *Anal. Chem.* **2013**, *85* (20), 9785-9792. DOI: 10.1021/ac402237v.
[30] Bagal, D.; Valliere-Doughlass, J. F.; Balland, A.; Schnier, P. D. Resolving Disulfide Structural Isoforms of IgG2 Monoclonal Antibodies by Ion Mobility MassSpectrometry. *Anal. Chem.* **2010**, *82*, 6751-6755. DOI: 10.1021/ac1013139.
[31] Debaene, F.; et al. Innovative Native MS Methodologies for Antibody Drug Conjugate Characterization: High Resolution Native MS and IM-MS for Average DAR and DAR Distribution Assessment. *Anal. Chem.* **2014**, *86* (21), 10674-10683. DOI: 10.1021/ac502593n.
[32] Dixit, S. M.; Polasky, D. A.; Ruotolo, B. T. Collision induced unfolding of isolated proteins in the gas phase: past, present, and future. *Curr. Opin. Chem. Biol.* **2018**, *42*, 93-100. DOI: 10.1016/j.cbpa.2017.11.010.
[33] Tian, Y.; Han, L.; Buckner, A. C.; Ruotolo, B. T. Collision Induced Unfolding of Intact Antibodies: Rapid Characterization of Disulfide Bonding Patterns, Glycosylation, and Structures. *Anal. Chem.* **2015**, *87* (22), 11509-11515. DOI: 10.1021/acs.analchem.5b03291.

[34] Tian, Y.; Ruotolo, B. T. Collision induced unfolding detects subtle differences in intact antibody glycoforms and associated fragments. *Int. J. Mass Spectrom.* **2018**, *425*, 1-9. DOI: 10.1016/j.ijms.2017.12.005.
[35] Upton, R.; et al. Hybrid mass spectrometry methods reveal lot-to-lot differences and delineate the effects of glycosylation on the tertiary structure of Herceptin®. *Chem. Sci.* **2019**, *10* (9), 2811-2820. DOI: 10.1039/c8sc05029e.
[36] Watanabe, Y.; et al. Signature of Antibody Domain Exchange by Native Mass Spectrometry and Collision-Induced Unfolding. *Anal. Chem.* **2018**, *90* (12), 7325-7331. DOI: 10.1021/acs.analchem.8b00573.
[37] Deslignière, E.; et al. State-of-the-Art Native Mass Spectrometry and Ion Mobility Methods to Monitor Homogeneous Site-Specific Antibody-Drug Conjugates Synthesis. *Pharmaceuticals* **2021**, *14* (6), 498. DOI: 10.3390/ph14060498.
[38] Tian, Y.; Lippens, J. L.; Netirojjanakul, C.; Campuzano, I. D. G.; Ruotolo, B. T. Quantitative collision-induced unfolding differentiates model antibody–drug conjugates. *Protein Sci.* **2019**, *28* (3), 598-608. DOI: 10.1002/pro.3560.
[39] Hernandez-Alba, O.; Wagner-Rousset, E.; Beck, A.; Cianférani, S. Native Mass Spectrometry, Ion Mobility, and Collision-Induced Unfolding for Conformational Characterization of IgG4 Monoclonal Antibodies. *Anal. Chem.* **2018**, *90* (15), 8865-8872. DOI: 10.1021/acs.analchem.8b00912.
[40] Marty, M. T.; et al. Bayesian Deconvolution of Mass and Ion Mobility Spectra: From Binary Interactions to Polydisperse Ensembles. *Anal. Chem.* **2015**, *87* (8), 4370-4376. DOI: 10.1021/acs.analchem.5b00140.
[41] Haynes, S. E.; et al. Variable-Velocity Traveling-Wave Ion Mobility Separation Enhancing Peak Capacity for Data-Independent Acquisition Proteomics. *Anal. Chem.* **2017**, *89* (11), 5669-5672. DOI: 10.1021/acs.analchem.7b00112.
[42] Richardson, K.; Langridge, D.; Dixit, S. M.; Ruotolo, B. T. An Improved Calibration Approach for Traveling Wave Ion Mobility Spectrometry: Robust, High-Precision Collision Cross Sections. *Anal. Chem.* **2021**, *93* (7), 3542-3550. DOI: 10.1021/acs.analchem.0c04948.
[43] Polasky, D. A.; Dixit, S. M.; Fantin, S. M.; Ruotolo, B. T. CIUSuite 2: Next-Generation Software for the Analysis of Gas-Phase Protein Unfolding Data. *Anal. Chem.* **2019**, *91* (4), 3147-3155. DOI: 10.1021/acs.analchem.8b05762.
[44] Kafader, J. O.; et al. Native vs Denatured: An in Depth Investigation of Charge State and Isotope Distributions. *J. Am. Soc. Mass Spectrom.* **2020**, *31* (3), 574-581. DOI: 10.1021/jasms.9b00040.
[45] Chowdhury, S. K.; Katta, V.; Chait, B. T. Probing conformational changes in proteins by mass spectrometry. *J. Am. Chem. Soc.* **1990**, *112* (24), 9012-9013. DOI: 10.1021/ja00180a074.
[46] Schachner, L.; et al. Characterization of Chain Pairing Variants of Bispecific IgG Expressed in a Single Host Cell by High-Resolution Native and Denaturing Mass Spectrometry. *Anal. Chem.* **2016**, *88* (24), 12122-12127. DOI: 10.1021/acs.analchem.6b02866.
[47] Eschweiler, J. D.; Martini, R. M.; Ruotolo, B. T. Chemical Probes and Engineered Constructs Reveal a Detailed Unfolding Mechanism for a Solvent-Free Multidomain Protein. *J. Am. Chem. Soc.* **2017**, *139* (1), 534-540. DOI: 10.1021/jacs.6b11678.

[48] Zhong, Y.; Han, L.; Ruotolo, B. T. Collisional and Coulombic Unfolding of Gas-Phase Proteins: High Correlation to Their Domain Structures in Solution. *Angew. Chem.* **2014**, *126* (35), 9363-9366. DOI: 10.1002/ange.201403784.

[49] Polasky, D. A.; Dixit, S. M.; Vallejo, D. D.; Kulju, K. D.; Ruotolo, B. T. An Algorithm for Building Multi-State Classifiers Based on Collision-Induced Unfolding Data. *Anal. Chem.* **2019**, *91* (16), 10407-10412. DOI: 10.1021/acs.analchem.9b02650 From NLM Medline.

[50] Botzanowski, T.; et al. Middle Level IM–MS and CIU Experiments for Improved Therapeutic Immunoglobulin Subclass Fingerprinting. *Anal. Chem.* **2020**, *92* (13), 8827-8835. DOI: 10.1021/acs.analchem.0c00293.

[51] Wozniak-Knopp, G.; Stadlmann, J.; Rüker, F. Stabilisation of the Fc Fragment of Human IgG1 by Engineered Intradomain Disulfide Bonds. *PLoS One* **2012**, *7* (1), e30083. DOI: 10.1371/journal.pone.0030083.

[52] Huber, R.; Deisenhofer, J.; Colman, P. M.; Matsushima, M.; Palm, W. Crystallographic structure studies of an IgG molecule and an Fc fragment. *Nature* **1976**, *264* (5585), 415-420. DOI: 10.1038/264415a0.

[53] Zhang, H.-M.; et al. Structural and Functional Characterization of a Hole–Hole Homodimer Variant in a "Knob-Into-Hole" Bispecific Antibody. *Anal. Chem.* **2017**, *89* (24), 13494-13501. DOI: 10.1021/acs.analchem.7b03830.

[54] Zheng, K.; Bantog, C.; Bayer, R. The impact of glycosylation on monoclonal antibody conformation and stability. *mAbs* **2011**, *3* (6), 568-576. DOI: 10.4161/mabs.3.6.17922.

[55] Kuglstatter, A.; et al. Structural differences between glycosylated, disulfide-linked heterodimeric Knob-into-Hole Fc fragment and its homodimeric Knob–Knob and Hole–Hole side products. *Protein Eng. Des. Sel.* **2017**, *30* (9), 649–656. DOI: 10.1093/protein/gzx041.

Chapter 3: Ion Mobility-Mass Spectrometry and Collision-Induced Unfolding Unveil Structure-Function Relationships of Human IgG2 Cysteine to Serine Exchange Variants

3.1 Original Publication

This chapter is being prepared for publication as: Rosendo C. Villafuerte-Vega, Isabel Elliott, Hayden Fisher, Michael R. Armbruster, Claude H.T. Chan, Tatyana Inzhelevskaya, Ian Mockridge, Christine A. Penfold, Patrick Duriez, Mark S. Cragg, and Brandon T. Ruotolo. "Ion Mobility-Mass Spectrometry and Collision-Induced Unfolding Unveil Structure-Function Relationships of Human IgG Cysteine to Serine Exchange Variants." 2024.

3.2 Author Contributions

R.C.V., I.E., H.F., M.S.C., and B.T.R. conceptualized and designed the experiments described. C.H.T.C., T.I., I.M., C.P., and P.D. generated IgG material. I.E. and H.F. were involved in the design and execution of NFκB assays and SAXS experiments, as well as the analysis and plotting of experimental data resulting in Appendix Figure C-6. R.C.V. collected, analyzed, and plotted all IM-MS and CIU data, as well as drafted the manuscript. M.R.A wrote the R script used to perform similarity scores. I.E., H.F., and M.S.C. provided guidance in interpreting all experimental results. M.S.C and B.T.R. supervised the work, as well as provided project guidance and funding.

3.3 Abstract

Antagonistic monoclonal antibodies (mAbs) have been converted into powerful agonists by isotype switching from human (*h*)IgG1 or *h*IgG4 into *h*IgG2. Such epitope-independent modulation in agonistic activity is leveraged by the ability of *h*IgG2 to undergo disulfide shuffling within its hinge region, creating various disulfide patterns that directly impact mAb conformation and flexibility. Structural analyses of these disulfide-switched constructs, however, have been limited due to the intrinsic dynamism of full-length *h*IgG. Herein, we describe a collision-induced unfolding (CIU)-based assay that rapidly probes the structures and stabilities of a series of *h*IgG2 variants with different cysteine to serine (C/S) exchanges in their hinge regions. Changes in collision cross section (Ω) and gas-phase stability are observed in a manner that correlates with levels of receptor agonism across full-length *h*IgG and $F(ab')_2$ fragments. These differences are attributed to the patterns of disulfide crossovers present in agonistic mAbs that dictate their conformationally dynamic ensembles. Our CIU results assist us in classifying C/S variants into categories having predicted levels of receptor agonism, and they further highlight the significance of hinge engineering in tuning structure-function relationships of antibodies.

3.4 Introduction

Monoclonal antibodies (mAbs) have emerged as powerful therapeutic modalities that offer targeted remedies for a myriad of diseases. They have revolutionized the therapeutic landscape as applied to cancer therapy, autoimmune disorders, and infectious diseases due to their bifunctional ability to specifically bind various targets and effectively harness potent immune effector functions.[1-3] These unique properties have led to the approval of approximately 120 antibody therapies by the U.S. Food and Drug Administration, while nearly 140 are

currently in late-stage clinical development.[4, 5] Target recognition is facilitated by two identical antigen-binding fragment (Fab) domains linked via a flexible hinge to a fragment crystallizable (Fc) domain that mediates various cellular effector functions such as the activation of the classical complement pathway.[6, 7] Antibody Fab domains can also elicit powerful effector mechanisms by mimicking endogenous ligands of immune cell surface receptors. This unique property has guided the design and development of agonist antibodies targeting immune checkpoint co-stimulatory receptors that lead to the activation of downstream signaling pathways.[8] Prominent costimulatory targets of these immunomodulatory mAbs include those of the tumor necrosis factor receptor (TNFR) superfamily such as CD40, 4-1BB, and OX40, which have offered a molecular adjuvant for antitumor immunity.[8-10]

Previous studies have demonstrated that immunomodulatory antibodies stimulate immune receptors in an isotype- or epitope-dependent manner.[11-13] For example, anti-human(*h*) CD40 mAbs that target the membrane-distal cysteine-rich domain 1 (CRD1) are highly agonistic, while those that bind CRD2-4 act as potent antagonists by blocking interactions with CD40L.[11] Specifically, agonistic anti-CD40 mAbs of the human immunoglobulin G (*h*IgG) isotype 1 (*h*IgG1) typically require the inhibitory FcγRIIB to promote CD40 crosslinking and impart an immune response. Alternatively, switching the mAb to an *h*IgG2 isotype has been shown to confer FcγR-independent agonism to various anti-CD40 mAbs, such as ChiLob7/4, SGN40, and 341G2, by promoting CD40 receptor clustering within the membrane that leads to enhanced downstream intracellular signaling.[13, 14] The exceptional ability of *h*IgG2 to optimize receptor agonism is driven, in part, by its ability to undergo disulfide switching within its C_H1 and hinge regions, resulting in two major disulfide structural isoforms: a flexible A-form (*h*IgG2A) and a rigid B-form (*h*IgG2B).[15, 16] These structural isoforms have demonstrated highly

opposing immunostimulatory activity in murine models, where *h*IgGA lacks immunostimulatory activity and *h*IgGB exhibits strong agonism.[11, 14] Building upon these observations, agonistic *h*IgG2B cysteine to serine (C/S) variants of ChiLob7/4 were shown to be less flexible and adopt the fewest conformations in solution due to a disulfide crossover between opposing heavy and light chains.[17] Therefore, the mechanistic underpinnings of *h*IgG2B agonism can be partly explained by its ability to confine receptor mobility, leading to enhanced receptor clustering and immune activation.[10]

However, establishing a quantitative molecular explanation for the structural effects of C/S hinge engineering on *h*IgG2 agonism has been limited to a single antibody series. Moreover, only $F(ab')_2$ fragments have been structurally probed due to the inherent dynamism of full-length *h*IgGs, a fact that complicates conventional X-ray crystallography measurements as described previously.[17, 18] These limitations necessitate the development and validation of new methodologies capable of rapidly probing the structure-function relationships of full-length, hinge-engineered agonist mAbs. Recently, native ion mobility-mass spectrometry (IM-MS) has become a useful tool for investigating the higher order structures (HOSs) of flexible proteins that possess a broad range of conformational states.[19] IM separates gas-phase protein ions by their charge and rotationally averaged collision cross section (Ω), the latter which is calculated based on the molecular architecture and size of the proteins being investigated.[20, 21] Recent efforts in IM-MS have been successful in distinguishing IgG2 disulfide isoforms, but standard IM separation is challenging to use alone to distinguish these closely-related mAb conformations.[22, 23] Alternatively, collision-induced unfolding (CIU) has enabled IM-MS to provide more refined structural and stability information based on the collisional heating of native-like proteins in the gas-phase, where the unfolded intermediates generated often reflect the intrinsic architectures of

the proteins being probed.[24] Although CIU has been shown to be sensitive to the disulfide-bond structures of IgG isotypes,[25-28] a clear understanding of how hinge disulfides impact the gas-phase stabilities of IgGs is also lacking, especially in the context of disulfide isoforms of *h*IgG2 and their relation to agonistic function.

Herein, we describe a methodology that rapidly probes the impact of C/S hinge engineering on the structures of agonist mAbs in the gas-phase. Specifically, we combine both IM-MS and CIU measurements to demonstrate that hinge disulfide modifications in ChiLob7/4 C/S variants influence the gas-phase structural collapse and stabilities of full-length *h*IgG and $F(ab')_2$ scaffolds in a manner that strongly correlates with hinge flexibility and receptor agonism. We then extend these structural studies to C/S variants of the anti-4-1BB (CD137) mAb, SAP1.3, where we observed comparable shifts in gas-phase structural compaction and stability. Finally, we applied our CIU approach in probing the gas-phase structures and stabilities of two novel C/S variants of ChiLob7/4 and SAP1.3 that possess unconventional hinge disulfide patterns. Taken together, our findings represent the first example that highlights the robustness of IM-MS and CIU-based assays in establishing structure-function relationships of potent agonist mAbs, thus enabling future high-throughput hinge disulfide engineering efforts.

3.5 Experimental Section

Antibody Production and Purification. Kabat numbering is utilized throughout the report. Anti-human(*h*) *h*CD40 ChiLob7/4 *h*IgG2 cysteine to serine (C/S) exchange variants C232S + C233S, C233S κC214S, C239S, C232S κC214S, C232S + T222C κE123C + C214S, and C232S + K228C κC214S were generated by site directed mutagenesis in Chinese hamster ovary cells. They were subsequently purified by protein A affinity chromatography using a HiTrap MabSelect SuRe protein A column (Cytiva) and confirmed to be endotoxin low (<10

EU/mg) using an Endosafe PTS device (Charles River Laboratories) and aggregate-free (<1%) via high-performance liquid chromatography (HPLC) as described previously[14, 17] Anti-*h*CD137 SAP1.3 C/S exchange variants C232S + C233S, C232S, C233S, C233S κC214S, C239S, C232S κC214S, C232S + T222C κE123C + C214S, and C232S + K228C κC214S were produced in a similar manner. To generate $F(ab')_2$ fragments, each antibody was digested with IdeS (FabRICATOR, Genovis) at a 1 unit IdeS per 1 μg IgG ratio for 1 hour in TRIS NaCl buffer at 37°C. Full-length IgG and $F(ab')_2$ fragments were then desalted into 500 mM ammonium acetate (pH ~7.0) followed by another round of desalting into 200 mM ammonium acetate (pH ~7.0) using Micro Bio-Spin P-6 columns (Bio-Rad). Final concentrations were then measured by UV absorbance using a NanoDrop 2000c spectrophotometer (Thermo Fisher Scientific). Prior to MS analysis, samples were further diluted with 200 mM ammonium acetate to a final concentration of 3 to 5 μM.

NFκB Assay and Small-angle X-ray scattering (SAXS). The NFκB assay was performed as previously described using the Jurkat NF-κB GFP reporter cell line (System Biosciences, USA).[13] SAXS experiments were performed as previously described.[17]

Native Ion Mobility-Mass Spectrometry (IM-MS). IM-MS experiments were performed on a quadrupole-ion mobility-time-of-flight mass spectrometer (Q-IM-ToF-MS) (Synapt G2 HDMS, Waters). Samples (3 μL) were transferred to gold-coated borosilicate capillaries (5-10 μm inner diameter, Harvard Apparatus) prepared in-house with a Sutter P-97 Micropipette Puller (Sutter Instrument) and Quorum SC7620 Mini Sputter Coater (Quorum Technologies), and ions were generated via static nano-electrospray ionization (nESI) using a NanoLockSpray source operated in positive mode. Settings throughout the instrument were adjusted to improve the desolvation and transmission of native-like protein ions without

significant activation prior to IM separation: capillary voltage, 1.1 to 1.3 kV; source temperature, 25°C; sample cone, 25 to 50 V; extraction cone, 0 V; trap collision voltage (CV), 4 to 10 V; trap DC bias, 40 to 50 V; helium cell DC: 45 V; and IMS bias, 5 V. The backing pressure was set between 7.3 to 7.9 mbar for improved ion transmission for all samples. The trap traveling-wave (TW) ion guide was pressurized to 5.2 x 10^{-2} mbar of argon gas. The helium cell flow rate was operated at 200 mL/min and pressurized to 1.4 x 10^{-3} mbar. The TWIM cell (a length of 0.254 m) was operated at 90 mL/min of nitrogen gas and pressurized to ~3.4 mbar. TWIM separation was achieved with a TW height and velocity of 40 V and 600 V, respectively. The ToF-MS was operated in the 1,000 to 12,000 *m/z* range in sensitivity mode at a pressure of 2.4 x 10^{-6} mbar. Mass calibration of the instrument from 100 to 10,000 *m/z* was performed using a solution of cesium iodide (100 mg/mL in 30% isopropanol). D, L polyalanine (PolyA), bovine serum albumin (BSA), and alcohol dehydrogenase (ADH) were prepared and used as collision cross section ($^{TW}\Omega_{N2}$) calibrants to convert IgG and F(ab')$_2$ drift times into $^{TW}\Omega_{N2}$ values as described previously.[29] All data was collected over 200 drift bins with a scan time of 0.5 s for 1 min. Three technical IM-MS measurements were acquired for each sample. IM-MS spectra shown in this work were visualized with MassLynx v4.2 and DriftScope v3.0 software (Waters) and assembled into figures using Adobe Illustrator.

Collision-Induced Unfolding (CIU). CIU experiments were performed using static spray nESI. Ions corresponding to a single charge state were selected using the high *m/z* quadrupole then subjected to collisions with argon gas in the trap TW ion guide prior to TWIM separation. Here, the trap CV was ramped from either 5 to 200 V in 5 V increments for full-length IgG or 4 to 140 V in 4 V increments for F(ab')$_2$ fragments to produce CIU data. The dwell time for each CV step was 12 s, and the scan time was 0.5 s. CIU method files and sample lists

were automatically generated using an in-house python script (MethodEditor). Up to 20 functions (CV steps) were combined into a single .raw file, and three technical CIU replicates were acquired for each sample.

IM-MS and CIU Data Processing and Analysis. Deconvolution of mass spectra was achieved using UniDec software.[30] IM and CIU .raw files were processed using a modified beta version of CIUSuite 2 (v2.3),[31] which encodes both TWIMExtract (v1.6)[32] and IMSCal (v1.0)[29] for semi-automated drift time extractions and $^{TW}\Omega_{N2}$ calibrations, respectively. Specifically, drift time distributions were extracted over an *m/z* range that covers a single protein charge state, and $^{TW}\Omega_{N2}$ values were determined using a calibration function that incorporates the operating conditions (TW height and velocity; TWIM cell length, pressure, and temperature) of the Synapt G2 instrument. Importantly, no unfolded protein calibrants were utilized to perform $^{TW}\Omega_{N2}$ calibrations.

Distributions of $^{TW}\Omega_{N2}$-calibrated IM data for individual charge states were fitted with a gaussian function to calculate centroid $^{TW}\Omega_{N2}$ and full width at half maximum (FWHM) values using Fityk curve fitting software.[33] Since IMSCal produces calibrated $^{TW}\Omega_{N2}$ values with a level of uncertainty, we estimated the total centroid $^{TW}\Omega_{N2}$ error (in nm^2) associated with three technical replicate measurements using the following equation:

$$error = \sqrt{\sigma^2 + \Omega_{N2}\_error^2 + cal\_rmse^2} \qquad \text{(Equation 3-1)}$$

where σ is the standard deviation of technical replicate values, $\Omega_{N2}\_error^2$ is the uncertainty of calibrated IgG or F(ab')$_2$ $^{TW}\Omega_{N2}$ values, and cal_rmse^2 is the $^{TW}\Omega_{N2}$ calibration root-mean-squared error (RMSE). Generally, we observed a % $^{TW}\Omega_{N2}$ calibration RMSE of less than 0.7%, and % uncertainties in IgG and F(ab')$_2$ $^{TW}\Omega_{N2}$ values were approximately 0.6 and 0.4%, respectively.

$^{TW}\Omega_{N2}$ calibrated CIU files were further processed using CIUSuite 2 (v2.3). Data was 2D smoothed using a Savitzky-Golay filter with a window size of 5 and 2 smooth iterations. CIU fingerprints were cropped in both $^{TW}\Omega_{N2}$ and CV axes for better visualization. Standard feature detection was performed using minimum feature length of 3 steps, an allowed width of 2.5 to 2.8 nm^2 in $^{TW}\Omega_{N2}$ axis units, and a maximum CV gap length of 2. CIU_{50} values were then calculated using max centroiding mode with a transition padding of 15 V and a maximum CV gap length of 2. Root-mean-square deviation (RMSD) analysis was performed using the compare function within CIUSuite 2. All CIU fingerprints shown are the average of three technical CIU replicates with replicate RMSD values of less than 8%. The classification algorithm within CIUSuite 2 was used to assemble and classify training and test (unknown) data sets, respectively.[31, 34] Classifiers were built in *All_Data* mode using three replicates for each class. Cross-validation was performed using a score tolerance of 0.02, and the cross-validation accuracy metric was used to choose the optimal classifier.

Similarity scores, defined here as one minus the square root of the Jensen-Shannon divergence,[35] were calculated as described previously.[27] Briefly, scores were calculated at every voltage step between CIU replicates using the package *philentropy* (v. 0.8.0) in R (v. 4.3.1).[36] The $^{TW}\Omega_{N2}$ distribution at each CIU voltage was interpolated to 1000 points across a common $^{TW}\Omega_{N2}$ axis and normalized to a sum of one prior to each similarity score calculation. Graphing of all data shown was performed using GraphPad Prism (v.10.2.0). All plots were then compiled into figures using Adobe Illustrator.

3.6 Results and Discussion

Disulfide hinge variation influences the gas-phase collapse of agonist mAbs. Prior reports have detailed the structural collapse of antibodies upon transitioning into the gas-phase

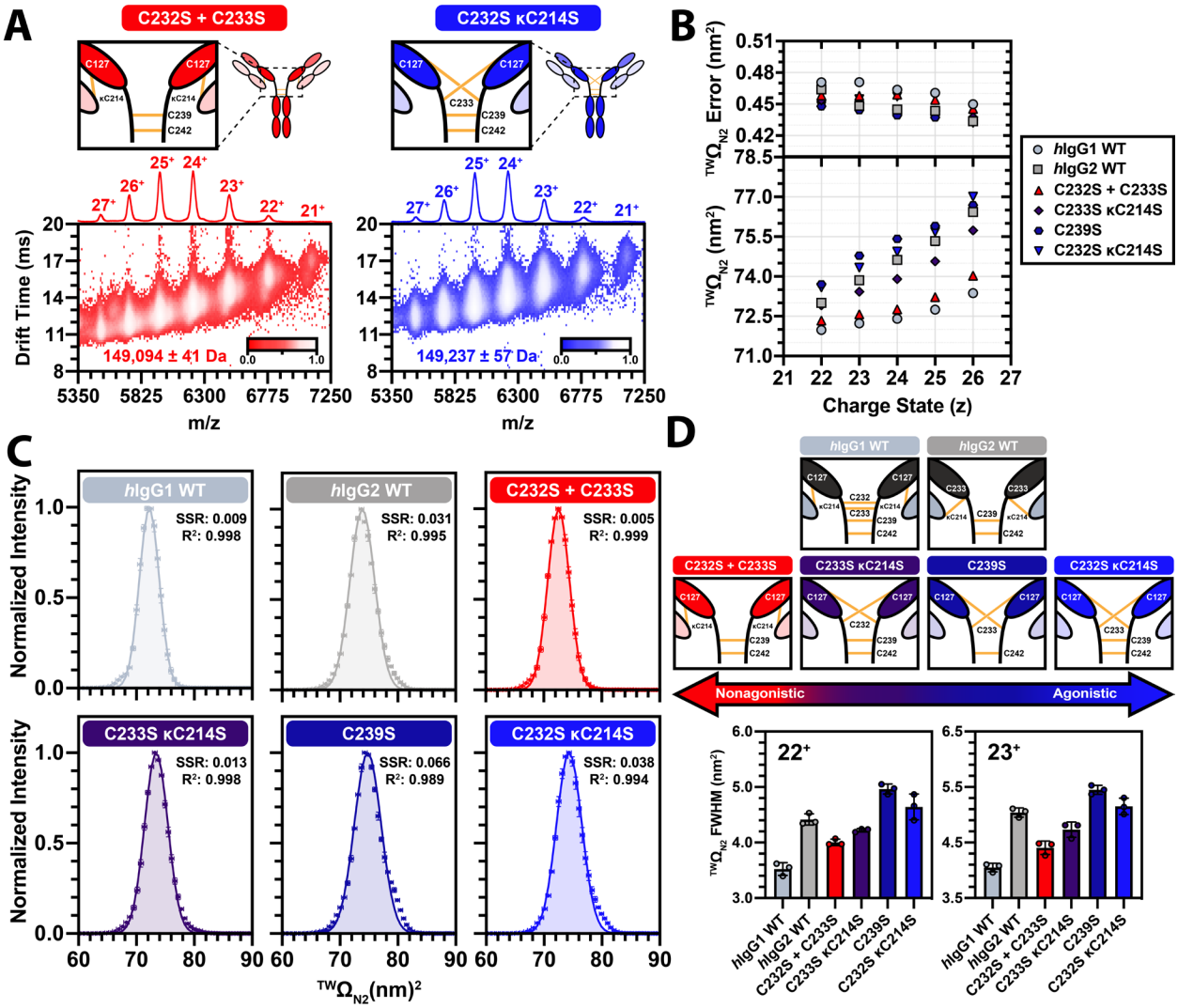

Figure 3-1: Native IM-MS measurements of ChiLob7/4 variants. (A) Representative IM-MS spectra of C232S + C233S and C232S κC214S variants reveal native-like charge state distributions. Masses ± mass error of the charge states sampled for mass deconvolution are shown. (B) $^{TW}\Omega_{N2}$ values as a function of charge state. $^{TW}\Omega_{N2}$ errors shown were obtained by propagating uncertainties associated with $n = 3$ technical replicates, calibrated $^{TW}\Omega_{N2}$ values of *h*IgGs, and experimental $^{TW}\Omega_{N2}$ values of the calibrants used (see Methods). (C) Gaussian peak fittings for the $^{TW}\Omega_{N2}$ distributions of charge state 23^+. Vertical error bars represent the s.d. in intensities technical replicates, while horizontal error bars represent the uncertainties in calibrated $^{TW}\Omega_{N2}$ values. (D) Top: structures of ChiLob7/4 variants highlighting an increase in agonistic activity from red to blue. *h*IgG1 and *h*IgG2 WT are nonagonistic and agonistic, respectively. Bottom: peak width analysis of charge states 22^+ and 23^+. Peak width data are plotted as mean ± s.d. of peak fittings of technical replicates.

from solution, as evidenced by a ~40% discrepancy between experimental Ω values and those calculated from crystal structures.[37-39] This collapse is, in part, is facilitated by the capacity of the IgG hinge to provide the necessary steric freedom for Fab and Fc domains to seamlessly form

into more compact structures during the nano-electrospray ionization (nESI) process.[37] Building upon these previous findings, we hypothesized that different disulfide bonding configurations within the IgG2 hinge region would impart different levels of gas-phase compaction, thus enabling the ability of IM-MS and CIU to differentiate IgG2A and IgG2B forms. To explore this, we performed native IM-MS experiments across a series of six anti-*h*CD40 ChiLob7/4 variants that have been described previously.[17] Here, cysteines in the hinge region suggested to participate in disulfide shuffling were exchanged with serine, generating "locked" *h*IgG2A (C232S + C233S) and *h*IgG2B (C233S κC214S, C239S, and C232S κC214S) states with varied of levels of flexibility and receptor agonism. Both wild type (WT) *h*IgG1 and *h*IgG2 ChiLob7/4 isotypes were also generated, which served as both negative and positive controls in developing our CIU-based agonistic activity assay, respectively.

By employing soft nESI conditions to avoid artifactual activation of each *h*IgG,[20, 40] we successfully captured compact, native-like ions as evidenced by narrow charge state distributions (Figure 3-1A, Appendix Figure C-1A). We assessed the gas-phase compaction of each variant by converting the arrival time distributions observed in our IM data to $^{TW}\Omega_{N2}$ values across all charge states (22^+ to 26^+) observed. Qualitatively, variants that feature a disulfide crossover exhibit broader $^{TW}\Omega_{N2}$ distributions, highlighting their wider range of structures (Appendix Figure C-1B). Comparing centroid $^{TW}\Omega_{N2}$ values further revealed variations in mAb gas-phase compaction across all *h*IgGs sampled (Figure 3-1B). For example, WT *h*IgG1, which has previously been shown to have minimal agonistic activity,[11, 14] adopted lower $^{TW}\Omega_{N2}$ values than the more rigid, agonistic WT *h*IgG2. The C232S + C233S $^{TW}\Omega_{N2}$ values we recorded were also lower, akin to those of the *h*IgG1 negative control, while the $^{TW}\Omega_{N2}$ values obtained for variants featuring a disulfide crossover (C233S κC214S, C239S, and C232S κC214S) approached those

of the agonistic *h*IgG2 control. To better quantitate the structural collapse of these variants, we used Gaussian fitting to precisely evaluate the widths of their $^{TW}\Omega_{N2}$ distributions (Figure 3-1C). For the data shown, we inspected widths recorded for mAb charge states 22^+ and 23^+, since the $^{TW}\Omega_{N2}$ distributions for these charge states showed stronger evidence of normal, symmetric Gaussian distributions and are also expected to better reflect native protein configurations.[41-43] Here, the agonistic crossover variants C233S κC214S, C239S, and C232S κC214S, as well as the *h*IgG2 WT, had larger peak widths compared to those of the nonagonistic C232S + C233S variant and *h*IgG1 WT (Figure 3-1D). These differences in peak widths showcase that more flexible mAbs adopt a narrower, more compact distribution of conformations in the gas-phase, reflective of their more pliable hinge regions. Furthermore, the trends that we observe in centroid $^{TW}\Omega_{N2}$ and peak width values correlate with an increase in agonistic activity in the order of C232S + C233S < C233S κC214S < C239S ≅ C232S κC214S as described previously.[17]

Additionally, we detected similar trends in the gas-phase compaction for the F(ab')$_2$ fragments of ChiLob7/4 variants generated via IdeS digestion (Appendix Figure C-2A). Variants with a disulfide crossover occupied a bimodal distribution of $^{TW}\Omega_{N2}$ values across charge states (19^+ to 21^+), while the more flexible C232S + C233S variant and *h*IgG1 WT showed more unimodal distributions, especially for lower charge states (Appendix Figure C-2B). Centroid $^{TW}\Omega_{N2}$ values for the more compact distributions in each C/S variant further revealed an increase in $^{TW}\Omega_{N2}$ values in the order of C232S + C233S < C233S κC214S < C239S ≅ C232S κC214S (Appendix Figure C-2C), which agree with our $^{TW}\Omega_{N2}$ measurements of full-length *h*IgGs. Since F(ab')$_2$ fragments of *h*IgG2 have been shown to elicit the same activity as full length *h*IgG2,[14, 17] our IM-MS results across all full-length *h*IgGs and F(ab')$_2$ fragments further support that

variations in hinge flexibility modulate the gas-phase collapse of *h*IgG2 antibodies in a manner that correlates with agonistic activity.

Disulfide crossover in the *h*IgG2 hinge induces changes in full-length mAb CIU pathways. Previous reports have detailed the potential of CIU-based assays to scrutinize the structures and stabilities of various mAb modalities.[44-48] In CIU, protein ions generated via nESI are subjected to collisions with background inert gas prior to IM separation. The activated ions then undergo structural changes, leading to changes in $^{TW}\Omega_{N2}$ representative of different conformational states or features.[24] Studies have shown that the extent of unfolding induced by these collisions is dependent on charge state, where lower charge states require more energy to initiate unfolding and higher charge states access more highly extended conformations.[41, 42] Since we observed that hinge flexibility modulates the gas-phase compaction of ChiLob7/4 C/S variants, we speculated that the underlying architecture of such collapsed structures would produce different unfolded intermediates during CIU.

When subjecting the most abundant ChiLob7/4 variant ions (23^+ to 25^+) to CIU, we observed remarkably different unfolding patterns for suspected *h*IgG2A and *h*IgG2B forms, allowing them to be distinguished (Appendix Figure C-3). Immediate differences in conformer families are evident at CVs above 100 V, where agonistic variants access unfolded structures with higher $^{TW}\Omega_{N2}$ values than those of nonagonistic variants. These distinctions are especially evident at higher charge states. For our analyses described below, we chose to further investigate 24^+ ions due to the higher intensities of these extended conformations compared to 23^+ ions, as well as their more compact, native-like structures relative to 25^+ ions (Figure 3-2).

A closer examination of individual CIU fingerprints revealed that all antibodies undergo a transition between 60 to 75 V to a second feature with a $^{TW}\Omega_{N2}$ value ranging from 87.0 to 91.0

nm^2 before further unfolding to extended states that differed significantly between mAbs (Figure 3-2A). For example, the agonistic *h*IgG2 WT first transitions to an intermediate third feature with a $^{TW}\Omega_{N2}$ of 94.50 ± 0.48 nm^2 before unfolding to a more elongated fourth feature with a $^{TW}\Omega_{N2}$ of 100.46 ± 0.3 nm^2. In contrast, the nonagonistic *h*IgG1 WT transitions to a third feature with a $^{TW}\Omega_{N2}$ of 95.60 ± 0.39 nm^2 without any subsequent unfolding. We attributed these differences in CIU features to the mixture of different disulfide isoforms within *h*IgG2 WT, where the *h*IgG2A and *h*IgGB forms predominately give rise to the third and fourth features observed in the *h*IgG2 WT, respectively. Within this scope, the highly agonistic C232S κC214S unfolds to produce a more extended fourth feature with a $^{TW}\Omega_{N2}$ of 101.40 ± 0.39 nm^2 without transitioning through a discrete intermediate third feature like *h*IgG2 WT. The modestly agonistic C233S κC214S variant behaves similarly, unfolding to a fourth feature with a $^{TW}\Omega_{N2}$ of 101.32 ± 0.42 nm^2. Like the *h*IgG1 WT, the nonagonistic C232S + C233S variant predominately transitions to a third feature with a $^{TW}\Omega_{N2}$ of 97.59 ± 0.39 nm^2. Combined, these results confirm that the disulfide isoforms of *h*IgG2 give rise to the different CIU transitions that we observe at higher CVs. Interestingly, the highly agonistic C239S variant undergoes CIU transitions similar to those of the *h*IgG2 WT, with the third and fourth features having $^{TW}\Omega_{N2}$ values of 94.46 ± 0.48 nm^2 and 100.46 ± 0.39 nm^2, respectively. Therefore, the C239S variant likely exhibits both *h*IgG2 disulfide isoforms, as evidenced by minimal full light chain ejection upon collisional activation, which supports the possible existence of an interchain disulfide bond between heavy and light chains (Appendix Figure C-4).

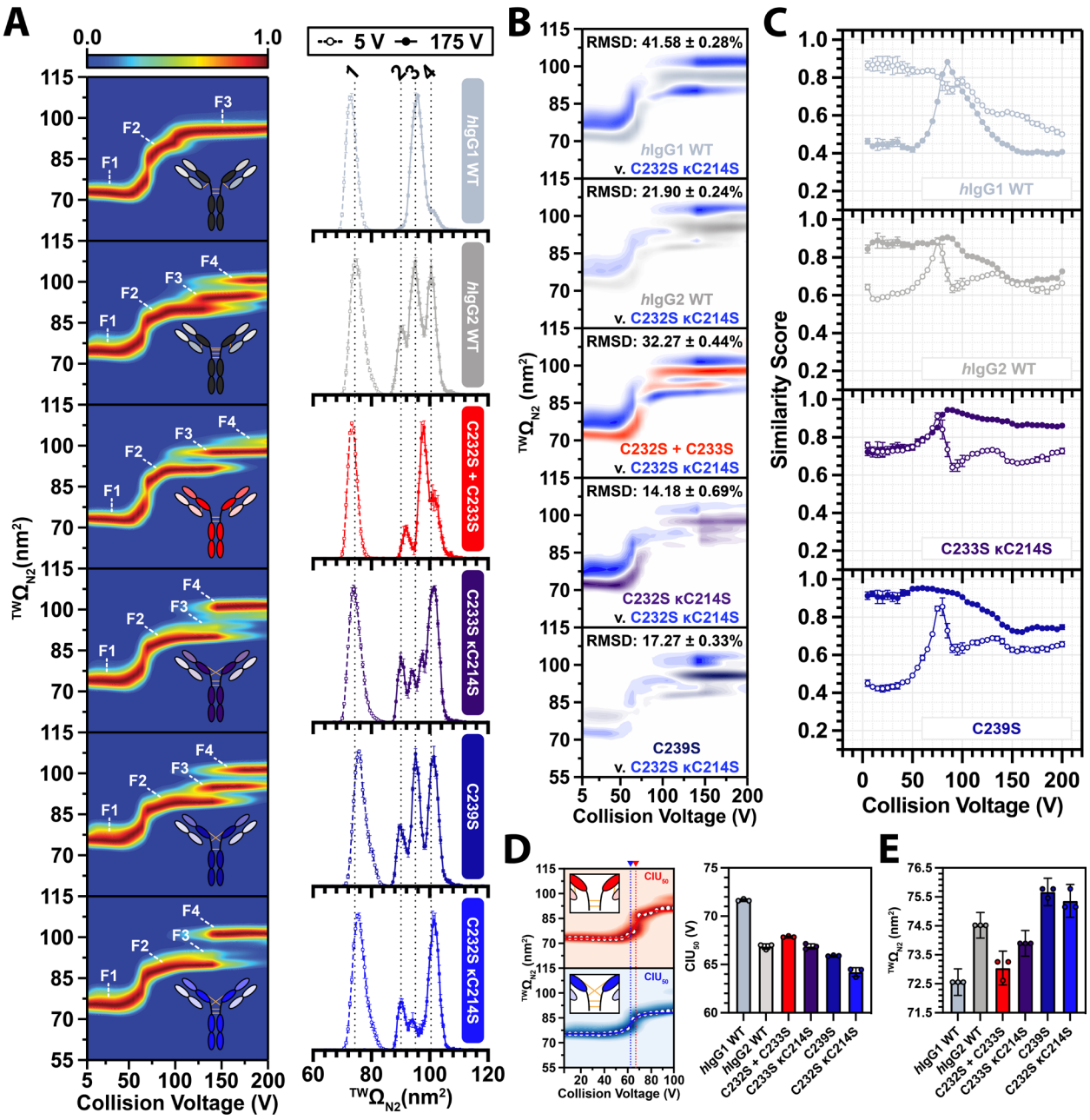

Figure 3-2: CIU analysis scrutinizes the effects of hinge disulfide variation on *h*IgG structure and stability. (A) Left: Averaged CIU fingerprints (n = 3) for the 24$^+$ charge state of ChiLob7/4 variants. Right: $^{TW}\Omega_{N2}$ distributions of each variant at 5 (dashed lines, open circles) and 175 V (solid lines, closed circles) during CIU. Vertical and horizontal error bars represent s.d. of technical replicates and calibrated $^{TW}\Omega_{N2}$ uncertainties, respectively. (B) Pairwise RMSD comparisons of C232S κC214S with other variants. (C) Similarity scores comparing the $^{TW}\Omega_{N2}$ distributions of either C232S + C233S (open circles) or C232S κC214S (closed circles) to those of other variants. (D) Left: representative plots showing sigmodal fitting of the first CIU transition. Right: CIU_{50} values for the first CIU transition shown as mean ± s.d. (E) $^{TW}\Omega_{N2}$ values of the first CIU feature shown as mean ± propagated $^{TW}\Omega_{N2}$ error. Data in (A) and (C) are shown as mean ± s.d. of nine comparisons between technical replicates of each variant.

To better quantify the relative differences between ChiLob7/4 C/S variants, we performed a total difference analysis of CIU data utilizing a root-mean-square deviation (RMSD) approach. We specifically compared the CIU fingerprints of each antibody to that of the highly agonistic C232S κC214S variant (Figure 3-2B). Comparisons to the nonagonistic *h*IgG1 WT and C232S + C233S variant yielded RMSD values greater than ~32% compared to replicate RMSD baselines of less than 5% (Appendix Figure C-3). Comparisons to other agonistic variants, however, produced RSMDs values lower than ~22%, emphasizing that the presence of a disulfide crossover causes *h*IgG2B variants to exhibit somewhat similar $^{TW}\Omega_{N2}$ distributions along their respective CIU pathways. Visually, some regions of differences are more pronounced than others across RMSD plots, indicating that the differences observed between the C232S κC214S variant and other mAbs vary significantly at each CV recorded. Therefore, we employed a Jensen-Shannon divergence metric to measure the similarity between Ω_{N2} distributions at each individual CV step. This similarity metric has been previously implemented in the differentiation of IgG1κ and IgG4κ antibodies.[27]

In this work, we calculated the similarity of each antibody to either the nonagonistic C232S + C233S or the highly agonistic C232S κC214S variant (Figure 3-2C). As expected, both the nonagonistic *h*IgG1 WT and C232S + C233S variant had higher similarity scores across multiple CVs since a similar number of features are observed in their CIU fingerprints. Higher similarity scores are observed from 50 to 80 V across all comparisons since all antibodies share a common second feature within this CIU fingerprint region. Globally, the agonistic *h*IgG2 WT mostly scored higher in similarity with the C232S κC214S variant, where lower scores are the direct result of *h*IgG2A isoforms being present within the *h*IgG2 WT. The C239S variant, on the other hand, scored higher in similarity with the C232S κC214S variant across all CVs,

underscoring that C239S is agonistic and more *h*IgG2B-like. Interestingly, the C233S κC214S scored higher in similarity to the C232S κC214S variant at higher CVs. The lower scores at voltages below 50 V are likely the result of the more compact structures adopted by the C233S κC214S variant as shown by the corresponding RMSD plot in Figure 3-2B.

Since the magnitude of gas-phase compaction influences the energy barriers required for proteins to unfold,[41] we shifted our focus to evaluating the energy levels required to initially unfold each antibody. Specifically, we determined quantitative stability values from our CIU data sets by fitting the transition region between the first two features in each antibody variant with a sigmoid function (Figure 3-2D). The midpoint voltage of this transition, which we term the "CIU_{50}" value, can then be obtained and used as a quantitative metric for gas-phase stability.[31] A comparison of CIU_{50} values for the first transition revealed that the *h*IgG1 isotype of ChiLob7/4 is more stable than its *h*IgG2 analogue. This difference is likely driven by the variations in hinge disulfide connectivity between *h*IgG isotypes and is further supported by the trends we observed in the C/S variants. Here, the nonagonistic C232S + C233S variant is more stable than the *h*IgGB variants, highlighting that the presence of a disulfide crossover and the lack of a disulfide bond between heavy and light chains destabilize the *h*IgG2B isoforms. Regarding the *h*IgGB variants studied here, we noticed a decrease in CIU_{50} values in a manner that correlates with an increase in agonism in the order of C233S κC214S < C239S ≅ C232S κC214S.[17] These variations in gas-phase stability are influenced by the differing degrees of compaction experienced by each variant, which can either increase or decrease the energy barriers required for unfolding (Figure 3-2E). As observed previously, the level of structural collapse experienced by each variant decreases as agonistic activity increases, where the highly agonistic C232S κC214S requires less collisional activation to unfold due to a less compact gas-

phase structure. Together, these data emphasize the broad applicability of CIU for identifying potentially agonistic antibodies based on quantifiable shifts in gas-phase stability.

Hinge variation produces comparable shifts in the CIU pathways of F(ab')$_2$ fragments. Previous studies have reported the potential of middle-level CIU in improving the differentiation of *h*IgG isotypes based on the unfolding pathways of F(ab')$_2$ fragments.[26, 49] To build on these studies, we subjected F(ab')$_2$ fragments of all ChiLob7/4 variants to CIU, each producing unique unfolding patterns across different charge states (Appendix Figure C-5). As expected, higher charge states produce more transitions during CIU, while lower charge states require higher acceleration voltages to unfold. We chose to further investigate the 21^+ charge state due to the emergence of discrete CIU features at higher CVs that varied between variants (Figure 3-3).

We observed up to five CIU features that varied in intensity across variants. As highlighted by our IM-MS analysis described above, F(ab')$_2$ fragments of agonistic variants display bimodal $^{TW}\Omega_{N2}$ distributions at lower CVs (Figure 3-3A). Interestingly, the first feature in these variants is highly unstable, as it readily transitions to a second feature at voltages below 20 V. CIU_{50} analysis further revealed that agonistic variants transition to a third CIU feature at lower voltages when compared to those detected for nonagonistic variants (Figure 3-3B). These variations in gas-phase stability are partially driven by the structural collapse of F(ab')$_2$ fragments, as we observe an increase in $^{TW}\Omega_{N2}$ values for agonistic variants that corresponds to a decrease in compaction and an increase in receptor agonism (Figure 3-3C). Since we observed similar trends in gas-phase compaction and stability for full-length *h*IgGs, we can further confirm that variations in hinge disulfides directly modulate the CIU pathways of the antibodies studied here.

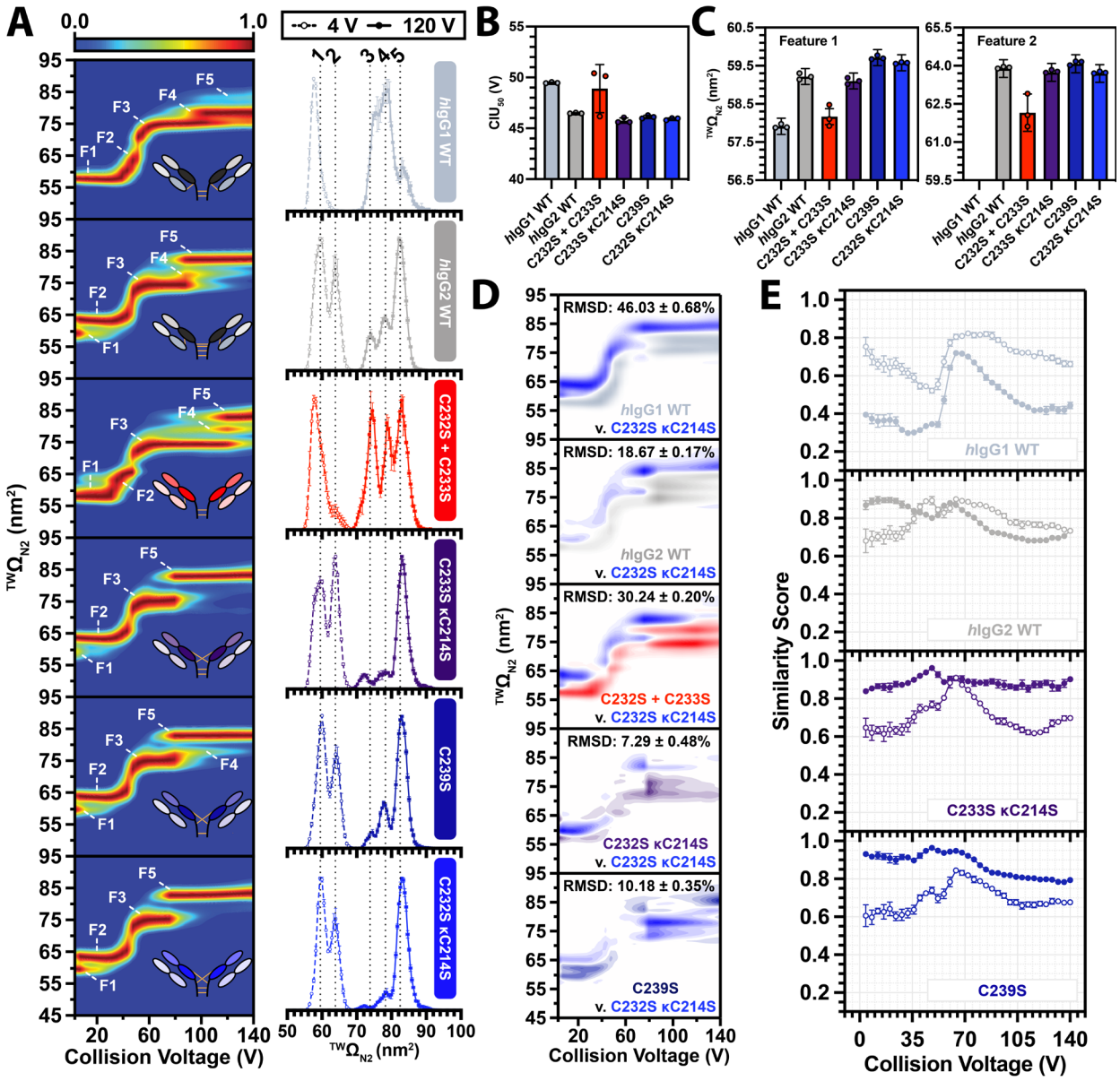

Figure 3-3: CIU detects comparable changes in the structures and stabilities of F(ab')$_2$ fragments. (A) Left: Averaged CIU fingerprints (n = 3) for the 21$^+$ charge state of ChiLob7/4 F(ab')$_2$ fragments. Right: $^{TW}\Omega_{N2}$ distributions of each variant at 4 (dashed lines, open circles) and 120 V (solid lines, closed circles) during CIU. Vertical and horizontal error bars represent s.d. of technical replicates and $^{TW}\Omega_{N2}$ uncertainties, respectively. (B) CIU_{50} values for the CIU transition between features two and three. Data are shown as mean ± s.d. (C) $^{TW}\Omega_{N2}$ values of features one (left) and two (right) shown as mean ± propagated $^{TW}\Omega_{N2}$ error. (D) Pairwise RMSD comparisons of C232S κC214S with other variants. (E) Similarity scores comparing the $^{TW}\Omega_{N2}$ distributions of either C232S + C233S (open circles) or C232S κC214S (closed circles) to those of other variants. Data in (D) and (E) are shown as mean ± s.d. of nine comparisons between technical replicates of each variant.

Though all variants share a common third feature, agonistic variants do not transition through a discrete intermediate fourth feature, but rather unfold to a more extended fifth feature

at lower voltages than those detected for nonagonistic variants. As shown by the $^{TW}\Omega_{N2}$ distributions of each variant at 120 V (Figure 3-3A), nonagonistic variants adopt a trimodal distribution of unfolded structures, while agonistic variants preferentially unfold to a population of more extended features with $^{TW}\Omega_{N2}$ centered around 82.30 nm^2. These differences in CIU features are reminiscent of our CIU results for full-length *h*IgG constructs, where variants possessed highly distinct CIU features at higher voltages. A pairwise RMSD analysis of $F(ab')_2$ fragments further revealed similar trends to those observed for full-length *h*IgGs. When comparing the highly agonistic C232S κC214S to the nonagonistic variants, we obtain RMSD values greater than 30% (Figure 3-3D). In contrast, comparisons to the C233S κC214S and C239S yielded RMSD values below ~ 10%, underscoring their structural similarity to the C232S κC214S variant during CIU. Similarity scoring further illustrated that these agonistic variants are highly similar to the C232S κC214S variant across all CVs (Figure 3-3E). Specifically, the *h*IgG1 WT is highly similar to the C232S + C233S variant across all voltages, whereas the *h*IgG2 WT varied in similarity due to the coexistence of disulfide isoforms. Together, our full-length *h*IgG2 and $F(ab')_2$ data are strongly correlated and both predictive of mAb hinge flexibility and agonism. Most importantly, the comparable trends in our CIU data for full-length *h*IgG2 and $F(ab')_2$ constructs eliminate the need for $F(ab')_2$ fragment generation that is often needed to perform other structurally-informative measurements.[17]

Hinge disulfide engineering induces comparable shifts in CIU data of other full-length antibodies. Next, we leveraged our CIU approach to study the structural effects of hinge disulfide variation in the clinically relevant anti-4-1BB (CD137) mAb, SAP1.3. Two extra

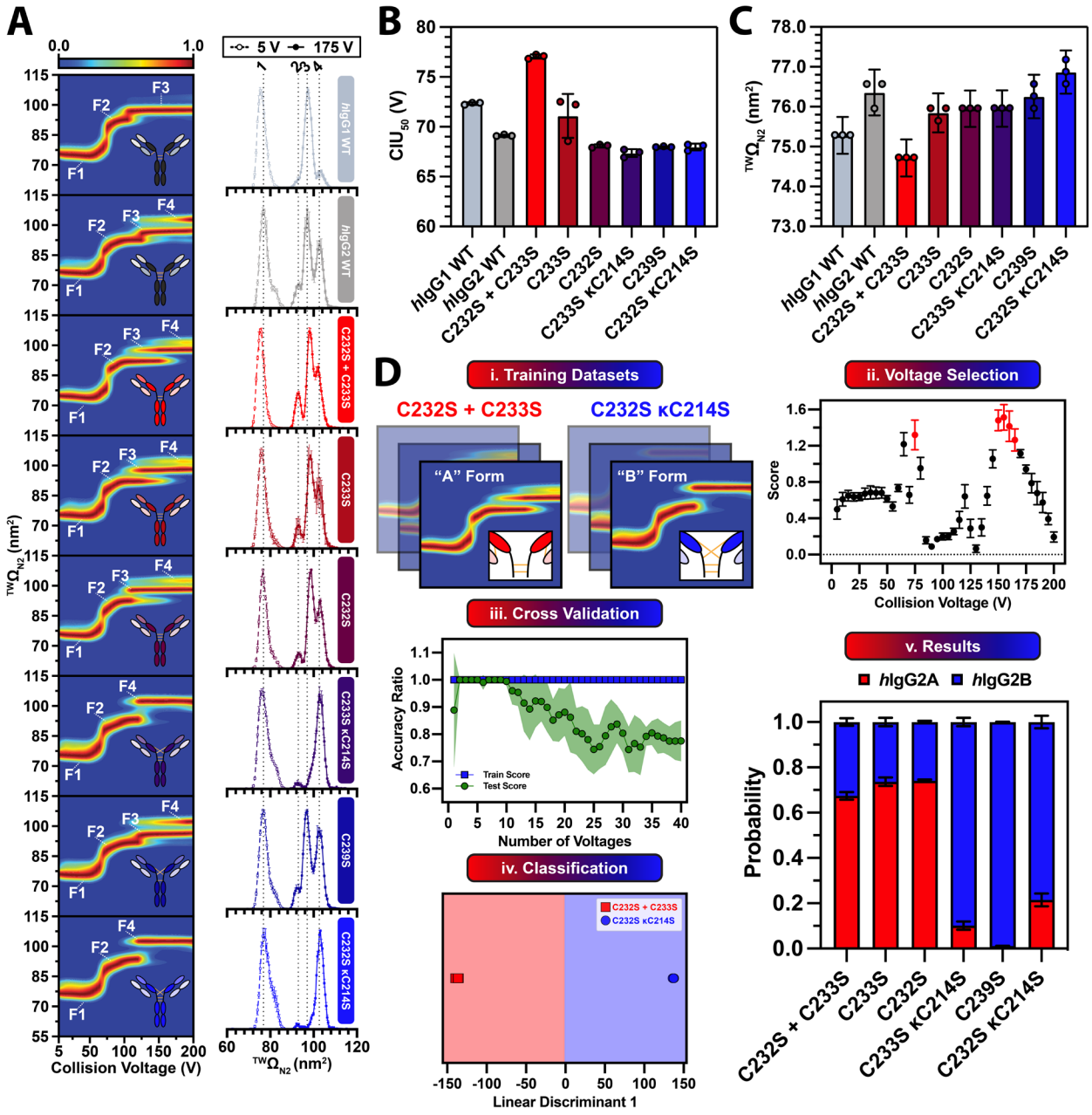

Figure 3-4: CIU rapidly classifies C/S variants of the anti-4-1BB (CD137) mAb, SAP1.3. (A) Left: averaged CIU fingerprints (n = 3) for the 24^+ charge state of each variant. Right: $^{TW}\Omega_{N2}$ distributions of each variant at 5 (dashed lines, open circles) and 175 V (solid lines, closed circles). Vertical and horizontal error bars represent s.d. of technical replicates and $^{TW}\Omega_{N2}$ uncertainties, respectively. (B) CIU_{50} values for the first CIU transition shown as mean ± s.d. (C) $^{TW}\Omega_{N2}$ values of the first CIU feature shown as mean ± propagated $^{TW}\Omega_{N2}$ error. (D) CIU classification workflow: (i) assignment of CIU training data sets to classes, (ii) selection of voltage steps better suited in distinguishing classes; nine voltages were selected (red), (iii) cross-validation analysis tests the accuracy of the classification model, (iv) linear discriminate analysis enables sorting of training data sets into two classes, (v) replicates not used as training data are correctly assigned to their respective classes. Probabilities are shown as mean ± s.d. of classification results for technical replicates.

single C/S variants (C232S and C233S), which are *h*IgG2A-like, were generated for this

analysis. Data recorded for the 24^+ charge state of SAP1.3 C/S and WT variants revealed CIU features that were comparable to those of the ChiLob7/4 variants, where variants featuring a disulfide crossover readily transitioned to CIU features with $^{TW}\Omega_{N2}$ values above 101 nm^2 at higher CVs (Figure 3-4A). As expected, an assessment of gas-phase stability further revealed a decrease in CIU_{50} values for the first CIU transition in a manner that correlates with an increase in the first feature's $^{TW}\Omega_{N2}$ values (Figure 3-4B,C). Importantly, these results are comparable to the trends we observed in our ChiLob7/4 variants described above, highlighting that C/S engineering leads to generalizable changes in mAb structure and stability across constructs that have different receptor targets.

Since we observed that different *h*IgG2 disulfide isoforms give rise to specific CIU features that are diagnostic of agonistic activity, we developed an automated classification algorithm and built a two-state classifier capable of predicting antibody function based on CIU data alone (Figure 3-4D). Briefly, our classification approach starts with providing the CIUSuite 2[31] classification algorithm with training data sets from the C232S + C233S and C232S κC214S variants, as they represent the "locked" *h*IgG2A and *h*IgG2B isoforms of SAP1.3, respectively (Figure 3-4D, i). Next, a univariate feature selection (UFS) method based on an analysis of variance (ANOVA) F-test is implemented to identify collision voltages that generate the greatest differences between the CIU fingerprints of each variant (Figure 3-4D, ii). A "leave-one-out" cross-validation analysis of the training data is then performed to scrutinize the accuracy of the classification scheme generated (Figure 3-4D, iii). The top five scoring voltages were then utilized to construct a classification scheme, allowing for the clear distinction of C232S + C233S and C232S κC214S data sets when plotted in linear discriminant (LD) space (Figure 3-4D, iv). Using this classification scheme, we were able to correctly identify both *h*IgG2A and *h*IgGB

isoforms with probability values greater than 80% (Figure 3-4D, v). Our classification results underscore the ability of CIU-based assays to rapidly identify potentially agonistic *h*IgG2 C/S variants in an automated, high-throughput mode of operation that culminates hundreds of CIU datapoints.

CIU of novel C/S *h*IgG2 variants reveal unique gas-phase unfolding pathways. We proceeded with assessing the capability of CIU to rapidly probe the structures and stabilities of two novel C/S variants of ChiLob7/4 and SAP1.3, C232S + T222C κE123C + C214S and C232S + K228C κC214S. These variants contain unconventional hinge disulfides that aim to further restrict antibody flexibility and conformational freedom (Figure 3-5A). Both of these variants possess a disulfide crossover unique to *h*IgG2B isoforms as well as new disulfide linkages between different chains. The C232S + T222C κE123C + C214S variant exhibits two disulfides linking opposing heavy and light chains outside of the hinge, while the C232S + K228C κC214S variant contains disulfides further up the hinge that link opposing heavy chains.

When 24^+ ions for these variants are subjected to CIU, they produce two discrete unfolding events (Figure 3-5B). Interestingly, the C232S + T222C κE123C + C214S variant of both ChiLob7/4 and SAP1.3 unfolded to produce a third feature that occupied a similar $^{TW}\Omega_{N2}$ space to that of C232S + C233S variants. In contrast, the C232S + K228C κC214S variant unfolded to generate a fourth feature similar in $^{TW}\Omega_{N2}$ to that of C232S κC214S variants. A more quantitative comparison of CIU fingerprints revealed that C232S + T222C κE123C + C214S variants scored higher in similarity to the nonagonistic C232S + C233S variant for both ChiLob7/4 and SAP1.3 at high voltages, while the C232S + K228C κC214S variants scored higher in similarity to the agonistic C232S κC214S across all voltages (Figure 3-5C). Interestingly, the C232S + T222C κE123C + C214S variant of ChiLob7/4 scored higher in

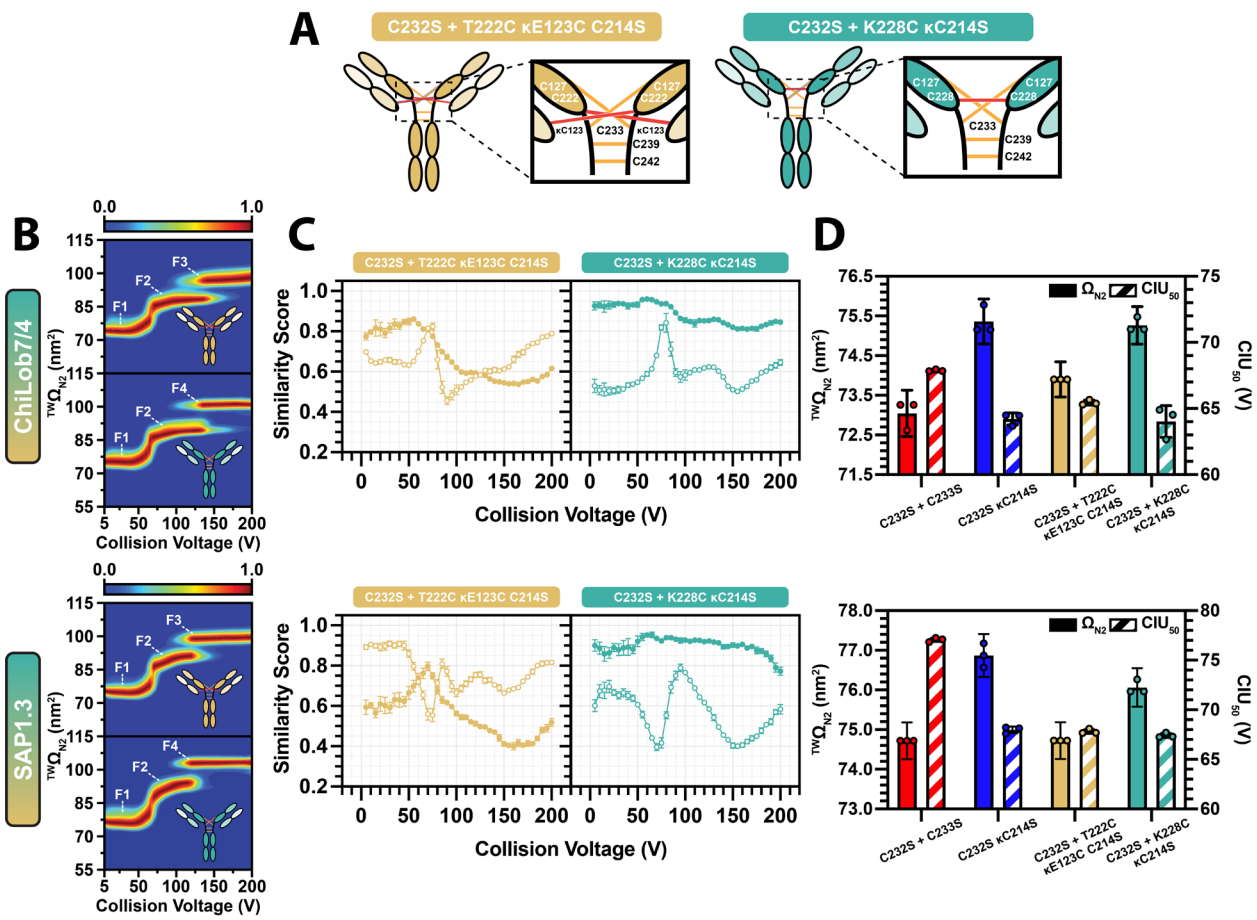

Figure 3-5: CIU probes the structures and stabilities of novel C/S *h*IgG2 variants. (A) Schemes for the full-length variants with insets highlighting the disulfides present in their hinge regions. (B) Averaged CIU fingerprints (n = 3) for the 24^+ charge state of ChiLob7/4 (top) and SAP1.3 (bottom). Vertical and horizontal error bars represent s.d. of technical replicates and $^{TW}\Omega_{N2}$ uncertainties, respectively. (C) Similarity scores acquired from comparisons to C232S + C233S (open circles) and C232S κC214S (closed circles) variants for ChiLob7/4 (top) and SAP1.3 (bottom). Scores are shown as mean ± s.d. of nine comparisons between technical replicates of each variant. (D) Summary of $^{TW}\Omega_{N2}$ (solid colors) and CIU_{50} values (color stripes) for ChiLob7/4 (top) and SAP1.3 (bottom) variants (n = 3). $^{TW}\Omega_{N2}$ values are shown as mean ± propagated $^{TW}\Omega_{N2}$ error. CIU_{50} values are shown as mean ± s.d.

similarity to the C232S κC214S variant at voltages less than 100 V, while the variant of SAP1.3 scored poorly with its respective C232S κC214S variant overall. Together, our similarity scoring trends suggest that the C232S + T222C κE123C + C214S variant of ChiLob7/4 and SAP1.3 exhibit different activity profiles as confirmed by NFκB assay results (Appendix Figure C-6).

A closer examination of the first feature in our CIU fingerprints revealed that the C232S + T222C κE123C + C214S variant of each antibody adopted structures with $^{TW}\Omega_{N2}$ values

similar to the structures of the each corresponding C232S + C233S variant (Figure 3-5D). In contrast, the first features of the C232S + K228C κC214S and C232S κC214S variants were comparable across both antibodies. On the other hand, an assessment of CIU_{50} values for the first CIU transition showed that both the C232S + T222C κE123C + C214S and C232S + K228C κC214S unfolded at CVs similar to those of the C232S κC214S variant for both ChiLob7/4 and SAP1.3 (Figure 3-5D). In a sense, our results indicate that both of these new variants share similar stability profiles when compared with other agonistic variants despite the differences in $^{TW}\Omega_{N2}$ values that we observe across CIU features in each C232S + T222C κE123C + C214S variant. These differences are likely due to the presence of a disulfide bond between opposing heavy and light chains within this variant that is commonly observed in *h*IgG2A isoforms. However, SAXS data showed that both of these variants showed smaller D_{max} values than nonagonistic variants, demonstrating that the interchain disulfides in the C232S + T222C κE123C + C214S variants lead to more compact, rigid structures in solution (Appendix Figure C-6). Therefore, although both C232S + T222C κE123C + C214S and C232S + C233S variants have gas-phase structures with similar $^{TW}\Omega_{N2}$ values, it is highly possible that their overall topologies are intrinsically distinct, leading to the differences in gas-phase stability that we observe.

3.7 Conclusions

In this study, we introduce a workflow that presents strong evidence indicating a correlation between the gas-phase unfolding of hinge disulfide engineered antibodies and their known levels of agonistic activity. Importantly, our assay incorporates elements of IM-MS and CIU for the first time to determine antibody structure-function relationships. This is especially

exciting, as CIU data can be collected in less than 30s and analyzed in an automated manner to enable mAb engineering campaigns.[50, 51] Our results indicate that hinge disulfides mitigate the collapse experienced by mAbs that typically occurs during the nESI process. In a general sense, agonistic, rigid *h*Ig2B disulfide isoforms experience less structural collapse towards the hinge compared to nonagonistic, flexible *h*IgG2A isoforms. These differences in gas-phase collapse, in turn, modulate antibody stability as highlighted by our CIU_{50} analysis, where more compact *h*IgG2 variants require more collisional activation to initially unfold. These differences in structure and stability are comparable between full-length *h*IgG2 and $F(ab')_2$ scaffolds of the anti-CD40 mAb, ChiLob7/4, and a combination of RMSD analysis and similarity scoring further revealed topological similarities among agonistic variants during CIU.

An extension of our CIU-based assay to C/S variants of the anti-4-1BB (CD137) mAb, SAP1.3, reveals that the effects of hinge disulfide engineering on antibody structure and function are generalizable across different receptor targets. By building a CIU-based classification scheme, we are able to confidently identify agonistic, *h*IgGB-like variants of SAP1.3, further highlighting the robustness of our CIU approach in accelerating agonistic candidate selection for the first time. The ability of CIU to rapidly classify full-length *h*IgG2 C/S variants of SAP1.3, in turn, eliminates the need for $F(ab')_2$ fragment generation that is often necessary to perform classical high-resolution structural analyses from solution.

Finally, we assessed the ability of CIU to probe the structures and stabilities of two novel C/S variants of ChiLob7/4 and SAP1.3. We find that these new variants, which feature new hinge disulfides linking different opposing chains, possess gas-phase stability profiles similar to those of conventional agonistic *h*IgG2B isoforms, identifying them as potentially agonistic candidates with different activity profiles between ChiLob7/4 and SAP1.3 as confirmed by

biological activity assays. We envision that the future incorporation of these novel variants in our CIU classification workflow would permit the construction of more robust classifiers, permitting the identification of other potentially agonistic variants with different hinge disulfides that aim to further limit antibody conformation and flexibility. Overall, our CIU-based approach demonstrates an alternative approach to establish connections between antibody structure and function without the need for extensive preparation protocols and lengthy data acquisition and processing.

3.8 References

[1] Lu, L. L.; Suscovich, T. J.; Fortune, S. M.; Alter, G. Beyond binding: antibody effector functions in infectious diseases. *Nat. Rev. Immunol.* **2018**, *18* (1), 46-61. DOI: 10.1038/nri.2017.106.

[2] Tsao, L.-C.; Force, J.; Hartman, Z. C. Mechanisms of Therapeutic Antitumor Monoclonal Antibodies. *Cancer Res.* **2021**, *81* (18), 4641-4651. DOI: 10.1158/0008-5472.can-21-1109.

[3] Carter, P. J.; Rajpal, A. Designing antibodies as therapeutics. *Cell* **2022**, *185* (15), 2789-2805. DOI: 10.1016/j.cell.2022.05.029.

[4] Lyu, X.; et al. The global landscape of approved antibody therapies. *Antib. Ther.* **2022**, *5* (4), 233-257. DOI: 10.1093/abt/tbac021.

[5] Crescioli, S.; et al. Antibodies to watch in 2024. *mAbs* **2024**, *16* (1). DOI: 10.1080/19420862.2023.2297450.

[6] Vidarsson, G.; Dekkers, G.; Rispens, T. IgG Subclasses and Allotypes: From Structure to Effector Functions. *Front. Immunol.* **2014**, *5*. DOI: 10.3389/fimmu.2014.00520.

[7] Dilillo, D. J.; Ravetch, J. V. Fc-Receptor Interactions Regulate Both Cytotoxic and Immunomodulatory Therapeutic Antibody Effector Functions. *Cancer Immuno. Res.* **2015**, *3* (7), 704-713. DOI: 10.1158/2326-6066.cir-15-0120.

[8] Mayes, P. A.; Hance, K. W.; Hoos, A. The promise and challenges of immune agonist antibody development in cancer. *Nat. Rev. Drug. Discov.* **2018**, *17* (7), 509-527. DOI: 10.1038/nrd.2018.75.

[9] Bullock, T. N. J. CD40 stimulation as a molecular adjuvant for cancer vaccines and other immunotherapies. *Cell. Mol. Immunol.* **2022**, *19* (1), 14-22. DOI: 10.1038/s41423-021-00734-4.

[10] Yu, X.; et al. TNF receptor agonists induce distinct receptor clusters to mediate differential agonistic activity. *Commun. Biol.* **2021**, *4* (1). DOI: 10.1038/s42003-021-02309-5.

[11] Yu, X.; et al. Complex Interplay between Epitope Specificity and Isotype Dictates the Biological Activity of Anti-human CD40 Antibodies. *Cancer Cell* **2018**, *33* (4), 664-675.e664. DOI: 10.1016/j.ccell.2018.02.009.

[12] Beers, S. A.; Glennie, M. J.; White, A. L. Influence of immunoglobulin isotype on therapeutic antibody function. *Blood* **2016**, *127* (9), 1097-1101. DOI: 10.1182/blood-2015-09-625343.
[13] Yu, X.; et al. Isotype Switching Converts Anti-CD40 Antagonism to Agonism to Elicit Potent Antitumor Activity. *Cancer Cell* **2020**, *37* (6), 850-866.e857. DOI: 10.1016/j.ccell.2020.04.013.
[14] White, A. L.; et al. Conformation of the Human Immunoglobulin G2 Hinge Imparts Superagonistic Properties to Immunostimulatory Anticancer Antibodies. *Cancer Cell* **2015**, *27* (1), 138-148. DOI: 10.1016/j.ccell.2014.11.001.
[15] Wypych, J.; et al. Human IgG2 Antibodies Display Disulfide-mediated Structural Isoforms. *J. Biol. Chem.* **2008**, *283* (23), 16194-16205. DOI: 10.1074/jbc.m709987200.
[16] Zhang, B.; Harder, A. G.; MConnelly, H. M.; Maheu, L. L.; Cockrill, S. L. Determination of Fab-Hinge Disulfide Connectivityin Structural Isoforms of a Recombinant HumanImmunoglobulin G2 Antibody. *Anal. Chem.* **2010**, *82* (3), 1090-1099. DOI: 10.1021/ac902466z.
[17] Orr, C. M.; et al. Hinge disulfides in human IgG2 CD40 antibodies modulate receptor signaling by regulation of conformation and flexibility. *Sci. Immunol.* **2022**, *7* (73). DOI: 10.1126/sciimmunol.abm3723.
[18] Jay, J.; et al. IgG Antibody 3D Structures and Dynamics. *Antibodies* **2018**, *7* (2), 18. DOI: 10.3390/antib7020018.
[19] Christofi, E.; Barran, P. Ion Mobility Mass Spectrometry (IM-MS) for Structural Biology: Insights Gained by Measuring Mass, Charge, and Collision Cross Section. *Chem. Rev.* **2023**, *123* (6), 2902-2949. DOI: 10.1021/acs.chemrev.2c00600.
[20] Ruotolo, B. T.; Benesch, J. L. P.; Sandercock, A. M.; Hyung, S.-J.; Robinson, C. V. Ion mobility–mass spectrometry analysis of large protein complexes. *Nat. Protoc.* **2008**, *3* (7), 1139-1152. DOI: 10.1038/nprot.2008.78.
[21] Gabelica, V.; et al. Recommendations for reporting ion mobility Mass Spectrometry measurements. *Mass Spectrom. Rev.* **2019**, *38* (3), 291-320. DOI: 10.1002/mas.21585.
[22] Bagal, D.; Valliere-Doughlass, J. F.; Balland, A.; Schnier, P. D. Resolving Disulfide Structural Isoforms of IgG2 Monoclonal Antibodies by Ion Mobility MassSpectrometry. *Anal. Chem.* **2010**, *82*, 6751-6755. DOI: 10.1021/ac1013139.
[23] Jones, L. M.; et al. Complementary MS Methods Assist Conformational Characterization of Antibodies with Altered S–S Bonding Networks. *J. Am. Soc. Mass Spectrom.* **2013**, *24* (6), 835-845. DOI: 10.1007/s13361-013-0582-4.
[24] Dixit, S. M.; Polasky, D. A.; Ruotolo, B. T. Collision induced unfolding of isolated proteins in the gas phase: past, present, and future. *Curr. Opin. Chem. Biol.* **2018**, *42*, 93-100. DOI: 10.1016/j.cbpa.2017.11.010.
[25] Tian, Y.; Han, L.; Buckner, A. C.; Ruotolo, B. T. Collision Induced Unfolding of Intact Antibodies: Rapid Characterization of Disulfide Bonding Patterns, Glycosylation, and Structures. *Anal. Chem.* **2015**, *87* (22), 11509-11515. DOI: 10.1021/acs.analchem.5b03291.
[26] Botzanowski, T.; et al. Middle Level IM–MS and CIU Experiments for Improved Therapeutic Immunoglobulin Subclass Fingerprinting. *Anal. Chem.* **2020**, *92* (13), 8827-8835. DOI: 10.1021/acs.analchem.0c00293.

[27] Gozzo, T. A.; Bush, M. F. Quantitatively Differentiating Antibodies Using Charge-State Manipulation, Collisional Activation, and Ion Mobility-Mass Spectrometry. *Anal. Chem.* **2024**, *96* (1), 505-513. DOI: 10.1021/acs.analchem.3c04638 From NLM Medline.

[28] Hernandez-Alba, O.; Wagner-Rousset, E.; Beck, A.; Cianférani, S. Native Mass Spectrometry, Ion Mobility, and Collision-Induced Unfolding for Conformational Characterization of IgG4 Monoclonal Antibodies. *Anal. Chem.* **2018**, *90* (15), 8865-8872. DOI: 10.1021/acs.analchem.8b00912.

[29] Richardson, K.; Langridge, D.; Dixit, S. M.; Ruotolo, B. T. An Improved Calibration Approach for Traveling Wave Ion Mobility Spectrometry: Robust, High-Precision Collision Cross Sections. *Anal. Chem.* **2021**, *93* (7), 3542-3550. DOI: 10.1021/acs.analchem.0c04948.

[30] Marty, M. T.; et al. Bayesian Deconvolution of Mass and Ion Mobility Spectra: From Binary Interactions to Polydisperse Ensembles. *Anal. Chem.* **2015**, *87* (8), 4370-4376. DOI: 10.1021/acs.analchem.5b00140.

[31] Polasky, D. A.; Dixit, S. M.; Fantin, S. M.; Ruotolo, B. T. CIUSuite 2: Next-Generation Software for the Analysis of Gas-Phase Protein Unfolding Data. *Anal. Chem.* **2019**, *91* (4), 3147-3155. DOI: 10.1021/acs.analchem.8b05762.

[32] Haynes, S. E.; et al. Variable-Velocity Traveling-Wave Ion Mobility Separation Enhancing Peak Capacity for Data-Independent Acquisition Proteomics. *Anal. Chem.* **2017**, *89* (11), 5669-5672. DOI: 10.1021/acs.analchem.7b00112.

[33] Wojdyr, M. J. Fityk: A general-purpose peak fitting program. *J. Appl. Cryst.* **2010**, *43* (43), 1126-1128. DOI: 10.1107/S0021889810030499.

[34] Polasky, D. A.; Dixit, S. M.; Vallejo, D. D.; Kulju, K. D.; Ruotolo, B. T. An Algorithm for Building Multi-State Classifiers Based on Collision-Induced Unfolding Data. *Anal. Chem.* **2019**, *91* (16), 10407-10412. DOI: 10.1021/acs.analchem.9b02650 From NLM Medline.

[35] Menéndez, M. L. The Jensen-Shannon Divergence. *J. Franklin. Inst.* **1997**, *334B* (2), 307-318.

[36] Drost, H.-G. Philentropy: Information Theory and Distance Quantification with R. *J. Open Source Softw.* **2018**, *3* (26), 765. DOI: 10.21105/joss.00765.

[37] Hansen, K.; et al. A Mass-Spectrometry-Based Modelling Workflow for Accurate Prediction of IgG Antibody Conformations in the Gas Phase. *Angew. Chem.* **2018**, *130* (52), 17440-17445. DOI: 10.1002/ange.201812018.

[38] Pacholarz, K. J.; et al. Dynamics of Intact Immunoglobulin G Explored by Drift-Tube Ion-Mobility Mass Spectrometry and Molecular Modeling. *Angew. Chem. Int. Ed.* **2014**, *53* (30), 7765-7769. DOI: 10.1002/anie.201402863.

[39] Devine, P. W. A.; et al. Investigating the Structural Compaction of Biomolecules Upon Transition to the Gas-Phase Using ESI-TWIMS-MS. *J. Am. Soc. Mass Spectrom.* **2017**, *28* (9), 1855-1862. DOI: 10.1007/s13361-017-1689-9 From NLM Medline.

[40] Hernández, H.; Robinson, C. V. Determining the stoichiometry and interactions of macromolecular assemblies from mass spectrometry. *Nat. Protoc.* **2007**, *2* (3), 715-726. DOI: 10.1038/nprot.2007.73.

[41] Hall, Z.; Politis, A.; Bush, M. F.; Smith, L. J.; Robinson, C. V. Charge-state dependent compaction and dissociation of protein complexes: insights from ion mobility and molecular dynamics. *J. Am. Chem. Soc.* **2012**, *134* (7), 3429-3438. DOI: 10.1021/ja2096859 From NLM Medline.

[42] Zhong, Y.; Han, L.; Ruotolo, B. T. Collisional and Coulombic Unfolding of Gas-Phase Proteins: High Correlation to Their Domain Structures in Solution. *Angew. Chem.* **2014**, *126* (35), 9363-9366. DOI: 10.1002/ange.201403784.
[43] Shelimov, K. B.; Clemmer, D. E.; Hudgins, R. R.; Jarrold, M. F. Protein Structure in Vacuo: Gas-Phase Conformations of BPTI and Cytochrome c. *J. Am. Chem. Soc.* **1997**, *119*, 2240-2248.
[44] Villafuerte-Vega, R. C.; et al. Ion Mobility-Mass Spectrometry and Collision-Induced Unfolding of Designed Bispecific Antibody Therapeutics. *Anal. Chem.* **2023**, *95* (17), 6962-6970. DOI: 10.1021/acs.analchem.3c00344.
[45] Desligniere, E.; et al. Combination of IM-Based Approaches to Unravel the Coexistence of Two Conformers on a Therapeutic Multispecific mAb. *Anal. Chem.* **2022**, *94* (22), 7981-7989. DOI: 10.1021/acs.analchem.2c00928.
[46] Tian, Y.; Lippens, J. L.; Netirojjanakul, C.; Campuzano, I. D. G.; Ruotolo, B. T. Quantitative collision-induced unfolding differentiates model antibody–drug conjugates. *Protein Sci.* **2019**, *28* (3), 598-608. DOI: 10.1002/pro.3560.
[47] Vallejo, D. D.; et al. Collision-Induced Unfolding Reveals Stability Differences in Infliximab Therapeutics under Native and Heat Stress Conditions. *Anal. Chem.* **2021**, *93* (48), 16166-16174. DOI: 10.1021/acs.analchem.1c03946.
[48] Zhao, R.; Liu, N.; Zheng, Z.; Li, G. Enhanced Stability Differentiation of Therapeutic Polyclonal Antibodies with All Ion Unfolding-Ion Mobility-Mass Spectrometry. *J. Am. Soc. Mass Spectrom.* **2023**, *34* (10), 2289-2295. DOI: 10.1021/jasms.3c00215 From NLM Medline.
[49] Deslignière, E.; et al. Toward Automation of Collision-Induced Unfolding Experiments through Online Size Exclusion Chromatography Coupled to Native Mass Spectrometry. *Anal. Chem.* **2020**, *92* (19), 12900-12908. DOI: 10.1021/acs.analchem.0c01426.
[50] Juliano, B. R.; et al. Development of an Automated, High-Throughput Methodology for Native Mass Spectrometry and Collision-Induced Unfolding. *Anal. Chem.* **2023**, *95* (45), 16717-16724. DOI: 10.1021/acs.analchem.3c03788.
[51] D'Amico, C. I.; Polasky, D. A.; Steyer, D. J.; Ruotolo, B. T.; Kennedy, R. T. Ion Mobility-Mass Spectrometry Coupled to Droplet Microfluidics for Rapid Protein Structure Analysis and Drug Discovery. *Anal. Chem.* **2022**, *94* (38), 13084-13091. DOI: 10.1021/acs.analchem.2c02307.

Chapter 4: Ion Mobility-Mass Spectrometry and Collision-Induced Unfolding Rapidly Characterize the Structural Polydispersity and Stability of an Fc-Fusion Protein

4.1 Original Publication

This chapter is originally published as: Rosendo C. Villafuerte-Vega, Henry W. Li, Addison E. Bergman, Thomas R. Slaney, Naresh Chennamsetty, Guodong Chen, Li Tao, and Brandon T. Ruotolo. "Ion Mobility-Mass Spectrometry and Collision-Induced Unfolding Rapidly Characterize the Structural Polydispersity and Stability of an Fc-Fusion Protein." *Anal. Chem.* 2024, DOI: 10.1021/acs.analchem.4c01408.

4.2 Author Contributions

R.C.V., B.T.R., T.R.S., G.C., N.C., and L.T. conceptualized and designed the experiments described. R.C.V. collected and analyzed all data and drafted the manuscript. H.W.L. assisted in collecting and analyzing Synapt G2 data. A.E.B. led cIM-MS method development and assisted in cIM-MS and CIU data collection and analysis. T.R.S., N.C., G.G., and L.T. provided the Fc-fusion protein characterized in this work.

4.3 Abstract

Fc-fusion proteins are an emerging class of protein therapeutics that combine the properties of biological ligands with the unique properties of the fragment crystallizable (Fc) domain of an immunoglobulin G (IgG). Due to their diverse higher-order structures (HOSs), Fc-

fusion proteins remain challenging characterization targets within biopharmaceutical pipelines. While high-resolution biophysical tools are available for HOS characterization, they frequently demand extended timeframes and substantial quantities of purified samples, rendering them impractical for swiftly screening candidate molecules. Herein, we describe the development of ion mobility-mass spectrometry (IM-MS) and collision-induced unfolding (CIU) workflows that aim to fill this technology gap, where we focus on probing the HOS of a model Fc-Interleukin-10 (Fc-IL-10) fusion protein engineered using flexible glycine-serine linkers. We evaluate the ability of these techniques to probe the flexibility of Fc-IL-10 in the absence of bulk solvent relative to other proteins of similar size, as well as localize structural changes of low charge state Fc-IL-10 ions to specific Fc and IL-10 unfolding events during CIU. We subsequently apply these tools to probe the local effects of glycine-serine linkers on the HOS and stability of IL-10 homodimer, which is the biologically active form of IL-10. Our data reveals that Fc-IL-10 produces significantly more structural transitions during CIU and broader IM profiles when compared to a wide range of model proteins, indicative of its exceptional structural dynamism. Furthermore, we use a combination of deglycosylation and domain-level approaches to annotate these intricate CIU data and localize specific transitions to the unfolding of domains within Fc-IL-10. Finally, we detect a strong positive, quadratic relationship between average linker mass and fusion protein stability, suggesting a cooperative influence between glycine-serine linkers and overall fusion protein stability. Overall, this is the first reported study on the use of IM-MS and CIU to characterize HOS of Fc-fusion proteins, illustrating the practical applicability of this approach.

4.4 Introduction

Fc-fusion proteins constitute an emerging class of protein therapeutics that have demonstrated great efficacy across a broad range of pathologies due to their diverse compositions and mechanisms of action.[1-3] Such therapeutic modalities combine the pharmacological properties of a broad range of biomolecules with the distinctive biological functions of the fragment crystallizable (Fc) region of an immunoglobulin G (IgG).[4, 5] The active components of Fc-fusion proteins can be peptides,[6, 7] cytokine traps,[3] recombinant enzymes,[8, 9] or the extracellular domains (ECDs) of receptors,[10, 11] where most are attached to both chains of the disulfide-linked, dimeric Fc domain. Most notably, Fc-fusion proteins possess increased serum half-life owing to their reduced renal clearance and neonatal Fc-receptor (FcRn)-mediated recycling from endosomes.[12, 13] Apart from half-life extension, the Fc domain can also greatly improve the solubility and stability of hydrophobic biomolecules, increase expression and secretion rates during production, enable facile purification via affinity for Protein A, and elicit Fc-mediated effector functions.[14, 15] Combined, these advantages have led to the approval of thirteen Fc-fusion proteins by the FDA to date, and approximately forty therapeutics are currently in clinical development.[16, 17]

The successful engineering of recombinant Fc-fusion proteins generally necessitates a suitable protein linker since the direct fusion of the Fc with protein domains can compromise appropriate folding and bioactivity.[18] Flexible linkers, which typically consist of glycine (Gly) and serine (Ser) repeats, are most widely utilized due to their tunable length and composition. An increase in Gly residues has been correlated with a decrease in linker rigidity, while an increase in polar residues like Ser has been shown to improve the stability of the linker in aqueous environments by promoting hydrogen bonds with surrounding water.[19, 20] This increase in

hydrophilicity prevents the formation of secondary structures and minimizes the likelihood of the linker disrupting the proper folding and function of the fusion protein. Within this context, a $(Gly4Ser)_n$ linker is most commonly used, where *n* can be adjusted to alter the structural flexibility of Fc-fusion proteins and the spatial mobility of protein domains. Thus, the optimal separation of adjacent domains can be achieved, or important interdomain non-covalent interactions can be preserved.[21, 22]

Indeed, controlling the ultimate structural flexibility of Fc-fusion proteins through alterations to their amino acid sequence represents a critical objective in their design and development as therapeutics. Furthermore, the higher-order structures (HOSs) of Fc-fusion protein constructs can be significantly influenced by post-translational modifications (PTMs) and chemical modifications produced under stress conditions, further complicating fusion protein engineering efforts. These alterations in HOS can significantly influence aggregation propensity, immunogenicity, serum half-life, and molecular binding.[23-26] Thus, discovering optimal Fc-fusion protein designs necessitates analytical methodologies capable of quantifying the structural contributions of individual protein domains to overall protein HOS and measuring the local effects of linker length and composition on Fc-fusion protein stability and conformational dynamics. Within this context, conventional high-resolution technologies for protein HOS characterization often require long timescales and complex sample preparation requirements that are not conducive for the rapid screening of candidate molecules, and they often fail to fully capture the diverse conformational ensembles adopted by highly dynamic Fc-fusion proteins.

Over the past two decades, mass spectrometry (MS)-based approaches have emerged as powerful orthogonal tools for the characterization of protein therapeutic HOS and stability in the gas-phase.[27, 28] For example, ion mobility combined with native mass spectrometry (IM-MS) has

been shown to be a valuable technology for the structural analyses of proteins and protein complexes, providing information regarding topologies, stoichiometries, sizes and shapes, with the latter two properties evaluated primarily through the measurement of rotationally-averaged collision cross sections (Ωs).[29, 30] Briefly, IM separates gas-phase protein ions based on their charge and Ω on the millisecond timescale, allowing for the separation of two conformationally different ions that share the same mass-to-charge (*m/z*) ratio. Furthermore, collision-induced unfolding (CIU) has enabled IM-MS to simultaneously probe the HOSs and stabilities of iso-cross-sectional proteins by collisionally activating ions to induce unique gas-phase unfolding profiles prior to IM separation.[31] Ongoing efforts in the development of native IM-MS and CIU-based workflows for the characterization of protein therapeutics have been successful in classifying IgG subclasses using both intact monoclonal antibodies (mAbs) and large fragments,[32, 33] detecting subtle differences between innovator and biosimilar therapeutics,[34-36] probing the complex structures of engineered multi-specific mAbs,[37, 38] and assessing stability shifts associated with conjugating small molecules to mAb sequences.[39, 40] However, the utility of native IM-MS and CIU in probing the highly dynamic structures of Fc-fusion proteins with flexible linkers remains largely unexplored.

Herein, we describe the first series of gas-phase measurements that leverage IM-MS and CIU to investigate the structural dynamics and stabilities of Fc-fusion proteins engineered with flexible linkers. Specifically, we characterize the HOS and stability of a model Fc-interleukin-10 (Fc-IL-10) fusion protein that links the C-termini of an IgG1 Fc domain with the N-termini of individual monomer units of human IL-10, which biologically exists as homodimer, via a flexible Gly-Ser linker (Appendix Figure D-1). We observe broadened IM peak widths for Fc-IL-10 ions and compare these data to a series of protein standards ranging from 36 to 150 kDa to

quantify the elevated conformational polydispersity of Fc-IL-10. In addition, our CIU data recorded for Fc-IL-10 reveal up to five gas-phase unfolding events, a value that is larger than what is typically observed for larger native protein ions, providing further evidence of the intricate structural ensemble adopted by Fc-IL-10 when compared to model proteins. Our findings allow us to isolate and evaluate HOS contributions from the Fc, IL-10, and Gly-Ser linker units to the overall gas-phase stability of the intact fusion protein. Here, we determined gas-phase stability by quantifying the relative collisional energy required to induce protein unfolding. Specifically, we find that the Fc region of the protein is sustainability more stable than the IL-10 dimer, a result that is strongly correlated with other biophysical measurements. In addition, we use a combination of deglycosylation steps to facilitate the modification or complete removal of Fc-localized *N*-linked glycans. These experiments produced fusion proteins of decreased stabilities, as expected, but stability shifts were observed to unequally influence the CIU transitions, which allowed us to annotate those features most associated with the Fc portion of the model fusion proteins studied here. Finally, we discern a positive, quadratic relationship between average linker length and IL-10 homodimer stability. We conclude our report by discussing the analytical implications of IM-MS and CIU methodologies for delineating the multifaceted biophysical underpinnings of Fc-fusion protein function and advancing future discovery and development efforts within the biopharmaceutical pipeline.

4.5 Experimental Section

Materials and Sample Preparation. Fc-IL-10 fusion protein (10 mg/mL) was produced, purified, and formulated at Bristol Myers Squibb (New Brunswick, NJ). Glycerol-free PNGase F (500,000 units/mL) was purchased from New England Labs (Ipswich, MA). EndoS2 (GlyCINATOR®), IdeS (FabRICATOR®), IgdE (FabALACTICA®), and GlySERIAS™ were

purchased from Genovis, Inc. (Cambridge, MA). D, L polyalanine (PolyA) (P9003), β-lactoglobulin (β-Lac) (L7880), bovine serum albumin (BSA) (P7656), concanavalin A (ConA) (C2010), alcohol dehydrogenase (ADH) (A7011), and dithiothreitol (DTT) were purchased from Sigma-Aldrich (St. Louis, MO). Humanized IgG1κ mAb reference material 8671 (NISTmAb) was purchased from the National Institute of Standards and Technology (NIST) (Gaithersburg, MD).

Native, unmodified Fc-IL-10 and protein standards were buffer exchanged into 200 mM ammonium acetate (pH ~7.0) using Micro Bio-Spin P-6 columns (Bio-Rad, Hercules, CA) and diluted to a final concentration ranging from 5 to 20 μM prior to IM and MS measurements. PolyA was prepared at a concentration of 1 mg/mL in a solution of acetonitrile/water/acetic acid (49%/49%/1%). For the generation of $F(ab')^2$, Fab, and Fc fragments, NISTmAb was first buffer exchanged into 150 mM sodium phosphate (pH 7.0), diluted to a working concentration of 1 mg/mL (~6.7 μM), then subsequently digested with either IdeS or IgdE (1 unit per 1 μg mAb) at 37°C overnight (16 to 18 h). Fragments were then separated and purified using Nab™ Protein A spin columns (Thermo Fisher Scientific, Waltham, MA) per the vendor's recommended protocol. Fc-IL-10 deglycosylation was achieved in its original formulation buffer with either PNGase F or EndoS2 under non-denaturing conditions overnight (16 to 18 h) at 37°C per each vendor's suggested mAb:enzyme ratios. To generate individual Fc and IL-10 domains, Fc-IL-10 was first buffer exchanged into PBS buffer (0.1 M sodium phosphate, 0.15 M sodium chloride, pH 7.2), diluted to a working concentration of 2 mg/mL (~22 μM), then digested with GlySERIAS™ (1 unit per 1 μg Fc-IL-10) at 37°C for 1 h. Deglycosylation of Fc fragments was achieved by concurrently adding EndoS2 (1 unit per 1 μg Fc-IL-10) to the GlySERIAS™ reaction. All digests were then buffer exchanged twice into 200 mM ammonium acetate using Micro Bio-Spin

P-6 columns. GlySERIAS^{TM} digests were further diluted to ~5 μM of starting Fc-IL-10 prior to MS analysis. Partial reduction of Fc fragments from GlySERIAS^{TM} digests was achieved by incubation in a solution of 0.5 mM DTT in 200 mM ammonium acetate for 1 h at room temperature. These non-denaturing conditions ensured that only interchain disulfide bonds were reduced, while intrachain disulfide bonds remained intact. No subsequent desalting steps were performed for reduced samples prior to MS analysis.

High-Resolution Native MS. Prepared intact and digested Fc-IL-10 samples (3 to 5 μL) were directly infused into a standard commercial Q Exactive Orbitrap MS with Ultra High Mass Range (QE-UHMR) platform (Thermo Fisher Scientific, San Jose, CA) via nano-electrospray ionization (nESI) in positive ion mode using gold-coated borosilicate capillaries (5 – 10 μm i.d., Harvard Apparatus, Holliston, MA) prepared in-house with a Sutter P-97 Micropipette Puller (Sutter Instrument, Novato, CA) and Quorum SC7620 Mini Sputter Coater (Quorum Technologies, Lewes, UK). Source settings were as follows: capillary voltage, 1.2 to 1.4 kV; source temperature, 250°C; S-lens RF level, 45 to 80. Nitrogen was used as the collision gas, and the trapping pressure was set between 2 and 4. Low *m/*z detector optimization and high *m/z* transfer optics were used. In-source trapping was enabled with desolvation voltages ranging from -20 and -100 V. Additional removal of non-specific salt adducts was achieved with the application of in-source collision induced dissociation (CID) that ranged from 0 to 25 V. For higher-energy collisional dissociation (HCD) of IL-10 homodimer, charge state 13^+ was first isolated in the quadrupole with an isolation window of 50 *m/z*. Dissociation of IL-10 homodimer into monomer was then achieved by applying 60 V of collision energy (CE). For partially reduced Fc samples, charge state 17^+ was isolated in the quadrupole with an isolation window of 50 *m/z* then dissociated into Fc/2 fragments with 100 V of CE. All QE-UHMR spectra were

collected with a noise threshold of 4.64, a resolution of 12,500 at *m/z* 400, AGC target of 2e5, and a maximum injection time of 200 ms. Five microscans were combined into a single scan, and between 50 and 100 scans were averaged for each spectrum. All data were then processed and deconvoluted using UniDec.[41] The NIST Mass and Fragment Calculator was utilized to calculate theoretical masses using International Union of Pure and Applied Chemistry (IUPAC) average elemental atomic masses.[42]

Native IM-MS and CIU. *Synapt G2 HDMS*. Piloting IM-MS and CIU experiments were performed on a quadrupole-ion mobility-time-of-flight mass spectrometer (Q-IM-ToF-MS) (Synapt G2 HDMS, Waters, Milford, MA). Samples (3 to 5 μL) were loaded into in-house gold coated borosilicate capillaries, and ions were generated by direct infusion using a nESI source in positive ion mode. Settings throughout the instrument were optimized to improve the desolvation and transmission of native-like protein ions prior to IM separation: capillary voltage, 1.2 to 1.4 kV; source temperature, 25°C; sample cone, 20 to 40 V; extraction cone, 0 V; trap collision voltage (CV), 5 V; and trap DC bias, 35 to 45 V. The capillary tip was positioned 5 – 10 mm from the cone orifice for all MS experiments, depending on the capillary voltage used.[43] Backing pressure was set to ~ 7 mbar for improved ion transmission for all samples. Gas flows (mL/min) were as follows: source, 50; trap, 10; helium cell, 200; and travelling wave ion mobility (TWIM) separator, 90. The trap travelling-wave ion guide was pressurized to 4.96×10^{-2} mbar of argon gas, and the TWIM separator was pressured to ~3.43 mbar of nitrogen gas. TWIM separation was achieved with a traveling wave height and velocity of 40 V and 600 m/s, respectively. The ToF-MS was operated in the 1000 to 12,000 *m/z* range in sensitivity mode at a pressure of 2.4×10^{-6} mbar. CIU experiments were performed for intact Fc-IL-10 and NISTmAb samples by subjecting ions to collisions in the travelling-wave ion trap prior to IM separation.

Here, CVs were ramped from 5 to 200 V in 5 V intervals. PolyA, BSA, and ADH ions were used as $^{TW}\Omega_{N2}$ calibrants.[44]

SELECT SERIES Cyclic IMS. IM-MS and CIU experiments for the GlySERIAS™ digests of Fc-IL-10 were performed on a quadrupole-cyclic ion mobility-time-of-flight mass spectrometer (Q-cIM-ToF-MS) (SELECT SERIES Cyclic IMS, Waters, Milford, MA) to better resolve linker length populations that remained attached to IL-10 and Fc domains. Details of this instrumentation and its operation have been described previously.[45, 46] Samples (3 to 5 μL) were loaded into in-house gold coated borosilicate capillaries, and ions were generated via nESI in positive ion mode. The quadrupole profile was set to manual and tuned to improve the transmission of IL-10 homodimer and Fc ions. As in our Synapt G2 experiments, cIM-MS settings were optimized to transmit ions without excessive activation prior to cIM separation: capillary voltage, 1.2 to 1.3 kV; source temperature, 25°C; sample cone, 0 V; source offset, 0 V; trap CV, 5 V; and post-trap bias, 35 V. These soft ionization parameters were essential to prevent significant activation of IL-10 homodimer. Gas flows (mL/min) were as follows: ion guide, 35; trap, 7; helium cell, 150; and cIM separator, 45. The backing pressure was 2.53 mbar. The trap travelling-wave ion guide was pressured to 3.95 x 10^{-2} mbar of nitrogen gas. The cIM separator was pressured to ~1.76 mbar with nitrogen gas, and cIM separation was achieved using a single pass with a wave height and velocity of 30 V and 375 m/s, respectively. A full list of settings for the multi-function array region is given in Appendix Table D-1. The ToF-MS was operated in the 50 to 8,000 *m/z* range in V-mode at a pressure of 4.9 x 10^{-7} mbar. CIU experiments were performed by ramping the CVs in the trap region from 4 to 160 V in 4 V intervals prior to cIM separation. PolyA and BSA ions were used as $^{TW}\Omega_{N2}$ calibrants.[44]

Data Processing and Analysis. IM and MS spectra were viewed using Driftscope v3.0 and Masslynx v4.2 software, respectively (Waters, Milford, MA). Mass spectra were deconvoluted using UniDec.[41] Arrival time distributions (ATDs) were extracted and converted to $^{TW}\Omega_{N2}$ using a modified version of CIUSuite 2 (v2.3),[47] which encodes both TWIMExtract[48] and IMSCal[44] for semi-automated drift time extractions and $^{TW}\Omega_{N2}$ calibrations, respectively. When comparing the relative stabilities of Fc and IL-10 homodimer subunits generated using GlySERIAS^{TM}, we need to account for the higher energy collisions experienced by higher charge states. Therefore, we converted the CV axes of applicable CIU files to laboratory frame energies (E_{lab}) as previously described.[49] All data were then further processed using the modified CIUSuite 2 software discussed above. CIU fingerprints were subjected to 2-D smoothing using a Savitzky-Golay function with a smoothing window of 5 and 2 smoothing iterations. The CV axis was interpolated with a scaling factor of 4 for Fc CIU data, while no interpolation was performed for intact Fc-IL-10 and IL-10 homodimer CIU data. Standard feature detection was performed using a minimum feature length of 2 steps and an allowed width of 1 to 1.5 nm^2 in $^{TW}\Omega_{N2}$ axis units. CIU_{50} values were then computed using max centroiding mode with a transition padding of 15 V and a maximum CV gap length of 0. Root-mean-square-deviation (RMSD) analysis was performed using the compare function within CIUSuite 2, and RMSD factor differences, where applicable, were calculated as previously described.[50] All CIU fingerprints shown are the average of three technical replicates with baseline RMSDs of < 5%. We define a technical replicate as a repeated measurement using the same sample and/or capillary taken on the same day of an experiment. $^{TW}\Omega_{N2}$ distributions of IM-MS data, where applicable, were fitted with a gaussian function using Fityk curve fitting software.[51] Data visualization and statistical analyses of IM-MS and CIU quantitative data were performed using GraphPad Prism (San Diego, CA). For

statistical analyses, we specifically used a one-way ordinary ANOVA with Tukey correction for multiple comparisons to analyze differences between three or more experimental datasets using an alpha value of 0.05. When comparing only two datasets, we performed a simple t-test using an alpha value of 0.05. All error bars correspond to the standard deviation of three technical replicates unless otherwise stated.

4.6 Results and Discussion

Native IM-MS and CIU Probe the Structural Dynamics of Fc-IL-10 in the Gas-Phase. IL-10 is a potent immunoregulatory cytokine that plays a critical role in modulating inflammatory responses and preserving cell homeostasis.[52, 53] Structurally, its biologically active form is a domain-swapped, noncovalent 37 kDa homodimer made of two intertwining monomers, each consisting of six α-helices (A-F) stabilized by two intrachain disulfide bonds.[54, 55] The domain-swapped dimeric nature of IL-10, which involves helices E and F from one monomer penetrating into the hydrophobic cleft of helices A-D of the other monomer, is pivotal for proper receptor binding.[56] However, IL-10 homodimer is known to be unstable owing to its short half-life and facile degradation *in vivo*, limiting its clinical applications.[57, 58] The Fc-IL-10 fusion protein in this work addresses this limitation by extending the half-life of IL-10 through FcRn-mediated recycling from endosomes. Importantly, the use of a flexible Gly-Ser linker permits the spatial mobility of IL-10 monomeric units, increasing their likelihood to interact and form the biologically active homodimer (Appendix Figure D-1). Within this scope, characterizing the HOS of Fc-IL-10 with current measurement technologies remains a major challenge, as its unique engineering complicates its structure and dynamics. Although there is no full-length Fc-IL-10 structure derived from X-ray crystallography, NMR, or Cryo-EM, we successfully leverage IM-MS and CIU to rapidly extract structural information of Fc-IL-10 by

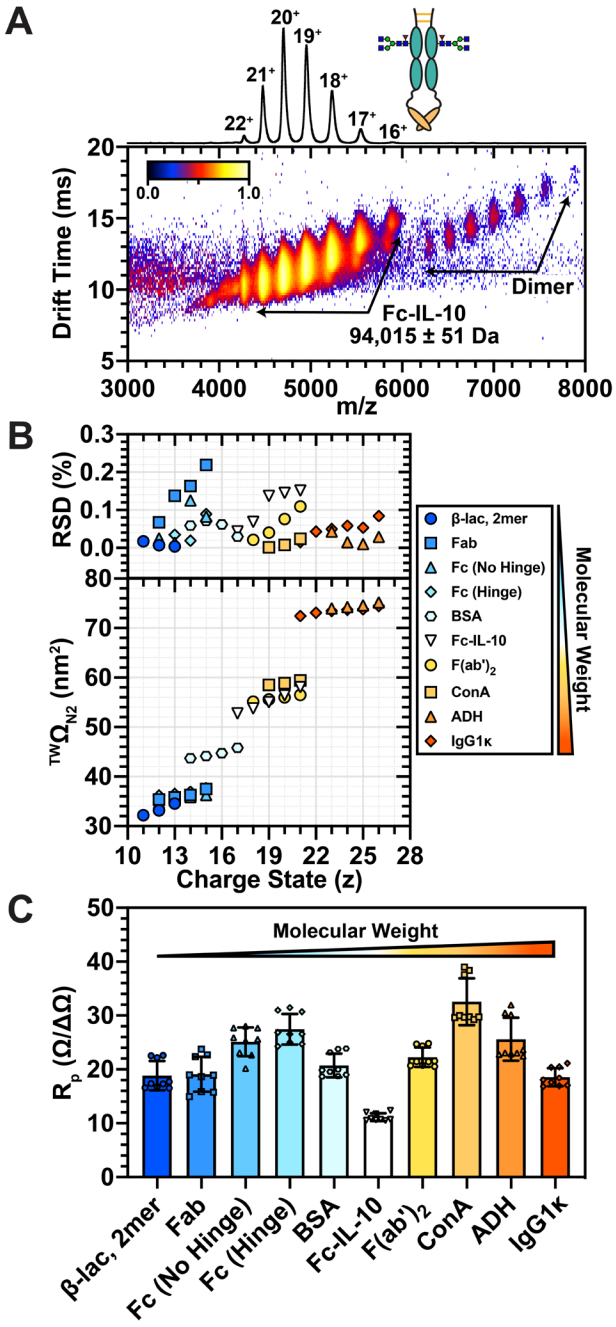

Figure 4-1: Native IM-MS measurements of Fc-IL-10 and a series of protein standards on a Waters Synapt G2 HDMS IM-MS platform. (A) Representative IM-MS spectrum of Fc-IL-10 reveals a narrow charge state distribution ranging from 16^+ to 22^+. (B). $^{TW}\Omega_{N2}$ values for native Fc-IL-10 and protein standards as a function of charge state. Corresponding RSDs (< 0.3%) are shown for technical replicates (n = 3). (C) Rp (Ω/ΔΩ) of Fc-IL-10 and protein standards. IM Rp values extracted from the three most prominent charge states observed for each protein in triplicate (n = 9).

monitoring its conformational ensemble and stability in the gas-phase. We first generated Fc-IL-10 ions via nESI under conditions that typically preserve compact, native-like ions that closely resemble the structural states in solution.[30, 43] Under these conditions, Fc-IL-10 adopted a narrow charge state distribution (16^+ to 22^+), allowing us to measure an intact molecular weight (MW) of ~94 kDa (Figure 4-1A). We also observed noncovalent dimeric Fc-IL-10 aggregates that are likely representative of those found in solution.[59, 60] Our measurements indicate that these dimers are present in low abundance (1.79 ± 0.08% of total monomer and dimer signal), and are likely dependent upon the solution conditions used to prepare our Fc-IL-10 samples prior to native IM-MS measurements.[61]

To benchmark our native IM-MS measurements of Fc-IL-10, we compared its $^{TW}\Omega_{N2}$ values to those obtained for a series of native protein standards ranging from 36 to 150 kDa in molecular mass (Figure 4-1B). The

average relative standard error (RSD) for technical replicates of these measurements was 0.06 ± 0.05%, and comparisons to reported $^{TW}\Omega_{N2}$ literature values (excluding NISTmAb fragments) yielded an average difference of -0.28 ± 1.68% (abs. Avg diff. of 1.28 ± 1.13%) (Appendix Figure D-2 and Appendix Table D-2). For Fc-IL-10, we observed an average $^{TW}\Omega_{N2}$ of 55.2 ± 2.0 nm^2 across all charge states, which is similar to the $^{TW}\Omega_{N2}$ values obtained for proteins of similar MW ($F(ab')_2$, ~98 kDa and ConA tetramer, ~103 kDa) as observed previously.[30] However, when we considered the IM resolving power (R_p) of our $^{TW}\Omega_{N2}$ distributions, we noticed drastic differences between Fc-IL-10 and other proteins (Figure 4-1C). Here, we define R_p as the centroid $^{TW}\Omega_{N2}$ of our IM distributions divided by their full width at half maximum (FWHM), $R_p = \Omega/\Delta\Omega$. We found that the average R_p for the three most abundant charge states of Fc-IL-10 (19^+ to 21^+) was approximately 50% and 66% less than that of $F(ab')_2$ and ConA tetramer, respectively. These differences, which result from the wider $^{TW}\Omega_{N2}$ distributions of Fc-IL-10 (Appendix Figure D-3), suggest that Fc-IL-10 is likely trapped in a wider array of solution conformations during nESI than the equivalently sized proteins measured in our survey. Interestingly, the R_p of Fc-IL-10 is also lower than that of NISTmAb (IgG1κ), differing by approximately 40%. Previous studies have shown that mAbs are inherently more flexible and dynamic than comparably sized protein complexes in terms of MW.[62, 63] Our results are consistent with these previously reported observations, as NISTmAb adopts a wider range of conformations than ADH, which is similar in MW (~148 kDa) and $^{TW}\Omega_{N2}$. We propose that the Gly-Ser linker, combined with the HOSs of individual Fc and IL-10 domains, significantly contribute to the overall flexibility of Fc-IL-10 compared to NISTmAb, as evidenced by its lower IM R_P and wider $^{TW}\Omega_{N2}$ distributions.

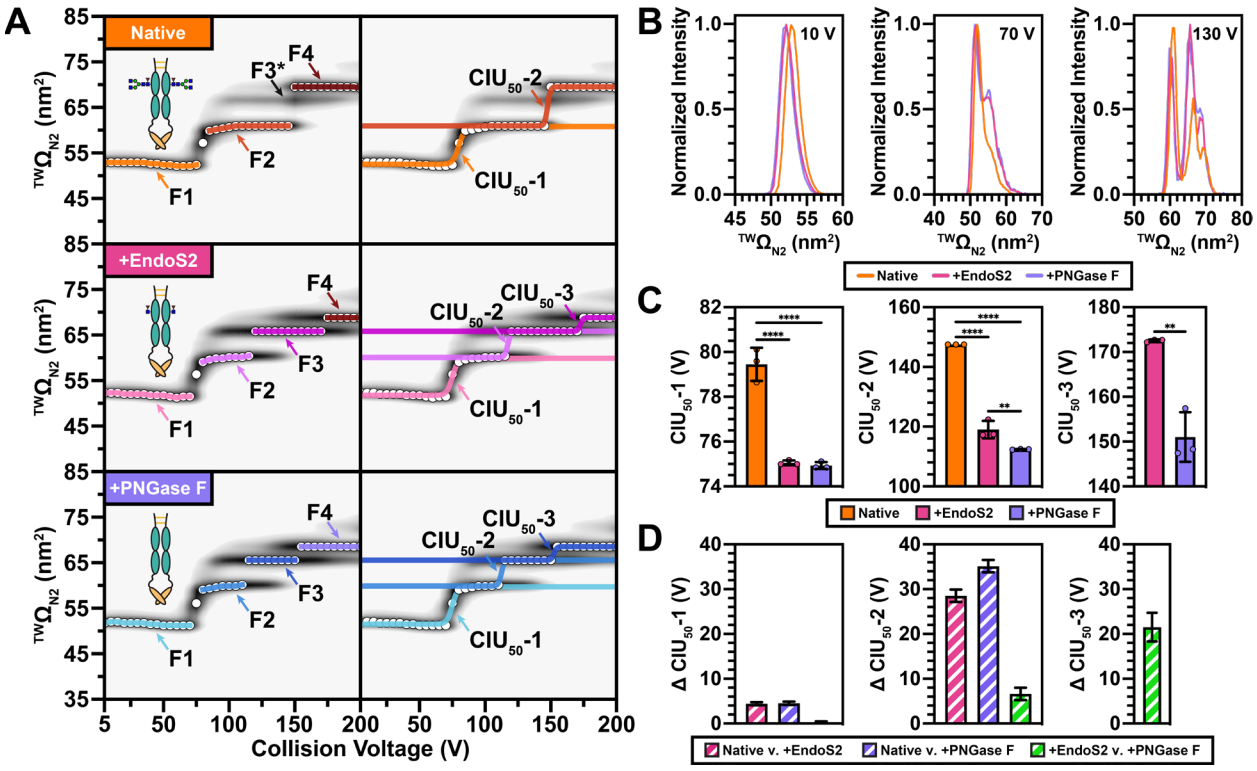

Figure 4-2: CIU experiments of Fc-IL-10 before and after treatment with EndoS2 or PNGase F. (A) CIU fingerprints for charge state 17^+. Features are detected by CIUSuite 2 (v2.3) (left) and subsequently utilized for CIU_{50} stability quantitation (right). Feature three (F3*) in native Fc-IL-10 is labeled but omitted during the fitting of CIU_{50} data. (B) $^{TW}\Omega_{N2}$ distributions of native and deglycosylated Fc-IL-10 at different trap collision voltages. More extended conformations increase in intensity with sequential removal of sugar moieties. (C) CIU_{50} analyses ($n = 3$) of each transition reveal significant destabilization of Fc-IL-10 after deglycosylation (**p < 0.01, **** < 0.0001). (D) Plots of mean differences in CIU_{50} values. Error bars of these mean differences are given in SEM obtained using a one-way ordinary ANOVA with Tukey correction for multiple comparisons within GraphPad Prism.

To further probe the conformational dynamics of Fc-IL-10, we performed CIU on charge states 17^+ to 21^+ (Appendix Figure D-4). Compared to previously reported CIU data acquired for ConA tetramer[64, 65] and F(ab')$_2$ fragment ions,[66, 67] which collectively only adopt up to four features during CIU, our CIU data for Fc-IL-10 qualitatively reveal three to six prominent features, further indicating the increased level of dynamism in Fc-IL-10 when compared to model proteins of similar MW. The ultimate number of CIU transitions we observe Fc-IL-10 is also higher than that of NISTmAb (Appendix Figure D-5), further underscoring the relatively diverse structural ensemble adopted by Fc-IL-10. Previous studies have established a strong,

positive correlation between the number of domains within a protein structure and the number of CIU transitions observed.[68, 69] Given this correlation, it is likely that Fc-IL-10 supersedes such a trend and produces sub-domain correlated unfolding in many of our CIU datasets.

Deglycosylation and Domain-Level Approaches Assist in the Annotation of Fc-IL-10 CIU Pathways. To establish a mechanistic understanding of Fc-IL-10 CIU, we designed a series of experiments aimed at evaluating its domain-level stabilities and assigning protein domains or regions to specific CIU transitions. First, we enzymatically removed the *N*-glycans attached within the C_H2 regions of the Fc domain of Fc-IL-10, as these regions have been shown to become destabilized after *N*-glycan removal.[70-73] Deglycosylation was achieved using either EndoS2, which leaves the core *N*-acetylglucosamine (GlcNAc) intact, or PNGase F, which completely hydrolyzes all *N*- glycans and deamidates the asparagine residue to produce aspartic acid. To monitor the progress of our deglycosylation reactions, we performed native orbitrap MS measurements to resolve individual glycoforms of Fc-IL-10 before and after the addition of each respective endoglycosidase (Appendix Figure D-6 and Appendix Table D-3). Our results for fully glycosylated Fc-IL-10 demonstrate the presence of various expected glycoforms (G0F, G1F, and G2F) that are commonly located in the Fc portion of therapeutic antibodies, as well as a small amount of afucosylated sugar structures (Appendix Figure D-6A).[74] Upon EndoS2 treatment, we successfully achieved the hydrolysis of the glycan structures after the core GlcNAc with or without the core fucose (Fuc) (Appendix Figure D-6B). Incubation with PNGase F, on the other hand, efficiently removed all *N*-glycans (Appendix Figure D-6C).

We proceeded with CIU experiments of Fc-IL-10 before and after endoglycosidase treatment. In general, we observe that lower charge states generate CIU transitions that strongly correlate with domain-specific unfolding. [68, 69] In contrast, higher charge states experience

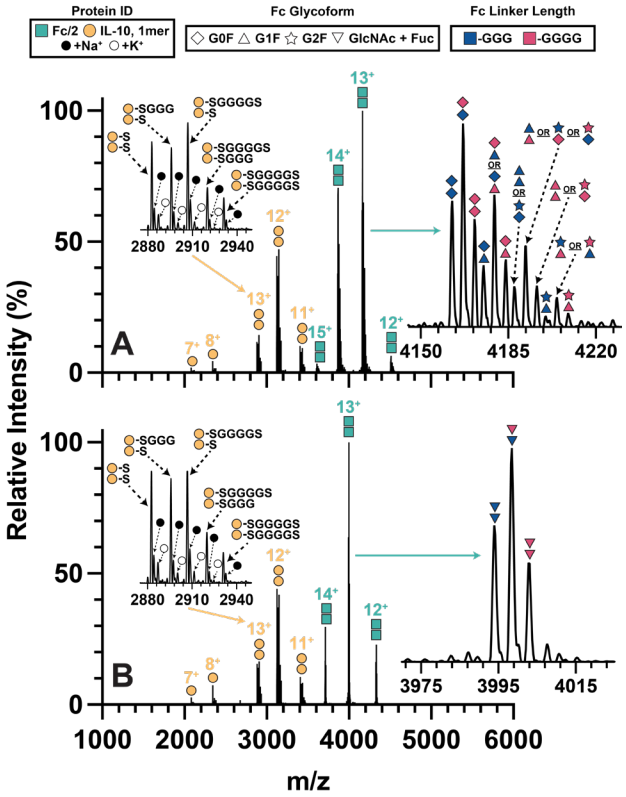

Figure 4-3: Representative MS spectra of Fc-IL-10 digested with GlySERIAS™ with or without EndoS2. Zoomed-in spectra of non-reduced Fc subunits show different glycoforms and linker variants (A) before and (B) after treatment with EndoS2. Zoomed-in spectra of IL-10 homodimer show comparable linker variants across both sample prep conditions.

increased Coulombic strain in the gas-phase, leading to more unfolding transitions upon collisional heating.[75] As such, we chose to focus on charge state 17^+ due to its relatively compact low-energy structure, more pronounced extended conformations, and easily quantifiable CIU_{50} transitions (Figure 4-2A). CIU fingerprints for native and deglycosylated Fc-IL-10 show the presence of three or four prominent conformational intermediates corresponding to two or three unfolding events, respectively. We detect a minor CIU feature with a $^{TW}\Omega_{N2}$ of ~66.5 nm^2 for the native, fully glycosylated Fc-IL-10. However, given the relatively low intensity of this feature, we have focused on the more intense feature with a $^{TW}\Omega_{N2}$ of ~69.5 nm^2 (feature four). We notice the greatest differences in the $^{TW}\Omega_{N2}$ distributions of native and deglycosylated Fc-IL-10 at higher trap collision voltages, where more extended conformations increase in intensity upon glycan removal (Figure 4-2B). We also observe prominent shifts in CIU_{50}-2 and CIU_{50}-3 values upon deglycosylation, suggesting a connection between these stability values and the Fc region of the fusion protein. This trend was general across the other Fc-IL-10 charge states detected (Appendix Figure D-7). A quantitative analysis of CIU_{50} values further supports these qualitative observations for 17^+ ions, where CIU_{50}-1 values of EndoS2 (75.05 ± 0.10 V)

and PNGase F (74.93 ± 0.16 V) treated samples were less than those of native Fc-IL-10 (79.45 ± 0.74 V) (Figure 4-2C). When we compare the CIU_{50}-1 stabilities between EndoS2 and PNGase F treated samples, however, we see no statistically significant changes in the CIU_{50}-1 values recorded, indicating that the PNGase F-driven removal of core GlcNAc and Fuc residues, which are conserved with EndoS2, do not induce stability shifts associated with this CIU transition. Conversely, removal of these core sugars greatly destabilizes the structures adopted by Fc-IL-10 at higher collision energies. We measure significant shifts in CIU_{50}-2 values that decrease with the successive removal of *N*-glycans (Native, 147.50 ± 0.01 V; EndoS2, 119.00 ± 2.93 V; PNGase F, 112.40 ± 0.10 V). The features that define CIU_{50}-3 exclusively appear in deglycosylated samples, where comparable decreases in stability are observed after the removal of core GlcNAc and Fuc sugars using PNGase F. By plotting the mean differences in CIU_{50} values recorded across all transitions observed in our dataset (Figure 4-2D), we are able to achieve a clearer annotation of our Fc-IL-10 CIU data. In brief, we quantify the greatest shifts in CIU_{50} values at higher-energy transitions, where CIU_{50}-2 and CIU_{50}-3 values shift by ~35% and ~21% after complete *N*-glycan removal, respectively. CIU_{50}-1 values, on the other hand, only shift by ~5%. Taken together, these results permit us to confidently assign CIU_{50}-2 and CIU_{50}-3 transitions for Fc-IL-10 as related to the unfolding of the Fc.

We continued our efforts to annotate Fc-IL-10 CIU transitions by enzymatically digesting the fusion protein into Fc and IL-10 fragments using GlySERIAS™, a unique enzyme that specifically cleaves flexible linkers rich in Gly and Ser residues. Analysis of these digests by native orbitrap MS showed that the enzymatic reaction liberates the IL-10 homodimer from the Fc (Figure 4-3). The Gly-Ser linker in this work contains many potential cleavage sites for GlySERIAS™, which generated several variants of Fc and IL-10 with different numbers of Gly

and Ser residues attached. Specifically, we observed IL-10 homodimers in five main variant forms, where each monomer possessed one of three main linker tails: S, SG_3, or SG_4S. These assignments were confirmed by dissociating IL-10 homodimer ions to monomers using HCD, where we are able to confidently detect each monomeric variant with S, SG_3, or SG_4S linker tails (Appendix Figure D-8). The native MS data collected reveals primarily homodimer signals, as expected for IL-10.[54] We also observed linker polydispersity following GlySERIAS^{TM} treatment within the Fc subunit, but the presence of different glycoforms complicated GS linker identification (Figure 4-3A). To reduce sample complexity, Fc glycans were removed using EndoS2, permitting us to detect two main linker tails: G_3 and G_4 (Figure 4-3B). These findings assisted us in assigning our mass spectra for fully glycosylated Fc, where we identified similar linker variants to those observed after EndoS2 treatment. To confirm our assignment of GS linker variants attached to the Fc subunit, we subjected partially reduced Fc, where only hinge disulfide bonds were reduced, to HCD (Appendix Figure D-9). Upon dissociation, we were successfully able to detect Fc/2 ions attached to both G_3 and G_4 linker tails, which matched our native MS results for non-reduced Fc fragments. Deconvoluted masses of all species detected during these experiments are summarized in Appendix Table D-4. We attribute the differences between theoretical and experimental masses observed to insufficient removal of PBS buffer salts used for GlySERIAS^{TM} digestion, as both sodium and potassium adducts are evident in our native MS spectra.

Next, we leveraged the higher ToF MS resolution of the SELECT SERIES Q-cIM-ToF-MS platform to better resolve the Fc and IL-10 linker variants detected in our orbitrap native MS data. Despite lower baseline resolution, cIM-MS analysis generates comparable MS spectra, where we are able to delineate all linker variants for both Fc and IL-10 subunits (Figure 4-4A

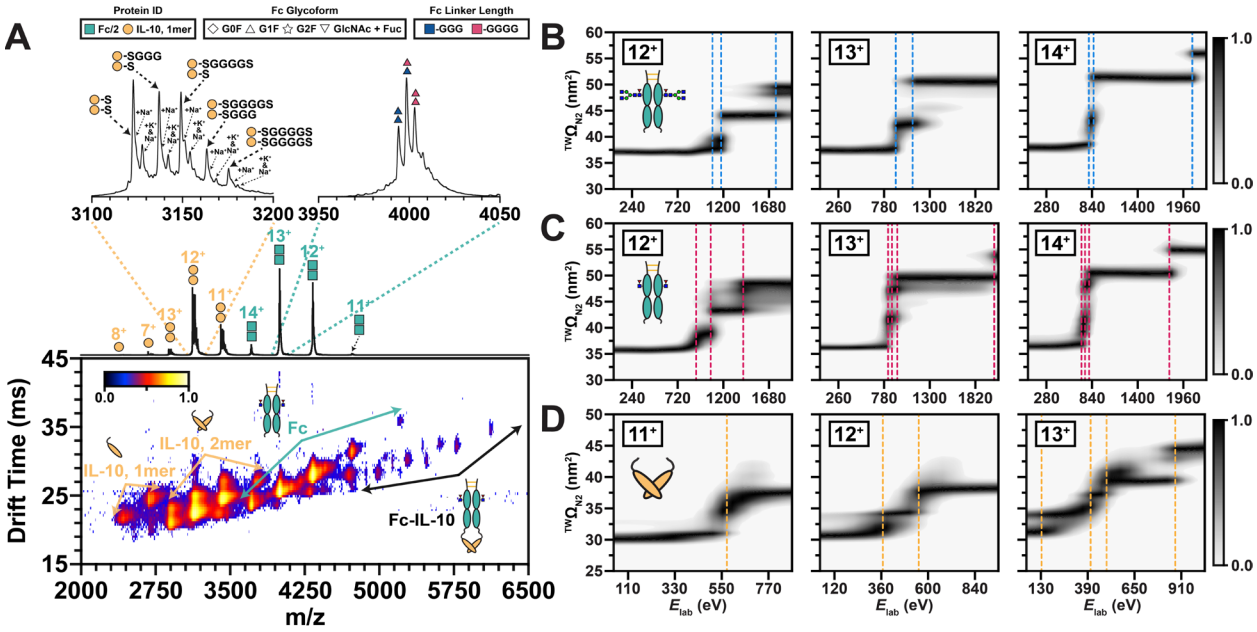

Figure 4-4: IM-MS and CIU measurements of Fc-IL-10 GlySERIAS digests on a Waters SELECT SERIES cIM-MS platform. (A) Representative cIM-MS spectrum of Fc-IL-10 digested with GlySERIAS^{TM} and EndoS2 at 5 V of trap CE. Zoomed-in spectra show the linker and glycoform polydispersity present in non-reduced Fc and IL-10 homodimer subunits. CIU fingerprints of (B) native Fc, (C) deglycosylated Fc, and (D) IL-10 homodimer subunits. Dashed blue, red, and yellow lines correspond to CIU transitions for native Fc, deglycosylated Fc, and IL-10 homodimer, respectively.

and Appendix Figure D-10). Collectively, the $^{TW}\Omega_{N2}$ distributions of IL-10 homodimer revealed at least two conformational families, while cIM-MS detects only one IM feature for Fc, including for samples subjected to deglycosylation with EndoS2 (Appendix Figure D-11). These differences in $^{TW}\Omega_{N2}$ distributions underscore that the IL-10 homodimer exhibits a conformational ensemble of greater polydispersity when compared to the Fc. These results, in part, suggest that the conformational ensemble of the IL-10 homodimer strongly contributes to the structural polydispersity of native, intact Fc-IL-10. Interestingly, the relative intensity of the most extended conformer for IL-10 homodimer increases as we approach higher charge states. This trend is likely the result of the higher local Coulombic strain experienced by the protein ions occupying higher charge states, leading to partial unfolding even under gentle conditions. However, the inter-domain connection between helices D and E of IL-10 has been shown to be

potentially flexible.[54] Therefore, the existence of two conformers of IL-10 homodimer in our IM data could be the direct result of this inherent flexibility. The flexibility of IL-10 homodimer is further reflected in our CIU data, where IL-10 ions readily unfold at considerably lower E_{lab} values (< 700 eV) when compared with Fc subunit ions (Figure 4-4B-D). Interestingly, we observe a bimodal distribution of unfolded intermediates for IL-10 homodimer ions just below 650 eV. We suspect that the IL-10 homodimer precursors shown in Figure S11 undergo unique CIU pathways that lead to different unfolded intermediates that vary across charge states, and a portion of these intermediates readily dissociate into IL-10 monomer. Regarding Fc subunits, we observe shifts in gas-phase stability after glycan removal with EndoS2 across all CIU_{50} transitions as expected. Despite these shifts in stability, a quantitative analysis of the first transition (CIU_{50}-1) reveals that IL-10 homodimer initially unfolds at significantly lower E_{lab} values (Av. 372.52 ± 168.25 eV) than Fc domains (Native, Av. 942.56 ± 156.03; EndoS2 treated, Av. 815.99 ± 82.05 eV) when accounting for data acquired across all charge states (Appendix Figure D-12). Collectively, these results indicate that lower energy CIU transitions observed in intact Fc-IL-10 ions are most likely related to unfolding within the IL-10 homodimer upon collisional heating.

Flexible Linkers of Different Lengths Induce Subtle Changes in IL-10 Homodimer CIU. Flexible Gly-Ser linkers have been shown to improve the folding and stability of fusion proteins.[21] To probe local changes in Fc-IL-10 subunit stability as a function of linker length, we extracted the $^{TW}\Omega_{N2}$ distributions generated during CIU for each Fc and IL-10 homodimer linker variant observed in our cIM-MS spectra by utilizing a narrower *m/z* extraction window within TWIMExtract. Using the cIM-MS platform was crucial for this analysis, as linker variants could not be sufficiently resolved on our linear TWIM platform. Here, we only conducted our analysis

targeting Fc subunits that had been deglycosylated with EndoS2, as native Fc subunits yielded poorly resolved linker variant populations on our cIM-MS platform. Importantly, we saw no changes in Fc subunit stability as the length of the linker tail increased. In contrast, we noticed significant differences in global IL-10 homodimer HOS and stability as the length of the GS linker tail on each IL-10 monomer increased (Figure 4-5). We performed our analyses on 11^+ IL-10 homodimer ions due to their more compact structure compared to higher charge states observed and to avoid overlap with IL-10 monomer ions (Appendix Figure D-11).

When comparing the CIU fingerprints for two of the linker variants detected, we observed a transitional CIU feature (Figure 4-5A) that is irreproducible across different fingerprints recorded for linker variants. As such, we have implemented a feature-skipping approach to enable the robust and reproduceable assessment of CIU_{50} values

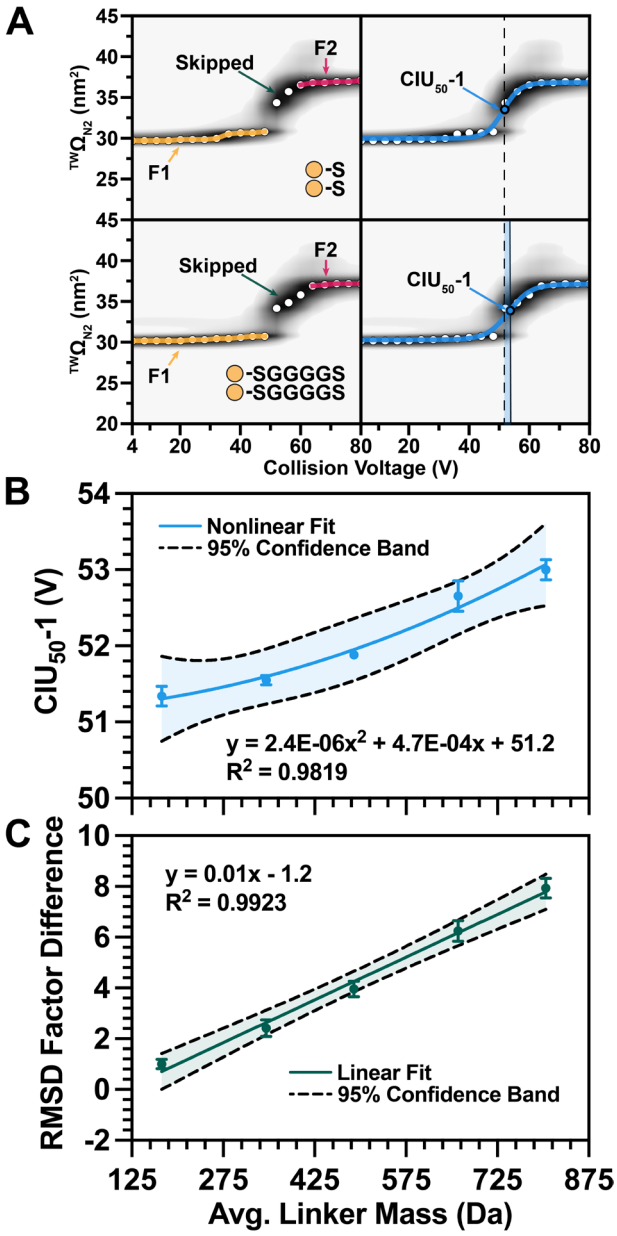

Figure 4-5: CIU of different Gly-Ser linker variants of IL-10 homodimer. (A) Representative CIU fingerprints of charge state 11^+ demonstrating the transitional state omitted using the feature skipping function deployed within our version of CIUSuite 2 (v2.3). Subsequent CIU_{50}-1 sigmoidal curve fitting reveals subtle shifts in stability between linker variants. (B) Plot of CIU_{50}-1 as a function of average linker mass. Averaged CIU_{50}-1 values (n = 3) were fitted with a quadratic function. (C) Plot of RMSD Factor Difference as a function of average linker mass. Averaged factor differences (n = 3) were fitted with a linear function. 95% confidence intervals (dashed lines) are displayed.

available in the remainder of the CIU datasets acquired.[76] By implementing this procedure, we detect shifts in CIU_{50}-1 values across linker variants, where an increase in linker length produces a stabilization in IL-10 dimers. By plotting CIU_{50}-1 values as a function of average linker mass, which encompasses all Gly and Ser residues on both IL-10 monomers, we are able to discern a strong, positive quadratic relationship ($R^2 = 0.9819$) between CIU_{50}-1 values and linker mass (Figure 4-5B). This trend is most likely related to cooperative interactions between linkers of increased length in a manner that increases overall dimer stability and induces changes in IL-10 dimer HOS, in addition to the larger number of degrees of freedom available to IL-10 dimers bearing longer remaining linker sequences. To build upon these observations, we executed a series of pairwise RMSD analyses between the CIU fingerprints recorded for each linker variant as a way to quantify global conformational differences in IL-10 dimers as a function of attached linker length (Figure 4-5C and Appendix Figure D-13). The RMSD factor differences shown here were calculated by dividing the RMSD values of each replicate by the average RMSD baseline obtained for technical replicates of IL-10 homodimer variants that contained one Ser residue on each monomer. Overall, we obtain a strong positive linear relationship ($R^2 = 0.9923$) when plotting RMSD factor differences as a function of average linker mass. We attribute these observed RMSD factor differences to the same factors as discussed above in our CIU_{50}-1 data. Although these trends in stability represent global shifts in IL-10 dimer HOS and stability as a product of an incomplete enzymatic digestion of GS linkers within the intact Fc-IL-10 construct, we are able to reproduce them with other GlySERIAS^{TM} digests performed using similar reaction conditions (Appendix Figure D-14). We interpret the small differences in CIU_{50}-1 values recorded between datasets as resulting from different levels of desolvation experienced by ions prior to cIM-MS and CIU analysis. To the best of our knowledge, these studies constitute the

first time that the effects of flexible linker lengths on biotherapeutic stability have been probed at the level of molecular specificity enabled by MS.

4.7 Conclusions

In this report, we describe a series of IM-MS and CIU measurements that, for the first time, thoroughly probe the HOS and stability of a model Fc-IL-10 fusion protein engineered using flexible Gly-Ser linkers. We find that Fc-IL-10 is substantially more flexible and conformationally dynamic when compared to a series of protein standards and IgG fragments. This high degree of flexibility is partly due to the increased mobility induced by flexible Gly-Ser linkers as well as the conformational polydispersity of IL-10 dimers. The intricate HOS of Fc-IL-10 is further probed using CIU, where we observe a broad range of features that result from structural changes within Fc and IL-10 subunits upon collisional activation. By using a combination of approaches that alter glycosylation patterns and isolate individual Fc and IL-10 domains, we are able to assign lower- and higher-energy CIU transitions of Fc-IL-10 to the unfolding of the IL-10 homodimer and Fc regions of the fusion protein, respectively.

Importantly, we extend the capabilities of IM-MS and CIU to probe the local effects of Gly-Ser linkers on the HOS and stability of IL-10 homodimer, which is the biologically active form of IL-10. Our results reveal a strong positive, quadratic relationship between average linker mass and gas-phase stability, revealing that Gly-Ser linkers cooperatively impact IL-10 homodimer HOS and stability. However, we acknowledge that the CIU_{50} values shown in Figure 4-5 and Appendix Figure D-14 for IL-10 homodimer might have a higher degree of uncertainty than the errors reported. In this case, performing these experiments across different days and capillaries would be beneficial. Taken together, our results further validate the usefulness of IM-MS and CIU in performing fast, information-rich HOS measurements within the

biopharmaceutical pipeline. Ongoing efforts in our group are leveraging the multi-pass and mobility selection functionalities of the cIM platform to gain further insights into the structural polydispersity of Fc-IL-10. Leveraging IM-selected-CIU (IM-CIU), for example, would provide further insights regarding the CIU pathways of different IL-10 homodimer ion precursors. Future efforts in our research group aim to extend these technologies to the characterization of other Fc-fusion protein formats, including those engineered with rigid and cleavable linkers, as well as establish connections between gas-phase and solution-phase unfolding pathways. Finally, we anticipate developing computational approaches to better interpret and predict the CIU pathways of this diverse class of protein therapeutics. Overall, we envision that the workflows demonstrated here will further enable the characterization of novel Fc-fusion proteins and promote the optimization of engineering methods for improved biomolecular stability and efficacy.

4.8 References

[1] Hoffman, H. M.; Yasothan, U.; Kirkpatrick, P. Rilonacept. *Nat. Rev. Drug. Discov.* **2008**, *7* (5), 385-386. DOI: 10.1038/nrd2579.

[2] Fenaux, P.; et al. Luspatercept in Patients with Lower-Risk Myelodysplastic Syndromes. *N. Eng. J. Med.* **2020**, *382* (2), 140-151. DOI: 10.1056/nejmoa1908892.

[3] De Oliveira Dias, J. R.; De Andrade, G. C.; Novais, E. A.; Farah, M. E.; Rodrigues, E. B. Fusion proteins for treatment of retinal diseases: aflibercept, ziv-aflibercept, and conbercept. *Int. J. Retina Vitreous* **2016**, *2* (1). DOI: 10.1186/s40942-016-0026-y.

[4] Czajkowsky, D. M.; Hu, J.; Shao, Z.; Pleass, R. J. Fc-fusion proteins: new developments and future perspectives. *EMBO Mol. Med.* **2012**, *4* (10), 1015-1028. DOI: 10.1002/emmm.201201379.

[5] Ebrahimi, S. B.; Samanta, D. Engineering protein-based therapeutics through structural and chemical design. *Nat. Commun.* **2023**, *14* (1). DOI: 10.1038/s41467-023-38039-x.

[6] Scheen, A. J. Dulaglutide for the treatment of type 2 diabetes. *Expert Opin. Biol. Ther.* **2017**, *17* (4), 485-496. DOI: 10.1080/14712598.2017.1296131.

[7] Bussel, J. B.; et al. A Review of Romiplostim Mechanism of Action and Clinical Applicability. *Drug Des. Devel. Ther.* **2021**, *15*, 2243–2268. DOI: 10.2147/DDDT.S299591.

[8] De La Croix Ndong, J.; et al. Asfotase-α improves bone growth, mineralization and strength in mouse models of neurofibromatosis type-1. *Nat. Med.* **2014**, *20* (8), 904-910. DOI: 10.1038/nm.3583.
[9] Frampton, J. E. Efmoroctocog Alfa: A Review in Haemophilia A. *Drugs* **2021**, *81* (17), 2035-2046. DOI: 10.1007/s40265-021-01615-w.
[10] Goffe, B.; Cather, J. C. Ethanercept: An overview. *J. Am. Acad. Dermatol.* **2003**, *49* (2), 105-111. DOI: 10.1016/mjd.2003.554.
[11] Wekerle, T.; Grinyó, J. M. Belatacept: from rational design to clinical application. *Transpl. Int.* **2012**, *25* (2), 139-150. DOI: 10.1111/j.1432-2277.2011.01386.x.
[12] Pyzik, M.; Kozicky, L. K.; Gandhi, A. K.; Blumberg, R. S. The therapeutic age of the neonatal Fc receptor. *Nat. Rev. Immunol.* **2023**, *23* (7), 415-432. DOI: 10.1038/s41577-022-00821-1.
[13] Rath, T.; et al. Fc-fusion proteins and FcRn: structural insights for longer-lasting and more effective therapeutics. *Crit. Rev. Biotechnol.* **2015**, *35* (2), 235-254. DOI: 10.3109/07388551.2013.834293.
[14] Zhang J, C. J., Siu S, O'Neill JW, Gates AH, Delaney J, Mehlin C. Fusion Partners as a Tool for the Expression of Difficult Proteins in Mammalian Cells. *Curr. Pharm. Biotechnol.* **2010**, *11* (3), 241 - 245. DOI: 10.2174/138920110791111898.
[15] Carter, P. J. Introduction to current and future protein therapeutics: a protein engineering perspective. *Exp. Cell. Res.* **2011**, *317* (9), 1261-1269. DOI: 10.1016/j.yexcr.2011.02.013.
[16] Duivelshof, B. L.; et al. Therapeutic Fc-fusion proteins: Current analytical strategies. *J. Sep. Sci.* **2021**, *44* (1), 35-62. DOI: 10.1002/jssc.202000765.
[17] Wu, B.; Sun, Y. N. Pharmacokinetics of Peptide-Fc fusion proteins. *J. Pharm. Sci.* **2014**, *103* (1), 53-64. DOI: 10.1002/jps.23783.
[18] Zhang, J.; Yun, J.; Shang, Z.; Zhang, X.; Pan, B. Design and optimization of a linker for fusion protein construction. *Pro. Nat. Sci.* **2009**, *19* (10), 1197-1200. DOI: 10.1016/j.pnsc.2008.12.007.
[19] Argos, P. An Investigation of Oligopeptides Linking Domains in Protein Tertiary Structures and Possible Candidates for General Gene Fusion. *J. Mol. Biol.* **1990**, *211* (4), 943-958.
[20] Van Rosmalen, M.; Krom, M.; Merkx, M. Tuning the Flexibility of Glycine-Serine Linkers To Allow Rational Design of Multidomain Proteins. *Biochemistry* **2017**, *56* (50), 6565-6574. DOI: 10.1021/acs.biochem.7b00902.
[21] Chen, X.; Zaro, J. L.; Shen, W.-C. Fusion protein linkers: Property, design and functionality. *Adv. Drug Deliv. Rev.* **2013**, *65* (10), 1357-1369. DOI: 10.1016/j.addr.2012.09.039.
[22] Wriggers, W.; Chakravarty, S.; Jennings, P. A. Control of protein functional dynamics by peptide linkers. *Peptide Sci.* **2005**, *80* (6), 736-746. DOI: 10.1002/bip.20291.
[23] Liu, L. Antibody glycosylation and its impact on the pharmacokinetics and pharmacodynamics of monoclonal antibodies and Fc-fusion proteins. *J. Pharm. Sci.* **2015**, *104* (6), 1866-1884. DOI: 10.1002/jps.24444.
[24] Mimura, Y.; et al. Glycosylation engineering of therapeutic IgG antibodies: challenges for the safety, functionality and efficacy. *Protein & Cell* **2018**, *9* (1), 47-62. DOI: 10.1007/s13238-017-0433-3.

[25] Wang, W.; et al. Impact of methionine oxidation in human IgG1 Fc on serum half-life of monoclonal antibodies. *Mol. Immunol.* **2011**, *48* (6-7), 860-866. DOI: 10.1016/j.molimm.2010.12.009.
[26] Strand, J.; Huang, C. T.; Xu, J. Characterization of Fc-fusion protein aggregates derived from extracellular domain disulfide bond rearrangements. *J. Pharm. Sci.* **2013**, *102* (2), 441-453. DOI: 10.1002/jps.23421.
[27] Castel, J.; Delaux, S.; Hernandez-Alba, O.; Cianferani, S. Recent advances in structural mass spectrometry methods in the context of biosimilarity assessment: from sequence heterogeneities to higher order structures. *J. Pharm. Biomed. Anal.* **2023**, *236*, 115696. DOI: 10.1016/j.jpba.2023.115696.
[28] Chen, G.; Tao, L.; Li, Z. Recent advancements in mass spectrometry for higher order structure characterization of protein therapeutics. *Drug. Discov. Today* **2022**, *27* (1), 196-206. DOI: 10.1016/j.drudis.2021.09.010.
[29] Christofi, E.; Barran, P. Ion Mobility Mass Spectrometry (IM-MS) for Structural Biology: Insights Gained by Measuring Mass, Charge, and Collision Cross Section. *Chem. Rev.* **2023**, *123* (6), 2902-2949. DOI: 10.1021/acs.chemrev.2c00600.
[30] Ruotolo, B. T.; Benesch, J. L. P.; Sandercock, A. M.; Hyung, S.-J.; Robinson, C. V. Ion mobility–mass spectrometry analysis of large protein complexes. *Nat. Protoc.* **2008**, *3* (7), 1139-1152. DOI: 10.1038/nprot.2008.78.
[31] Dixit, S. M.; Polasky, D. A.; Ruotolo, B. T. Collision induced unfolding of isolated proteins in the gas phase: past, present, and future. *Curr. Opin. Chem. Biol.* **2018**, *42*, 93-100. DOI: 10.1016/j.cbpa.2017.11.010.
[32] Botzanowski, T.; et al. Middle Level IM–MS and CIU Experiments for Improved Therapeutic Immunoglobulin Subclass Fingerprinting. *Anal. Chem.* **2020**, *92* (13), 8827-8835. DOI: 10.1021/acs.analchem.0c00293.
[33] Tian, Y.; Han, L.; Buckner, A. C.; Ruotolo, B. T. Collision Induced Unfolding of Intact Antibodies: Rapid Characterization of Disulfide Bonding Patterns, Glycosylation, and Structures. *Anal. Chem.* **2015**, *87* (22), 11509-11515. DOI: 10.1021/acs.analchem.5b03291.
[34] Pisupati, K.; et al. Biosimilarity under stress: A forced degradation study of Remicade® and Remsima™. *mAbs* **2017**, *9* (7), 1197-1209. DOI: 10.1080/19420862.2017.1347741.
[35] Vallejo, D. D.; et al. Collision-Induced Unfolding Reveals Stability Differences in Infliximab Therapeutics under Native and Heat Stress Conditions. *Anal. Chem.* **2021**, *93* (48), 16166-16174. DOI: 10.1021/acs.analchem.1c03946.
[36] Pisupati, K.; et al. A Multidimensional Analytical Comparison of Remicade and the Biosimilar Remsima. *Anal. Chem.* **2017**, *89* (9), 4838-4846. DOI: 10.1021/acs.analchem.6b04436.
[37] Villafuerte-Vega, R. C.; et al. Ion Mobility-Mass Spectrometry and Collision-Induced Unfolding of Designed Bispecific Antibody Therapeutics. *Anal. Chem.* **2023**, *95* (17), 6962-6970. DOI: 10.1021/acs.analchem.3c00344.
[38] Desligniere, E.; et al. Combination of IM-Based Approaches to Unravel the Coexistence of Two Conformers on a Therapeutic Multispecific mAb. *Anal. Chem.* **2022**, *94* (22), 7981-7989. DOI: 10.1021/acs.analchem.2c00928.
[39] Deslignière, E.; et al. State-of-the-Art Native Mass Spectrometry and Ion Mobility Methods to Monitor Homogeneous Site-Specific Antibody-Drug Conjugates Synthesis. *Pharmaceuticals* **2021**, *14* (6), 498. DOI: 10.3390/ph14060498.

[40] Tian, Y.; Lippens, J. L.; Netirojjanakul, C.; Campuzano, I. D. G.; Ruotolo, B. T. Quantitative collision-induced unfolding differentiates model antibody–drug conjugates. *Protein Sci.* **2019**, *28* (3), 598-608. DOI: 10.1002/pro.3560.

[41] Marty, M. T.; et al. Bayesian Deconvolution of Mass and Ion Mobility Spectra: From Binary Interactions to Polydisperse Ensembles. *Anal. Chem.* **2015**, *87* (8), 4370-4376. DOI: 10.1021/acs.analchem.5b00140.

[42] Kilpatrick, E. L.; Liao, W. L.; Camara, J. E.; Turko, I. V.; Bunk, D. M. Expression and characterization of 15N-labeled human C-reactive protein in Escherichia coli and Pichia pastoris for use in isotope-dilution mass spectrometry. *Protein Expr. Purif.* **2012**, *85* (1), 94-99. DOI: 10.1016/j.pep.2012.06.019 From NLM Medline.

[43] Hernández, H.; Robinson, C. V. Determining the stoichiometry and interactions of macromolecular assemblies from mass spectrometry. *Nat. Protoc.* **2007**, *2* (3), 715-726. DOI: 10.1038/nprot.2007.73.

[44] Richardson, K.; Langridge, D.; Dixit, S. M.; Ruotolo, B. T. An Improved Calibration Approach for Traveling Wave Ion Mobility Spectrometry: Robust, High-Precision Collision Cross Sections. *Anal. Chem.* **2021**, *93* (7), 3542-3550. DOI: 10.1021/acs.analchem.0c04948.

[45] Giles, K.; et al. A Cyclic Ion Mobility-Mass Spectrometry System. *Anal. Chem.* **2019**, *91* (13), 8564-8573. DOI: 10.1021/acs.analchem.9b01838.

[46] Eldrid, C.; et al. Gas Phase Stability of Protein Ions in a Cyclic Ion Mobility Spectrometry Traveling Wave Device. *Anal. Chem.* **2019**, *91* (12), 7554-7561. DOI: 10.1021/acs.analchem.8b05641.

[47] Polasky, D. A.; Dixit, S. M.; Fantin, S. M.; Ruotolo, B. T. CIUSuite 2: Next-Generation Software for the Analysis of Gas-Phase Protein Unfolding Data. *Anal. Chem.* **2019**, *91* (4), 3147-3155. DOI: 10.1021/acs.analchem.8b05762.

[48] Haynes, S. E.; et al. Variable-Velocity Traveling-Wave Ion Mobility Separation Enhancing Peak Capacity for Data-Independent Acquisition Proteomics. *Anal. Chem.* **2017**, *89* (11), 5669-5672. DOI: 10.1021/acs.analchem.7b00112.

[49] Hall, Z.; Politis, A.; Bush, M. F.; Smith, L. J.; Robinson, C. V. Charge-state dependent compaction and dissociation of protein complexes: insights from ion mobility and molecular dynamics. *J. Am. Chem. Soc.* **2012**, *134* (7), 3429-3438. DOI: 10.1021/ja2096859 From NLM Medline.

[50] Vallejo, D. D.; et al. A Modified Drift Tube Ion Mobility-Mass Spectrometer for Charge-Multiplexed Collision-Induced Unfolding. *Anal. Chem.* **2019**, *91* (13), 8137-8146. DOI: 10.1021/acs.analchem.9b00427.

[51] Wojdyr, M. J. Fityk: A general-purpose peak fitting program. *J. Appl. Cryst.* **2010**, *43* (43), 1126-1128. DOI: 10.1107/S0021889810030499.

[52] Carlini, V.; et al. The multifaceted nature of IL-10: regulation, role in immunological homeostasis and its relevance to cancer, COVID-19 and post-COVID conditions. *Front. Immunol.* **2023**, *14*. DOI: 10.3389/fimmu.2023.1161067.

[53] Saraiva, M.; Vieira, P.; O'Garra, A. Biology and therapeutic potential of interleukin-10. *J. Exp. Med.* **2020**, *217* (1), jem.20190418. DOI: 10.1084/jem.20190418.

[54] Zdanov, A.; et al. Crystal structure of interleukin-10 reveals the functional dimer with an unexpected topological similarity to interferon γ. *Structure* **1995**, *3* (6), 591-601. DOI: 10.1016/s0969-2126(01)00193-9.

[55] Walter, M. R.; Nagabhushan, T. L. Crystal structure of interleukin 10 reveals an interferon gamma-like fold. *Biochemistry* **1995**, *34* (38), 12118-12125. DOI: 10.1021/bi00038a004.
[56] Josephson, K.; Logsdon, N. J.; Walter, M. R. Crystal Structure of the IL-10/IL-10R1 Complex Reveals a Shared Receptor Binding Site. *Immunity* **2001**, *15* (1), 35-46. DOI: 10.1016/s1074-7613(01)00169-8.
[57] Minshawi, F.; et al. The Generation of an Engineered Interleukin-10 Protein With Improved Stability and Biological Function. *Front. Immunol.* **2020**, *11*. DOI: 10.3389/fimmu.2020.01794.
[58] Syto, R.; et al. Structural and Biological Stability of the Huan Interleukin 10 Homodimer. *Biochemistry* **1998**, *37* (48), 16943 - 16951. DOI: 10.1021/bi981555y.
[59] Aliyari, E.; Konermann, L. Atomistic Insights into the Formation of Nonspecific Protein Complexes during Electrospray Ionization. *Anal. Chem.* **2021**, *93* (37), 12748-12757. DOI: 10.1021/acs.analchem.1c02836.
[60] Konermann, L.; Ahadi, E.; Rodriguez, A. D.; Vahidi, S. Unraveling the mechanism of electrospray ionization. *Anal. Chem.* **2013**, *85* (1), 2-9. DOI: 10.1021/ac302789c.
[61] Vallejo, D. D.; et al. Ion Mobility–Mass Spectrometry Reveals the Structures and Stabilities of Biotherapeutic Antibody Aggregates. *Anal. Chem.* **2022**, *94* (18), 6745-6753. DOI: 10.1021/acs.analchem.2c00160.
[62] Campuzano, I. D. G.; Larriba, C.; Bagal, D.; Schnier, P. D. Ion Mobility and Mass Spectrometry Measurements of the Humanized IgGk NIST Monoclonal Antibody. *ACS Symp. Ser.* **2015**, *1202*, 75-112.
[63] Pacholarz, K. J.; et al. Dynamics of Intact Immunoglobulin G Explored by Drift-Tube Ion-Mobility Mass Spectrometry and Molecular Modeling. *Angew. Chem. Int. Ed.* **2014**, *53* (30), 7765-7769. DOI: 10.1002/anie.201402863.
[64] Zheng, X.; Kurulugama, R. T.; Laganowsky, A.; Russell, D. H. Collision-Induced Unfolding Studies of Proteins and Protein Complexes using Drift Tube Ion Mobility-Mass Spectrometer. *Anal. Chem.* **2020**, *92* (10), 7218-7225. DOI: 10.1021/acs.analchem.0c00772.
[65] Niu, S.; Ruotolo, B. T. Collisional unfolding of multiprotein complexes reveals cooperative stabilization upon ligand binding. *Protein Sci.* **2015**, *24* (8), 1272-1281. DOI: 10.1002/pro.2699.
[66] Watanabe, Y.; et al. Signature of Antibody Domain Exchange by Native Mass Spectrometry and Collision-Induced Unfolding. *Anal. Chem.* **2018**, *90* (12), 7325-7331. DOI: 10.1021/acs.analchem.8b00573.
[67] van Schaick, G.; et al. Online Collision-Induced Unfolding of Therapeutic Monoclonal Antibody Glyco-Variants through Direct Hyphenation of Cation Exchange Chromatography with Native Ion Mobility-Mass Spectrometry. *Anal. Chem.* **2023**, *95* (8), 3932-3939. DOI: 10.1021/acs.analchem.2c03163.
[68] Zhong, Y.; Han, L.; Ruotolo, B. T. Collisional and Coulombic Unfolding of Gas-Phase Proteins: High Correlation to Their Domain Structures in Solution. *Angew. Chem.* **2014**, *126* (35), 9363-9366. DOI: 10.1002/ange.201403784.
[69] Eschweiler, J. D.; Martini, R. M.; Ruotolo, B. T. Chemical Probes and Engineered Constructs Reveal a Detailed Unfolding Mechanism for a Solvent-Free Multidomain Protein. *J. Am. Chem. Soc.* **2017**, *139* (1), 534-540. DOI: 10.1021/jacs.6b11678.

[70] Tian, Y.; Ruotolo, B. T. Collision induced unfolding detects subtle differences in intact antibody glycoforms and associated fragments. *Int. J. Mass Spectrom.* **2018**, *425*, 1-9. DOI: 10.1016/j.ijms.2017.12.005.
[71] Upton, R.; et al. Hybrid mass spectrometry methods reveal lot-to-lot differences and delineate the effects of glycosylation on the tertiary structure of Herceptin®. *Chem. Sci.* **2019**, *10* (9), 2811-2820. DOI: 10.1039/c8sc05029e.
[72] Zheng, K.; Bantog, C.; Bayer, R. The impact of glycosylation on monoclonal antibody conformation and stability. *mAbs* **2011**, *3* (6), 568-576. DOI: 10.4161/mabs.3.6.17922.
[73] Hristodorov, D.; et al. Generation and Comparative Characterization of Glycosylated and Aglycosylated Human IgG1 Antibodies. *Mol. Biotechnol.* **2013**, *53* (3), 326-335. DOI: 10.1007/s12033-012-9531-x.
[74] Reusch, D.; Tejada, M. L. Fc glycans of therapeutic antibodies as critical quality attributes. *Glycobiology* **2015**, *25* (12), 1325-1334. DOI: 10.1093/glycob/cwv065.
[75] Shelimov, K. B.; Clemmer, D. E.; Hudgins, R. R.; Jarrold, M. F. Protein Structure in Vacuo: Gas-Phase Conformations of BPTI and Cytochrome c. *J. Am. Chem. Soc.* **1997**, *119*, 2240-2248.
[76] Anders, A.; Tidwell, E.; Gadkari, V.; Koutmos, M.; Ruotolo, B. Collision Induced Unfolding Reveals Disease-Associated Stability Shifts in Mitochondrial tRNAs. *J. Am. Chem. Soc.* **2023**. DOI: 10.1021/jacs.3c09230.

Chapter 5: A Novel *In Vitro* Serum Stability Assay for Antibody Therapeutics Incorporating Internal Standards

5.1 Original Publication

The work in this chapter was performed during a summer internship at AbbVie and is being prepared for publication as: Yihan Li, Rosendo C. Villafuerte-Vega, Gary J. Jenkins, and Hetal Sarvaiya. "A Novel *In Vitro* Serum Stability Assay for Antibody Therapeutics Incorporating Internal Standards." 2024.

5.2 Author Contributions

Y.L. and H.S. conceptualized the project and designed the experiments and LC-MS methods. R.C.V. designed and executed experiments as well as collected and analyzed LC-MS data. Y.L. optimized protocol designed by R.C.V. to generate and purify Fc fragments, leading to Figures 5-1B, 5-4, and 5-5, as well as Appendix Figures E-1, E-4, and E-5. H.S and G.J.J. provided project guidance and supervision. Y.L. and R.C.V. contributed equally to the work presented in this chapter.

5.3 Abstract

In vitro stability assessments play a pivotal role in identifying potential liabilities of antibody therapeutics prior to animal studies. However, current workflows do not account for any random or systemic errors that can occur during sample preparation and instrumental analysis. These uncompensated errors can lead to inaccurate sample percent (%) recoveries,

leading to erroneous assessments of *in vitro* therapeutic antibody stability. To address these limitations, we describe the development of a liquid chromatography-mass spectrometry (LC-MS)-based *in vitro* serum stability assay that incorporates NISTmAb and its Fc fragment as internal standards (ISs). We show that NISTmAb and its Fc fragment demonstrate excellent stability profiles across different animal serums, underscoring their potential use as ISs in the absence of aggregation or biotransformation. When assessing the *in vitro* stability of 19 antibodies in the serums of various preclinical species, we find the accuracy and precision of % sample recoveries improved from a range of 75 – 125% to 90 – 110% after the incorporation of either NISTmAb or its Fc fragment as ISs. Combined, our results suggest that this *in vitro* stability assay can be utilized as a routine screening tool in the early stages of antibody therapeutic drug discovery.

5.4 Introduction

Monoclonal antibody (mAb) therapeutics have proven to achieve powerful therapeutic responses that were previously unattainable with conventional small molecule drugs.[1-3] However, they are susceptible to a variety of biotransformations and degradation events *in vivo*, which may affect their half-life, safety, efficacy, and pharmacokinetic/pharmacodynamic (PK/PD) profiles.[4-6] Examples of such biotransformation that occur while in circulation include deamidation, isomerization, oxidation, glycation, Fab-arm exchange, and disulfide shuffling, in addition to degradation pathways such as fragmentation, aggregation, and precipitation.[6-8] These modifications in structure and function are mediated by rapid changes in temperature, pH, pressure, and salt concentrations in the absence of stabilizers from formulation buffer.[4, 9]

Probing the stability of antibody therapeutics *in vivo* using animal and human models is not routinely feasible during drug discovery.[10] Therefore, an *in vitro* stability assessment is often

used to identify potential liabilities and prioritize candidates for *in vivo* studies.[11, 12] Successful translation of stability outcomes from *in vitro* to *in vivo* can lead to a substantial reduction of unnecessary animal studies, improving efficiency at the early discovery stage. To develop an *in vitro* model that would mimic and simulate *in vivo* conditions, key parameters should be similar to those of *in vivo* study designs, such as drug exposure post-dose, duration of drug exposure, types of body fluid or surrogate, and animal models.[12, 13] Importantly, these *in vitro* studies necessitate robust analytical methodologies that can accurately characterize biotransformation and degradation profiles.

In the last two decades, intact high-resolution protein mass-spectrometry (HRMS)-based approaches and improved sample preparation strategies have enabled the characterization and quantitation of antibody therapeutics from biological matrices.[14-17] In this regard, liquid chromatography-mass spectrometry (LC-MS)-based *in vitro* stability assays have been developed and adopted in the biopharmaceutical industry to qualitatively and quantitatively monitor a wide range of biotransformations and degradation products with great sensitivity.[18-21] These stability assays typically involve three main steps: the incubation of antibody therapeutics in biological matrices, affinity purification, and LC-MS analysis. However, current methodologies do not fully account for operational errors during sample preparation and instrument operation, as well as variations in sample evaporation or protein precipitation, sample recovery after affinity purification, and matrix effects during LC-MS analysis. These limitations, in turn, can lead to inaccurate stability quantitation at the intact protein level. The use of a reference standard or quality control can address these limitations, but the only documented study to pursue such an approach incorporated standards that are not readily available and applicable to other antibody modalities.[8]

The National Institute of Standards and Technology monoclonal antibody (NISTmAb) is a recombinant humanized IgG1κ expressed in murine suspension culture.[22] NISTmAb has been extensively described in the literature, and it has been utilized as a reference standard in the development and assessment of biochemical and biophysical methods for the characterization of antibody therapeutics.[23-27] In general, NISTmAb has demonstrated a favorable developability profile, and its stability and aggregation propensity has been characterized across different buffer conditions.[24, 28] As a result, this commercially available antibody and its subunits can potentially serve as stable internal standards (ISs) to monitor the *in vitro* stability of antibody therapeutics across different biological matrices. However, its utility and effectiveness as an IS has not been explored.

Herein, we present an *in vitro* serum stability assay that incorporates both NISTmAb and its fragment crystallizable (Fc) region as internal standards to compensate for variations in sample recoveries and correct for any random or systematic errors that occur during sample preparation and instrumental analysis. The stability of 19 biologics, either in current clinical use or clinical development, were assessed in the serums of preclinical species such as mouse, rat and cynomolgus monkey. We find that the accuracy and precision of percent (%) recovery calculations are improved after the incorporation of NISTmAb and its Fc fragment as internal standards, enabling a more confident stability assessment in the absence of biotransformation or aggregation. Taken together, our results demonstrate that this *in vitro* assay can serve as a routine screening tool to select and advance stable antibody therapeutic candidates for subsequent *in vivo* studies and PK/PD analysis in the biopharmaceutical pipeline.

5.5 Experimental Section

Reagents and Materials. All antibody therapeutics except NISTmAb (Appendix Table E-1) were produced in-house with publicly available amino acid sequence information. Therefore, the modifications and stability of each antibody may not represent the antibody therapeutics that are in clinical use or trials.

NISTmAb humanized IgG1κ was purchased from National Institute of Standards and Technology (Gaitherburg, MD). IgdE was purchased from Genovis (Cambridge, MA). MabSelect PrismA protein A resin was purchased from Cytiva (Marlborough, MA). Biotinylated goat anti-human IgG was purchased from SouthernBiotech (Birmingham, AL). CD-1 (ICR) Mouse serum, Sprague Dawley rat serum, and cynomolgus monkey serum were purchased from BioIVT (Dallas, TX). AssayMAP 5 µL streptavidin cartridges were purchased from Agilent (Santa Clara, CA). Tris buffered saline (TBS) was purchased from Bio-Rad (Hercules, CA). Phosphate buffered saline (PBS, pH 7.4 ± 0.1) was purchased from Corning (Corning, NY). Sodium azide was purchased from Teknova (Hollister, CA). Sodium phosphate monobasic monohydrate, sodium phosphate dibasic dihydrate, and bovine serum albumin (BSA) were purchased from Sigma-Aldrich (St. Louis, MO). IgG elution buffer, 0.1% formic acid (FA) in acetonitrile, and 0.1% FA in water were purchased from Thermo Fisher Scientific (Pittsburg, PA).

Generation of NISTmAb Fc Fragment. Lyophilized IgdE was suspended in deionized water at a concentration of 20 units/µL. NISTmAb (10 mg/mL) was diluted with 150 mM sodium phosphate buffer to 1 mg/mL. 4 mg of NISTmAb was digested with 4000 units of IgdE at 37°C for 30 hours. 200 µL of protein A resin slurry was washed with 1 mL of PBS buffer twice, and the supernatant was discarded after centrifugation at 1000×g for 1 min. The digest

was mixed with protein A resin and incubated on a rotator for 15 min at room temperature for the immunocapture of Fc fragment. The supernatant was discarded after centrifugation at 1000×g for 1 min. The protein A resin was washed with 1 mL of PBS buffer three times to remove residual Fab fragment, and the supernatant was discarded after centrifugation at 1000×g for 1 min. 1 mL of IgG elution buffer was added to the protein A resin for Fc fragment elution, and the mixture was incubated on a rotator for 10 min at room temperature. The supernatant was collected after centrifugation at 1000×g for 1 min then neutralized with 50 µL of 2 M ammonium bicarbonate. This neutralized solution was characterized by LC-MS and liquid chromatography-ultraviolet/visible absorbance (LC-UV/Vis). It contained approximately 92.2% of Fc fragment, 3.5% of partially digested NISTmAb without one Fab fragment, and 4.3% of NISTmAb (Figure S1). The total protein concentration was estimated as 1.1 mg/mL.

***In vitro* Serum Incubation.** Tidutamab, INBRX-105, Zanidatamab, CTX-009, Tarlatamab, Glofitamab, and TNB-738 were spiked into mouse serum at 0.1 mg/mL, with 0.01% (w/v) sodium azide and 0.1 mg/mL NISTmAb. Tibulizumab and Erfonrilimab were spiked into mouse, rat, and cynomolgus serum at 0.1 mg/mL, with 0.01% (w/v) sodium azide and 0.1 mg/mL NISTmAb. All these *in vitro* serum samples were incubated at 37°C and collected after 10 min, 1, 4, and 7 days. Tidutamab, INBRX-105, Zanidatamab, CTX-009, Tarlatamab, Glofitamab, TNB-738, Tibulizumab, and Erfonrilimab were spiked into PBS at 0.1 mg/mL, with 0.01% (w/v) sodium azide, 0.1 mg/mL NISTmAb, and 0.5% (w/v) BSA. Samples spiked in PBS served as buffer controls. Blank serum was prepared with 0.01% (w/v) sodium azide and 0.1 mg/mL NISTmAb. Blank PBS buffer was prepared with 0.01% (w/v) sodium azide, 0.1 mg/mL NISTmAb, and 0.5% (w/v) BSA. The PBS buffer controls, blank serum, and blank PBS buffer

were incubated at 37°C and collected after 10 min and 7 days. All the samples were stored in a -80°C freezer right after collection until analysis.

Palivizumab, Faricimab, Ixekizumab, Evolocumab, Denosumab, Emicizumab, Amivantamab, Teclistamab, Erfonrilimab, and Glofitamab were spiked into mouse serum at 0.1 mg/mL, with 0.01% (w/v) sodium azide and 0.05 mg/mL Fc fragment. Bevacizumab and Dupilumab were spiked into mouse, rat, and cynomolgus serum at 0.1 mg/mL, with 0.01% (w/v) sodium azide and 0.05 mg/mL Fc fragment. All these in vitro serum samples were incubated at 37°C and collected after 10 min, 1, 4, and 7 days. Bevacizumab, Dupilumab, Palivizumab, Faricimab, Ixekizumab, Evolocumab, Denosumab, Emicizumab, Amivantamab, Teclistamab, Erfonrilimab, and Glofitamab were spiked into PBS at 0.1 mg/mL, with 0.01% (w/v) sodium azide, 0.05 mg/mL Fc fragment, and 0.5% (w/v) BSA. Blank serum was prepared with 0.01% (w/v) sodium azide and 0.05 mg/mL Fc fragment. Blank PBS buffer was prepared with 0.01% (w/v) sodium azide, 0.05 mg/mL Fc fragment, and 0.5% (w/v) BSA. The PBS buffer controls, blank serum, and blank PBS buffer were incubated at 37°C and collected after 10 min and 7 days. All the samples were stored in a -80°C freezer right after collection until analysis.

Immunoaffinity Purification and LC-MS Analysis. All *in vitro* samples and controls were affinity purified using a Bravo AssayMAP platform (Agilent Technologies, Santa Clara, CA). 25 µg of biotinylated goat anti-human IgG (anti-Fc) was immobilized onto the streptavidin cartridges followed by two washes with TBS. 50 µL of each sample or control was diluted to 100 µL with TBS then loaded onto streptavidin cartridges at a flow rate of 5 µL/min. After two washes with TBS, the captured antibodies and internal standards were eluted with 50 µL of 0.25% formic acid (v/v) at a flow rate of 5 µL/min.

The eluted samples were subjected to LC-MS analysis on a 1290 Infinity II LC system coupled to a 6545xt qTOF mass spectrometer (Agilent Technologies, Santa Clara, CA). 0.5 µg of each antibody was loaded along with the internal standard onto a PLRP-S column (1000 Å, 2.1 × 50 mm, 5 µm, Agilent Technologies, Santa Clara, CA) maintained at 80°C. The separation gradient was delivered at a flow rate of 0.2 mL/min with 0.1% formic acid (v/v) in water as mobile phase A and 0.1% formic acid (v/v) in acetonitrile as mobile phase B: mobile phase B was held at 20% from 0 to 2 min; ramped up to 75% from 2 to 10 min; ramped up 95% by 10.5 min; held at 95% from 10.5 to 13.2 min; returned to 20% by 13.3 min; then held at 20% from 13.3 to 15 min. MS data was acquired in positive electrospray ionization mode with an acquisition range of 500 to 5000 m/z, with the gas temperature at 350°C, gas flow at 12 L/min, nebulizer gas at 60 psi, sheath gas temperature at 400°C, sheath gas flow at 12 L/min, VCap voltage at 5500 V, nozzle voltage at 2000 V, fragmentor voltage at 380 V, skimmer1 voltage at 140 V, and Octopole RF voltage at 750 V.

Data Processing and Analysis. Deconvolution of mass spectra was performed with Byos software, version 4.5 (Protein Metrics, Cupertino, CA). MS spectra from 5 to 8 min were averaged and deconvoluted. The input mass range was set as 800 to 5000, output mass range as 20000 to 200000, charge vectors spacing as 1, baseline radius as 15, smoothing sigma as 0.02, spacing as 0.04, mass smoothing sigma as 3, mass spacing as 0.5, iteration max as 25, charge range as 5 to 200, blur skewness as 1.10, range as 8.00, and blur type as gaussian. Integration of deconvoluted mass area was performed by computing the areas of the mass peaks with a mass area width of 1000 Da. The mass peak area ratio of antibody and internal standard was calculated with (Equation 5-1.

$$Mass\ Peak\ Area\ Ratio = \frac{Antibody\ Mass\ Peak\ Area}{Internal\ Standard\ Mass\ Peak\ Area} \qquad \text{(Equation 5-1)}$$

Percent recoveries were calculated with (Equation 5-2 by normalizing the mass peak area ratios of samples collected on Day 1, Day 4 and Day 7 to samples collected on Day 0.

$$Percent\ (\%)\ Recovery = \frac{Mass\ Peak\ Area\ Ratio\ on\ Day\ X}{Mass\ Peak\ Area\ Ratio\ on\ Day\ 0} \times 100\% \qquad \text{(Equation 5-2)}$$

5.6 Results and Discussion

Assessing the in vitro serum stabilities of NISTmAb and its Fc Fragment. Although NISTmAb has demonstrated to have a favorable developability profile, there is a lack of studies that have evaluated its stability across complex biological matrices. To establish NISTmAb as an appropriate IS for *in vitro* serum stability assays, we assessed its stability in the serums of mouse, rat, and cynomolgus monkey. The % recoveries of NISTmAb over the seven-day incubation period ranged between 92.9% to 102.1% across animal serums and the PBS buffer control (Figure 5-1A). We evaluated these results using previously recommended acceptance criteria for hybrid immunoaffinity-LC-MS/MS quantitative assays, where the accuracy should be ± 20% of Day 0 % recoveries and the precision should be ± 20% between replicate injections.[29] Accuracy and precision values of these stability assays are summarized in Appendix Table E-2 to E-4. The precision (0.3% to 1.9%) and accuracy (-7.2% to 2.1%) of NISTmAb fell well within the acceptance criteria, highlighting that NISTmAb exhibits favorable stability profiles in the serums of preclinical species.

Next, we evaluated the serum stability of Fc fragment in the same fashion as NISTmAb in order to assess its potential as a stable IS (Figure 5-1B). We generated Fc fragments of NISTmAb via an IgdE digestion, which cleaves NISTmAb at a specific site above the hinge (KSCDKT / HTCPPC). Here, the Fc fragment's binding capacity for goat anti-human IgG (anti-

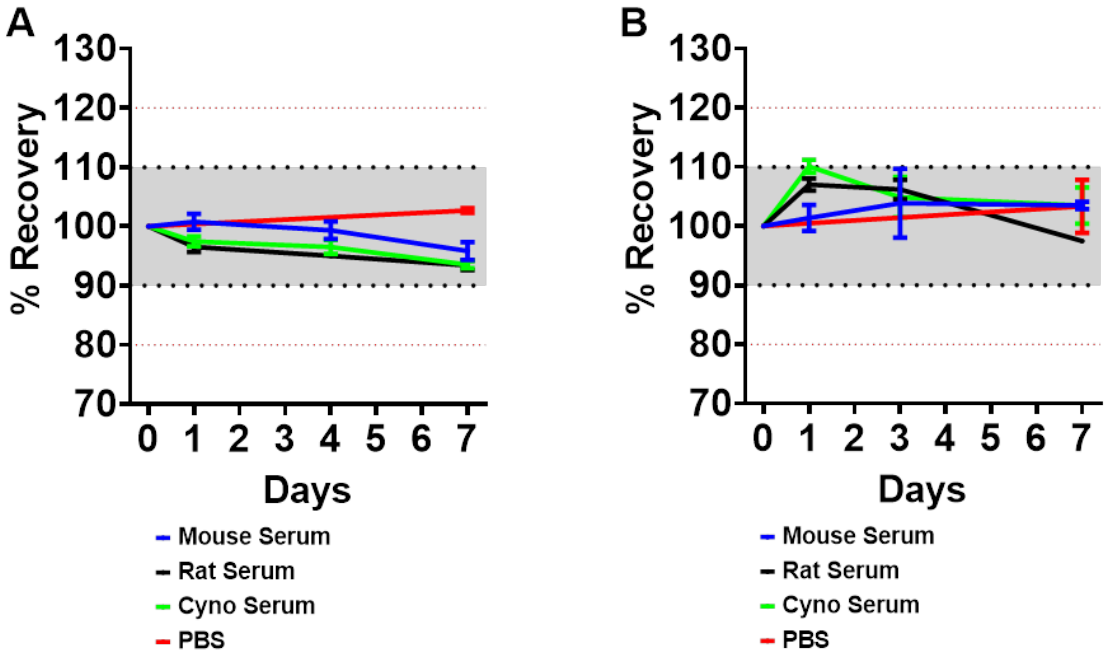

Figure 5-1: The stabilities of (A) NISTmAb and (B) NISTmAb Fc fragment in PBS buffer and serum of three different species: mouse, rat and cynomolgus monkey.

Fc) is retained, allowing it to be incubated, purified, and analyzed using our immunoaffinity purification workflow. Our data for the isolated Fc fragment showed optimal % recoveries over the seven-day incubation period, ranging between 97.5% and 109.2% across all serum and PBS buffer control conditions. The precision (0.3% to 10.2%) and accuracy (-7.2% to 11.3%) of the Fc fragment were also within the acceptable range (Appendix Table E-5 to E-7). Though these results do not compensate for any systemic or random errors during sample preparation and instrumental analysis, our % recoveries are well within acceptance criteria, demonstrating that NISTmAb has a favorable stability profile at the intact and Fc level across all serums studied.

NISTmAb as an IS compensates for variations in % sample recoveries. To assess the suitability of NISTmAb as an IS in *in vitro* stability assays, we incubated it alongside nine bispecific antibodies (bsAbs) in mouse serum (Figure 5-2). All nine bsAbs exhibited favorable stability profiles in mouse serum, with % precision values between 0.1% and 6.3% and %

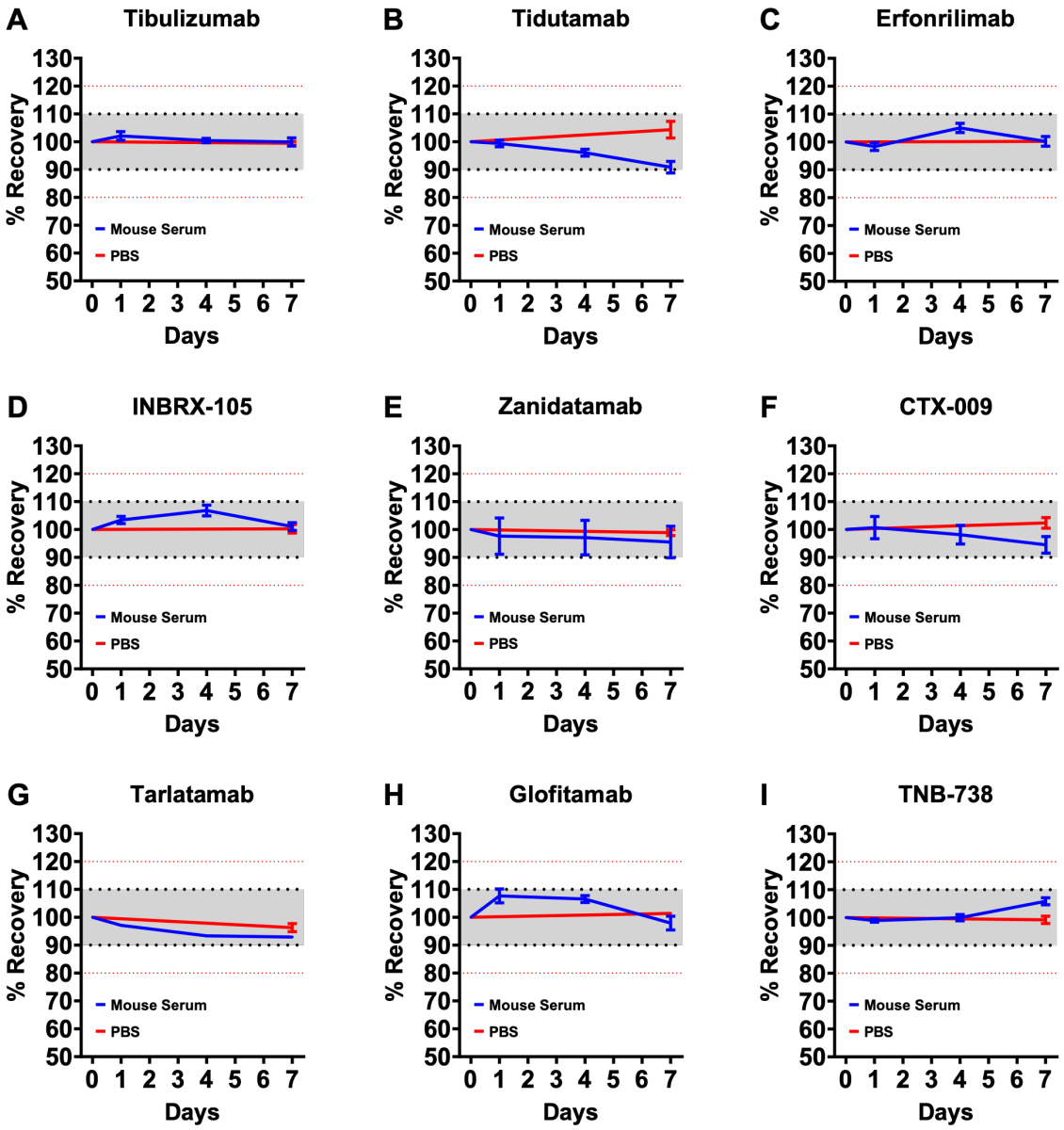

Figure 5-2: The stabilities of (A) Tibulizumab, (B) Tidutamab, (C) Erfonrilimab, (D) INBRX-105, (E) Zanidatamab, (F) CTX-009, (G) Tarlatamab, (H) Glofitamab, and (I) TNB-738 in mouse serum with NISTmAb as internal standard.

accuracies within ± 10.0% except for Tidutamab (-10.4% to 7.7%) and Zanidatamab (-11.0% to 3.3%) when NISTmAb was incorporated as an IS. Evidently, we achieved % recoveries within ± 10% of Day 0 values across both serum and PBS buffer conditions, further supporting that these antibodies are stable in the presence of degradants within mouse serum. In contrast, the %

accuracies of these nine antibodies ranged from -22.5% to 3.1% when NISTmAb was not used as an IS, while the precision of replicate % recoveries remained in the same range (0.3% to 4.3%). As shown in Appendix Figure E-2, the data quality of Tibulizumab, Tidutamab, INBRX-105, Zanidatamab, CTX-009, Tarlatamab, and Glofitamab was improved after the incorporation of NISTmAb as an IS. In comparison, the % accuracies of Erfonrilimab and TNB-738 were well within ± 10.0% even without the inclusion of NISTmAb as an IS. These data suggest that there are cases where systemic and random errors occur less frequently during sample preparation and instrumental analysis. In the case of Erfonrilimab and TNB-738, the data quality was not impacted by the addition of an IS, further demonstrating that NISTmAb qualifies as an appropriate internal standard in *in vitro* stability assays. Clearly, our results are well within the recommended ± 20% criteria established in the literature, indicating that the inclusion of NISTmAb as an IS greatly addresses variations in % sample recoveries generated during sample preparation and instrumental analysis.

Since other preclinical species can be utilized for *in vitro* stability assays outside of mice, we assessed the stabilities of two representative antibodies, Tibulizumab and Erfonrilimab, in both rat and cynomolgus monkey serums alongside NISTmAb as an IS. Our stability results show comparable trends in mouse, rat, and cynomolgus monkey serums, where both antibodies exhibited favorable stability profiles (Appendix Figure E-3). These results were well within an acceptance criteria of ± 10.0% of Day 0 recoveries like those of PBS buffer controls. Taken together, our results indicate that NISTmAb can serve as a suitable internal standard for *in vitro* serum stability assays across different preclinical animal serums.

NISTmAb Fc fragment as an alternate IS for stability assessment. Since the mass peak areas of deconvoluted masses are utilized for % recovery calculations, it is critical that the

masses of both IS and antibody samples do not overlap substantially in order to ensure the accurate integration of mass peak areas. Thus, NISTmAb was not an ideal IS for antibodies of similar molecular weight as illustrated by the case of Amivantamab (Figure 5-3). In this case, NISTmAb coeluted with Amivantamab during LC separation (Figure 5-3A), which resulted in overlapping mass spectra (Figure 5-3B). A closer examination at the mass deconvoluted spectra of co-eluted NISTmAb and Amivantamab showed indistinguishable mass distributions (Figure 5-3C). Therefore, accurately integrating the mass peak areas of either NISTmAb or Amivantamab became difficult to perform.

To address the limitations of full-length NISTmAb as an IS, we probed the suitability of its Fc

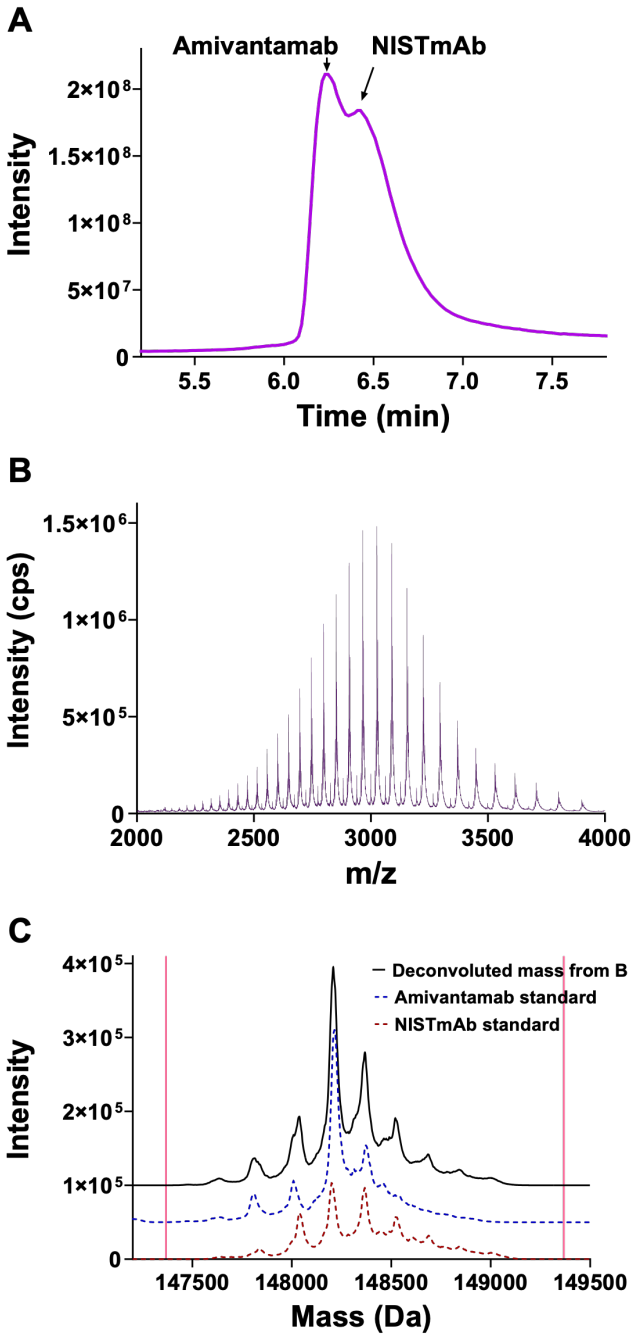

Figure 5-3: (A) NISTmAb and Amivantamab were not baseline resolved during LC separation. (B) NISTmAb and Amivantamab had overlapped protein envelops in raw MS1 spectra extracted from 6 to 7 min. (C) The deconvoluted mass data of raw MS1 spectra in B (solid black line) was a combination of NISTmAb and Amivantamab. The deconvoluted mass data of NISTmAb standard (dashed red line) and Amivantamab standard (dashed blue line) analyzed individually in LC-MS were provided as a comparison. Mass peak area was integrated between 147,367.5 and 149,367.5 Da (solid pink lines).

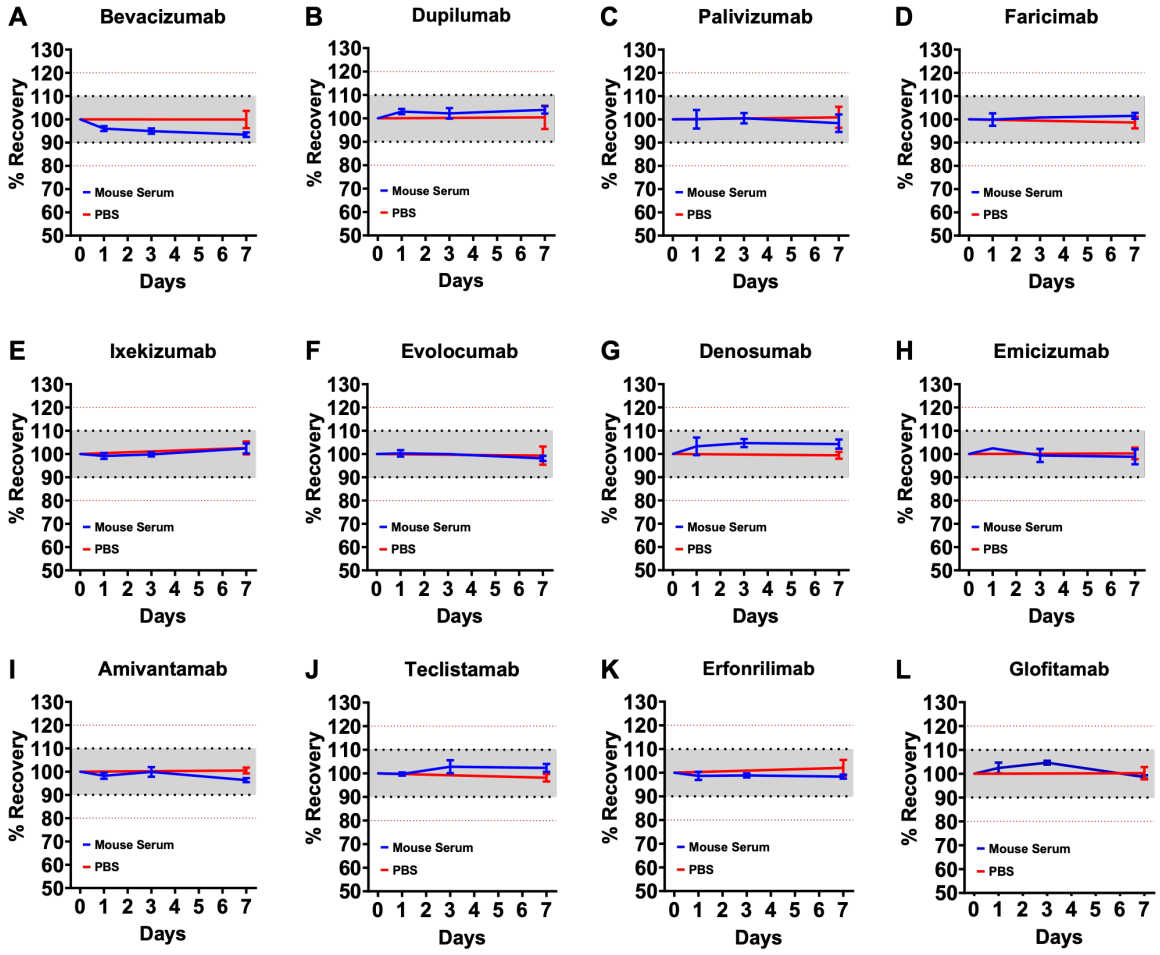

Figure 5-4: The stabilities of (A) Bevacizumab, (B) Dupilumab, (C) Palivizumab, (D) Faricimab, (E) Ixekizumab, (F) Evolocumab, (G) Denosumab, (H) Emicizumab, (I) Amivantamab, (J) Teclistamab, (K) Erfonrilimab, (L) Glofitamab in mouse serum with Fc fragment as internal standard.

fragment (~50 kDa) as an alternative IS. In this case, we assessed the stabilities of six mAbs and six bsAbs in mouse serum alongside NISTmAb Fc fragment as the IS (Figure 5-4). All 12 molecules exhibited favorable stability profiles in mouse serum, with replicate precisions between 0.3% and 5.5% and accuracies of % recoveries well within the recommended ± 20.0% acceptance criteria across the seven-day incubation time. When qualitatively comparing stability data with or without the Fc fragment as an IS, we observed an increase in data quality for Palivizumab, Faricimab, Evolocumab, Emicizumab, Amivantamab, and Erfonrilimab, while the

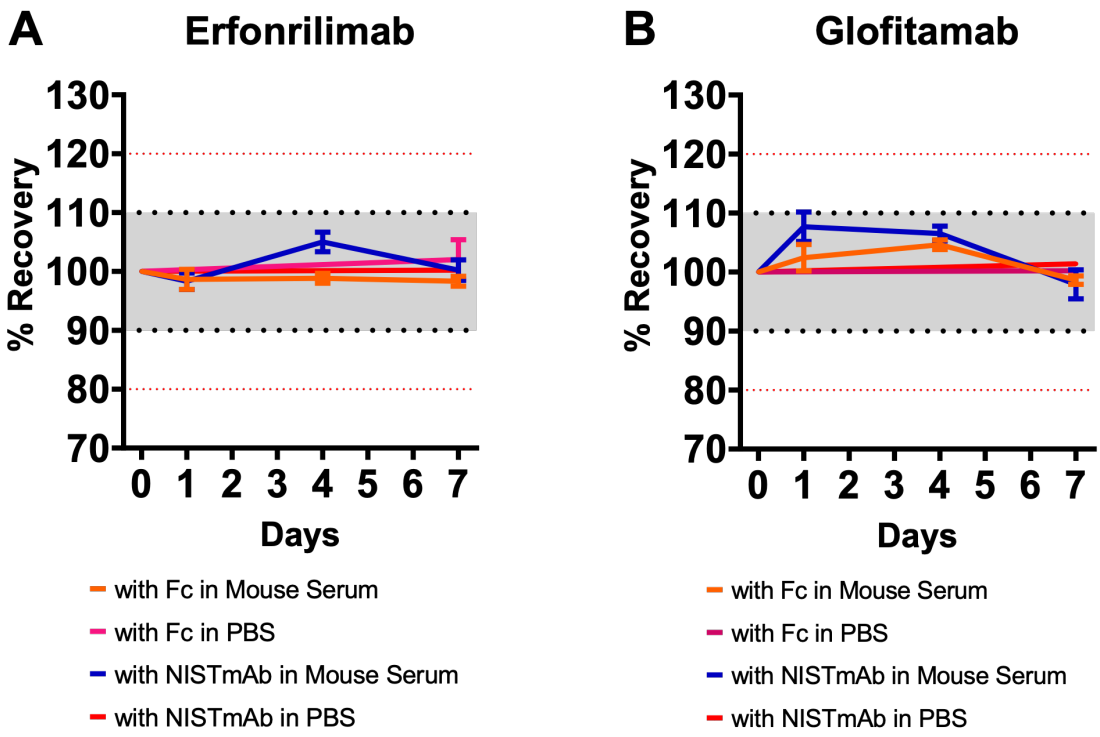

Figure 5-5: Mouse serum stability of (A) Erfonrilimab and (B) Glofitamab with NISTmAb and Fc fragment as internal standards.

data quality for the remaining molecules was not significantly impacted (Appendix Figure E-4). When the Fc fragment was not utilized as an IS, replicate precision values ranged between 0.2% and 10.0%, while the accuracies of % recoveries were all within ± 10.0% of Day 0 values with the exception of Palivizumab (-11.0% to -2.9%). These results indicated that % sample recoveries were not significantly affected by any errors that occurred during sample preparation and instrumental analysis.

We further assessed the suitability of the Fc fragment as an IS in the serums of different preclinical species. In this case, we chose to assess the stabilities of two antibodies, Bevacizumab and Dupilumab, in rat and cynomolgus monkey serums. As expected, both antibodies showed favorable stability profiles across all animal serums and PBS buffer controls, where we observed % recoveries within ± 10.0% of Day 0 values (Appendix Figure E-5). Taken together, these

results demonstrate that the Fc fragment is a highly versatile IS that can be utilized across different preclinical animal serums.

Finally, we examined the capacity of the Fc fragment to serve as a universal IS for *in vitro* serum stability assays. In this case, we examined the stability profiles of Erfonrilimab and Glofitamab using either NISTmAb or the Fc fragment as an IS in mouse serum (Figure 5-5). We observed comparable trends in stability when using either molecule as an IS, highlighting that the Fc fragment can be utilized as a universal IS since its mass does not overlap with the masses of all antibody therapeutics tested. However, the in-house bulk generation of Fc fragment via IgdE digestion is a costly, time-consuming process. To our knowledge, there is not a commercially available recombinant IgG1 Fc fragment with good *in vitro* serum stability that can be utilized in our current workflow. Therefore, full-length NISTmAb remains the best option as an IS for antibody therapeutics that are < 140 kDa and > 160 kDa in molecular weight when an Fc fragment is not needed. Nevertheless, our combined results have demonstrated that both NISTmAb and its Fc fragment are suitable ISs for the *in vitro* serum stability assessment of antibody therapeutics.

5.7 Conclusions

In this work, we have established an *in vitro* serum stability assay workflow incorporating ISs that has improved assay data quality across 19 different antibody therapeutics. We have previously noticed that the biotransformation and aggregation of antibody therapeutics in serum often lead to poor serum stability outcomes. As such, molecules undergoing biotransformation or aggregation might not be captured during our immunoaffinity purification workflow. With the absence of detectable biotransformation or aggregation in our MS analysis, the assessment of serum stability has relied on calculating % recoveries of intact molecules

across the incubation period. However, the accuracy and precision of these % recoveries are sensitive to systematic and random errors that arise during sample preparation (i.e., sample evaporation during incubation) or instrumental analysis (i.e., improper column loading), leading to potential misinterpretations of serum stability. To address this, we utilized both full-length NISTmAb and its Fc fragment, which showed favorable stability profiles across different animal serums, as ISs for a more confident *in vitro* assessment of antibody therapeutic stability in serum.

Prior to the incorporation of ISs, broad acceptance criteria (± 20.0% for both accuracies of % recoveries and precisions of technical replicates) were used to identify stable molecules during routine screening and advance them as candidates in the biopharmaceutical pipeline. However, these broad criteria made the interpretation of stability profiles challenging. For example, in the case of CTX-009, the % recoveries of individual replicates on day seven of incubation in mouse serum were 84.0%, 79.0% and 77.5% without the utilization of NISTmAb as an IS (Appendix Figure E-2F). Here, it would be misleading if CTX-009 was classified as an unstable molecule due to % recoveries of < 80.0% for two of these replicates since these recoveries might be underestimated due to uncompensated discrepancies in the workflow. Although CTX-009 can be recognized as a stable molecule using a broad acceptance criteria, the average 19.9% loss of intact CTX-009 molecule after a seven-day incubation period necessitates further interpretation. Moreover, discrepancies were seen between these results and those of other developability screening assays, further emphasizing that the *in vitro* serum results of CTX-009 acquired without an IS do not accurately depict its stability profile. In turn, the incorporation of NISTmAb as an IS resulted in a narrower range of % recoveries for CTX-009 over the seven-day incubation, allowing us to designate this antibody more confidently as a stable candidate.

Combined, our results showcase that the incorporation of stable ISs in *in vitro* serum stability assays leads to a narrower range of % recoveries (90 to 110%) across the majority of the antibodies tested with good precision between replicates. As a result, all 19 antibodies described in this work were determined to have favorable stability profiles with high confidence. In this case, a ~10.0% or lower loss of intact molecule in serum after a seven-day incubation was deemed indicative of a stable molecule. We also observed similar trends in % recoveries across the serums of different preclinical species, further highlighting the suitability of NISTmAb and its Fc fragment as ISs in these assays. We envision this improved stability screening strategy to be applied to any molecule that can be affinity captured and subsequently analyzed via LC-MS. Importantly, we anticipate this workflow to enable the identification and advancement of therapeutic antibody candidates that exhibit excellent stability for subsequent *in vivo* studies and PK/PD analysis, expanding its utility in significantly reducing costs associated with preclinical animal studies.

5.8 References

[1] Carter, P. J.; Rajpal, A. Designing antibodies as therapeutics. *Cell* **2022**, *185* (15), 2789-2805. DOI: 10.1016/j.cell.2022.05.029.

[2] Jin, S.; et al. Emerging new therapeutic antibody derivatives for cancer treatment. *Signal Transduct. Target Ther.* **2022**, *7* (1). DOI: 10.1038/s41392-021-00868-x.

[3] Qian, L.; et al. The Dawn of a New Era: Targeting the "Undruggables" with Antibody-Based Therapeutics. *Chem. Rev.* **2023**, *123* (12), 7782-7853. DOI: 10.1021/acs.chemrev.2c00915.

[4] Wang, W.; Singh, S.; Zeng, D. L.; King, K.; Nema, S. Antibody Structure, Instability, and Formulation. *J. Pharm. Sci.* **2007**, *96* (1), 1-26. DOI: 10.1002/jps.20727.

[5] Mahmood, I.; Green, M. D. Pharmacokinetic and Pharmacodynamic Considerations in the Development of Therapeutic Proteins. *Clin. Pharmacokinet.* **2005**, *44* (4), 331-347. DOI: 10.2165/00003088-200544040-00001.

[6] Correia, I. Stability of IgG isotypes in serum. *mAbs* **2010**, *2* (3), 221-232. DOI: 10.4161/mabs.2.3.11788.

[7] Nowak, C.; et al. Forced degradation of recombinant monoclonal antibodies: A practical guide. *mAbs* **2017**, *9* (8), 1217-1230. DOI: 10.1080/19420862.2017.1368602.

[8] Li, W.; et al. Characterizing and Quantitating Therapeutic Tethered Multimeric Antibody Degradation Using Affinity Capture Mass Spectrometry. *Anal. Chem.* **2020**, *92* (10), 6839-6843. DOI: 10.1021/acs.analchem.9b05739.
[9] Saurabh, S.; et al. Understanding the Stabilizing Effect of Histidine on mAb Aggregation: A Molecular Dynamics Study. *Mol. Pharmaceutics* **2022**, *19* (9), 3288-3303. DOI: 10.1021/acs.molpharmaceut.2c00453.
[10] Schuster, J.; et al. In Vivo Stability of Therapeutic Proteins. *Pharm. Res.* **2020**, *37* (2). DOI: 10.1007/s11095-019-2689-1.
[11] Avery, L. B.; et al. Establishing *in vitro in vivo* correlations to screen monoclonal antibodies for physicochemical properties related to favorable human pharmacokinetics. *mAbs* **2018**, *10* (2), 244-255. DOI: 10.1080/19420862.2017.1417718.
[12] Fourie-O'Donohue, A.; et al. Improved translation of stability for conjugated antibodies using an in vitro whole blood assay. *mAbs* **2020**, *12* (1), 1715705. DOI: 10.1080/19420862.2020.1715705.
[13] Vugmeyster, Y. Pharmacokinetics and toxicology of therapeutic proteins: Advances and challenges. *World J. Biol. Chem.* **2012**, *3* (4), 73. DOI: 10.4331/wjbc.v3.i4.73.
[14] Sawyer, W. S.; et al. High-throughput antibody screening from complex matrices using intact protein electrospray mass spectrometry. *PNAS* **2020**, *117* (18), 9851-9856. DOI: 10.1073/pnas.1917383117.
[15] Mans, J.; Oyugi, M.; Asmelash, B.; Sommers, C.; Rogstad, S. The Use of Mass Spectrometry in Therapeutic Protein Biologics License Applications: A Retrospective Review Revisited. *J. Am. Soc. Mass Spectrom.* **2023**, *34* (11), 2575-2584. DOI: 10.1021/jasms.3c00286.
[16] Song, J. G.; et al. Quantitative analysis of therapeutic proteins in biological fluids: recent advancement in analytical techniques. *Drug Delivery* **2023**, *30* (1). DOI: 10.1080/10717544.2023.2183816.
[17] Schneck, N. A.; et al. Separation techniques for intact antibody analysis by mass spectrometry. *J. Liq. Chromatogr. Relat. Technol.* **2022**, *45* (17-20), 271-283. DOI: 10.1080/10826076.2023.2199328.
[18] Chen, L.; Jiang, S.; Roos, D.; Yu, H. Y. Investigation of Potential in vivo Cleavage of Biotherapeutic Protein by Immunocapture-LC/MS. *J. Appl. Bioanal.* **2020**, *6* (1), 12-25. DOI: 10.17145/jab.20.004.
[19] Kotapati, S.; et al. Universal Affinity Capture Liquid Chromatography-Mass Spectrometry Assay for Evaluation of Biotransformation of Site-Specific Antibody Drug Conjugates in Preclinical Studies. *Anal. Chem.* **2020**, *92* (2), 2065-2073. DOI: 10.1021/acs.analchem.9b04572.
[20] Xu, K.; et al. Characterization of intact antibody-drug conjugates from plasma/serum in vivo by affinity capture capillary liquid chromatography-mass spectrometry. *Anal. Biochem.* **2011**, *412* (1), 56-66. DOI: 10.1016/j.ab.2011.01.004.
[21] Schneck, N. A.; Mehl, J. T.; Kellie, J. F. Protein LC-MS Tools for the Next Generation of Biotherapeutic Analyses from Preclinical and Clinical Serum. *J. Am. Soc. Mass Spectrom.* **2023**, *34* (9), 1837-1846. DOI: 10.1021/jasms.3c00064.
[22] Schiel, J. E.; Turner, A. The NISTmAb Reference Material 8671 lifecycle management and quality plan. *Anal. Bioanal. Chem.* **2018**, *410* (8), 2067-2078. DOI: 10.1007/s00216-017-0844-2.

[23] Karageorgos, I.; Gallagher, E. S.; Galvin, C.; Gallagher, D. T.; Hudgens, J. W. Biophysical characterization and structure of the Fab fragment from the NIST reference antibody, RM 8671. *Biologicals* **2017**, *50*, 27-34. DOI: 10.1016/j.biologicals.2017.09.005.
[24] Schiel, J. E.; et al. The NISTmAb Reference Material 8671 value assignment, homogeneity, and stability. *Anal. Bioanal. Chem.* **2018**, *410* (8), 2127-2139. DOI: 10.1007/s00216-017-0800-1.
[25] Hamuro, Y.; Derebe, M. G.; Venkataramani, S.; Nemeth, J. F. The effects of intramolecular and intermolecular electrostatic repulsions on the stability and aggregation of NISTmAb revealed by HDX-MS, DSC, and nanoDSF. *Protein Sci.* **2021**, *30* (8), 1686-1700. DOI: 10.1002/pro.4129.
[26] Turner, A.; et al. Development of orthogonal NISTmAb size heterogeneity control methods. *Anal. Bioanal. Chem.* **2018**, *410* (8), 2095-2110. DOI: 10.1007/s00216-017-0819-3.
[27] *State-of-the-Art and Emerging Technologies for Therapeutic Monoclonal Antibody Characterization Volume 2. Biopharmaceutical Characterization: The NISTmAb Case Study*; Schiel, J. E., Davis, D. L., Borisov, O. V., Eds.; ACS Symposium Series; American Chemical Society, 2015. DOI: 10.1021/bk-2015-1201.
[28] Saro, D.; et al. Developability Assessment of a Proposed NIST Monoclonal Antibody. In *State-of-the-Art and Emerging Technologies for Therapeutic Monoclonal Antibody Characterization Volume 2. Biopharmaceutical Characterization: The NISTmAb Case Study*; Schiel, J. E., Davis, D. L., Borisov, O. V., Eds.; ACS Symposium Series; American Chemical Society, 2015; pp 329-355. DOI: 10.1021/bk-2015-1201.ch007.
[29] Jenkins, R.; et al. Recommendations for Validation of LC-MS/MS Bioanalytical Methods for Protein Biotherapeutics. *AAPS J.* **2015**, *17* (1), 1-16. DOI: 10.1208/s12248-014-9685-5.

Chapter 6: Conclusions and Future Directions

6.1 Conclusions

The HOS of antibody-based therapeutics greatly influences their function, and even a minor deviation from their native conformation can diminish their clinical effectiveness and safety. Structural integrity can be compromised at any stage during their discovery and development, underscoring the need for robust, sensitive, and reliable analytical methods to monitor the coherence of protein therapeutic HOS.[1, 2] While advanced structural biology tools exist that can offer atomic-level resolution regarding protein HOS, they are not well-suited for the routine biophysical characterization of conformationally intricate antibody therapeutics and related products.[3] Recently, CIU has enabled native IM-MS to detect subtle changes in antibody HOS and stability induced by PTMs[4, 5] and degradation.[6-8] However, the adoption of IM-MS and CIU within the biopharmaceutical industry has been a slow process and is still considered niche.[9, 10] From a technical perspective, the analytical methodologies presented in this dissertation aim to further expand and validate the applicability of IM-MS and CIU technologies within the biopharmaceutical pipeline. Taken holistically, this work presents a basic mechanistic understanding of the compaction and unfolding pathways of antibodies and their derivatives in the gas-phase, as well as reveals structure-function relationships that can assist in therapeutic candidate screening and selection.

In Chapter 2, we leveraged IM-MS and CIU to scrutinize HOS correlations between an engineered KiH bsAb and its parent mAbs, permitting the annotation of antibody CIU pathways

for the first time. In a general sense, our analysis suggested that the KiH bsAb adopts an intermediate conformational and stability profile between those of its parent mAbs. This intermediate behavior stemmed from the supposition that each parent halfmer contributes to the overall stability of the bsAb. Using a combination of enzymatic approaches that generated a pool of middle-level fragments and deglycosylated constructs, we found evidence that lower- and high-energy CIU transitions of the KiH bsAb relate to the unfolding of Fab and Fc domains, respectively. A thorough quantitative analysis of CIU data further indicated that the lower-energy unfolding event is driven by the stability of the hole Fab domain, while the higher-energy CIU transition is modulated by the C_H2 and C_H3 domains of the knob portion of the Fc. Taken together, these results underscore the ability of CIU to improve our understanding of KiH bsAb structure and stability, providing crucial information in support of bsAb engineering efforts.

Chapter 3 introduced an IM-MS and CIU-based assay that, for the first time, can accurately determine the function of therapeutic mAbs. Using a series of anti-CD40 *h*IgG2 C/S exchange variants, we showed that hinge disulfides modulate the gas-phase collapse and stability of agonist antibodies in a manner that correlates with agonistic activity. Here, rigid, agonistic mAbs underwent less gas-phase structural collapse than flexible, less agonistic mAbs, leading to lower gas-phase stabilities across both full-length IgG and $F(ab')_2$ scaffolds. These shifts in gas-phase structure and stability were then utilized to build a CIU-based classification scheme that can rapidly identify agonistic variants with high precision and accuracy. In a broader sense, this work presented concrete evidence of how hinge flexibility mitigates the collapse of antibodies in the gas-phase, and it provides an experimental dataset that can assist in the gas-phase modeling of these constructs in future molecular dynamics efforts.

Extending beyond the conventional IgG scaffold, Chapter 4 demonstrated the ability of IM-MS and CIU to probe the structural polydispersity and stability of an Fc-IL-10 fusion protein engineered using a flexible Gly-Ser linker. Compared to a range of protein standards that differ in mass and flexibility, the Fc-IL-10 adopted a wider range of gas-phase conformations as evidenced by an assessment of $^{TW}\Omega_{N2}$ values and IM peak widths. The gas-phase structural dynamism of Fc-IL-10, in turn, led to significantly more structural transitions during CIU, highlighting that the Fc, IL-10, and linker components contribute to the stability of the intact fusion protein. By employing middle-level approaches reminiscent of those presented in Chapter 2, we assigned lower- and higher-energy CIU transitions of intact Fc-IL-10 to the unfolding of the IL-10 homodimer and Fc regions, respectively. Finally, we leveraged CIU to show that Gly-Ser linkers cooperatively impact the gas-phase structure and stability of isolated IL-10 homodimers. These studies constitute the first instance that CIU has probed these emerging class of therapeutics, further highlighting its applicability to other antibody-based modalities.

In addition to IM-MS-based approaches, Chapter 5 presented a new *in vitro* serum stability assay that incorporates NISTmAb as an internal standard that compensates for any discrepancies in sample recoveries during immunoaffinity purification and LC-MS analysis. Using this assay, we probed the serum stabilities of 19 clinically relevant antibodies, where we achieved sample recoveries that more accurately represent *in vitro* serum stability. This workflow has the potential to facilitate the discovery and progression of therapeutic antibody candidates with optimal stability profiles for subsequent *in vivo* studies and PK/PD analyses, thus significantly lowering costs associated with preclinical animal studies. Current efforts in this area aim to draw correlations between *in vitro* and *in vivo* studies in order to further establish the validity of this assay.

6.2 Future Directions

6.2.1 Expanding CIU beyond Knob-into-Hole Bispecific Antibodies

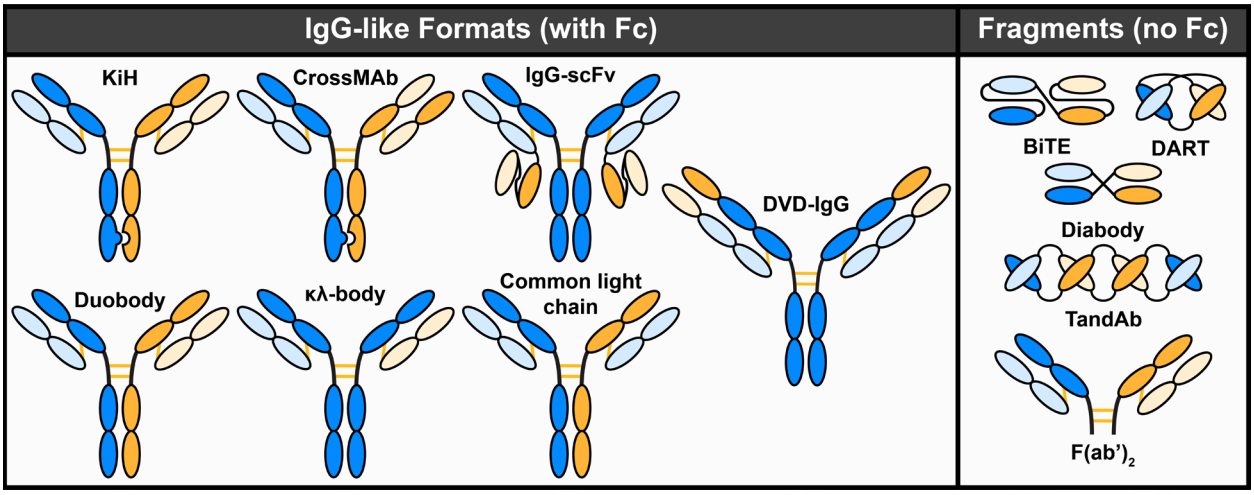

Figure 6-1: Schematic representations of various IgG-like and fragment-based formats for bsAbs. IgG-like formats include KiH, CrossMAb, IgG-scFv, DVD-IgG, Duobody, κλ-body, and formats with common light chains. Fragment-based formats include BiTE, DART, Diabody, TandAbs, and F(ab')$_2$. Heavy chains are shown in blue and yellow. Light chains are shown in light blue and yellow. Abbreviations: KiH, knobs-into-holes; scFv, single-chain variable fragment; DVD-Ig, dual-variable-domain immunoglobulin; BiTE, bispecific T-cell engager; DART, dual-affinity-retargeting; TandAb, tandem diabody.

Over the past two decades, advances in genetic engineering have transformed the development of bsAbs, generating a diverse pool of molecular structures beyond KiH scaffold studied in Chapter 2 that offer different benefits and drawbacks (Figure 6-1).[11, 12] For example, fragment-based formats circumvent the chain association issue encountered during the production of heterodimeric IgG scaffolds, as well as exhibit better tissue-penetrating abilities, minimal immunogenicity, and less nonspecific activation of the innate immune system.[11, 12] However, these Fc-deficient formats possess a shorter *in vivo* half-life, as they lack the ability to bind to FcRn. To extend the half-life of these formats, most strategies aim to increase their molecular weight and increase their stability while in circulation via the multimerization of fragments with peptide linkers (e.g., a tandem diabody, TandAb) and covalent attachment to other molecules such as polyethylene glycol (PEG) and human serum albumin (HSA).[12] These

approaches can potentially impact the HOS of these fragments, leading to potential aggregation issues that would necessitate re-engineering of the final product. In this case, IM-MS and CIU-based approaches can be valuable in delineating the implications of these approaches on the HOS of fragment-based bsAbs, especially when choosing appropriate peptide linkers during the assembly of multi-fragment constructs that exhibit minimal aggregation propensity.

IgG-like formats, on the other hand, employ various approaches to ensure the proper heterodimerization of heavy and light chains. The different molecular architectures of these formats, in turn, can have a significant effect on bsAb potency and efficacy. For instance, a dual-variable domain immunoglobulin (DVD-Ig) has been shown to have a stronger binding affinity and antitumor activity than a KiH bsAb, even though they targeted the same antigens (EGFR and PD-L1).[13] These differences in activity were attributed to the flexibility of the DVD-Ig molecule and its capacity to bind two molecules of each antigen simultaneously. As shown in Chapters 3 and 4, flexibility can greatly impact the gas-phase structures and unfolding pathways of antibody-based therapeutics during CIU; therefore, IM-MS and CIU can potentially reveal more structural insights into these promising IgG-like bispecific formats and their respective antigen-binding mechanisms. Moreover, various strategies using either steric or electrostatic steering effects have been developed to produce a complementary interface favoring heterodimerization of heavy chains as exemplified by the KiH platform.[14] Within this context, CIU would be useful in rapidly identifying the best heterodimerization approach that would generate the most stable bsAb candidates. In a more general sense, the plethora of different bsAb formats poses a major challenge in engineering stable bsAb molecules, and we aim to further develop CIU as a tool that can systematically identify bsAbs formats with favorable developability profiles in a high-throughput fashion.

6.2.2 Isotype Switching and Its Implications on IgG Gas-Phase Structure and Stability

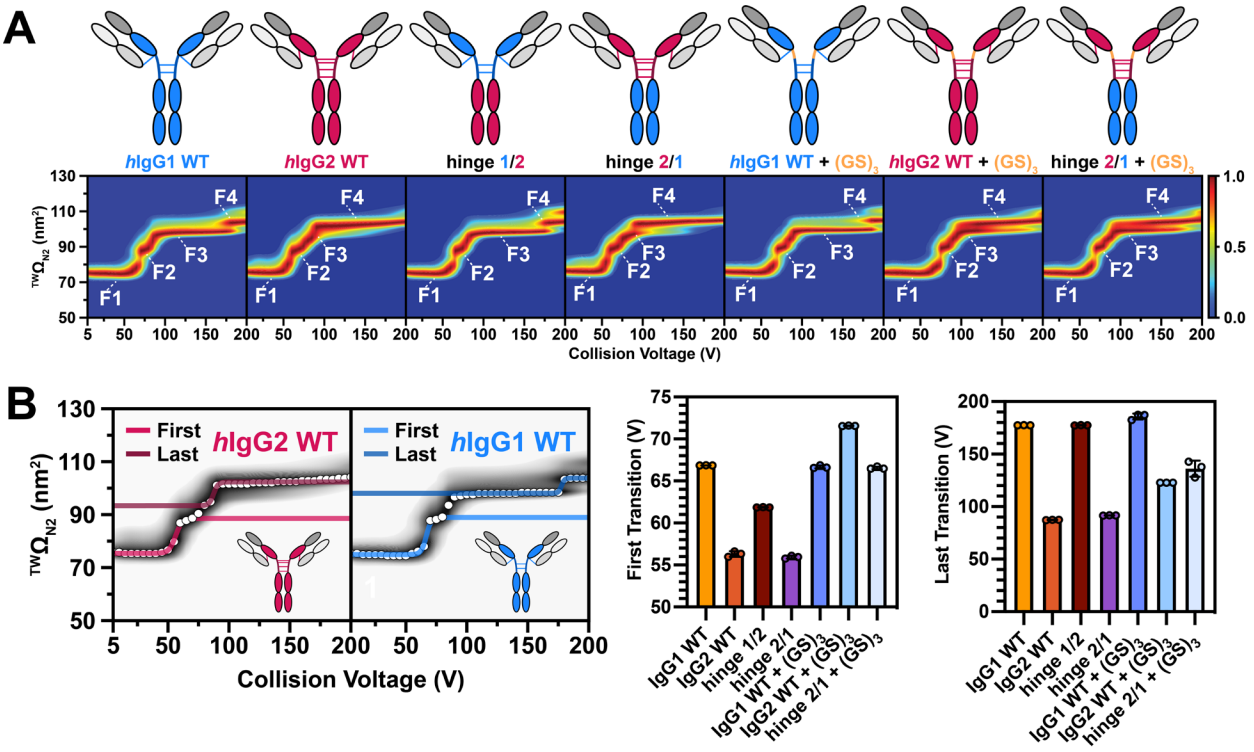

Figure 6-2: CIU (charge state 27^{+}) of hinge-swapped antibody variants with or without $(GS)_3$ linker insertions. (A) Fingerprints across all variants show four main features that differ across variants, where the appearance of feature three is more prevalent in flexible variants. Feature four is more prevalent in rigid *h*IgG2 variants. (B) Fitting of CIU_{50} values for the first and last CIU transitions (left). *h*IgG2-like variants possessed lower stability values compared to more flexible variants across both transitions (right).

In Chapter 3, we showed that rigid, *h*IgG2B isoforms underwent less structural compaction and exhibited lower gas-phase stability than nonagonistic, flexible *h*IgG2A isoforms. These results underscored that the IgG hinge greatly impacts the gas-phase structures and stabilities of antibody ions in a manner that correlates with receptor agonism. Previous studies have shown that inserting a short flexible Gly-Ser linker ("GSGSGS") into the hinge region of a *h*IgG2 reduces its immunostimulatory activity compared to control *h*IgG2 antibodies.[15] Our collaborators at the University of Southampton have also shown that isotype switching to *h*IgG2 converts antagonist antibodies to powerful agonists.[16]

To further support our claims presented in Chapter 3, we aim to apply our IM-MS and CIU-based assay to monitor HOS changes provoked by isotype hinge-swapping and the insertion of flexible Gly-Ser linkers within the IgG hinge. Our preliminary experiments in this area probed *h*IgG1(antagonist) and *h*IgG2 (agonist) forms of an antagonistic anti-CD40 mAb, 341G2, as well as hinge-swapped *h*IgG1/2 (*h*IgG1 C_H1 + hinge and *h*IgG2 C_H2 + C_H3) and *h*IgG2/1 (*h*IgG2 C_H1 + hinge and C_H2 + C_H3) variants (Figure 6-2). A qualitative assessment of CIU features revealed that increasing the flexibility of these antibodies greatly influenced higher-energy CIU features (Figure 6-2A). Moreover, hinge swapping from *h*IgG1 to *h*IgG2 or *h*IgG2 to *h*IgG1 resulted in CIU profiles similar to wild type *h*IgG2 and *h*IgG1, respectively. In terms of stability, flexible variants exhibited greater gas-phase stabilities than rigid variants in the first and last CIU transitions (Figure 6-2B). Interestingly, the insertion of a $(GS)_3$ linker in the hinge regions of *h*IgG2 WT and the hinge 2/1 variant led to a decrease in CIU stability for the first transition, as well as stabilized the third feature from unfolding to feature four. These shifts in stability skewed towards the stability profiles of *h*IgG1 variants, further confirming that hinge dynamics greatly impact gas-phase structure and stability.

Our results indicate that hinge disulfides modulate the structural collapse of mAbs that typically occurs during the nESI process, though a clear mechanistic understanding of how hinge disulfides mitigate this collapse in a way that correlates with agonism is still lacking. Ongoing efforts in this project space aim to employ charge reducing strategies to screen a wider range of charge states that would help us better understand the gas-phase compaction and unfolding mechanisms of antibodies as a whole. We also anticipate to support our experimental IM-MS findings with molecular dynamics simulations of these IgG scaffolds in the absence of bulk solvent, which can provide further insights into these compaction events. Results from these

experiments can then be compared to differential scanning calorimetry (DSC) and differential scanning fluorimetry (DSF) measurements, which can subsequently be used to establish more direct correlations between solution- and gas-phase stability measurements of therapeutically relevant antibodies.

6.2.3 Exploring the Effects of Linker Type, Length, and Composition on the HOS of Fc-Fusion Proteins

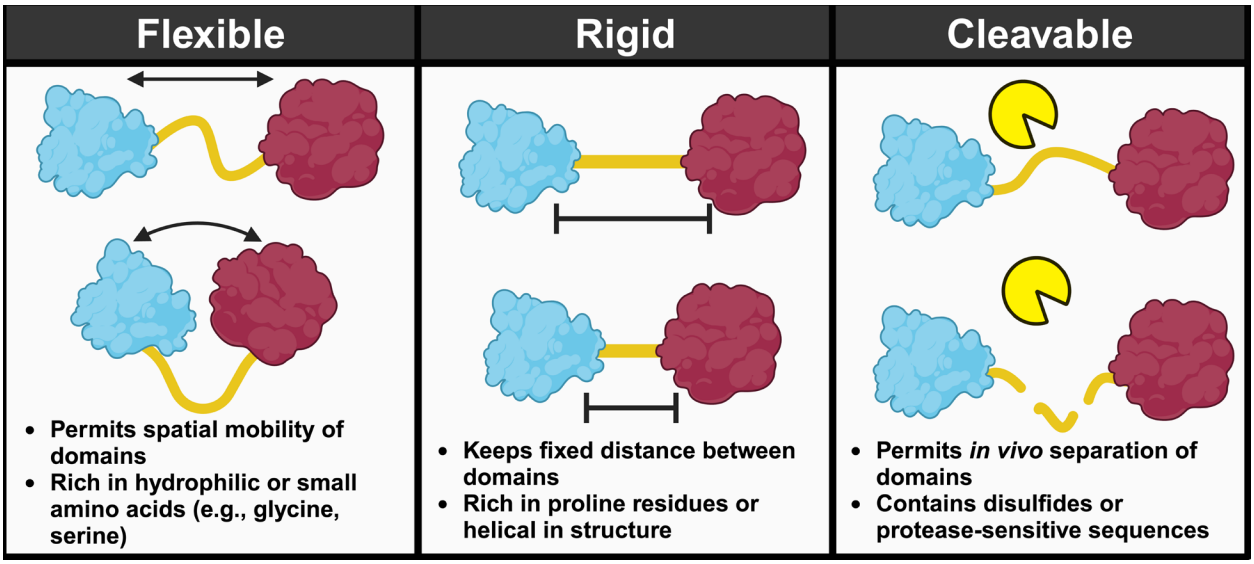

Figure 6-3: Summary of linker types used in fusion protein construction. Created with BioRender.com.

In Chapter 4, we explored a model Fc-IL-10 fusion protein assembled using flexible Gly-Ser linkers. Yet, other linker types exist beyond flexible linkers, and each are employed to achieve specific functionalities (Figure 6-3). While flexible linkers permit the spatial mobility of protein domains, rigid linkers aim to achieve an optimal distance between domains and prevent unfavorable interactions.[17] Rigid linkers are often chosen when the spatial separation of domains is needed to preserve the stability and activity of the fusion protein. In contrast, cleavable linkers are utilized to release functional domains in the presence of *in vivo* reducing agents or proteases.

This linker design is often necessitated when the isolation of active protein moieties is needed to achieve a desirable pharmacokinetic (PK) profile and biodistribution *in vivo*.[18]

Notably, the composition and length of these linkers can greatly impact bioactivity, modulate expression levels, alter pharmacokinetic profiles, and mitigate the *in vivo* targeting of Fc-fusion proteins.[19, 20] While numerous examples of different linker types exists, the systemic design of linkers for constructing stable and functional fusion proteins is still relatively new. Therefore, there is a clear need for analytical technologies that can deepen our understanding of the relationship between linker composition and Fc-fusion protein structure and function. We anticipate CIU to be sensitive to these differences in linker length and composition, as well as inform the construction of biologically active and stable recombinant Fc-fusion proteins for drug delivery applications.

6.2.4 Development of Automated Native MS Approaches to Measure *In Vitro* Serum Stability of Antibody Therapeutics

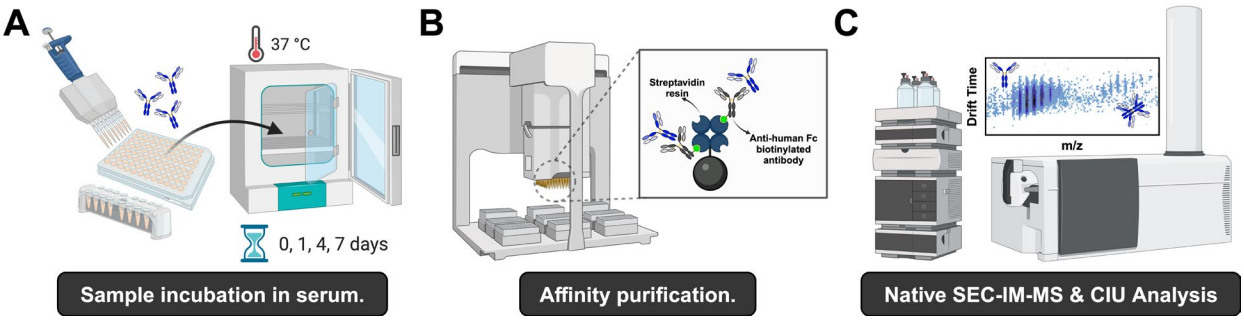

Figure 6-4: *In vitro* serum stability assay workflow. (A) *h*IgG samples are spiked into mouse, rat, or cynomolgus monkey serum and incubated at 37°C for 0, 1, 4, and 7 days. (B) Samples are then purified using an Agilent AssayMAP Bravo affinity purification system, where biotinylated anti-human IgG is immobilized on streptavidin resin and used to capture and purify *h*IgG samples. This purification step needs to be amended to preserve the folded structures of the antibodies being characterized. (C) Purified samples will then be introduced into an Agilent 6560C IM-Q-ToF system using online sample introduction and desalting via the coupling of an Agilent RapidFire system or an alternative SEC platform. Created with BioRender.com

In Chapter 6, we presented an *in vitro* serum stability assay that employed automated immunoaffinity purification and online LC-MS separations. However, this approach solely relied

on sample recoveries as a metric to assess antibody therapeutic stability in serum across different preclinical species. Since the separations in this assay were performed using denaturing conditions, noncovalent aggregates captured during purification steps are compromised, and changes in the HOS and stability of constructs are overlooked. To address this limitation, we anticipate to optimize this workflow for native IM-MS and CIU measurements using an Agilent 6560C IM-Q-ToF platform, which would permit us to perform a more accurate assessment of antibody stability based on shifts in collision cross section distributions and gas-phase stabilities (Figure 6-4).[21] This endeavor implies that immunoaffinity purifications must be amended to preserve the folded structures of the antibodies being purified. Recently, our group has developed an automated, high-throughput workflow coupling the Agilent RapidFire 400 platform with the Agilent 6560 to perform online native IM-MS and CIU measurements.[22] Incorporating this technology into our IM-MS and CIU workflow would make online sample introduction and desalting possible, which can potentially increase the usage of IM-MS and CIU in performing routine *in vitro* stability assessments within the biopharmaceutical industry.

6.3 References

[1] Weiss, W. F.; et al. Technical Decision Making With Higher Order Structure Data: Perspectives on Higher Order Structure Characterization From the Biopharmaceutical Industry. *J. Pharm. Sci.* **2016**, *105* (12), 3465-3470. DOI: 10.1016/j.xphs.2016.09.003.

[2] Nowak, C.; et al. Forced degradation of recombinant monoclonal antibodies: A practical guide. *mAbs* **2017**, *9* (8), 1217-1230. DOI: 10.1080/19420862.2017.1368602.

[3] Chen, G.; Tao, L.; Li, Z. Recent advancements in mass spectrometry for higher order structure characterization of protein therapeutics. *Drug. Discov. Today* **2022**, *27* (1), 196-206. DOI: 10.1016/j.drudis.2021.09.010.

[4] Tian, Y.; Han, L.; Buckner, A. C.; Ruotolo, B. T. Collision Induced Unfolding of Intact Antibodies: Rapid Characterization of Disulfide Bonding Patterns, Glycosylation, and Structures. *Anal. Chem.* **2015**, *87* (22), 11509-11515. DOI: 10.1021/acs.analchem.5b03291.

[5] Tian, Y.; Ruotolo, B. T. Collision induced unfolding detects subtle differences in intact antibody glycoforms and associated fragments. *Int. J. Mass Spectrom.* **2018**, *425*, 1-9. DOI: 10.1016/j.ijms.2017.12.005.

[6] Vallejo, D. D.; et al. Ion Mobility–Mass Spectrometry Reveals the Structures and Stabilities of Biotherapeutic Antibody Aggregates. *Anal. Chem.* **2022**, *94* (18), 6745-6753. DOI: 10.1021/acs.analchem.2c00160.
[7] Vallejo, D. D.; et al. Collision-Induced Unfolding Reveals Stability Differences in Infliximab Therapeutics under Native and Heat Stress Conditions. *Anal. Chem.* **2021**, *93* (48), 16166-16174. DOI: 10.1021/acs.analchem.1c03946.
[8] Kerr, R. A.; Keire, D. A.; Ye, H. The impact of standard accelerated stability conditions on antibody higher order structure as assessed by mass spectrometry. *mAbs* **2019**, *11* (5), 930-941. DOI: 10.1080/19420862.2019.1599632.
[9] Campuzano, I. D.; Lippens, J. L. Ion mobility in the pharmaceutical industry: an established biophysical technique or still niche? *Current Opinion in Chemical Biology* **2018**, *42*, 147-159. DOI: 10.1016/j.cbpa.2017.11.008.
[10] Campuzano, I. D. G. CHAPTER 13. The Role of Ion Mobility for Antibody Characterisation: A Biopharmaceutical Perspective. Royal Society of Chemistry, 2021; pp 336-366.
[11] Labrijn, A. F.; Janmaat, M. L.; Reichert, J. M.; Parren, P. W. H. I. Bispecific antibodies: a mechanistic review of the pipeline. *Nat. Rev. Drug. Discov.* **2019**, *18* (8), 585-608. DOI: 10.1038/s41573-019-0028-1.
[12] Li, H.; Er Saw, P.; Song, E. Challenges and strategies for next-generation bispecific antibody-based antitumor therapeutics. *Cell. Mol. Immunol.* **2020**, *17* (5), 451-461. DOI: 10.1038/s41423-020-0417-8.
[13] Mohan, N.; et al. Comparative Characterization of Different Molecular Formats of Bispecific Antibodies Targeting EGFR and PD-L1. *Pharmaceutics* **2022**, *14* (7), 1381. DOI: 10.3390/pharmaceutics14071381.
[14] Brinkmann, U.; Kontermann, R. E. The making of bispecific antibodies. *mAbs* **2017**, *9* (2), 182-212. DOI: 10.1080/19420862.2016.1268307.
[15] Liu, X.; et al. Human immunoglobulin G hinge regulates agonistic anti-CD40 immunostimulatory and antitumour activities through biophysical flexibility. *Nat. Commun.* **2019**, *10* (1). DOI: 10.1038/s41467-019-12097-6.
[16] Yu, X.; et al. Isotype Switching Converts Anti-CD40 Antagonism to Agonism to Elicit Potent Antitumor Activity. *Cancer Cell* **2020**, *37* (6), 850-866.e857. DOI: 10.1016/j.ccell.2020.04.013.
[17] George, R. A.; Heringa, J. An analysis of protein domain linkers: their classification and role in protein folding. *Protein Engineering, Design and Selection* **2002**, *15* (11), 871-879. DOI: 10.1093/protein/15.11.871.
[18] Chen, X.; Bai, Y.; Zaro, J. L.; Shen, W.-C. Design of an in vivo cleavable disulfide linker in recombinant fusion proteins. *BioTechniques* **2010**, *49* (1), 513-518. DOI: 10.2144/000113450.
[19] Chen, X.; Zaro, J. L.; Shen, W.-C. Fusion protein linkers: Property, design and functionality. *Adv. Drug Deliv. Rev.* **2013**, *65* (10), 1357-1369. DOI: 10.1016/j.addr.2012.09.039.
[20] Chen, X.; Zaro, J.; Shen, W.-C. Fusion Protein Linkers: Effects on Production, Bioactivity, and Pharmacokinetics. John Wiley & Sons, Inc., 2013; pp 57-73.
[21] Vallejo, D. D.; et al. A Modified Drift Tube Ion Mobility-Mass Spectrometer for Charge-Multiplexed Collision-Induced Unfolding. *Anal. Chem.* **2019**, *91* (13), 8137-8146. DOI: 10.1021/acs.analchem.9b00427.

[22] Juliano, B. R.; et al. Development of an Automated, High-Throughput Methodology for Native Mass Spectrometry and Collision-Induced Unfolding. *Anal. Chem.* **2023**, *95* (45), 16717-16724. DOI: 10.1021/acs.analchem.3c03788.

Appendices

Appendix A: The *Ruminococcus bromii* amylosome protein Sas6 binds single and double helical α-glucan structures in starch

A.1 Original Publication

This work is partially adapted from: Amanda L. Photenhauer, Rosendo C. Villafuerte-Vega, Filipe M. Cerqueira, Krista M. Armbruster, Filip Mareček, Tiantian Chen, Zdzislaw Wawrzak, Jesse B. Hopkins, Craig W. Vander Kooi, Štefan Janeček, Brandon T. Ruotolo, and Nicole M. Koropatkin. "The *Ruminococcus bromii* amylosome protein Sas6 binds single and double helical α-glucan structures in starch." *Nat. Struct. Mol. Bio.* 2024, 21, 255 – 265.

A.2 Overview

Resistant starch, defined as starch that is resistant to digestion in the upper gastrointestinal tract, is a prebiotic fiber accessed by gut bacteria with specialized amylases and starch-binding proteins.[1] The human gut symbiont *Ruminococcus bromii* is a Gram-positive anaerobe that is able to degrade resistant potato or corn starch.[2-4] In particular, *R. bromii* synthesizes multi-protein starch degrading complexes, known as amylosomes, through protein-protein interactions between dockerin and complementary cohesion domains.[5-7] As many as 32 *R.bromii* proteins have predicted cohesion or dockerin domains, and many have carbohydrate-binding modules (CBMs) that presumably assist in binding starch and tether the bacterium to its food source.[5, 8, 9] The *R. bromii* starch adherence system protein 6 (Sas6), in particular, is a secreted protein that consists of five discrete domains: an amino-terminal CBM26 (*Rb*CBM26), a

CMB74 (*Rb*CBM74) flanked by bacterial immunoglobulin-like (BIg) domains, and a C-terminal type I dockerin.[10-12]

The Koropatkin Group at the University of Michigan's Department of Microbiology and Immunology successfully captured the crystal structures of Sas6 and isolated *Rb*CBM74. Interestingly, the crystal structure of *Rb*CBM74 showed a bound double helical dimer of maltodecaose (G10), which mimics the architecture of double helical amylopectin in starch granules. As such, the *Rb*CBM74 starch-binding groove complements the double helical α-glucan geometry of amylopectin, suggesting that this module selects this feature in starch granules. However, isothermal calorimetry (ITC) experiments revealed a binding stoichiometry of 1:1 between *Rb*CBM74 and G10, even though the co-crystal structure demonstrated that two molecules of G10 are accommodated. To better determine stoichiometry and the proportion of single versus double helical maltooligosaccharide in solution, we employed native mass spectrometry (MS) in the presence of varying concentrations of G10 or maltotetradecaose (G14), which further permitted us to calculate dissociation constants (K_d) that agreed with ITC data.

A.3 Experimental Section

Native Mass Spectrometry (MS). Stock solutions of BIg–*Rb*CBM74–BIg and truncated Sas6 (Sas6T, residues 31 – 665) were provided by the Koropatkin Group were desalted and solvent exchanged into 200 mM ammonium acetate (pH 6.8 – 7.0) using Amicon Ultra-0.5 ml centrifugal filters (MilliporeSigma) with a 10 kDa molecular weight cutoff. Ten consecutive washing steps were performed to achieve sufficient desalting. The final concentrations of each protein stock solution after desalting were estimated by UV absorbance at 280 nm. A stock solution of G10 was prepared by dissolving a known mass in 200 mM ammonium acetate to achieve a final concentration of 200 μM. For native MS titration experiments used to

quantify K_d values, the concentration of protein was fixed at 5 μM, and enough G10 was added to achieve final concentrations of 0, 5, 25, 50, 100 and 150 μM. Protein–G10 mixtures were then incubated at 4 °C overnight to achieve equilibration before native MS analysis.

All native binding experiments were performed using a Q Exactive Orbitrap MS with Ultra High Mass Range (UHMR) platform (ThermoFisher Scientific).[13] Each sample (~3 μM) was transferred to a gold-coated borosilicate capillary needle (prepared in-house), and ions were generated by direct infusion using an nESI source operated in positive mode. The capillary voltage was held at 1.2 kV, the inlet capillary was heated to 250 °C and the S-lens RF level was kept at 80. Low *m*/*z* detector optimization and high *m*/*z* transfer optics were used, and the trapping gas pressure was set to two. In-source trapping was enabled with the desolvation voltage fixed at −25 V for improved ion transmission and efficient salt adduct removal. Transient times were set at 128 ms (resolution of 25,000 at *m*/*z* 400), and five microscans were combined into a single scan. A total of ~50 scans were averaged to produce the presented mass spectra. All full scan data were acquired using a noise threshold of zero to avoid pre-processing of mass spectra. A total of three measurements for each ligand concentration were performed. Data were then processed and deconvoluted using UniDec software.[14]

***K_d* Measurements by Native MS.** We performed titration experiments for both BIg–*Rb*CBM74–BIg and Sas6T using G10 and acquired modeled titration curves. Each bound state differed by ~1,639 Da, which agrees with the theoretical mass of G10. To obtain the binding constants, we summed the peak intensities of all abundant charge states in our mass spectra. Kd values were calculated using the relative intensities of unbound protein and each ligand-bound species from the mass spectra as previously described.[15] In brief, the protein–ligand binding

equilibrium of BIg–*Rb*CBM74–BIg with G10 in solution can be described by equation Appendix Equation A-11:

$$\begin{array}{ccc} & \overset{L}{} & \\ P & \rightleftharpoons & PL \\ 1\downarrow L & & 1\downarrow L \\ Pl & & PLl \end{array} \qquad \text{Appendix Equation A-1}$$

where L is the ligand and P and PL are the free protein and protein with one specifically bound ligand, respectively. As the concentration of ligand is increased, ligand molecules can bind nonspecifically during the nESI process, generating artifactual peaks in the mass spectra corresponding to a two-ligand-bound complex. Here, we presume that nonspecific binding arises equally for free protein and that which possesses one specifically bound ligand, represented by Pl and PLl in equation (Appendix Equation A-11). Based on these assumptions, the equations of mass balance and binding states can be described by equations Appendix Equation A-2 to A-5:

$$c_p = [P] + ([PL] + [Pl]) + [PLl] \qquad \text{Appendix Equation A-2}$$

$$c_L = [L] + ([PL] + [Pl]) + 2[PLl] \qquad \text{Appendix Equation A-3}$$

$$K_d = \frac{[P][L]}{[PL]} \qquad \text{Appendix Equation A-4}$$

$$K_n = \frac{[P][L]}{[Pl]} = \frac{[PL][L]}{[PLl]} \qquad \text{Appendix Equation A-5}$$

where C_P and C_L represent the total concentrations of protein and ligand, respectively, and concentrations in brackets represent those at equilibrium. K_d and K_n represent the dissociation constants for specific and nonspecific binding steps, respectively. If the peak intensities of free protein and ligand-bound complexes are proportional to the abundances of those in solution and

the spray and detection efficiency of all species is the same, then the fractional intensities of each species can be determined by equation Appendix Equation A-11:

$$F_i = \frac{\sum_n I(PL_i^{n+})/\, n}{\sum_{i=0}^{2} \sum_n (PL_i^{n+})/n} \qquad \text{Appendix Equation A-6}$$

Here, the fractional intensities are calculated as the sum of the intensities of main peak ions at all charge states. Since a Fourier transform MS method is used, signal intensities are proportional to both ion abundance and charge state. Therefore, ion intensities are normalized for each charge state, n.[16, 17] These fractional intensities can be calculated from the titration experiment at each ligand concentration and can then be related to the equilibrium constants by equations Appendix Equation A-7 to A-9:

$$F_0 = \frac{K_d K_n}{K_d K_n + [L](K_d + K_n) + [L]^2} \qquad \text{Appendix Equation A-7}$$

$$F_1 = \frac{[L](K_d + K_n)}{K_d K_n + [L](K_d + K_n) + [L]^2} \qquad \text{Appendix Equation A-8}$$

$$F_2 = \frac{[L]^2}{K_d K_n + [L](K_d + K_n) + [L]^2} \qquad \text{Appendix Equation A-9}$$

[L] can also be determined from nESI-MS titration data:

$$[L] = c_L - c_P(F_1 + 2F_2) \qquad \text{Appendix Equation A-10}$$

$[L]$ was then obtained at each ligand concentration and applied to Appendix Equation A-7 to A-9. Appendix Equation A-7 to A-9 were then fitted to experimental fractional intensities using nonlinear least-squares curve fitting using the *lsqnonlin.m*. function in MATLAB. A more detailed derivation of these equations is provided elsewhere,[15] along with the approach used for Sas6, which possesses two sites for specific binding (*Rb*CBM74 and *Rb*CBM26) and exhibits a third nonspecific bound state as shown in equation Appendix Equation A-11:

$$\begin{array}{ccccc} & & L & & L \\ & & & & \\ P & \rightleftharpoons & PL & \rightleftharpoons & PL_2 \\ 1\downarrow & & L & & 1\downarrow L \quad 1\downarrow L \\ Pl & \rightleftharpoons & PLl & \rightleftharpoons & PL_2l \end{array}$$

Appendix Equation A-11

These calculations were performed in a similar fashion for experiments performed using G14.

High-Resolution MS. Stocks of G10 or G14 were diluted to 5, 25, 50, 100, 150 and 300 μM with 200 mM ammonium acetate. Tuning parameters similar to those in native MS experiments were used with a few exceptions. All experiments were performed in negative mode, and low m/z detector optimization and low m/z transfer optics were used. The negative mode was selected, as positive mode spectra were heavily adducted with common cations present in solution. In-source trapping was 0 and −25 V for G10 and G14, respectively. G14 required more activation to assist in sufficient desolvation. We noticed that higher energies would generate excessive fragments of both G10 and G14. Transient times were set at 1,024 ms (resolution of 200,000 at m/z 400), and approximately six scans were averaged to produce the presented mass spectra.

An overlap of monoisotopic m/z peaks corresponding to single, double, and triple helices was observed at high concentrations. To approximate the relative abundance of each oligomeric state, we first simulated the isotopic distribution of each state using enviPat and then calculated the theoretical proportion of the monoisotopic species with respect to the proceeding peak that corresponds to a difference in carbon-13 composition.[18] We then manually used these proportion factors to approximate the intensities of each oligomeric state in our experimental data. Calculations were performed for six individual scans and averaged.

A.4 Results and Discussion

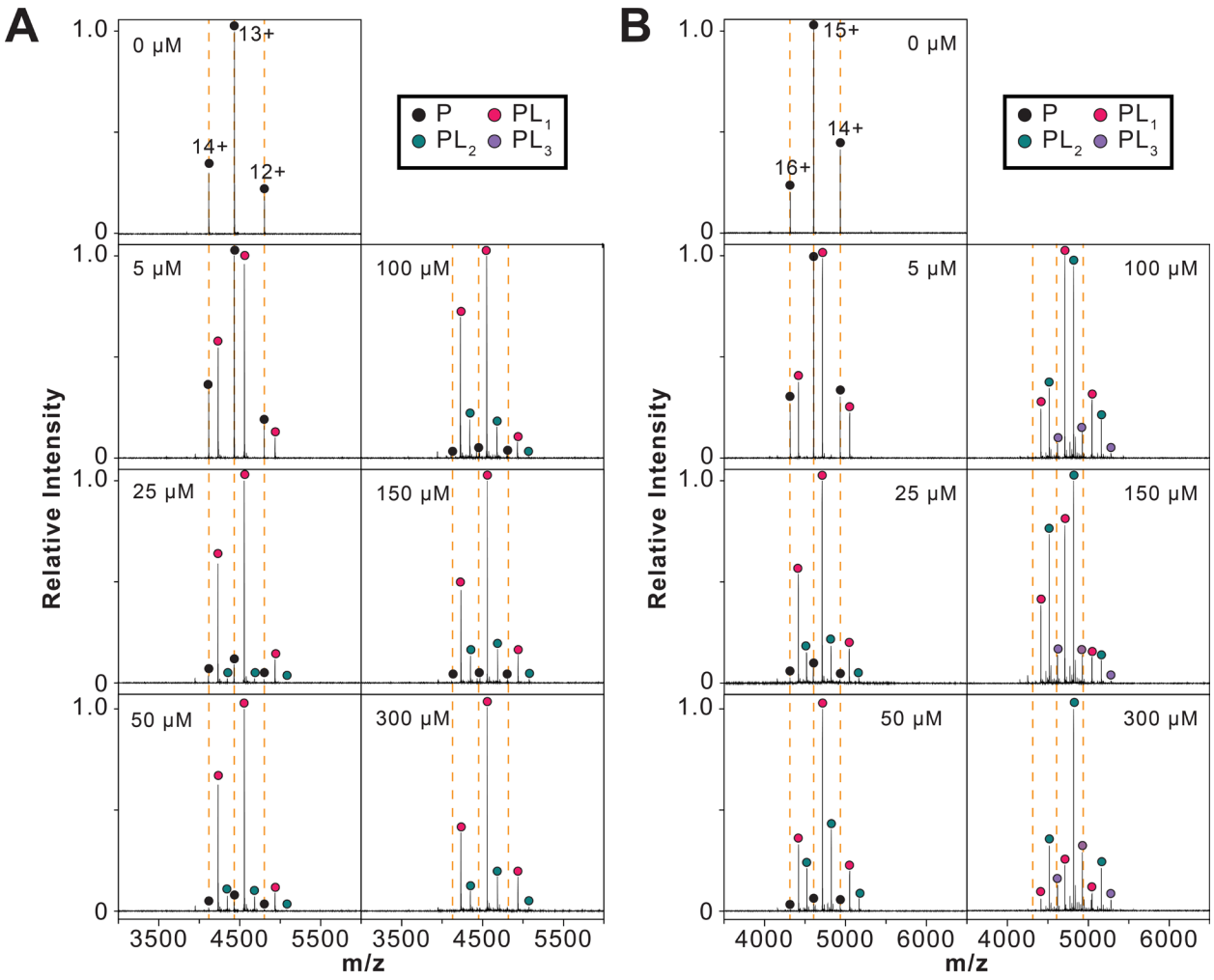

Appendix Figure A-1: Spectra of (A) BIg-*Rb*CBM74-BIg or (B) Sas6T in equilibrium with G10. Charge states for unbound protein are annotated with an orange dashed line. Peaks corresponding to different bound states are observed after each charge state of the unbound protein.

Appendix Table A-1: Average masses assigned to native MS peaks in equilibrium with G10 across all concentrations of G10 probed.

P	0 bound (Da)	1 bound (Da)	2 bound (Da)	3 bound (Da)	Av Diff. (Da)[a]
BIg-*Rb*CBM74-Big	57635.3 ± 0.8	59274.7 ± 0.6	60913.8 ± 0.2	N/A	1639.4 ± 0.8
Sas6T	69064.9 ± 0.6	70704.3 ± 0.5	72343.8 ± 1.8	73982.1 ± 0.6	1639.3 ± 1.0

[a]Average difference between bound states across all ligand concentrations.

Native MS experiments for experiments of BIg-*Rb*CBM74-BIg and G10 revealed a number of bound states (Appendix Figure A-1A). Each observed state differed by ~1,639 Da,

A G10

P	Charge States	K_{d1} (μM)	K_{d2} (μM)	K_n (μM)[a]	SSR[b]
BIg-*Rb*CBM74-Big	12+ to 14+	2.16 ± 0.53	N/A	922.73 ± 259.93	0.0375
Sas6	14+ to 16+	2.30 ± 0.25	104.64 ± 8.63	737.48 ± 142.57	0.0094

[a] K_n - dissociation constant for nonspecific binding step during nESI. Values reported with 95% confidence interval. [b] SSR - sum of squared residuals

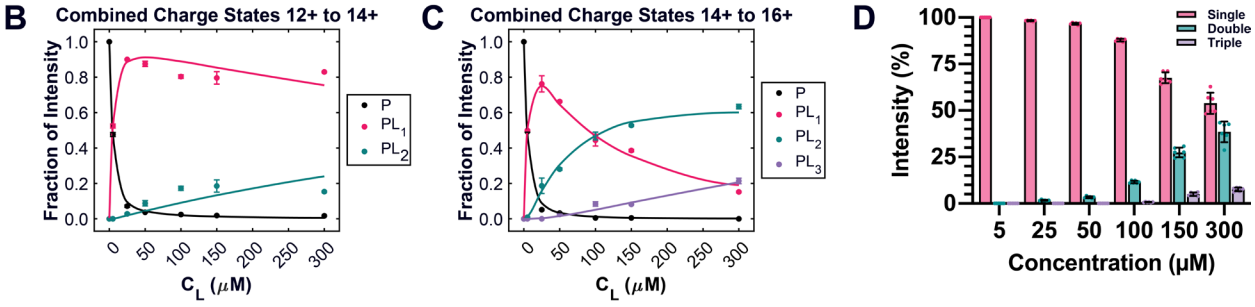

E G14

P	Charge States	K_{d1} (μM)	K_{d2} (μM)	K_n (μM)[a]	SSR[b]
BIg-*Rb*CBM74-Big	12+ to 14+	1.29 ± 0.10	N/A	125.50 ± 5.13	0.0030
Sas6	14+ to 16+	0.17 ± 0.03	64.44 ± 4.83	494.80 ± 63.10	0.0083

[a] K_n - dissociation constant for nonspecific binding step during nESI. Values reported with 95% confidence interval. [b] SSR - sum of squared residuals

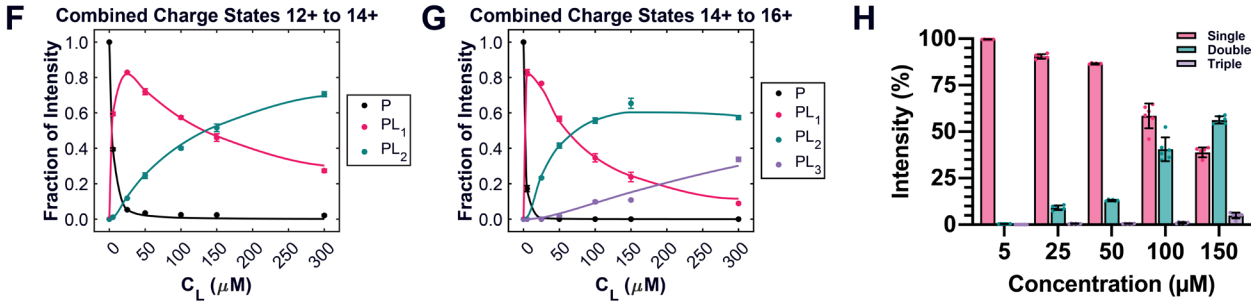

Appendix Figure A-2: Native MS of 5 µM protein and ligand. Intensities of each species, combined across multiple charge states, were extracted from the mass spectra and used to calculate the fractional abundance of unbound and bound states at equilibrium. (A) Binding affinities (K_d) calculated from the fractional intensity of each species for G10. N/A, not available. (B,C) Nonlinear least-squares fitting of fractional abundance of unbound and bound states for 0–300 µM G10 with BIg–*Rb*CBM74–BIg (B) and Sas6T (C). Error bars represent standard deviation of three technical replicates. (B), Mean of isotopic distribution of single, double, and triple helices over different concentrations of G10. Error bars represent standard deviation of six scans. (E) K_d calculated from the fractional intensity of each species for G14. (F,G) Nonlinear least-squares fitting of fractional abundance of unbound and bound states for 0–300 µM G14 with BIg–*Rb*CBM74–BIg (F) and Sas6T (G). Error bars represent standard deviation of three technical replicates. (H), Mean of isotopic distribution of single, double, and triple helices over different concentrations of G14. Error bars represent standard deviation of six scans. CL, concentration of the ligand; P, protein; PL, protein–ligand.

the theoretical mass of G10 (Appendix Table A-1). To obtain binding affinities, we summed the peak intensities of all abundant charge states in our spectra and analyzed these intensity values as described previously.[19] The K_d for BIg–*Rb*CBM74–BIg was determined to be 2.16 ± 0.53 µM,

which agrees with our ITC data (Appendix Figure A-1A and Appendix Figure A-2A,B). As the concentration of ligand is increased, ligand molecules can bind nonspecifically during the nano-electrospray ionization (nESI) process, generating artifactual peaks in the mass spectra corresponding to a two-ligand-bound complex. This step is given by K_n, which corresponds to the dissociation constant for the nonspecific binding step during the nESI process; this variable also captures multimers of the ligand itself or nESI artifacts that encompass high concentrations of ligand trapped within individual droplets. Our K_n of 922.7 ± 259.9 μM suggests that an additional binding site on BIg–*Rb*CBM74–BIg is highly unlikely (Appendix Figure A-2A).

For Sas6T, the binding state distribution was markedly different (Appendix Figure A-1B and Appendix Figure A-2A,C). At low G10 concentrations, there is a mix of one-bound and two-bound states, and as G10 increases, the two-bound fraction dominates. K_d values for 1:1 and 1:2 protein:ligand complexes were calculated to be 2.30 ± 0.25 μM and 104.64 ± 8.63 μM, respectively, in reasonable agreement with ITC data for BIg–*Rb*CBM74–BIg and *Rb*CBM26 alone (Appendix Figure A-2A). These data best support a model whereby *Rb*CBM26 and *Rb*CBM74 each bind one molecule of G10 independently.

Longer maltooligosaccharides form double helices in solution, and high-resolution MS with G10 showed a wide range of charged state distributions corresponding to single, double and triple helical structures depending on concentration (Appendix Figure A-2D and Appendix Figure A-3). G10 forms double and triple helices at high concentrations (300 μM), the latter of which may be an artifact of the ESI process, or by double helix formation from overlapping G10 molecules (Appendix Figure A-3). Although we could not resolve peaks from higher concentrations of G10, we can conclude that at 1 mM, the concentration used for crystallization, most of the ligand forms double helices. However, as *Rb*CBM74 does not absolutely require a

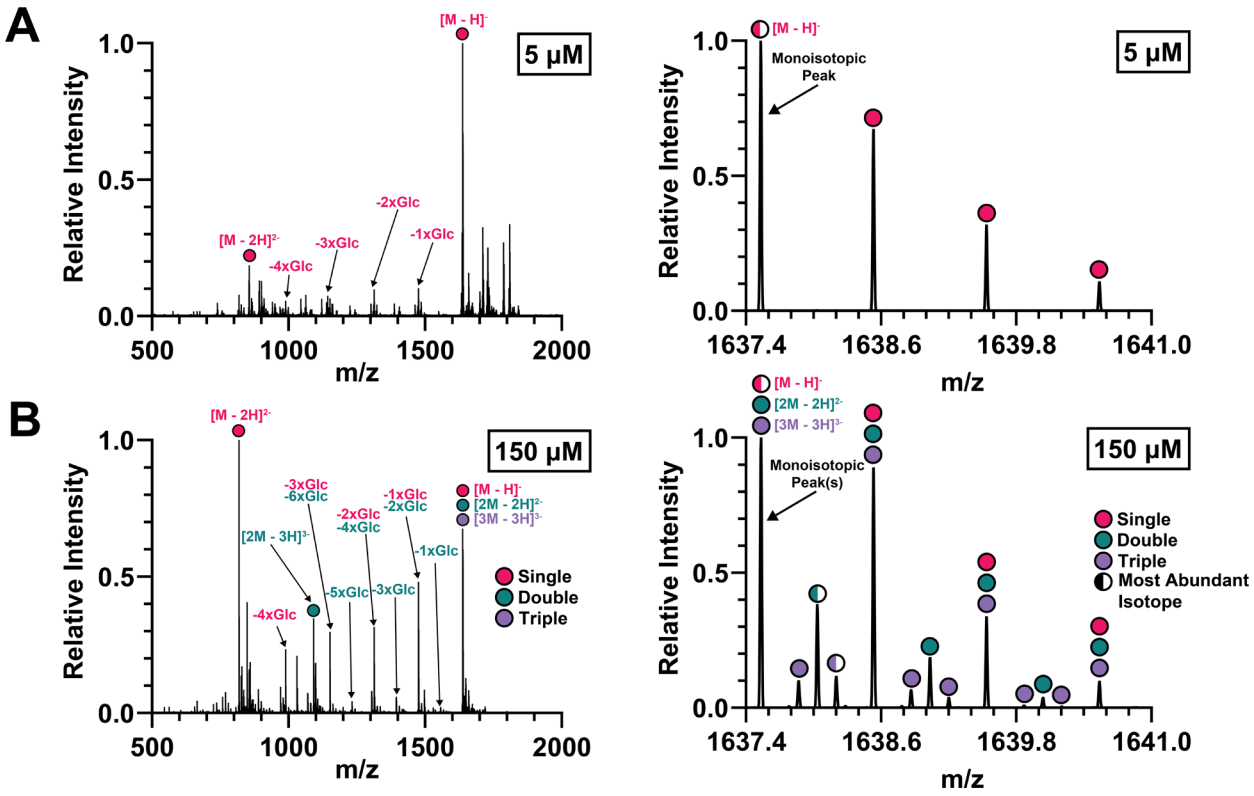

Appendix Figure A-3: High-resolution MS experiments of G10 alone at (A) 5 µM and (B) 150 µM. A zoomed-in mass spectrum (right) shows the isotopic distributions of oligomeric states at each respective concentration.

double helix but rather α-glucan that adopts the correct geometry, it is not surprising to see our high-affinity binding site saturated by a single G10 by both ITC and native MS, as this is the more abundant species at low concentrations.

Given that this protein binds solubilized potato amylopectin with ~tenfold better affinity than G10, we performed native MS with maltotetradecaose (G14). Each observed state differed by the expected theoretical mass of G14 (~2288 Da) (Appendix Table A-2). BIg–*Rb*CBM74–BIg exhibits a modestly higher affinity for G14 ($K_d = 1.29 \pm 0.10$ µM) than G10 ($K_d = 2.16 \pm 0.53$ µM) (Appendix Figure A-2E,F). The binding state distribution for BIg–*Rb*CBM74–BIg demonstrated that the two-bound state becomes the dominant species at higher G14 concentrations (Appendix Figure A-4A). For Sas6T, we observed a binding state distribution similar to that with G10 (Appendix Figure A-2G). Notably, we observed higher

Appendix Table A-2: Average masses assigned to native MS peaks in equilibrium with G14 across all concentrations of G14 probed.

P	0 bound (Da)	1 bound (Da)	2 bound (Da)	3 bound (Da)	Av Diff. (Da)[a]
BIg-*Rb*CBM74-Big	57635.8 ± 0.9	59923.5 ± 0.9	62211.2 ± 0.5	N/A	2287.6 ± 0.9
Sas6T	69064.1 ± 0.2	71352.5 ± 0.7	73640.5 ± 0.4	75928.2 ± 0.2	2288.1 ± 0.9

[a]Average difference between bound states across all ligand concentrations.

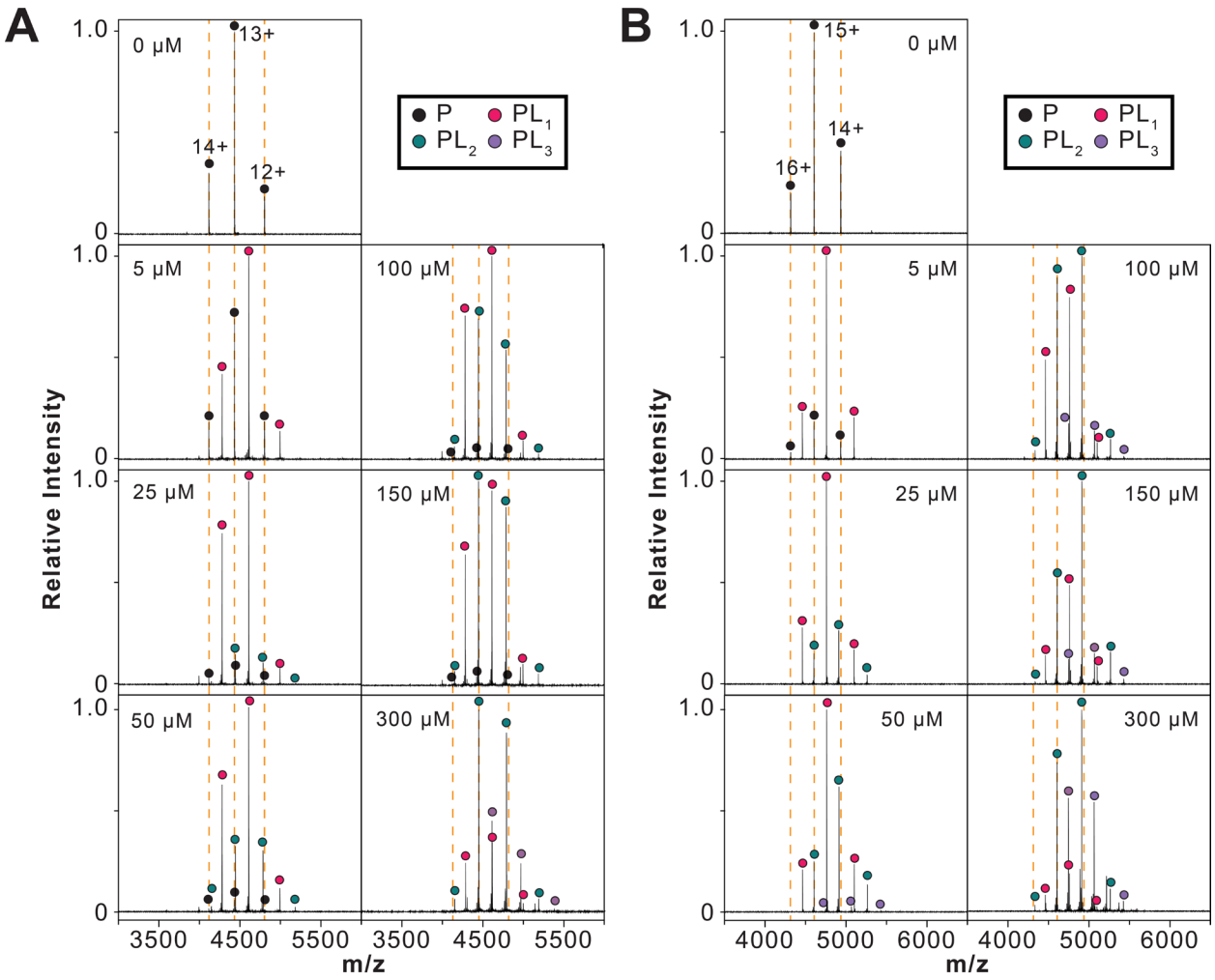

Appendix Figure A-4: Spectra of (A) BIg-*Rb*CBM74-BIg or (B) Sas6T in equilibrium with G14. Charge states for unbound protein are annotated with an orange dashed line. Peaks corresponding to different bound states are observed after each charge state of the unbound protein.

affinities for G14 for both one-bound and two-bound states (K_d values of 0.17 ± 0.03 μM and 64.44 ± 4.83 μM, respectively) (Appendix Figure A-2E). This suggests that the *Rb*CBM74 binding platform extends beyond what we see in our crystal structure. Our lower K_n for both

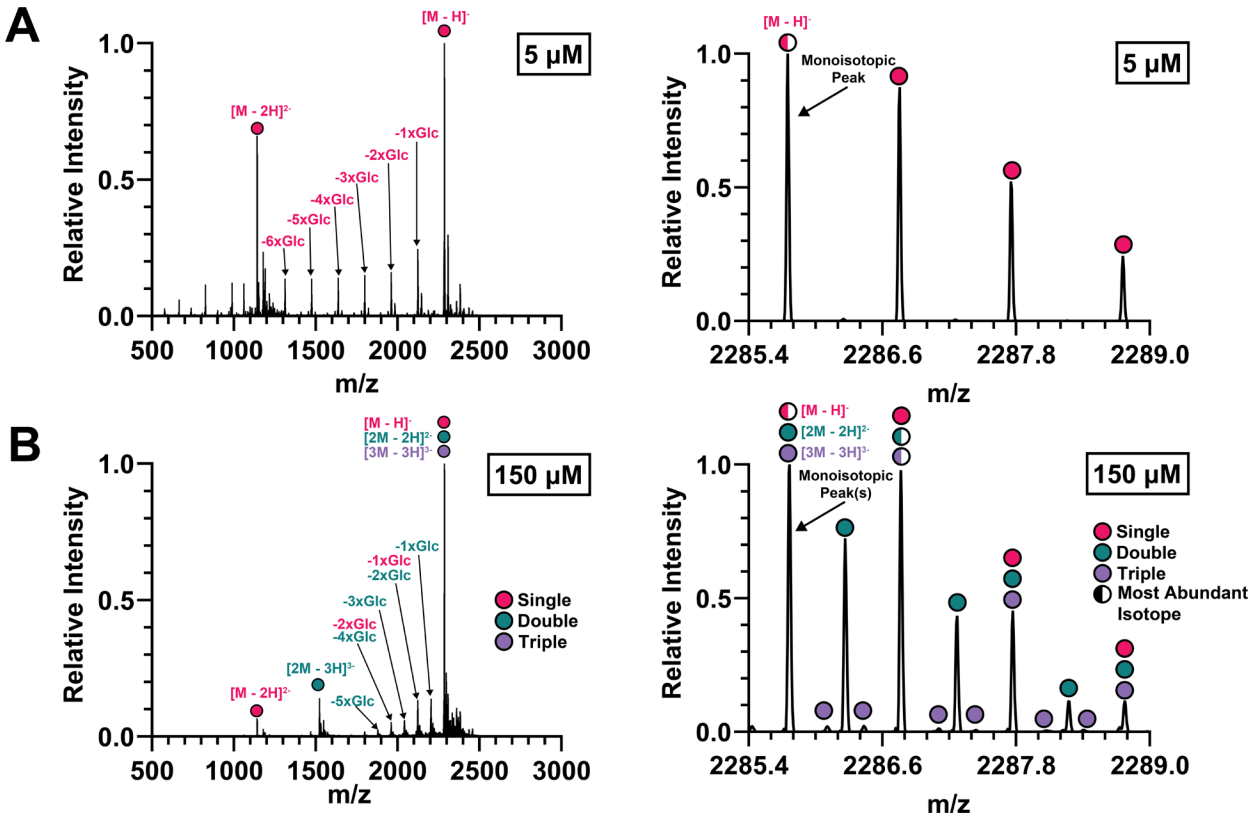

Appendix Figure A-5: High-resolution MS experiments of G14 alone at (A) 5 µM and (B) 150 µM. A zoomed-in mass spectrum (right) shows the isotopic distributions of oligomeric states at each respective concentration.

constructs with G14 may be an artifact of the nESI process, as described above, rather than an additional binding site, although we cannot completely rule out this possibility. The higher affinity observed for Sas6T over the *Rb*CBM74 may be because binding by the longer ligand is aided by the juxtaposition of the CBM26, which then becomes saturated at higher concentrations. It is possible that there is some synergy in binding at the two sites with longer ligands, although further work is needed to investigate this possibility. High-resolution MS of G14 alone demonstrates both single and double helical populations, with more than half of the ligand forming double helices at 150 µM (Appendix Figure A-2H and Appendix Figure A-5). As these states are in equilibrium, we cannot test binding to a single versus a double helical structure. However, the *Rb*CBM74 site clearly selects maltooligosaccharides that adopt the geometry found in double helical α1,4-linked glucose. Taken together, our native MS results

suggest that both single and double helical α-glucans that adopt the geometry of double helical amylopectin are recognized by *Rb*CBM74.

A.5 References

[1] Zaman, S. A.; Sarbini, S. R. The potential of resistant starch as a prebiotic. *Crit. Rev. Biotechnol.* **2015**, 1-7. DOI: 10.3109/07388551.2014.993590.

[2] Ze, X.; Duncan, S. H.; Louis, P.; Flint, H. J. *Ruminococcus bromii* is a keystone species for the degradation of resistant starch in the human colon. *ISME J.* **2012**, *6* (8), 1535-1543. DOI: 10.1038/ismej.2012.4.

[3] Venkataraman, A.; et al. Variable responses of human microbiomes to dietary supplementation with resistant starch. *Microbiome* **2016**, *4* (1). DOI: 10.1186/s40168-016-0178-x.

[4] Baxter, N. T.; et al. Dynamics of Human Gut Microbiota and Short-Chain Fatty Acids in Response to Dietary Interventions with Three Fermentable Fibers. *mBio* **2019**, *10* (1), e02566-02518. DOI: 10.1128/mbio.02566-18.

[5] Ze, X.; et al. Unique Organization of Extracellular Amylases into Amylosomes in the Resistant Starch-Utilizing Human Colonic Firmicutes Bacterium *Ruminococcus bromii*. *mBio* **2015**, *6* (5), e01058-01015. DOI: 10.1128/mbio.01058-15.

[6] Smith, S. P.; Bayer, E. A. Insights into cellulosome assembly and dynamics: from dissection to reconstruction of the supramolecular enzyme complex. *Curr. Opin. Struct. Biol.* **2013**, *23* (5), 686-694. DOI: 10.1016/j.sbi.2013.09.002.

[7] Bayer, E. A.; Morag, E.; Lamed, R. The cellulosome — A treasure-trove for biotechnology. *Trends Biotechnol.* **1994**, *12* (9), 379-386. DOI: 10.1016/0167-7799(94)90039-6.

[8] Mukhopadhya, I.; et al. Sporulation capability and amylosome conservation among diverse human colonic and rumen isolates of the keystone starch-degrader *Ruminococcus bromii*. *Environ. Microbiol.* **2018**, *20* (1), 324-336. DOI: 10.1111/1462-2920.14000.

[9] Janeček, Š.; Mareček, F.; Macgregor, E. A.; Svensson, B. Starch-binding domains as CBM families–history, occurrence, structure, function and evolution. *Biotechnol. Adv.* **2019**, *37* (8), 107451. DOI: 10.1016/j.biotechadv.2019.107451.

[10] Zhang, H.; et al. dbCAN2: a meta server for automated carbohydrate-active enzyme annotation. *Nucleic Acids Res.* **2018**, *46* (W1), W95-W101. DOI: 10.1093/nar/gky418.

[11] Lombard, V.; Golaconda Ramulu, H.; Drula, E.; Coutinho, P. M.; Henrissat, B. The carbohydrate-active enzymes database (CAZy) in 2013. *Nucleic Acids Res.* **2014**, *42* (D1), D490-D495. DOI: 10.1093/nar/gkt1178.

[12] Blum, M.; et al. The InterPro protein families and domains database: 20 years on. *Nucleic Acids Res.* **2021**, *49* (D1), D344-D354. DOI: 10.1093/nar/gkaa977.

[13] van De Waterbeemd, M.; et al. High-fidelity mass analysis unveils heterogeneity in intact ribosomal particles. *Nat. Methods* **2017**, *14* (3), 283-286. DOI: 10.1038/nmeth.4147.

[14] Marty, M. T.; et al. Bayesian Deconvolution of Mass and Ion Mobility Spectra: From Binary Interactions to Polydisperse Ensembles. *Anal. Chem.* **2015**, *87* (8), 4370-4376. DOI: 10.1021/acs.analchem.5b00140.

[15] Gülbakan, B.; et al. Native Electrospray Ionization Mass Spectrometry Reveals Multiple Facets of Aptamer–Ligand Interactions: From Mechanism to Binding Constants. *J. Am. Chem. Soc.* **2018**, *140* (24), 7486-7497. DOI: 10.1021/jacs.7b13044.
[16] Wang, W.; Kitova, E. N.; Klassen, J. S. Influence of Solution and Gas Phase Processes on Protein−Carbohydrate Binding Affinities Determined by Nanoelectrospray Fourier Transform Ion Cyclotron Resonance Mass Spectrometry. *Anal. Chem.* **2003**, *75* (19), 4945-4955. DOI: 10.1021/ac034300l.
[17] Báez Bolivar, E. G.; et al. Submicron Emitters Enable Reliable Quantification of Weak Protein–Glycan Interactions by ESI-MS. *Anal. Chem.* **2021**, *93* (9), 4231-4239. DOI: 10.1021/acs.analchem.0c05003.
[18] Loos, M.; Gerber, C.; Corona, F.; Hollender, J.; Singer, H. Accelerated Isotope Fine Structure Calculation Using Pruned Transition Trees. *Anal. Chem.* **2015**, *87* (11), 5738-5744. DOI: 10.1021/acs.analchem.5b00941.
[19] Soper, M. T.; Detoma, A. S.; Hyung, S.-J.; Lim, M. H.; Ruotolo, B. T. Amyloid-β–neuropeptide interactions assessed by ion mobility-mass spectrometry. *Phys. Chem. Chem. Phys.* **2013**, *15* (23), 8952. DOI: 10.1039/c3cp50721a.

Appendix B: Supporting Information for Chapter 2

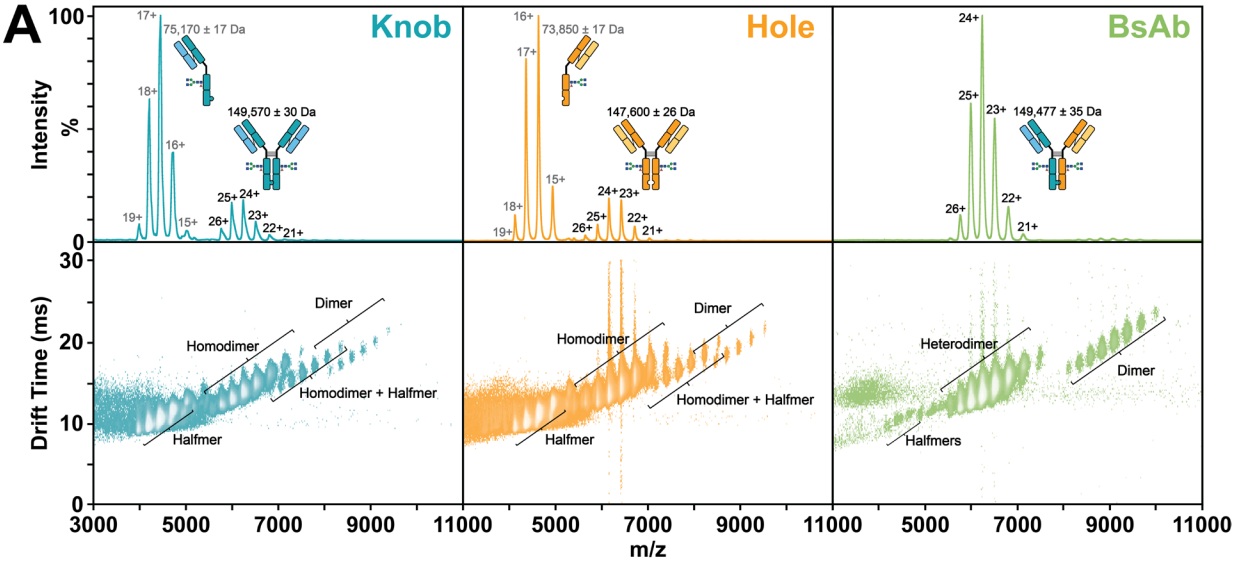

B

Knob	
ID	Average Mass (Da)
Deglycosylated	146,148
G0F + G0F	149,039
G0F + G1F	149,201
G1F + G1F	149,363
G1F + G2F	149,525
G2F + G2F	149,688

Hole	
ID	Average Mass (Da)
Deglycosylated	144,148
G0F + G0F	147,039
G0F + G1F	147,201
G1F + G1F	147,363
G1F + G2F	147,525
G2F + G2F	147,687

BsAb	
ID	Average Mass (Da)
Deglycosylated	145,148
G0F + G0F	148,039
G0F + G1F	148,201
G1F + G1F	148,363
G1F + G2F	148,525
G2F + G2F	148,688

Appendix Figure B-1: (A) Native IM-MS spectra of knob, hole, and KiH bsAb constructs at a collision voltage of 5 V. Intact homodimer and heterodimer are observed, as well as low and high molecular weight species. Here, 'dimer' refers to a dimer of homodimer or heterodimer. (B) Theoretical average masses of glycoforms typically observed in antibodies. All native intact masses are non-reduced and include the cyclization of all N-terminal glutamines to pyroglutamate forms.

A

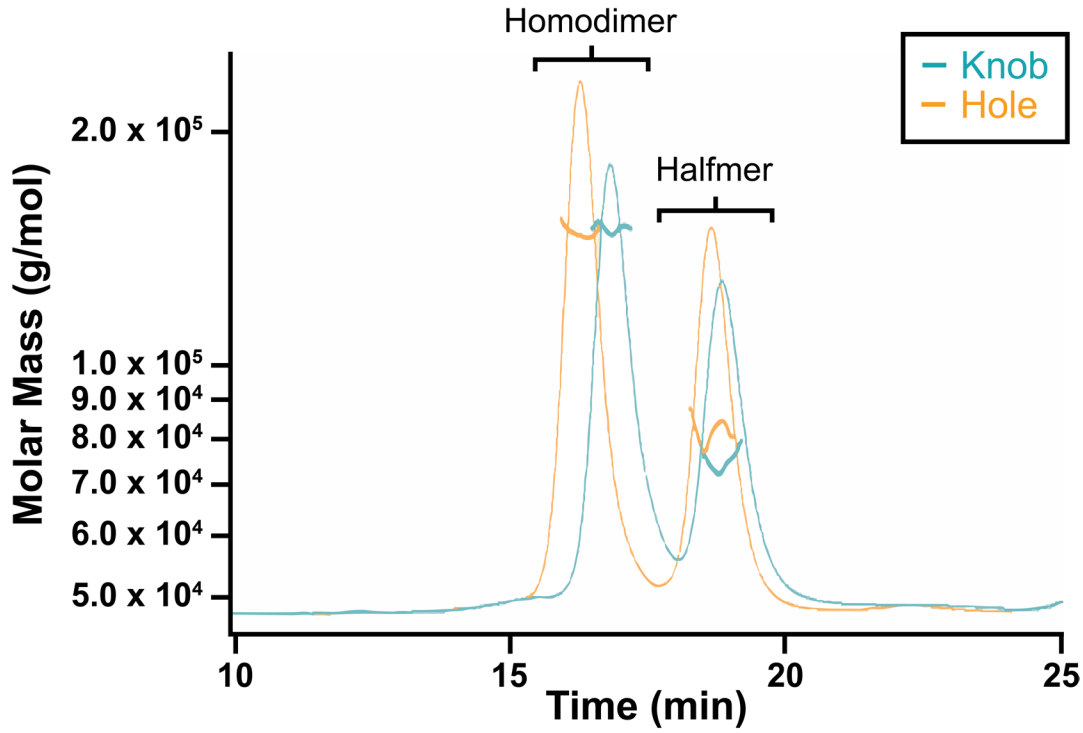

B

Sample	Homodimer		Halfmer	
	Mass (kDa)	Mass Fraction (%)	Mass (kDa)	Mass Fraction (%)
Knob	149.5 (± 3.2%)	56.4	74.3 (± 8.6%)	43.6
Hole	147.6 (± 2.3%)	56.9	81.3 (± 6.7%)	43.1

Appendix Figure B-2: SEC-MALS for Knob and Hole samples. (A) SEC-MALS profile of Knob and Hole homodimers and halfmers. (B) Calculated masses of homodimer and halfmer species for both Knob and Hole samples.

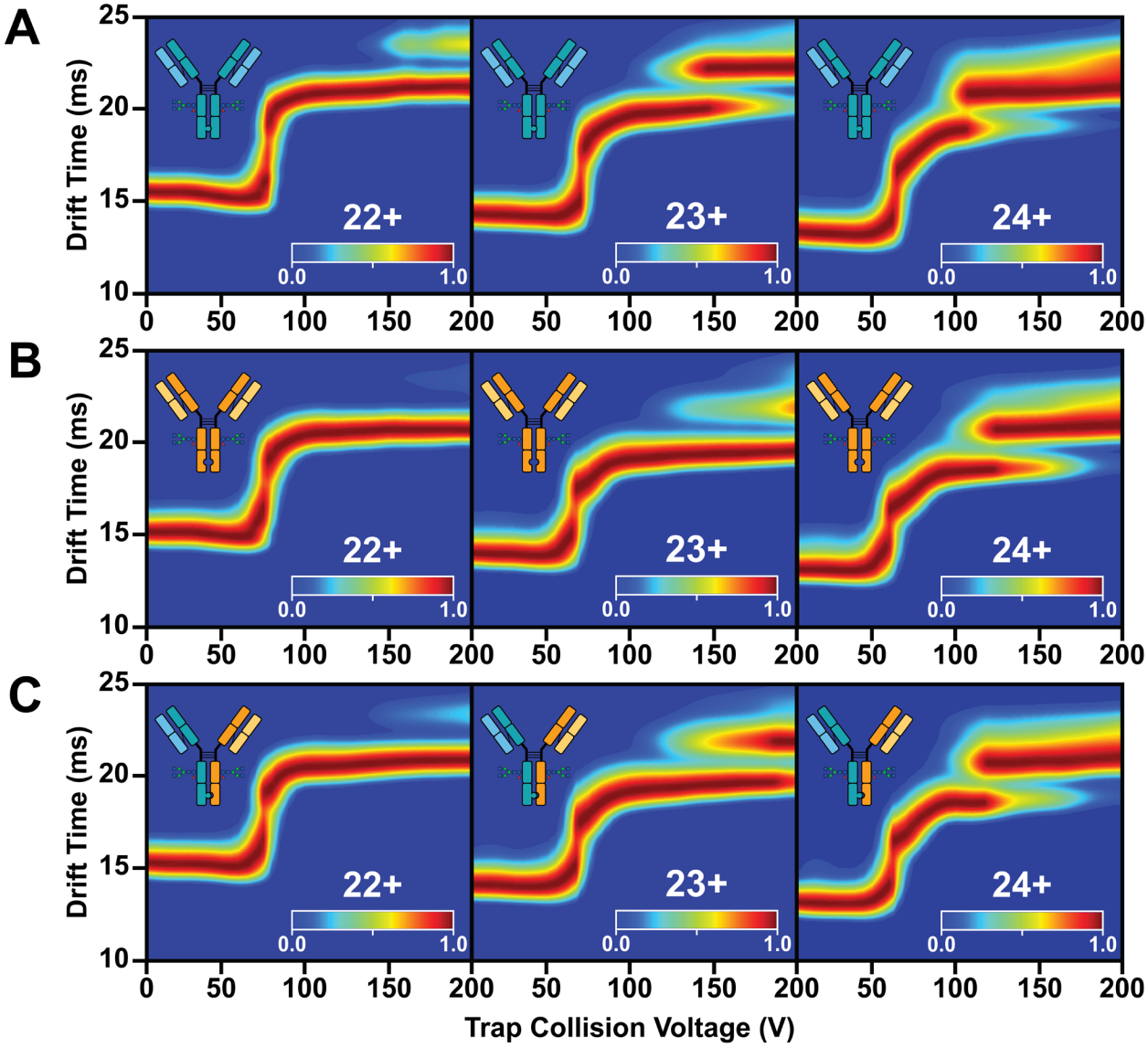

Appendix Figure B-3: CIU fingerprints of knob (A) and hole (B) homodimers and KiH bsAb heterodimer (C) for charge states 22^+ to 24^+.

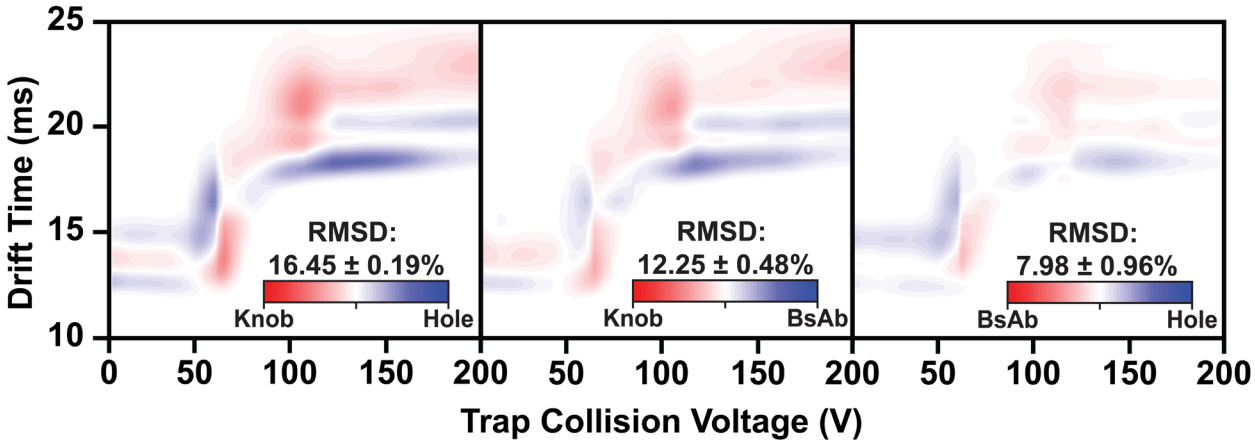

Appendix Figure B-4: RMSD plots of the 24^{+} charge state of knob and hole homodimers and KiH bsAb heterodimer.

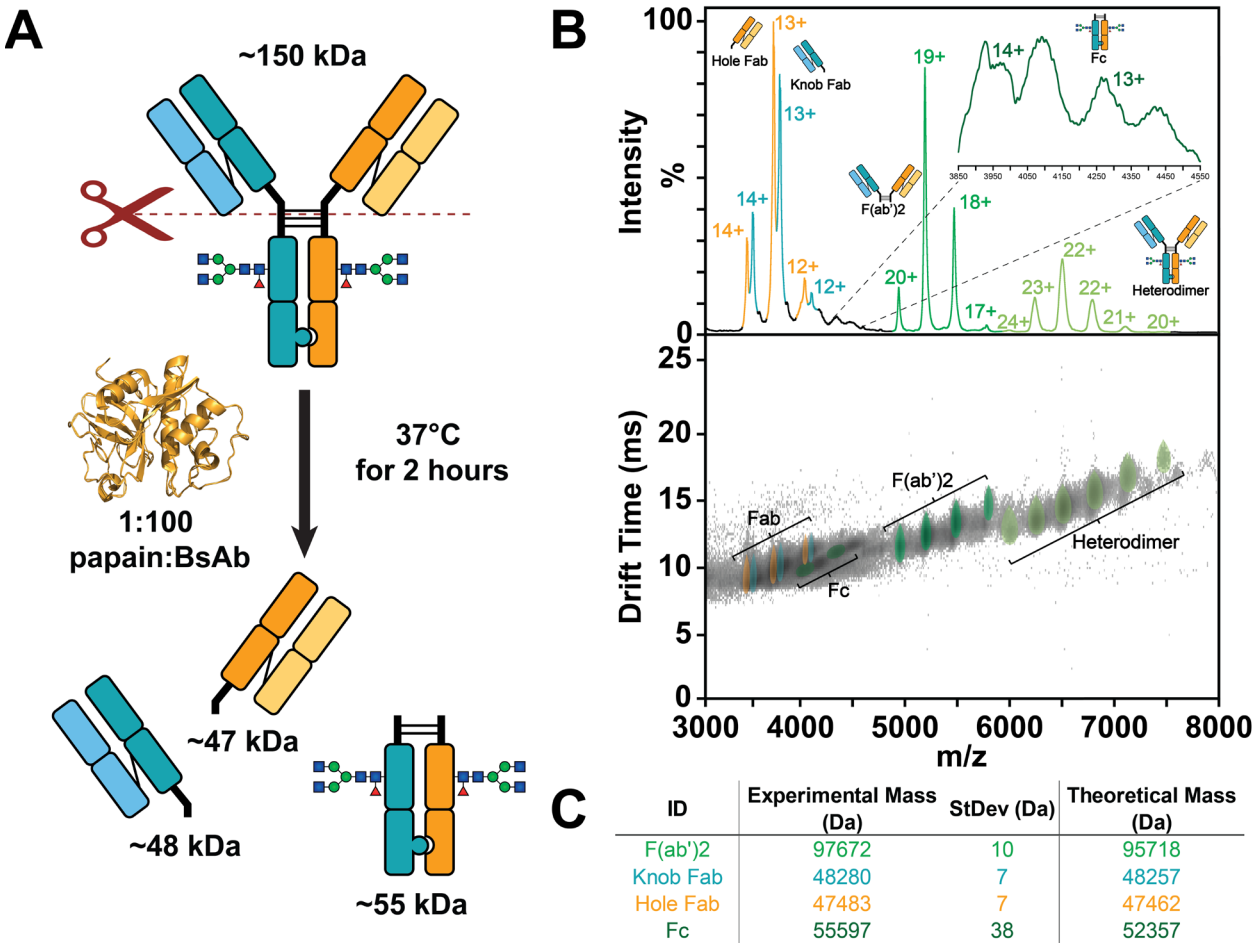

C

ID	Experimental Mass (Da)	StDev (Da)	Theoretical Mass (Da)
F(ab')2	97672	10	95718
Knob Fab	48280	7	48257
Hole Fab	47483	7	47462
Fc	55597	38	52357

Appendix Figure B-5: Papain digestion of KiH bsAb. (A) Proposed cleavage site of papain above the hinge region, generating Fab and Fc fragments. (B) IM-MS spectra of KiH bsAb papain digest and (C) comparison of experimental and average theoretical masses. Differences observed between experimental and theoretical masses of $F(ab')_2$ are attributed to non-specific cleavage of the bsAb by papain. The theoretical mass for Fc accounts for two G0F glycosylation sites and cyclization of all N-terminal glutamines to pyroglutamate forms. The experimental mass of the Fc domain accounts all possible glycoforms.

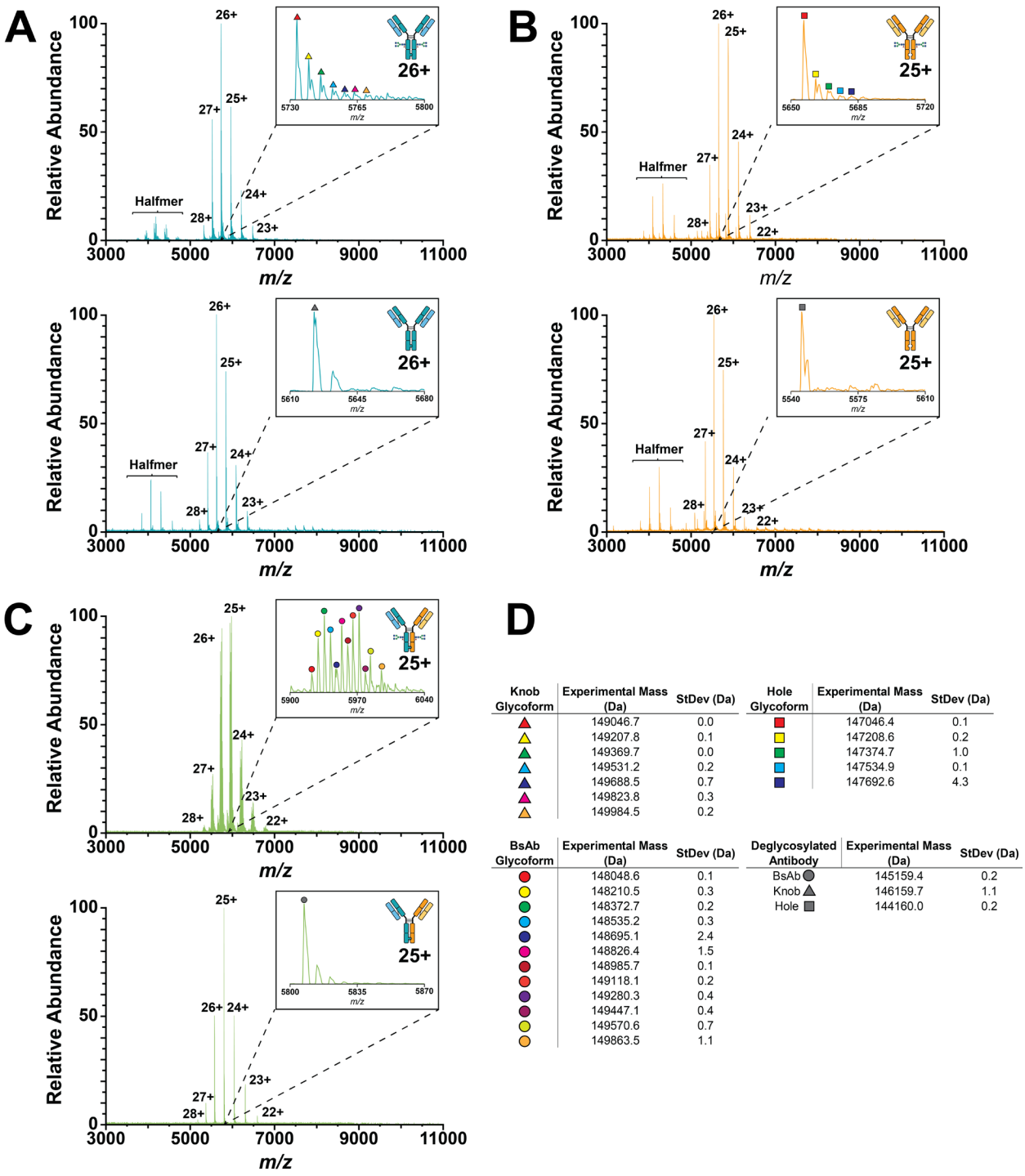

Knob Glycoform	Experimental Mass (Da)	StDev (Da)
▲	149046.7	0.0
△	149207.8	0.1
▲	149369.7	0.0
△	149531.2	0.2
▲	149688.5	0.7
△	149823.8	0.3
△	149984.5	0.2

Hole Glycoform	Experimental Mass (Da)	StDev (Da)
■	147046.4	0.1
■	147208.6	0.2
■	147374.7	1.0
■	147534.9	0.1
■	147692.6	4.3

BsAb Glycoform	Experimental Mass (Da)	StDev (Da)
●	148048.6	0.1
●	148210.5	0.3
●	148372.7	0.2
●	148535.2	0.3
●	148695.1	2.4
●	148826.4	1.5
●	148985.7	0.1
●	149118.1	0.2
●	149280.3	0.4
●	149447.1	0.4
●	149570.6	0.7
●	149863.5	1.1

Deglycosylated Antibody	Experimental Mass (Da)	StDev (Da)
BsAb ●	145159.4	0.2
Knob ▲	146159.7	1.1
Hole ■	144160.0	0.2

Appendix Figure B-6: Native Orbitrap MS of (A) knob and (B) hole homodimers and (C) KiH bsAb heterodimer before and after treatment with PNGase F. Each antibody exhibits different levels of heterogeneity resulting from glycosylation. The increased intensities of homodimer ions compared to halfmer ions is the result of utilizing high *m/z* transfer optics. Neighboring peaks correspond to unresolved adducts, where mass differences range from 18 – 40 Da. (D) Deconvoluted masses of control and deglycosylated knob and hole homodimers and KiH bsAb heterodimer.

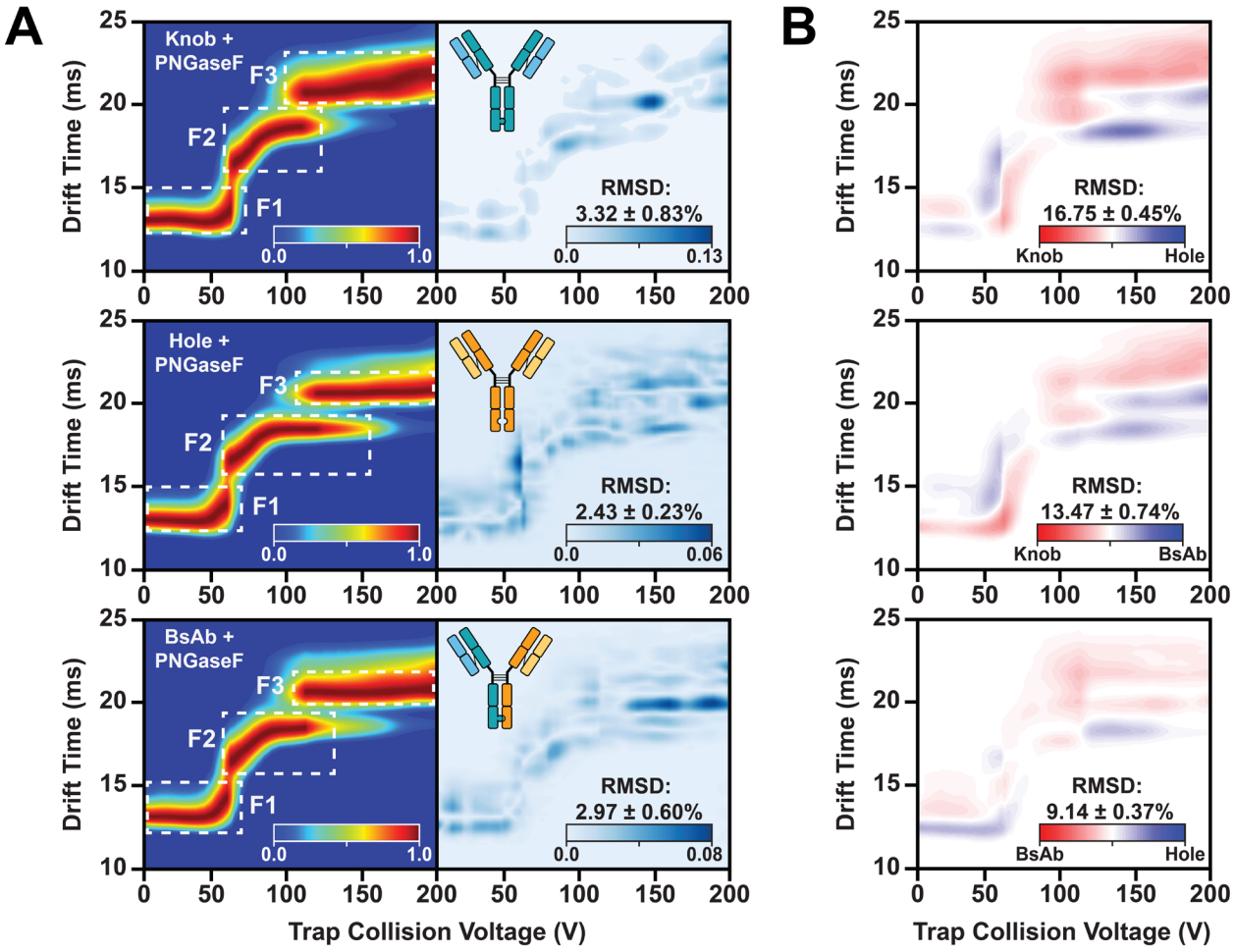

Appendix Figure B-7: CIU fingerprints of native, deglycosylated knob and hole homodimers and KiH bsAb heterodimer. (A) Averaged CIU fingerprints ($n = 3$) for the 24^{+} charge state (left) with corresponding replicate RMSD baselines (right). (B) Pairwise RMSD analysis comparing deglycosylated knob and hole homodimers and KiH bsAb heterodimer.

Appendix C: Supporting Information for Chapter 3

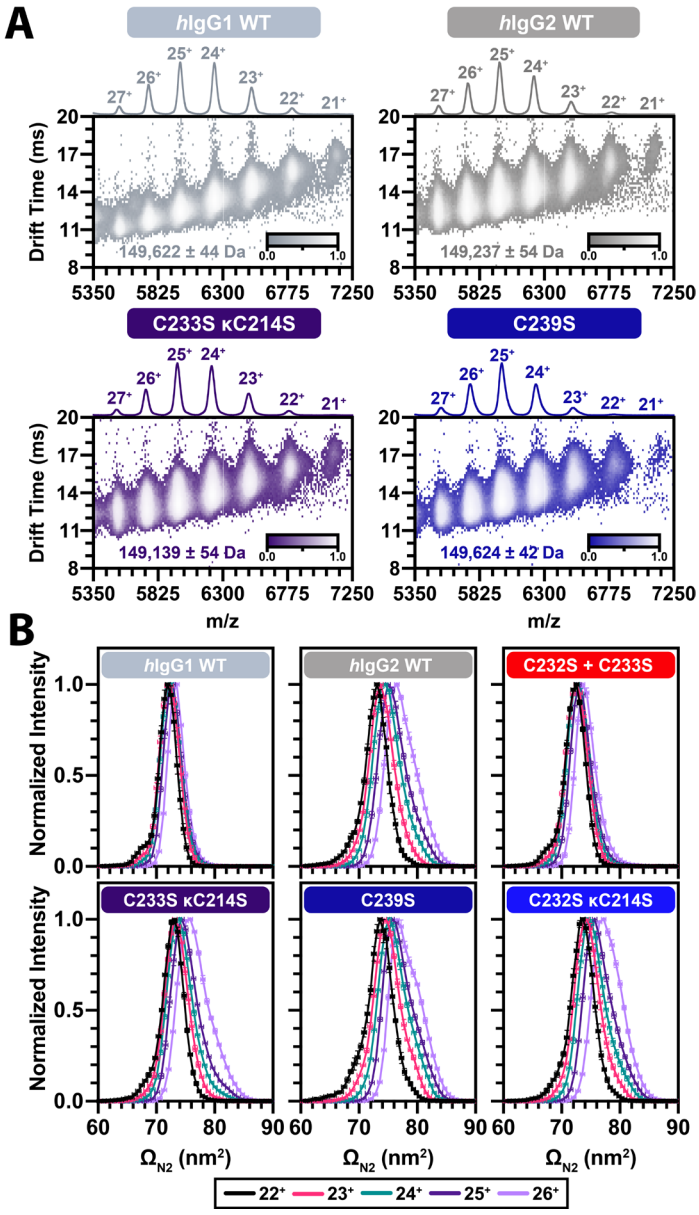

Appendix Figure C-1: IM-MS analysis of ChiLob7/4 variants. (A) Representative IM-MS spectra of variants. Corresponding masses ± mass error of the charge states sampled for mass deconvolution are shown. (B) $^{TW}\Omega_{N2}$ distributions of variants across charge states. Vertical and horizontal error bars represent s.d. of technical replicates (n = 3) and $^{TW}\Omega_{N2}$ uncertainties, respectively.

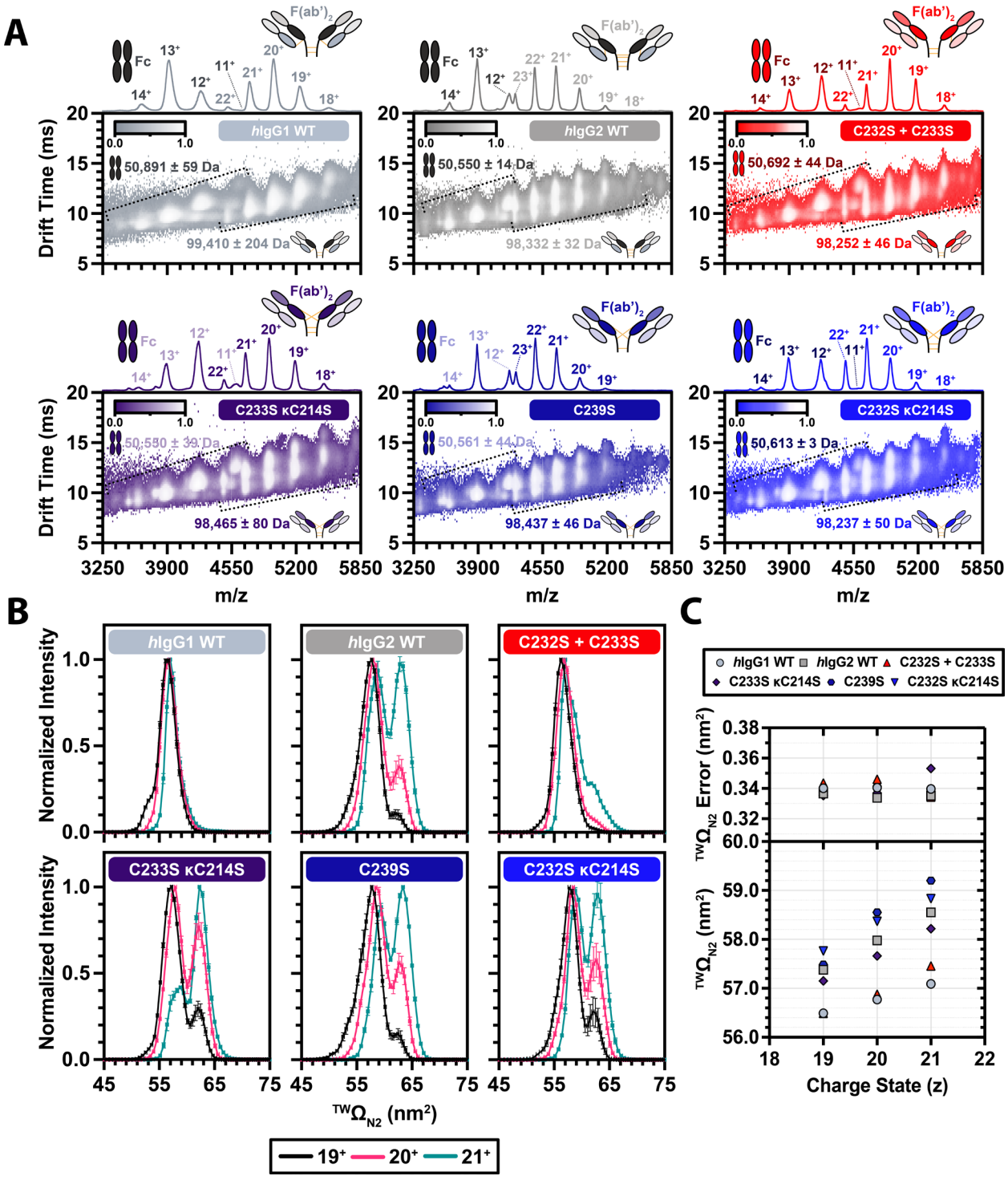

Appendix Figure C-2: IM-MS analysis of F(ab')$_2$ fragments of ChiLob7/4 variants generated via IdeS digestion. (A) Representative IM-MS spectra of IdeS digests across variants indicate presence and separation of F(ab')$_2$ and Fc fragments. Corresponding masses ± mass error of the charge states sampled for mass deconvolution are shown. (B) $^{TW}\Omega_{N2}$ distributions of variants across different charge states. Vertical and horizontal error bars represent s.d. of technical replicates (n = 3) and $^{TW}\Omega_{N2}$ uncertainties, respectively. **c.** $^{TW}\Omega_{N2}$ values as a function of charge state for the most compact feature in (C) Propagated Ω_{N2} errors are shown.

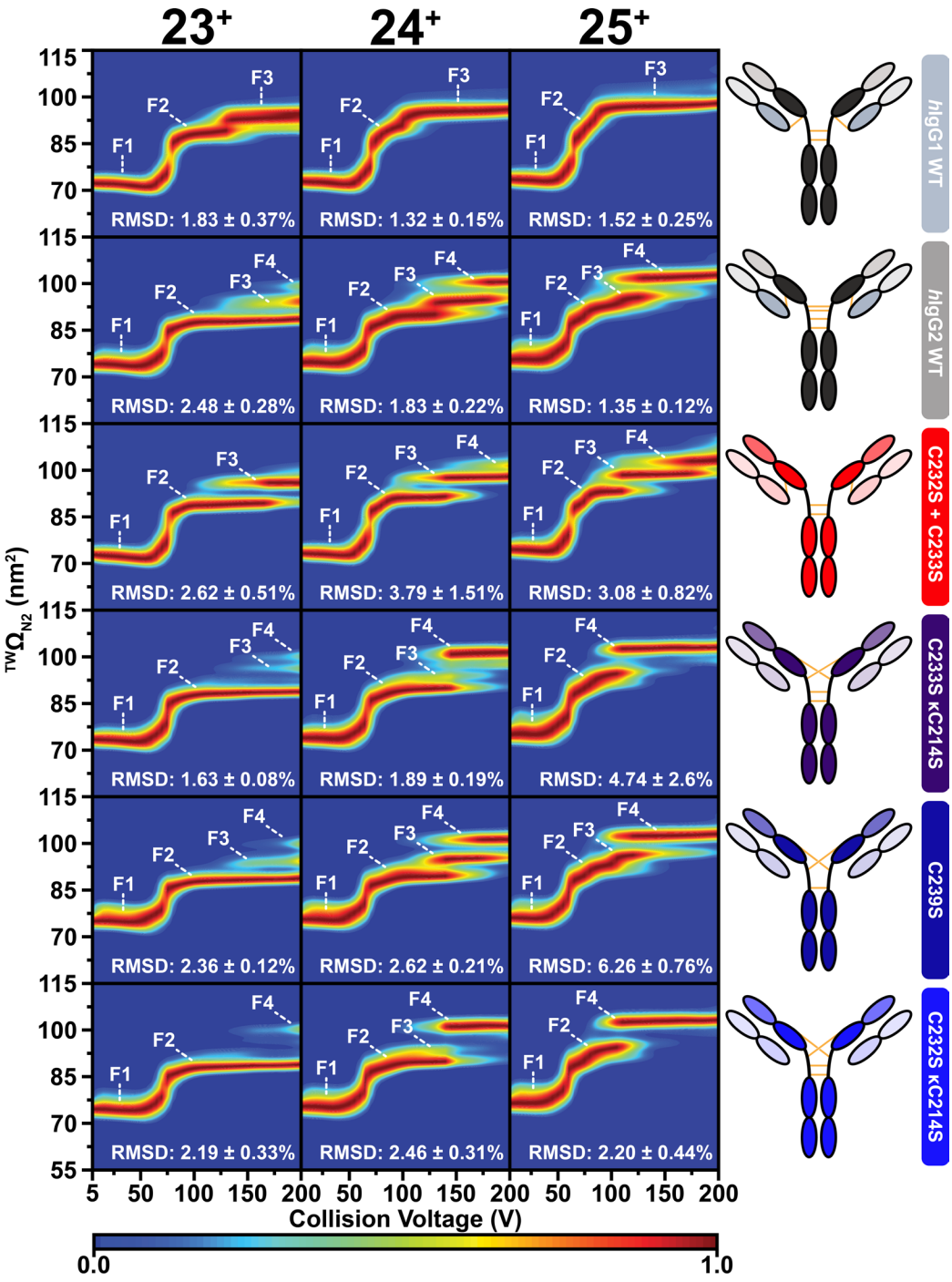

Appendix Figure C-3: Averaged CIU fingerprints for charge states 23^+ to 25^+ of ChiLob7/4 full-length variants. RMSDs values shown as mean ± s.d. from comparisons performed between technical replicates (n = 3).

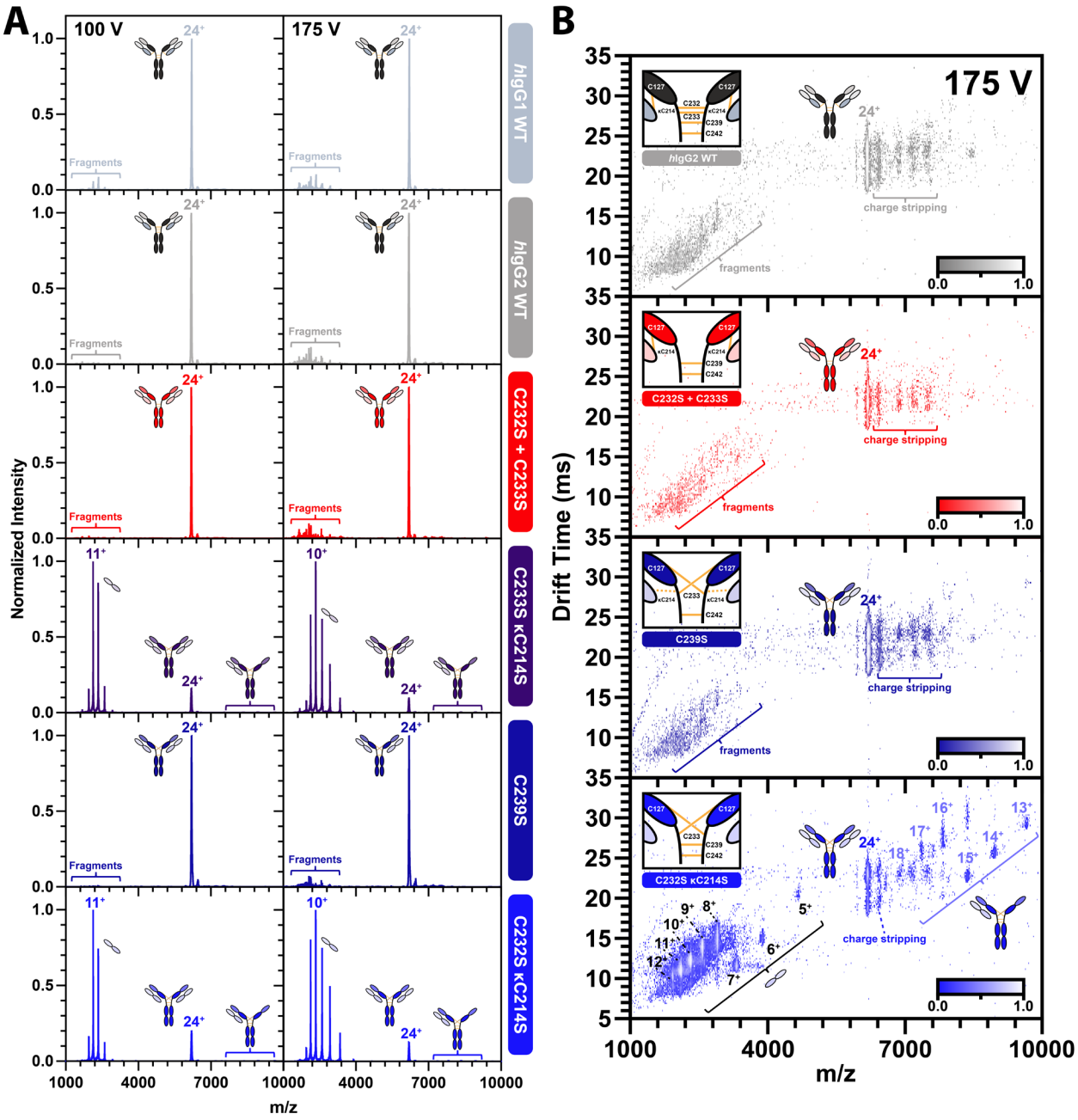

Appendix Figure C-4: Light chain is dissociated upon collisional activation during CIU. (A) Representative MS/MS spectra of charge state 24^+ at 100 and 175 V across ChiLob7/4 variants. (B) IM-MS/MS spectra of selected variants at 175 V showing evidence of possible interchain disulfide bonds in the C239S variant (shown as dashed yellow lines in the inset cartoon).

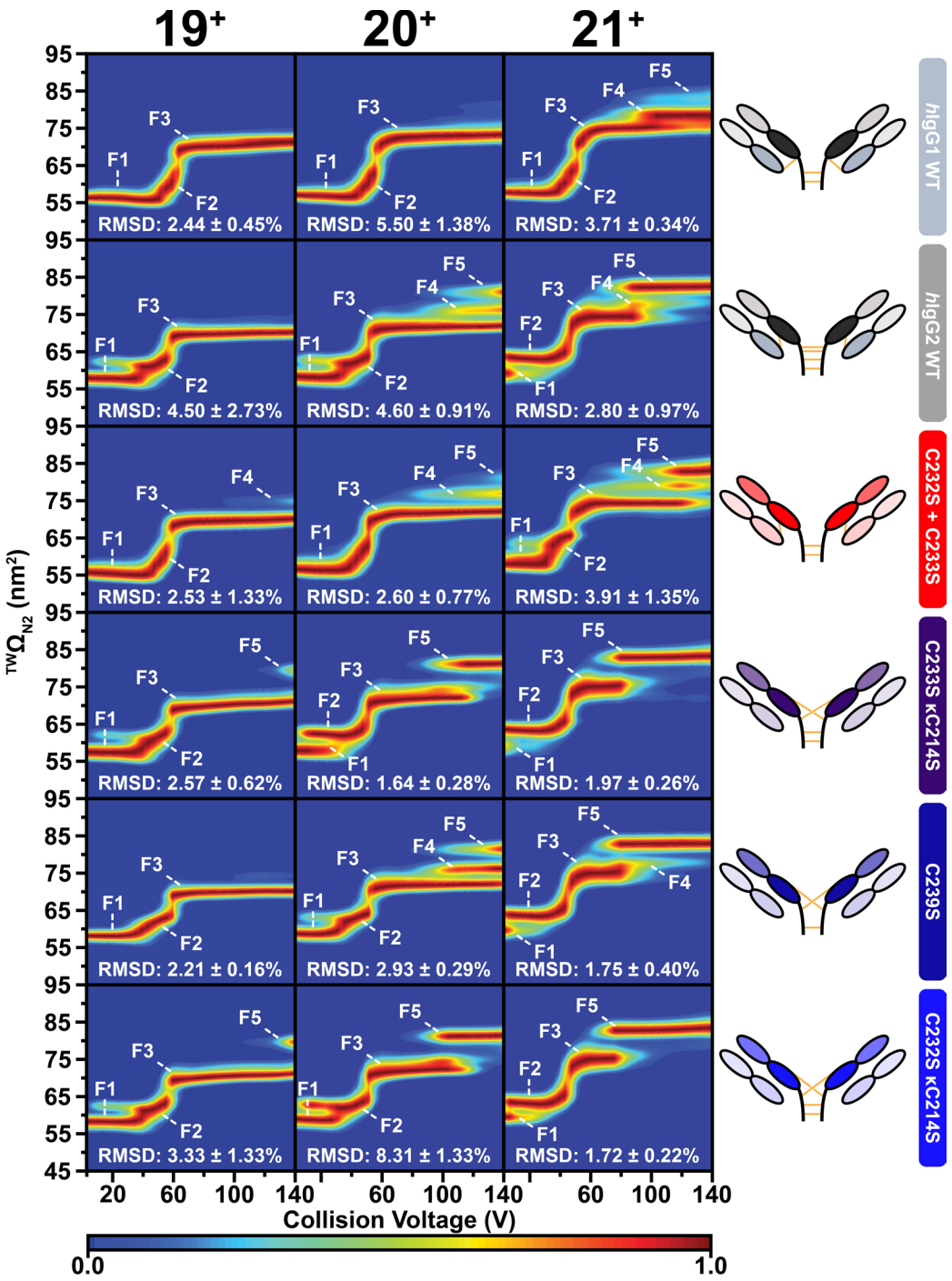

Appendix Figure C-5: Averaged CIU fingerprints for charge states 19^+ to 21^+ of ChiLob7/4 F(ab')$_2$ fragments. RMSDs values shown as mean ± s.d. from comparisons performed between technical replicates (n = 3).

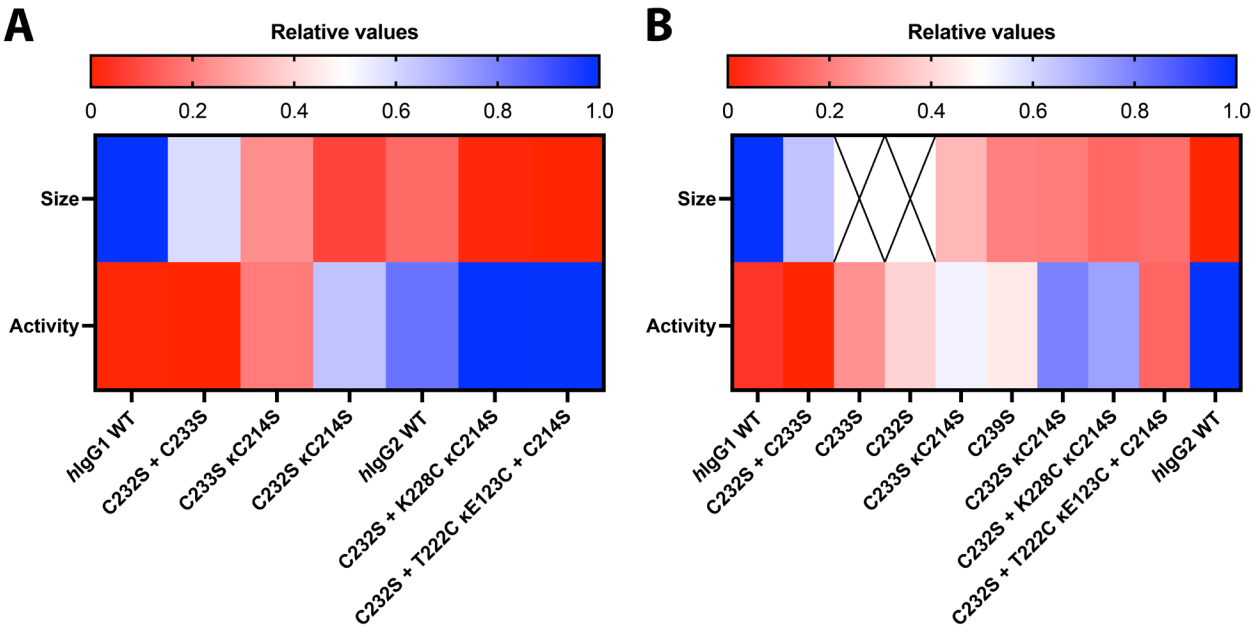

Appendix Figure C-6: Relative activity and size of (A) ChiLob7/4 and (B) SAP1.3 variants. Activity was assessed using the NFκB GFP Jurkat reporter assay. Relative size represents the maximum intramolecular distance (D_{max}) determined from SAXS experiments.

Appendix D: Supporting Information for Chapter 4

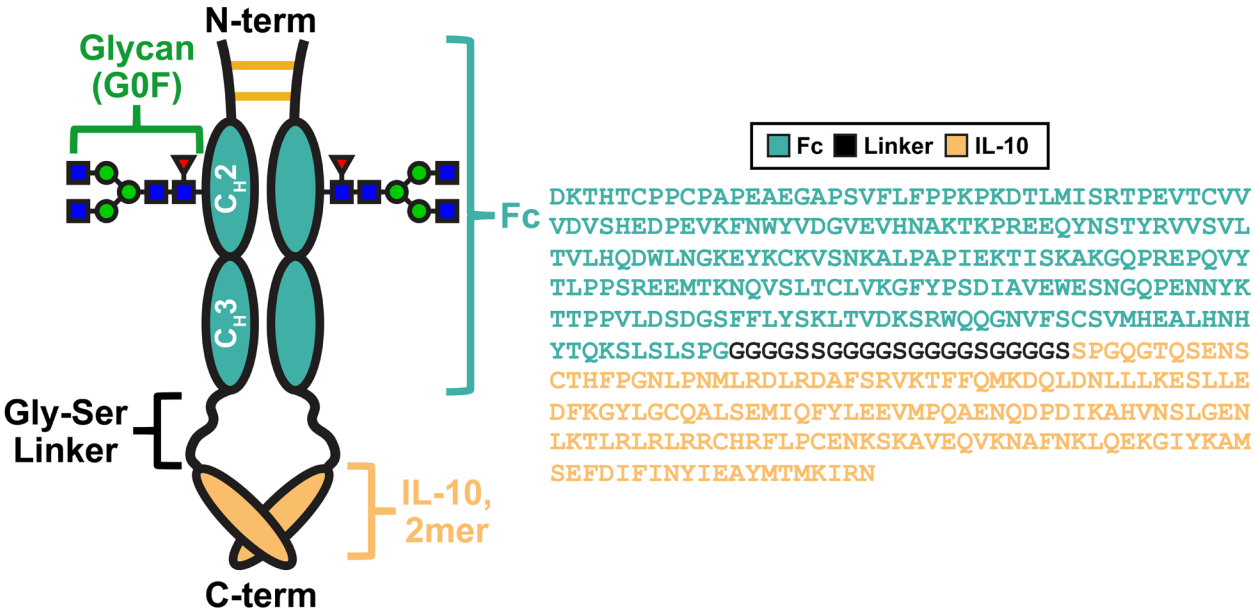

Appendix Figure D-1: Design and corresponding amino acid sequence of Fc-IL-10. Fc-IL-10 is a ~90 kDa Fc-fusion protein that consists of wild-type human IL-10 connected to the C-terminus of a human IgG1 Fc domain via a flexible Gly-Ser linker. An N-glycosylation site is present on the Fc polypeptide chain, which increases the mass of the Fc-fusion protein to ~94 kDa. Adapted from patent WO/2021/158938.[1]

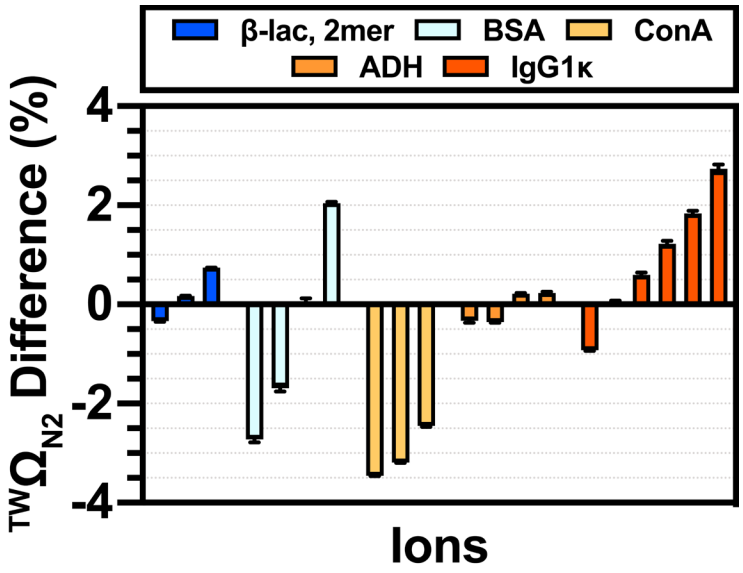

Appendix Figure D-2: Comparison of experimental measurements versus the measurements reported by Bush et al.[2] and Campuzano et al.[3] These measurements from the literature were performed with a modified Synapt G1 HDMS instrument with an RF-confining drift cell and a commercial Synapt G2 HDMS instrument, respectively. Error bars represent the standard deviation of three comparisons (n = 3) between our experimental data and literature values.

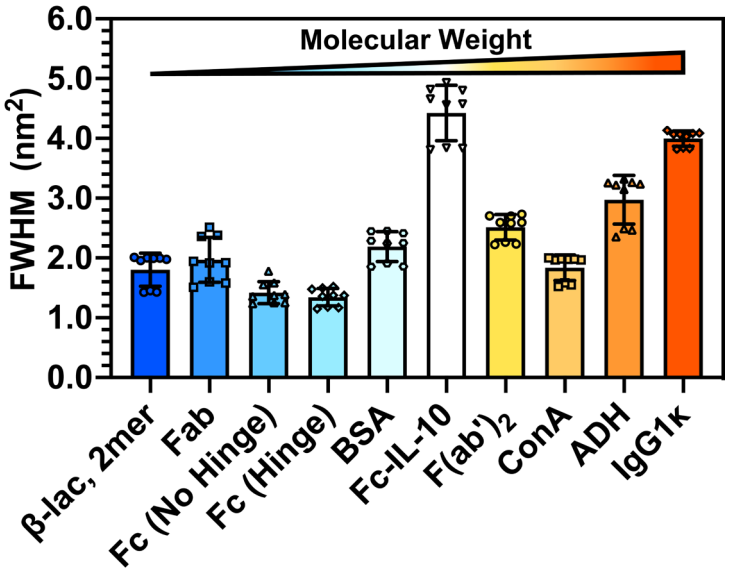

Appendix Figure D-3: Peak widths at half maximum of $^{TW}\Omega_{N2}$ distributions of Fc-IL-10 and protein standards on a Waters Synapt G2 HDMS. Peak widths are calculated from the three most prominent charge states in triplicate (n = 9). Error bars represent the standard deviation of these measurements.

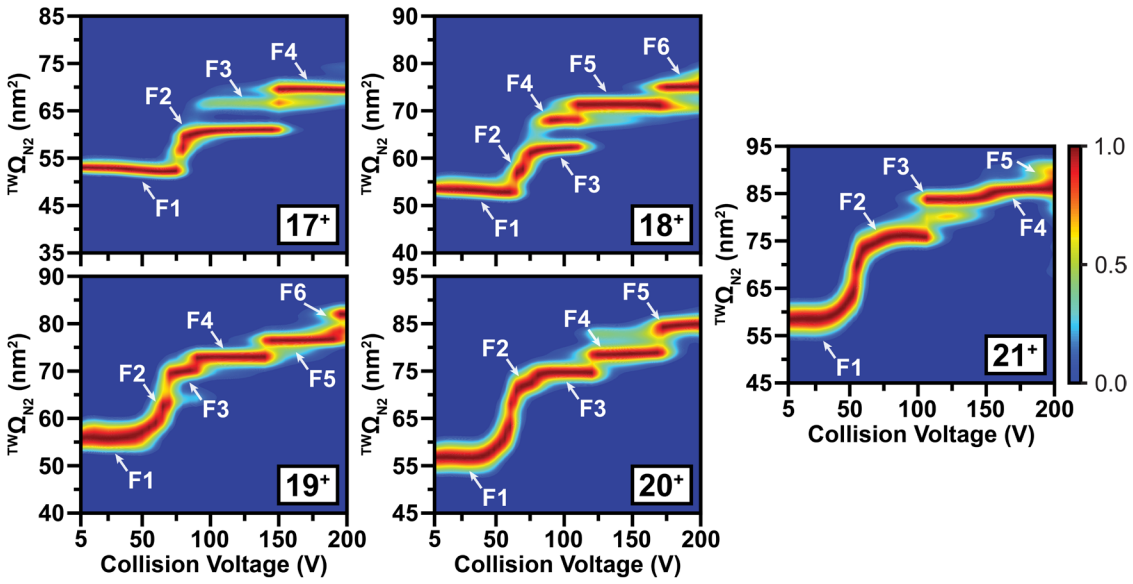

Appendix Figure D-4: CIU fingerprints of Fc-IL-10 for charge states 17^+ to 21^+ performed on a Waters Synapt G2 HDMS. Three to six features are qualitatively evident across charge states, highlighting that Fc-IL-10 adopts complex structural ensembles along its gas-phase unfolding pathway.

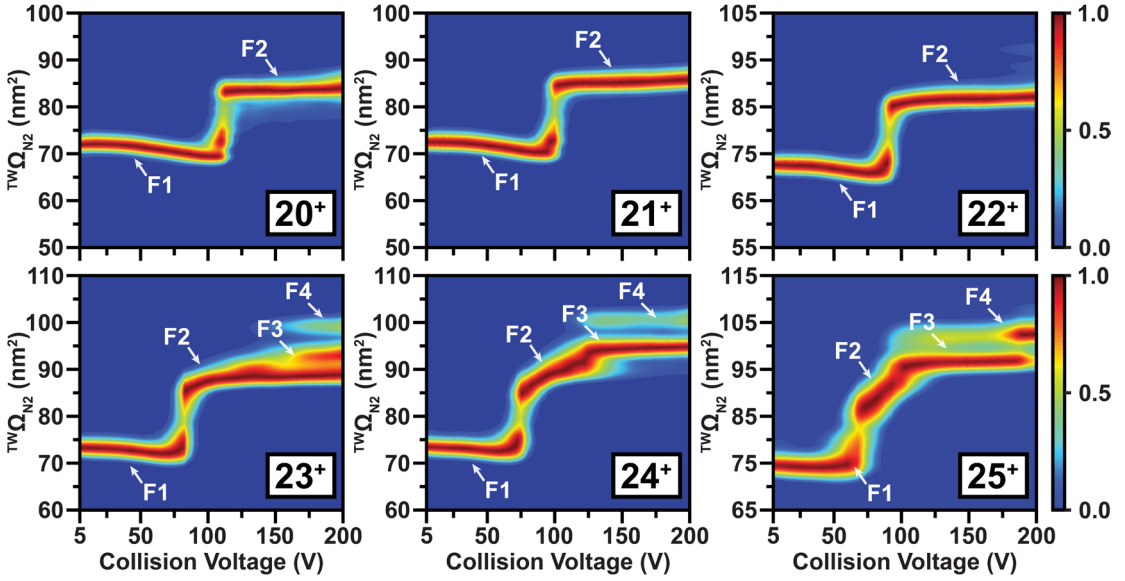

Appendix Figure D-5: CIU fingerprints of NISTmAb for charge states 20^+ to 25^+ performed on a Waters Synapt G2 HDMS. Two to four features are qualitatively observed across charge states.

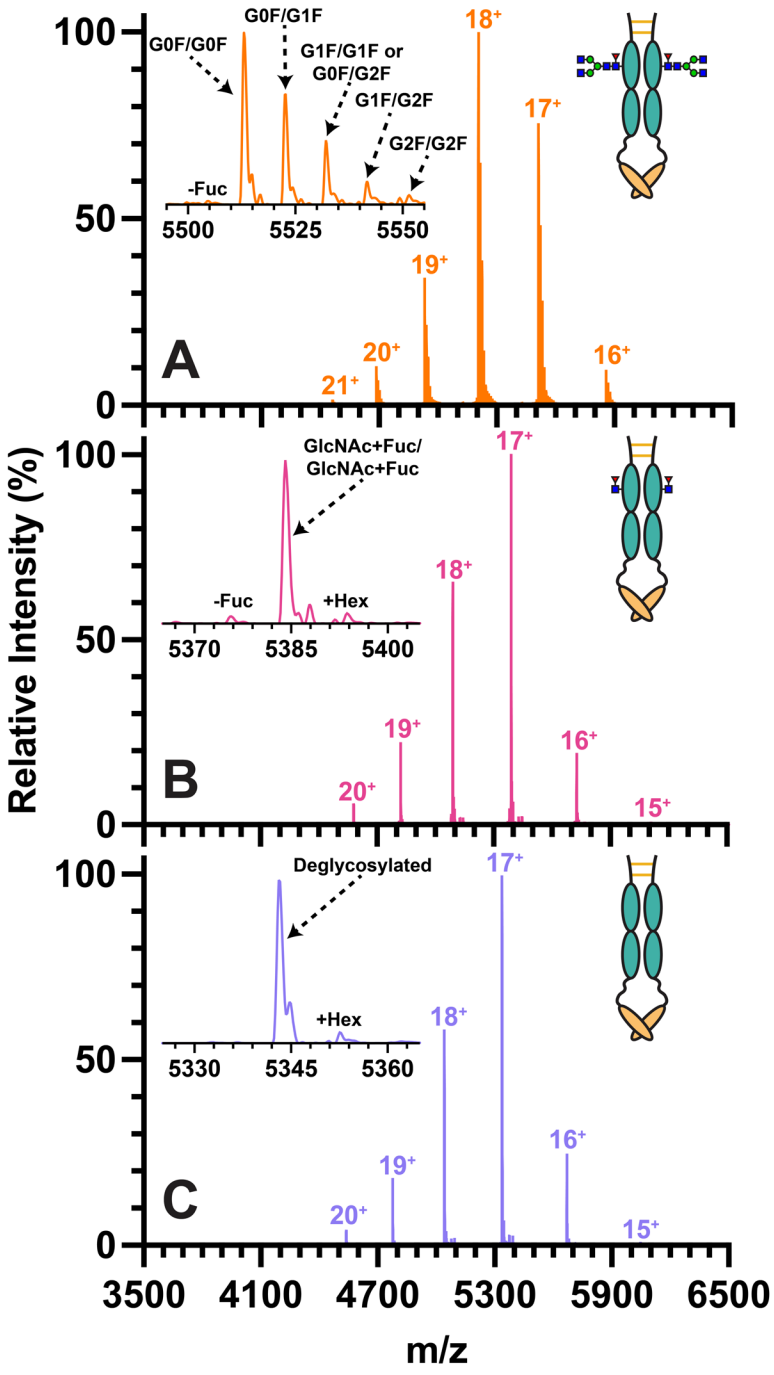

Appendix Figure D-6: Representative MS spectra of Fc-IL-10 prior to (A) and after the addition of either EndoS2 (B) or PNGase F (C). Zoomed-in spectra of charge state 18^+ reveal the presence different glycoforms.

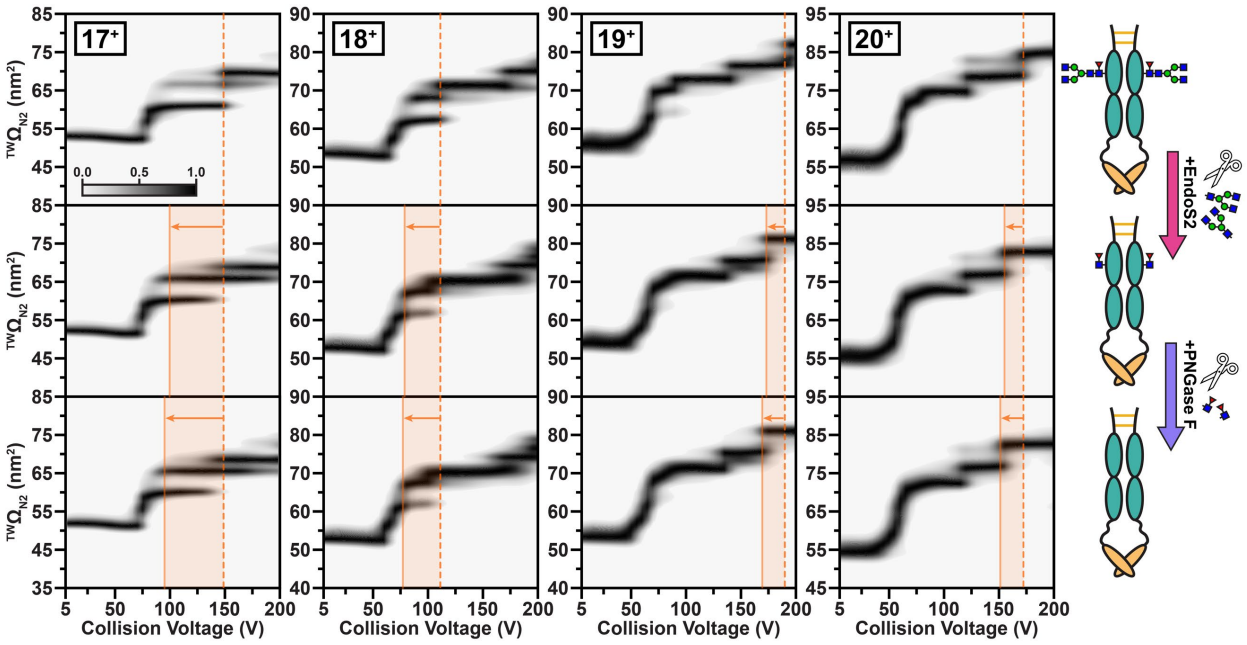

Appendix Figure D-7: CIU analyses of Fc-IL-10 after treatment with EndoS2 or PNGase F for charge states 17^{+} to 20^{+}. For the sake of clarity, only regions corresponding to the greatest shifts in gas-phase stability are shown in orange. Dashed and solid lines correspond to the CIU transitions of native and deglycosylated Fc-IL-10, respectively.

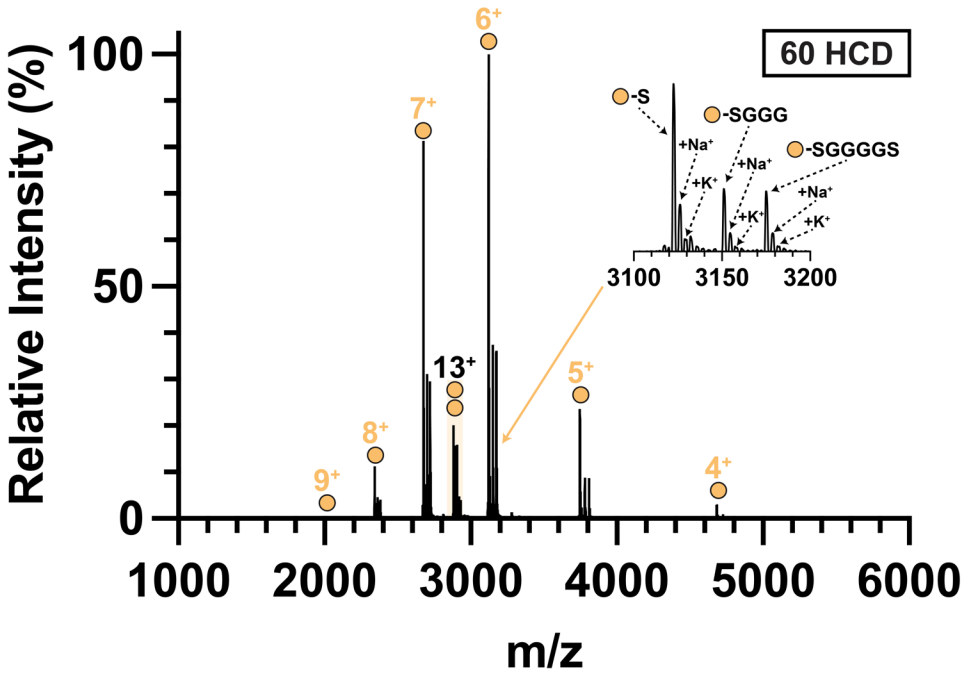

Appendix Figure D-8: Representative HCD MS/MS spectrum of IL-10 homodimer (charge state 13^+). The zoomed-in spectrum reveals the presence of three major Gly-Ser linker variants of IL-10 monomer at 60 CE.

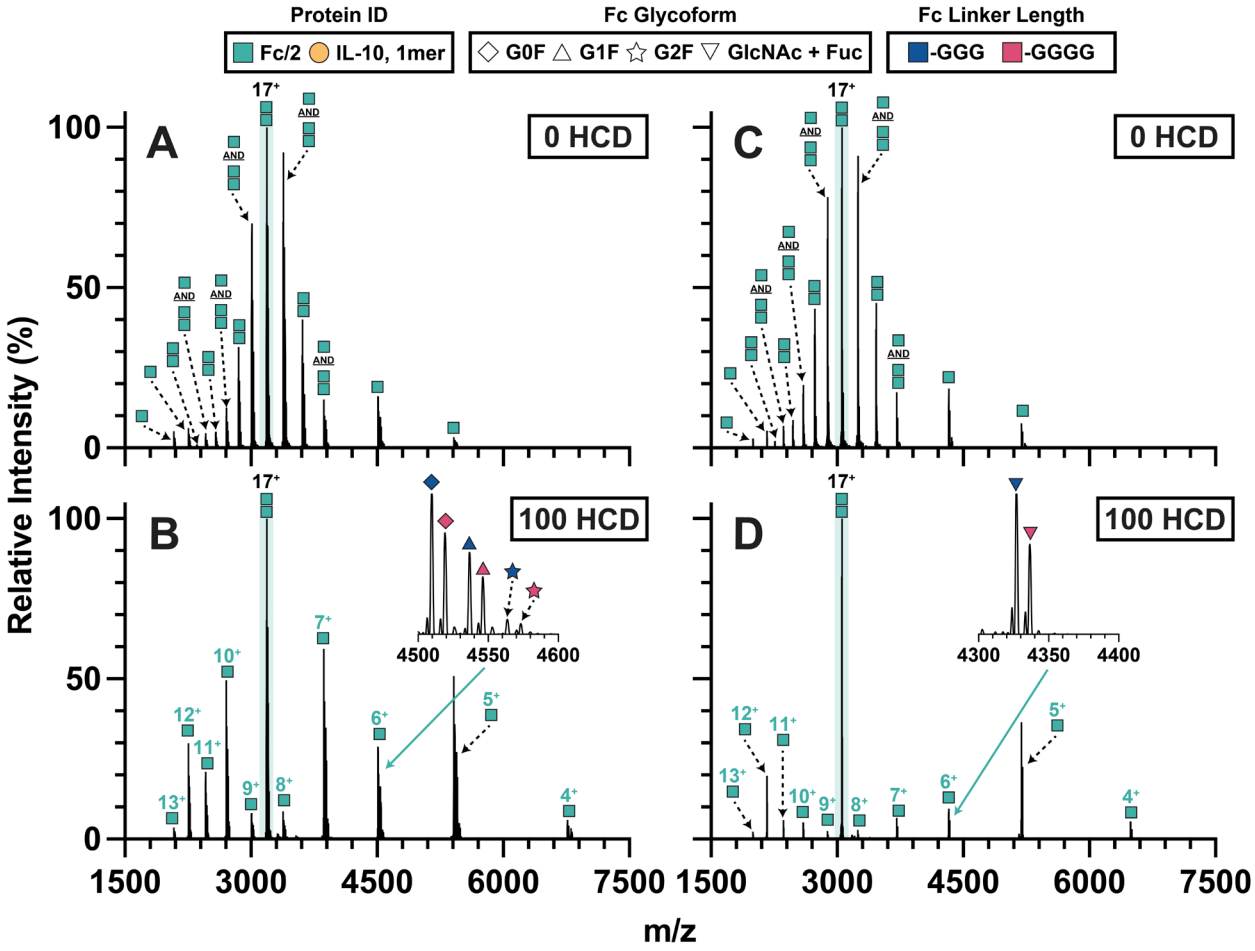

Appendix Figure D-9: Representative HCD MS/MS spectra of partially reduced Fc subunits. Both native (A,B) and EndoS2-treated (C,D) digests showed both Fc/2 subunits as well as noncovalent dimeric Fc subunits. Dissociation of noncovalent dimeric Fc (charge state 17^{+}) was achieved using 100 CE, where zoomed-in spectra reveal the presence of two major Gly-Ser linker variants.

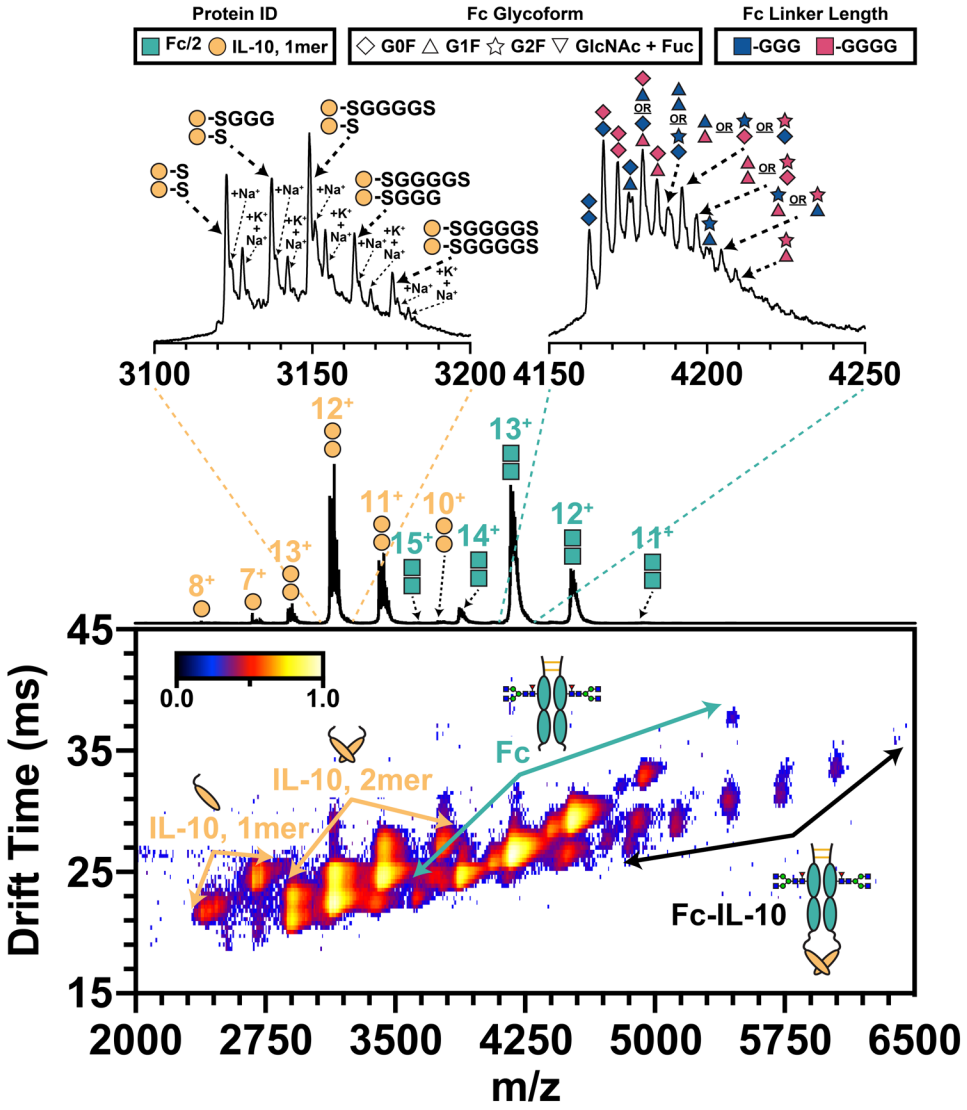

Appendix Figure D-10: Representative cIM-MS spectrum of native Fc-IL-10 digested with only GlySERIAS^{TM}. Zoomed-in spectra highlight the linker and glycoform polydispersity present in non-reduced Fc and IL-10 homodimer subunits. Spectrum was collected at 5 V of trap CE.

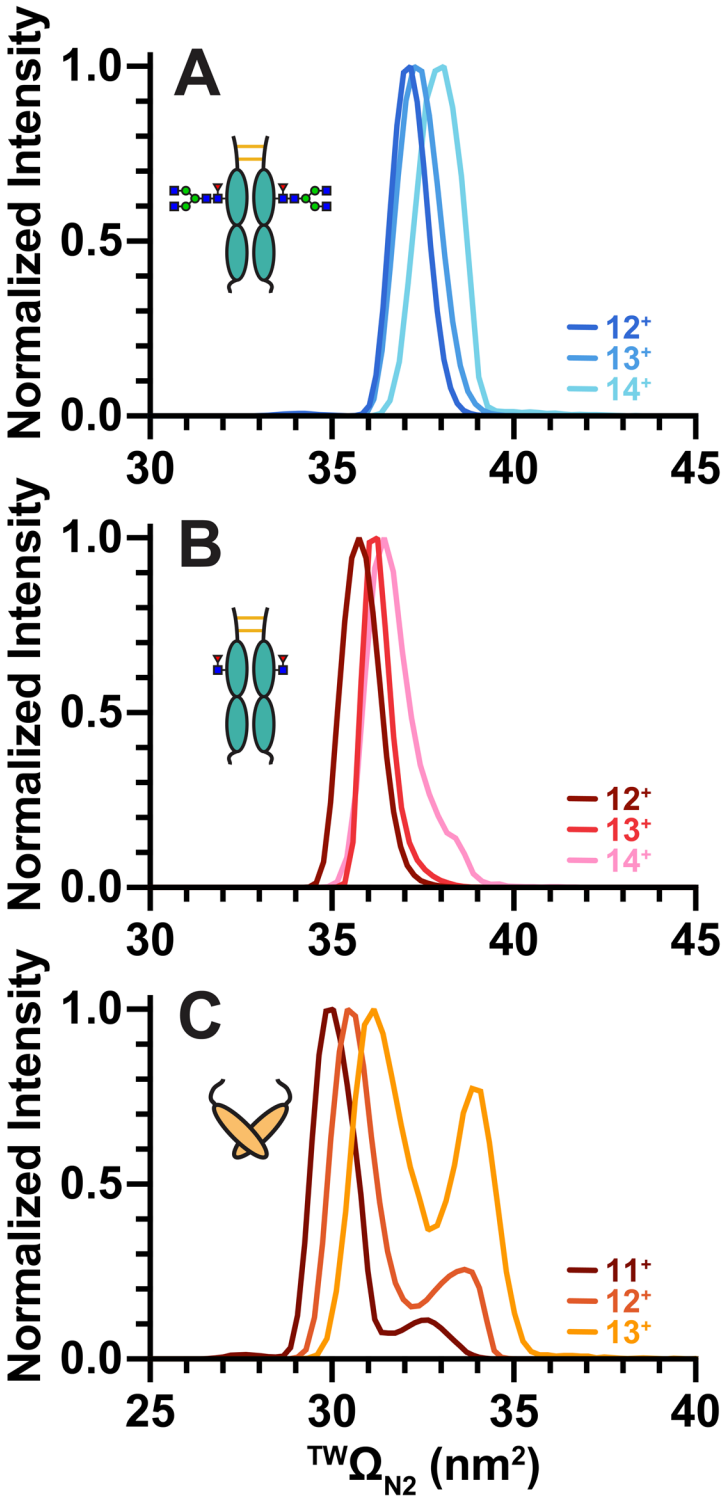

Appendix Figure D-11: Cyclic $^{TW}\Omega_{N2}$ distributions of non-reduced native Fc (A), EndoS2-treated Fc (B), and IL-10 homodimer (C) at 4 V of trap CE across different charge states.

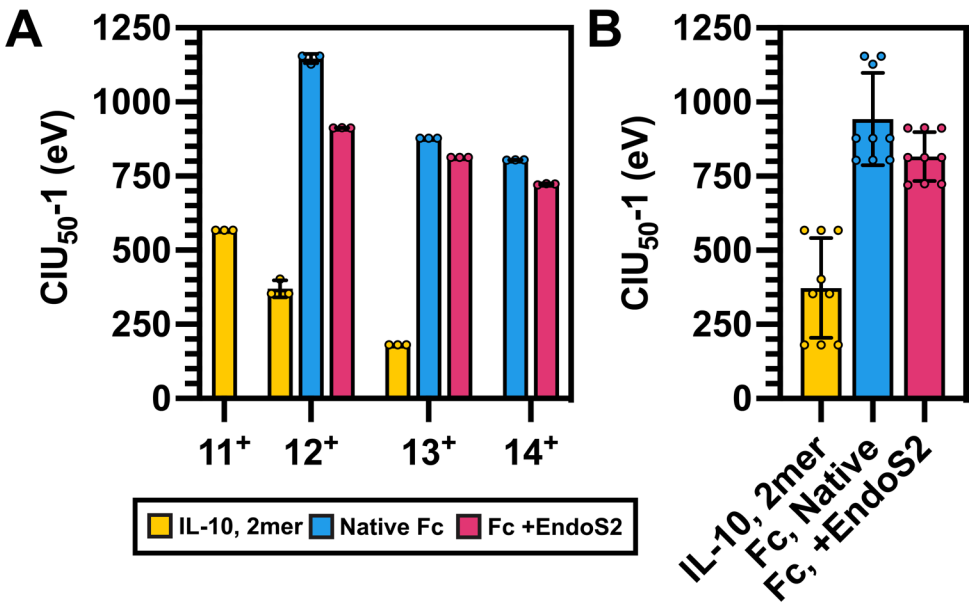

Appendix Figure D-12: CIU_{50}-1 analysis of non-reduced Fc and IL-10 homodimer subunits. (A) IL-10 homodimer unfolds at significantly lower E_{lab} values (n = 3) than Fc subunits across all detectable charge states. (B) Combined E_{lab} values of all charge states (n = 9) for Fc and IL-10 homodimer subunits.

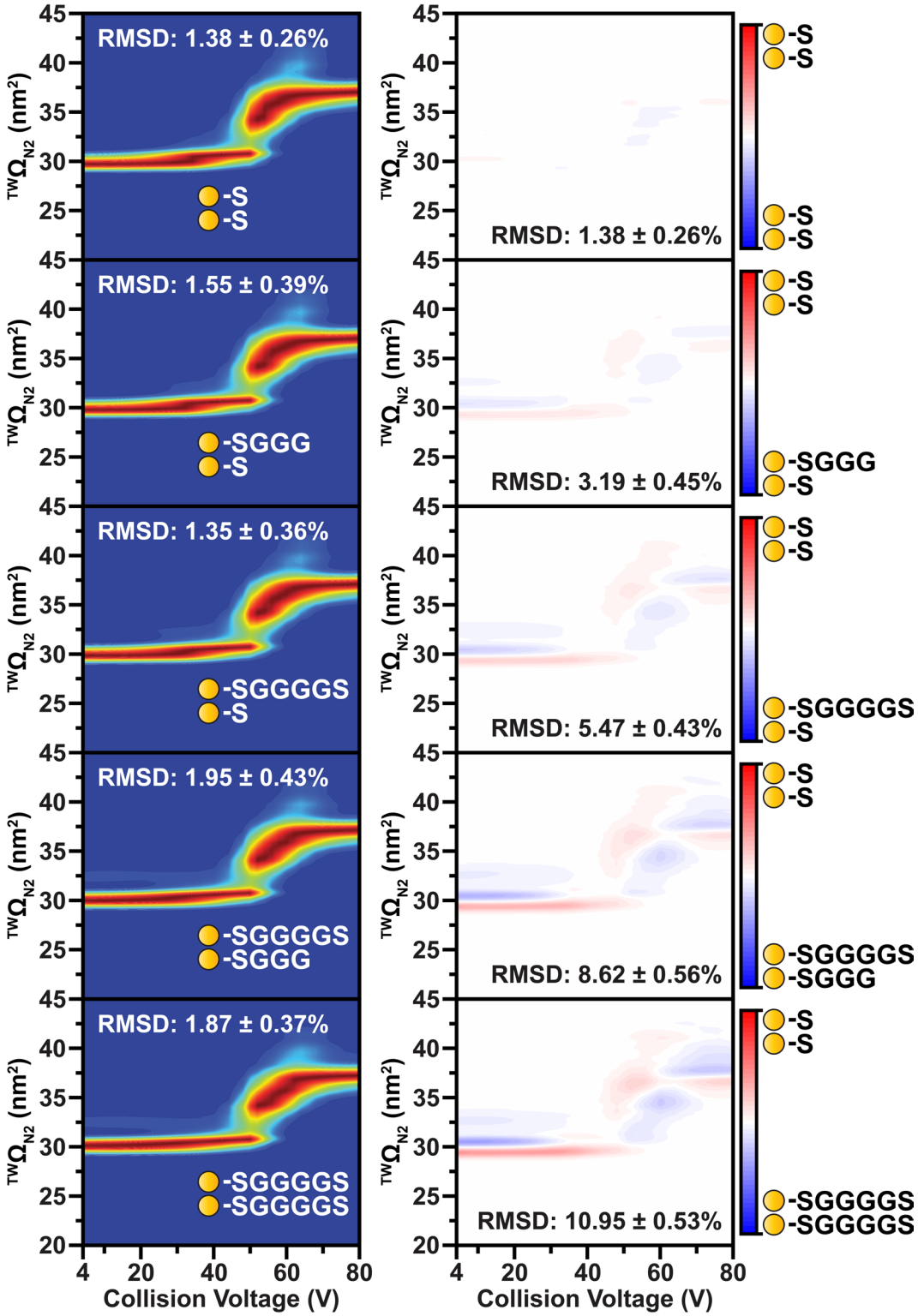

Appendix Figure D-13: Representative CIU fingerprints of different Gly-Ser linker variants of IL-10 homodimer. A qualitative comparison of CIU fingerprints (left) show no immediate differences between linker variants. By performing pairwise RMSD comparisons (right) of these variants, global conformational differences can be detected and quantified. RMSD baseline values are shown for each CIU fingerprint (left).

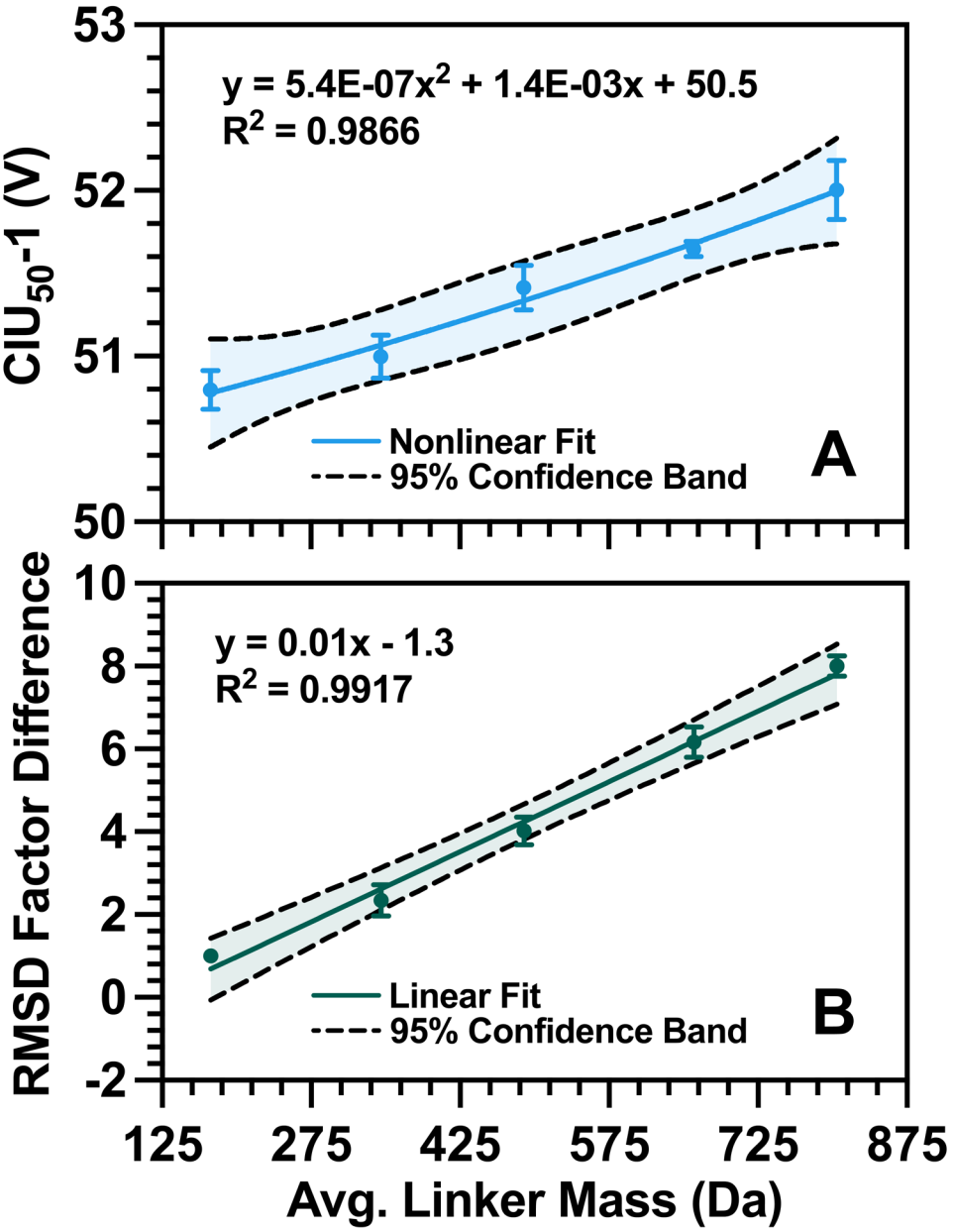

Appendix Figure D-14: Effects of linker length on stability and global conformational differences between linker variants of IL-10 homodimer. Plot of (A) CIU_{50}-1 and (B) RMSD Factor Difference as a function of linker mass. Quadratic and linear functions were fitted to each plot, respectively. Averaged values are shown (n =3) with errors bars shown as standard deviation. 95% confidence intervals of each fit are shown (dashed lines).

Appendix Table D-1: Optimized cIM sequence settings for native cIM and CIU experiments.

Parameter	Inject	Separate	Eject and Acquire
Time	10.0	2.0	69.6
Time Abs	10.0	12.0	81.6
Pre Array Gradient	85.0	85.0	85.0
Pre Array Bias	70.0	70.0	70.0
Array Entrance	10.0	30.0	50.0
Array TW Height	3.0	0.0	25.0
Array Offset	60.0	70.0	45.0
Array Mode	Forward	Sideways	Forward Eject
Array Exit	50.0	30.0	2.0
Post Array Gradient	35.0	35.0	35.0
Post Array Bias	10.0	10.0	10.0

Appendix Table D-2: Comparisons of averaged experimental and literature $^{TW}\Omega_{N2}$ values of protein standards.

Species Name	MW (kDa)	Oligomer	Charge (z)	Avg. Exp. $^{TW}\Omega_{N2}$ (nm^2)	Lit. $^{TW}\Omega_{N2}$ (nm^2)	% Difference Exp. vs. Lit.	$^{TW}\Omega^{N2}$ Lit. Ref.
β-lactoglobulin	37	2	11	32.2	32.3	-0.3	Bush et al.[2]
			12	33.2	33.1	0.2	
			13	34.6	34.3	0.7	
Serum albumin	66	1	14	43.7	44.9	-2.8	Bush et al.[2]
			15	44.1	44.9	-1.7	
			16	44.7	44.7	0.1	
			17	45.8	44.9	2.0	
Concanavalin A	103	4	19	58.5	60.6	-3.6	Bush et al.[2]
			20	58.9	60.8	-3.3	
			21	59.4	60.9	-2.5	
Alcohol dehydrogenase	148	4	23	74.0	74.2	-0.3	Bush et al.[2]
			24	74.2	74.5	-0.4	
			25	74.6	74.4	0.2	
			26	75.2	75.0	0.2	
IgG1κ	148	1	21	72.4	73.1	-0.9	Campuzano et al.[3]
			22	73.1	73.1	0.0	
			23	73.4	73.0	0.6	
			24	73.7	72.8	1.2	
			25	73.8	72.5	1.8	
			26	74.5	72.5	2.7	

Appendix Table D-3: Deconvoluted masses of Fc-IL-10 before and after treatment with EndoS2 or PNGase F.

Condition	Glycoform	Theoretical Avg. Mass (Da)	Experimental Avg. Mass (Da)	StDev (Da)[a]	Mass Error (ppm)[b]
Native	G0/G0F	93558.2	93560.3 ± 2.4	2.4	22.1
	G0F/G0F	93704.4	93703.7 ± 0.5	0.5	-7.1
	G0F/G1F	93866.5	93867.1 ± 0.9	0.9	6.3
	G1F/G1F or G0F/G2F	94028.7	94029.1 ± 1.9	1.9	4.8
	G1F/G2F	94190.8	94191.6 ± 1.7	1.7	8.6
	G2F/G2F	94352.9	94357.4 ± 11.3	11.3	47.3
+ EndoS2	GlcNAc/GlcNAc+Fuc	91366.2	91367.9 ± 0.8	0.8	18.2
	GlcNAc+Fuc/GlcNAc+Fuc	91512.4	91513.5 ± 0.7	0.7	12.3
+ PNGase F	Deglycosylated	90815.7	90814.7 ± 0.4	0.4	-10.8

[a] Mass error of the charge states sampled for mass deconvolution. [b] Mass difference between theoretical and experimental average masses.

Appendix Table D-4: Deconvoluted masses of Fc and IL-10 subunits generated via GlySERIAS™ digestion

Oligomer	Linker Variant	Theoretical Avg. Mass (Da)	Experimental Avg. Mass (Da)	StDev (Da)[a]	Mass Error (ppm)[b]
IL-10, 1mer	S	18,730.3	18,730.3	0.3	-0.6
	SGGG	18,901.5	18,901.2	0.1	-14.1
	SGGGGS	19,045.6	19,045.2	0.2	-20.8
IL-10, 2mer	S/S	37,460.6	37,460.6	0.1	-0.5
	S/SGGG	37,631.8	37,631.9	0.3	2.9
	S/SGGGGS	37,775.9	37,775.9	0.3	-0.3
	SGGG/SGGGGS	37,947.1	37,947.3	0.2	6.4
	SGGGGS/SGGGGS	38,091.2	38,091.4	0.3	5.5
Fc/2	G0F+GGG	27,051.9	27,051.9	0.5	-1.0
	G0F+GGGG	27,109.0	27,109.1	0.4	4.5
	G1F+GGG	27,214.1	27,214.0	0.4	-2.5
	G1F+GGGG	27,271.1	27,271.2	0.3	2.9
	G2F+GGG	27,376.2	27,376.0	0.6	-8.0
	G2F+GGGG	27,433.3	27,433.5	0.7	8.8
Fc/2 + EndoS2	GlcNAc+Fuc+GGG	25,955.9	25,956.4	0.4	18.1
	GlcNAc+Fuc+GGGG	26,013.0	26,013.5	0.5	20.0
Fc	2x(G0F+GGG)	54,099.8	54,100.0	0.6	3.3
	G0F+GGG/G0F+GGGG	54,156.9	54,158.3	0.2	26.4
	2x(G0F+GGGG)	54,213.9	54,218.1	0.4	77.1
	G0F+GGG/G1F+GGG	54,262.0	54,263.0	0.6	19.2
	G0F+GGGG/G1F+GGG ***or*** G0F+GGG/G1F+GGGG	54,319.0	54,320.8	0.4	33.0
	G0F+GGGG/G1F+GGGG	54,376.1	54,378.7	0.4	48.6
	2x(G1F+GGG) ***or*** G0F+GGG/G2F+GGG	54,424.1	54,424.5	0.4	7.4
	G1F+GGGG/G1F+GGG ***or*** G0F+GGGG/G2F+GGG ***or*** G0F+GGG/G2F+GGGG	54,481.2	54,482.0	0.1	15.6
	2x(G1F+GGGG) ***or*** G0F+GGGG/G2F+GGGG	54,538.2	54,540.1	0.6	34.8
	G1F+GGG/G2F+GGG	54,586.2	54,585.6	5.5	-11.7
	G1F+GGGG/G2F+GGG ***or*** G1F+GGG/G2F+GGGG	54,643.3	54,643.8	0.5	9.3
	G1F+GGGG/G2F+GGGG	54,700.3	54,702.9	1.5	46.6
Fc + EndoS2	2x(GlcNAc+Fuc+GGG)	51,907.8	51,909.2	0.7	26.6
	GlcNAc+Fuc+GGGG/GlcNAc+Fuc+GGG	51,964.9	51,966.3	0.2	27.3
	2x(GlcNAc+Fuc+GGGG)	52,021.9	52,024.9	0.9	57.1

[a] Mass error of the charge states sampled for mass deconvolution. [b] Mass difference between theoretical and experimental average masses.

D.1 References

[1] Coker, S.; et al. IL-10 and uses thereof. WO 2021/158938 A1, 2021.

[2] Bush, M. F.; et al. Collision Cross Sections of Proteins and Their Complexes: A Calibration Framework and Database for Gas-Phase Structural Biology. *Anal. Chem.* **2010**, *82* (22), 9557-9565.

[3] Campuzano, I. D. G.; Larriba, C.; Bagal, D.; Schnier, P. D. Ion Mobility and Mass Spectrometry Measurements of the Humanized IgGk NIST Monoclonal Antibody. *ACS Symp. Ser.* **2015**, *1202*, 75-112.

Appendix E: Supporting Information for Chapter 5

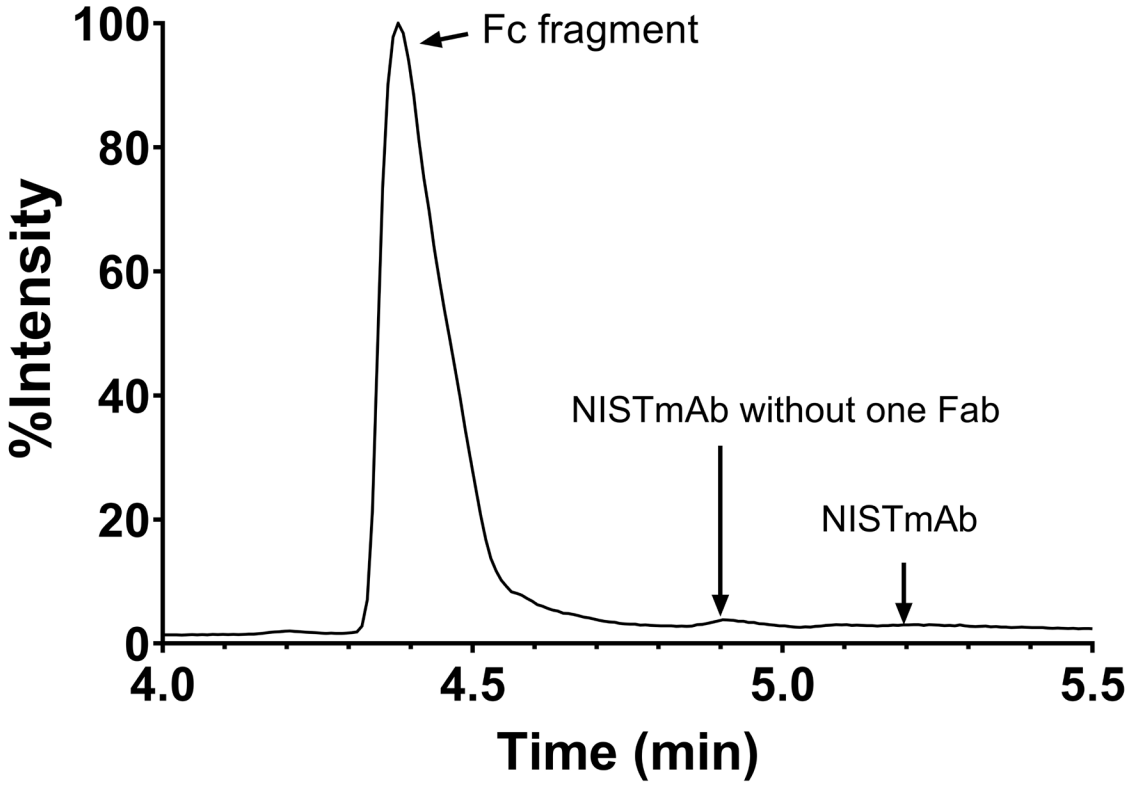

Appendix Figure E-1: Total ion chromatography (TIC) of Fc fragment. Both NISTmAb and partially digested NISTmAb without one Fab arm were observed with low intensities.

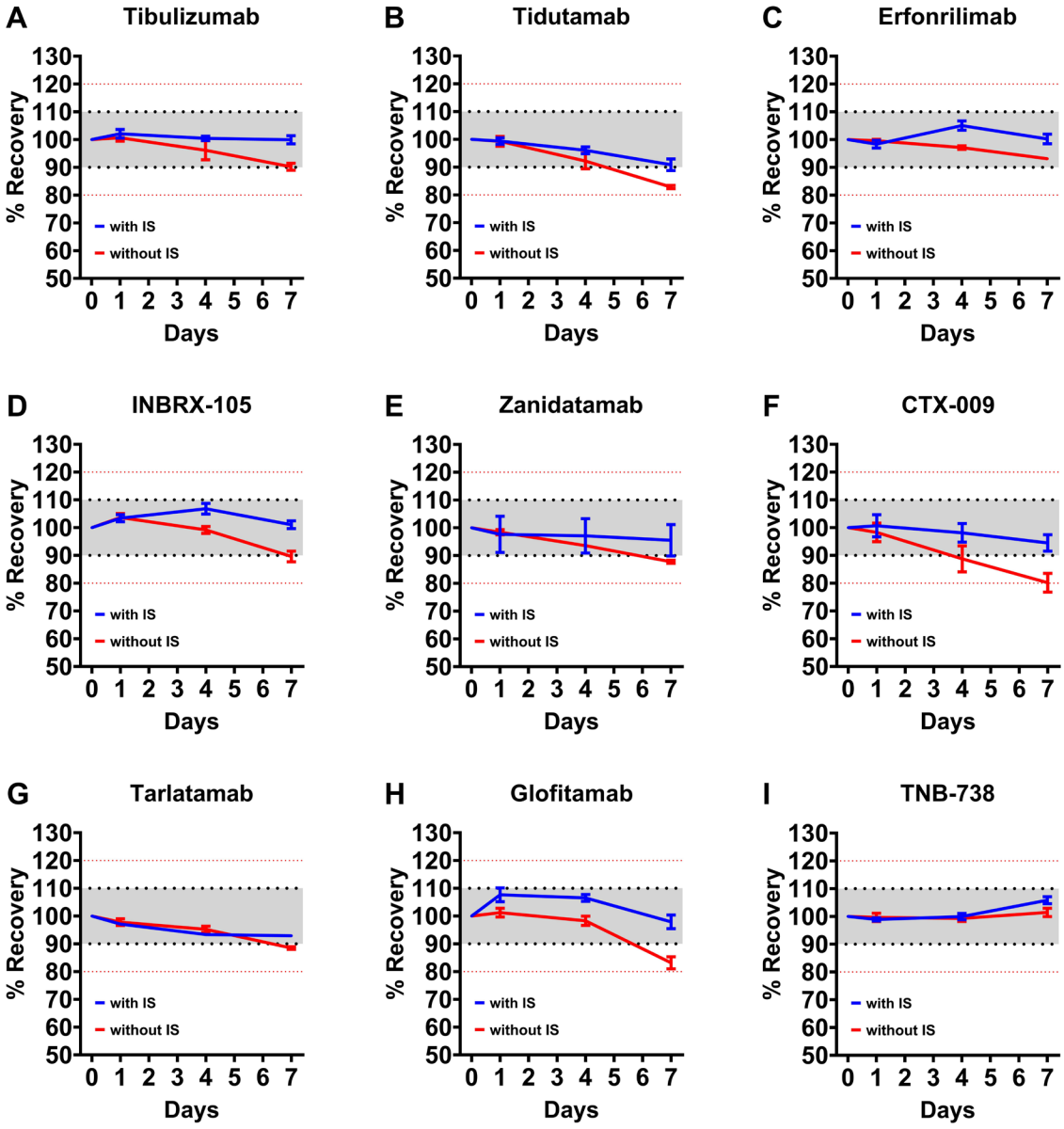

Appendix Figure E-2: Stability analysis of (A) Tibulizumab, (B) Tidutamab, (C) Erfonrilimab, (D) INBRX-105, (E) Zanidatamab, (F) CTX-009, (G) Tarlatamab, (H) Glofitamab, and (I) TNB-738 with or without NISTmAb as internal standard.

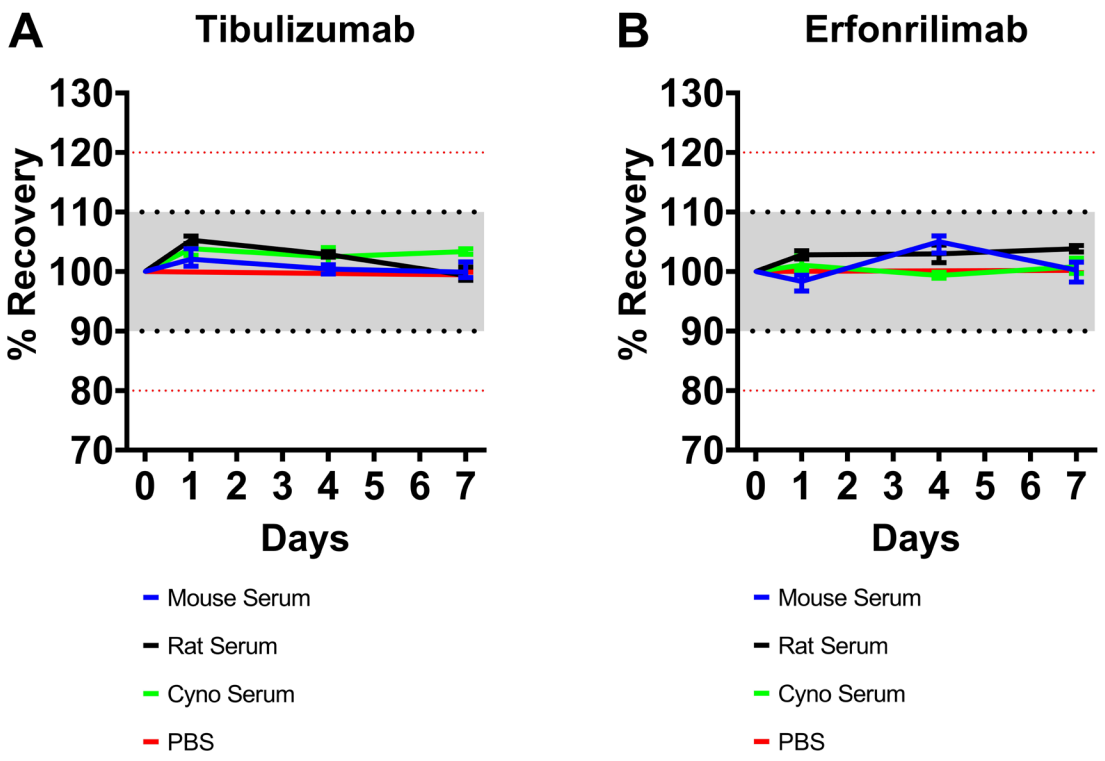

Appendix Figure E-3: Serum stabilities of (A) Tibulizumab and (B) Erfonrilimab with NISTmAb as internal standard in serum of three different species: mouse, rat and cynomolgus monkey.

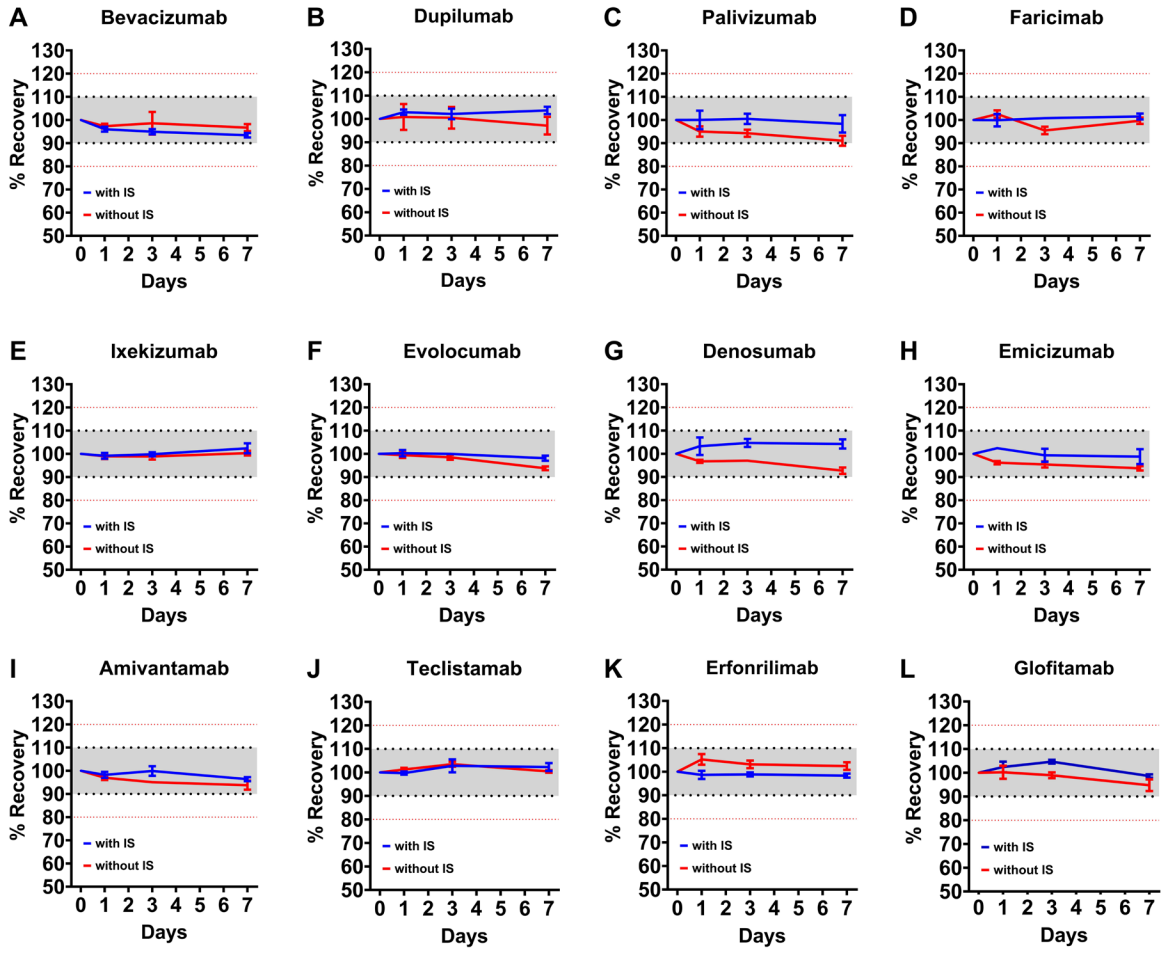

Appendix Figure E-4: Stability results of (A) Bevacizumab, (B) Dupilumab, (C) Palivizumab, (D) Faricimab, (E) Ixekizumab, (F) Evolocumab, (G) Denosumab, (H) Emicizumab, (I) Amivantamab, (J) Teclistamab, (K) Erfonrilimab, (L) Glofitamab with or without Fc fragment as internal standard.

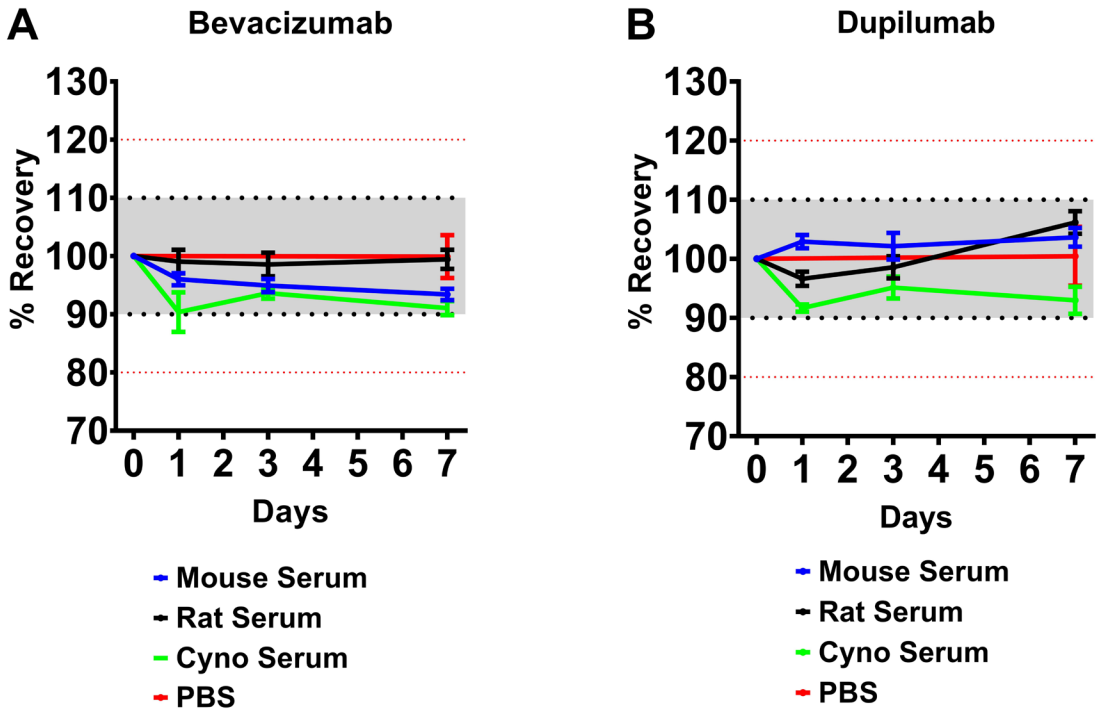

Appendix Figure E-5: Serum stabilities of (A) Bevacizumab and (B) Dupilumab with Fc fragment as internal standard in serums of three different species: mouse, rat and cynomolgus monkey.

Appendix Table E-1: International Nonproprietary Names (INNs) of antibodies assessed in this work.

INN	Target	Phase	Format	Average Mass (Da)*
Bevacizumab	VEGF-A	Approved	mAb	146563.24
Dupilumab	IL-4/IL-13	Approved	mAb	147154.04
Palivizumab	RSV protein F	Approved	mAb	145296.94
Ixekizumab	IL-17A	Approved	mAb	146191.05
Evolocumab	PCSK9	Approved	mAb	141789.71
Denosumab	RANKL	Approved	mAb	144717.51
Amivantamab	cMET/EGFR	Approved	Bispecific	145900.86
Emicizumab	FX/FIXa	Approved	Bispecific	145637.74
Teclistamab	BCMA/CD3	Approved	Bispecific	143660.97
Faricimab	Ang-2/VEGF-A	Approved	Bispecific	146428.7
Glofitamab	CD20/CD3	Approved	Bispecific	194342.69
Tibulizumab	IL17A/BAFF	2/3	Bispecific	201421.4
CTX-009	VEGF-A/DLL4	2/3	Bispecific	199632.87
Zanidatamab	HER2/HER2	3	Bispecific	124647.84
Tidutamab	SSTR2/CD3	1b/2, discontinued	Bispecific	126509.18
Erfonrilimab	PD-L1/CTLA4	3	Bispecific	107420.2
INBRX-105	PD-L1/4-1BB	1/2	Bispecific	101881.98
Tarlatamab	DLL3/CD3	2	Bispecific	105201.89
TNB-738	CD38	1	Bispecific	111200.93

*Includes all possible disulfide bonds. No other modifications included.

Appendix Table E-2: *In vitro* serum results for NISTmAb in mouse serum.

	Replicate 1			Replicate 2			Replicate 3			
Time (Day)	**Mass Peak Area**	**Recovery (%)**	**Accuracy (%)**	**Mass Peak Area**	**Recovery (%)**	**Accuracy (%)**	**Mass Peak Area**	**Recovery (%)**	**Accuracy (%)**	**Precision (%CV)**
0	2.29E+07	Defined as 100.0	N/A	2.27E+07	Defined as 100.0	N/A	2.22E+07	Defined as 100.0	N/A	1.7
1	2.28E+07	99.4	-0.6	2.29E+07	100.8	0.8	2.26E+07	102.1	2.1	0.5
4	2.27E+07	99	-1	2.22E+07	98.1	-1.9	2.24E+07	100.9	0.9	1.1
7	2.17E+07	94.4	-5.6	2.17E+07	95.8	-4.2	2.16E+07	97.4	-2.6	0.3

Appendix Table E-3: *In vitro* serum results for NISTmAb in rat serum.

	Replicate 1			Replicate 2			Replicate 3			
Time (Day)	**Mass Peak Area**	**Recovery (%)**	**Accuracy (%)**	**Mass Peak Area**	**Recovery (%)**	**Accuracy (%)**	**Mass Peak Area**	**Recovery (%)**	**Accuracy (%)**	**Precision (%CV)**
0	2.39E+07	Defined as 100.0	N/A	2.35E+07	Defined as 100.0	N/A	2.33E+07	Defined as 100.0	N/A	1.2
1	2.28E+07	95.6	-4.4	2.28E+07	97.1	-2.9	2.26E+07	97	-3	0.6
4	2.27E+07	95	-5	2.24E+07	95.3	-4.7	2.21E+07	94.8	-5.2	1.3
7	2.22E+07	92.9	-7.1	2.18E+07	93.1	-6.9	2.20E+07	94.4	-5.6	0.7

Appendix Table E-4: *In vitro* serum results for NISTmAb in cynomolgus monkey serum.

	Replicate 1			Replicate 2			Replicate 3			
Time (Day)	**Mass Peak Area**	**Recovery (%)**	**Accuracy (%)**	**Mass Peak Area**	**Recovery (%)**	**Accuracy (%)**	**Mass Peak Area**	**Recovery (%)**	**Accuracy (%)**	**Precision (%CV)**
0	2.08E+07	Defined as 100.0	N/A	2.05E+07	Defined as 100.0	N/A	2.03E+07	Defined as 100.0	N/A	1.4
1	2.01E+07	96.5	-3.5	2.01E+07	98.2	-1.8	1.98E+07	97.7	-2.3	0.9
4	1.98E+07	95.2	-4.8	2.00E+07	97.5	-2.5	1.96E+07	96.9	-3.1	0.9
7	1.95E+07	93.8	-6.2	1.93E+07	94	-6	1.88E+07	92.8	-7.2	1.9

Appendix Table E-5: *In vitro* serum results for NISTmAb Fc fragment in mouse serum.

	Replicate 1			Replicate 2			Replicate 3			
Time (Day)	**Mass Peak Area**	**Recovery (%)**	**Accuracy (%)**	**Mass Peak Area**	**Recovery (%)**	**Accuracy (%)**	**Mass Peak Area**	**Recovery (%)**	**Accuracy (%)**	**Precision (%CV)**
0	3.41E+06	Defined as 100.0	N/A	3.13E+06	Defined as 100.0	N/A	3.13E+06	Defined as 100.0	N/A	5
1	3.43E+06	100.6	0.6	3.25E+06	103.8	3.8	3.12E+06	99.7	-0.3	4.8
4	3.73E+06	109.4	9.4	3.27E+06	104.5	4.5	3.06E+06	97.8	-2.2	10.2
7	3.55E+06	104.1	4.1	3.24E+06	103.5	3.5	3.22E+06	102.9	2.9	5.5

Appendix Table E-6: *In vitro* serum results for NISTmAb Fc fragment in rat serum.

	Replicate 1			Replicate 2			Replicate 3			
Time (Day)	**Mass Peak Area**	**Recovery (%)**	**Accuracy (%)**	**Mass Peak Area**	**Recovery (%)**	**Accuracy (%)**	**Mass Peak Area**	**Recovery (%)**	**Accuracy (%)**	**Precision (%CV)**
0	3.20E+06	Defined as 100.0	N/A	3.20E+06	Defined as 100.0	N/A	3.15E+06	Defined as 100.0	N/A	0.9
1	3.39E+06	105.9	5.9	3.43E+06	107.2	7.2	3.40E+06	107.9	7.9	0.6
4	3.39E+06	105.9	5.9	3.35E+06	104.7	4.7	3.40E+06	107.9	7.9	0.8
7	3.11E+06	97.2	-2.8	3.12E+06	97.5	-2.5	3.08E+06	97.8	-2.2	0.7

Appendix Table E-7: *In vitro* serum results for NISTmAb Fc fragment in cynomolgus monkey serum.

	Replicate 1			Replicate 2			Replicate 3			
Time (Day)	**Mass Peak Area**	**Recovery (%)**	**Accuracy (%)**	**Mass Peak Area**	**Recovery (%)**	**Accuracy (%)**	**Mass Peak Area**	**Recovery (%)**	**Accuracy (%)**	**Precision (%CV)**
0	4.29E+06	Defined as 100.0	N/A	4.17E+06	Defined as 100.0	N/A	4.06E+06	Defined as 100.0	N/A	2.7
1	4.71E+06	109.8	9.8	4.55E+06	109.2	9.2	4.52E+06	111.3	11.3	2.2
4	4.33E+06	100.9	0.9	4.44E+06	106.6	6.6	4.35E+06	107	7	1.4
7	4.30E+06	100.4	0.4	4.31E+06	103.5	3.5	4.33E+06	106.5	6.5	0.3